Siam Photon

SURANAREE UNIVERSITY OF TECHNOLOGY

สมาคมฟิสิกส์ไทย
THAI PHYSICS SOCIETY

PROCEEDINGS of
The First National Symposium on Physics Graduate Research

1st NSPG
29 June - 1 July 2006

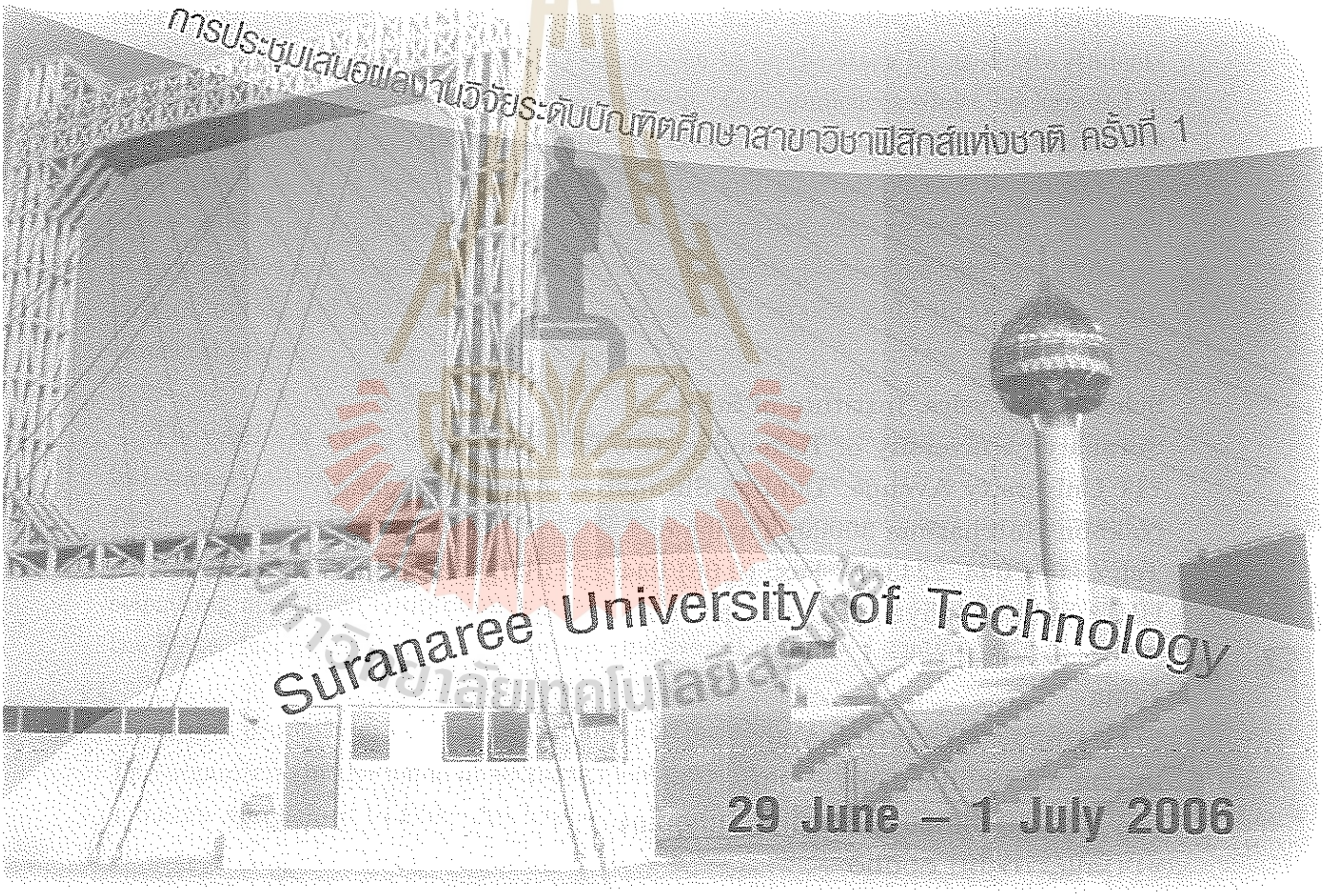

การประชุมเสนอผลงานวิจัยระดับบัณฑิตศึกษาสาขาวิชาฟิสิกส์แห่งชาติ ครั้งที่ 1

Suranaree University of Technology

29 June – 1 July 2006

ptt

PTTEP

PROCEEDINGS

The First National Symposium on Physics Graduate Research (1^{st} NSPG)
29 June – 1 July 2006
Chulabhorn Dam, Tambon Thung Lui Lai,
Amphoe Khon San, Chaiyaphum, Thailand
`http://physics3.sut.ac.th/symposium.asp`

รายงานการประชุม

การประชุมเสนอผลงานวิจัยระดับบัณฑิตศึกษาสาขาวิชาฟิสิกส์แห่งชาติครั้งที่ ๑
๒๙ มิถุนายน – ๑ กรกฎาคม ๒๕๔๙
ณ เขื่อนจุฬาภรณ์ ตำบลทุ่งลุยลาย
อำเภอคอนสาร จังหวัดชัยภูมิ

Organized by
School of Physics, Institute of Science,
Suranaree University of Technology (SUT),
111 University Avenue, Tambon Suranaree, Amphoe Muang,
Nakhon Ratchasima 30000, Thailand
Tel. (+66) 044–224319, Fax. (+66) 044–224185
URL: `http://physics3.sut.ac.th`

จัดโดย
สาขาวิชาฟิสิกส์ สำนักวิชาวิทยาศาสตร์
มหาวิทยาลัยเทคโนโลยีสุรนารี (มทส)
๑๑๑ ถนนมหาวิทยาลัย ตำบลสุรนารี อำเภอเมือง
จังหวัดนครราชสีมา ๓๐๐๐๐
โทรศัพท์ (+๖๖) ๐๔๔–๒๒๔๓๑๙ โทรสาร (+๖๖) ๐๔๔–๒๒๔๑๘๕

Preface

This is the First National Symposium on Physics Graduate Research (1^{st} NSPG) organized by the School of Physics, Institute of Science, Suranaree University of Technology (SUT). The symposium brought together graduate students in physics from 11 universities in Thailand. Over a hundred physicists participated in this symposium including 87 students and 18 academics.

The 1^{st} NSPG surpassed expectations. The arrangement of 20 minute presentation with two parallel sessions allowed the students to present their works in a friendly atmosphere. However, no one took it for granted. Many of the research works and presentations were excellent. Plenary sessions given by invited speakers and a special discussion in one evening on "Thai Physics: Past, Present and Future" by distingue physicists helped to increase the academic atmosphere of the symposium. The social program in the evening gave ample time for everyone to get to know each other, beneficial for future collaborations. In addition, the NSPG has proven to be the stage for graduate students in physics to practice their presentations in front of the audiences whose background in physics are more or less in the same level, enable them to broaden their physics knowledge in various fields including, condensed matter and material physics, astronomy and astrophysics, accelerator physics and synchrotron radiation sciences, cosmology and high energy physics, ion beam and plasma physics, nanoscale physics, nuclear and radiation physics, optics and photonics, industrial and applied physics, and educational and fundamental physics.

The results of a pilot project concerning with the expected research situation on physical science of the science faculties of 8 universities supported by the Thailand Research Fund show that there are very small numbers of Thai physicists and mathematicians who have potential in carrying out research. However, it is not too late if we start to do something now. This symposium is another effort that will help to bring Thai physics to the better future. So it is very important that we get supported continually.

In this proceeding, the full papers and abstracts of the presentations are collected. The organizers, in the name of all participants, wish to express their deep thanks to all sponsors who helped to make this happen.

We wish to thank everyone for his contribution to this symposium including, firstly, Assoc. Prof. Dr. Prasart Suebka, Rector of SUT (the first physicist to become a rector in Thailand), for leading us to the success of organizing the 1$^{\mathrm{st}}$ NSPG, secondly, the active students and staffs of the School of Physics, Institute of Science, SUT. Especially we want to thank Dr. Khanchai Khosonthongkee and Ms. Thunyaluck Theerapattaranggoon for their leading role in organizing this symposium and also a Ph.D. candidate at the School of Physics, SUT, Mr. Supiya Siranan and Mr. Ayut Limphirat for their hard working of formatting this proceeding. Last but by no means least, we would like to thank all participants for joining the symposium.

Prapan Manyum
Chair, Organizing Committee

Contents

APSRS05

AA01

CMMP02

CMMP03

CMMP04

CMMP09

Part I

Full Papers

Initial Magnetic Measurements of Soft X-Ray Undulator for the Siam Photon Source

การวัดสนามแม่เหล็กเริ่มต้นของอันดูเลเตอร์ผลิตแสงรังสีเอ็กซ์พลังงานต่ำของเครื่องกำเนิดแสงสยาม

THANANCHAI DASRI,[1,*] SUPACHAI PRAWANTA,[2] VISITCHAI SOOKSRIMUANG,[2]
SARAYUT SIRIWATTANAPITOON,[2] APICHAI KWANKASEM,[2] NATTHAWUT SURADET,[2]
PICIT KAEWBUTTA,[2] WINIT CHACHAI,[2] and SUPAGORN RUGMAI[1,2]
[1]*School of Physics, Institute of Science, Suranaree University of Technology,*
Nakhon Ratchasima, 30000, Thailand
[2]*National Synchrotron Research Center, P. O. Box 93,*
Nakhon Ratchasima, 30000, Thailand

Undulator is an insertion device installed in a synchrotron light source to enhance photon flux. The U60 is an undulator, having a magnetic period length of 60 mm, designed to generate intense soft x-rays for the soft x-ray beamline of the Siam Photon Source. A high precision magnetic measurement system has been constructed for magnetic field measurement of the device. Magnetic field distribution of the U60 has been measured with Hall probe scans. Measured magnetic fields are used to calculate field integrals and phase error of the undulator, in order to evaluate electron trajectories and deviation of electron path lengths in each magnetic period inside the undulator field which determine the quality of undulator light.

อันดูเลเตอร์เป็นอุปกรณ์แทรกในเครื่องกำเนิดแสงซินโครตรอนเพื่อเพิ่มความเข้มแสง อุปกรณ์ U60 เป็นอันดูเลเตอร์ที่มีความยาวคาบสนามแม่เหล็ก 60 มม. ออกแบบมาเพื่อเป็นแหล่งกำเนิดแสงซินโครตรอนความเข้มสูงย่านรังสีเอ็กซ์พลังงานต่ำ สำหรับระบบลำเลียงแสงรังสีเอ็กซ์พลังงานต่ำ ของเครื่องกำเนิดแสงสยาม ระบบวัดสนามแม่เหล็กความแม่นยำสูงได้ถูกสร้างขึ้น เพื่อทำการวัดสนามแม่เหล็กของอุปกรณ์ U60 โดยการวัดการกระจายค่าสนามแม่เหล็กด้วย Hall probe ค่าสนามแม่เหล็กที่วัดได้ถูกนำมาใช้คำนวณ field integral และ phase error ของอันดูเลเตอร์ดังกล่าว เพื่อที่จะหาแนวการเคลื่อนที่ของลำอิเล็กตรอน และความแตกต่างของระยะทางการเคลื่อนที่ของอิเล็กตรอนในแต่ละคาบแม่เหล็กของอันดูเลเตอร์ ซึ่งปริมาณดังกล่าว จะเป็นตัวกำหนดคุณภาพของแสงซินโครตรอนจากอันดูเลเตอร์

PACS numbers: 07.85.Qe
Keywords: Insertion Device, Synchrotron radiation, Magnetic measurement.

INTRODUCTION

The Siam Photon Source (SPS) is located in the campus of Suranaree University of Technology, Nakhon Ratchasima, the North Eastern Part of Thailand. The SPS is now operating at the electron beam energy of 1.2 GeV. It has three experimental stations which consist of Photoemission spectroscopy (BL-4), X-ray Lithography (BL-6) and X-ray Absorption Spectroscopy (BL-8) [1]. Synchrotron light used by all of station is generated by the bending magnets with synchrotron radiation critical energy of 1.32 keV.

However, the synchrotron light emitted by bending magnets is not intense enough for more sophisticated, high resolution research. The storage ring of SPS has been designed for 'Insertion Devices', having in four straight sections. Each of the straight section is 5.2 meters long. These devices consist of magnet blocks of alternating polarity that repetitively bend electron beam back and forth. Undulator is one type of Insertion devices. Due to the constructive interference of the radiation emitted by electron beam at the various poles, the opening angle at any given wavelength of the radiation is decreased by $\sqrt{N}$, where

N is the number of periods, and radiation intensity per solid angle is proportional to N^2 [2–6]. Therefore, the undulator radiation is emitted in narrower cone and more intense than the bending magnet radiation.

However, the intensities of synchrotron light from real undulators are lower than the theoretical calculations [7–10]. This fact arises from magnetic field errors which can be represented by first and second field integrals [9, 11], phase error [7, 8] and error storage [12]. Therefore, the undulator magnetic field distribution must be measured to obtain the first and second field integrals, phase error and error storage. The most common method of undulator magnet field distribution measurements is the point by point measurement performed by Hall probe scanning. The integrated field measurements can be performed by the long flipping coil techniques.

This report presents the undulator magnetic field measurement with Hall probe technique as well as the results field errors calculation.

THE UNDULATOR OF THE SPS (U60)

The general characteristic

The U60 undulator is a pure permanent magnet planar (PPM) undulator. It is designed to utilize the radiation in the photon energy range of 27–900 eV. The main parameters are shown in the table I.

The magnetic structure

The magnetic structure of the U60 undulator is shown in the Figure 1. Figure 1a) shows the U60 undulator, having the total length of 2510 mm. Figure 1b) shows magnetic structure. It consists of 40.5 full of full size periods and added by the end a horizontally magnetized block. This special end block reduces the field integral variation with gap.

Table I: Parameters of the U60.

parameters	data
Magnet material	NdFeB
Period length	60 mm
Gap distance	26–200 mm
Number of full size periods	40.5
Number of full size poles	81
Total number of poles	83
Peak flux density (average at 26 mm gap)	0.5733 T
Transverse roll off (at 26 mm gap):	
$x = \pm 5$ mm (average)	0.072%
$x = \pm 10$ mm (average)	0.31%
Minimum photon energy (26 mm gap, 1 GeV beam)	27.1 eV

The magnetic field simulation

Simulations of the magnetic field of the U60 are performed by using the code RADIA [10]. Figure 2a) shows the on axis ($x = y = 0$ mm) magnetic field at the minimum gap (26 mm). Figure 2b) shows the undulator peak magnetic field as a function of undulator gap.

FIELD DISTRIBUTION MEASUREMENTS

Description

Figure 2a) is the simulated field distribution of the U60, the most common technique for obtaining detail information about the field distribution of an undulator is by the Hall probe scanning. A high density of points is generally used between 20 and 100 points per periods, which is sufficient for trajectory and radiation [3]. In order to minimize the measurement time, data are taken "on-the-fly" rather than "step-by-step" and speed of between 20 and 50 mm/s are commonly used. However, factors of the position accuracy of probe along the z-axis, resolution and noise of the Hall signals, and the accurate calibration of the Hall probe must to be taken into consideration [3, 11].

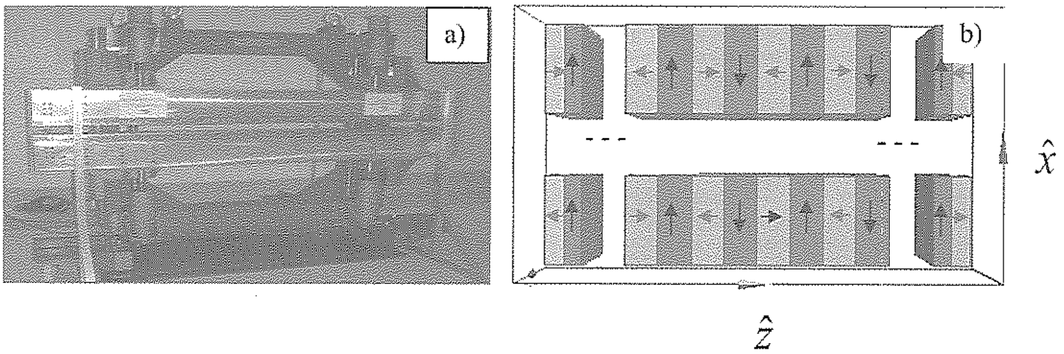

Figure 1: (color online). a) the U60 undulator and b) the magnetic structure, where arrows indicate direction of magnetization of each magnet block.

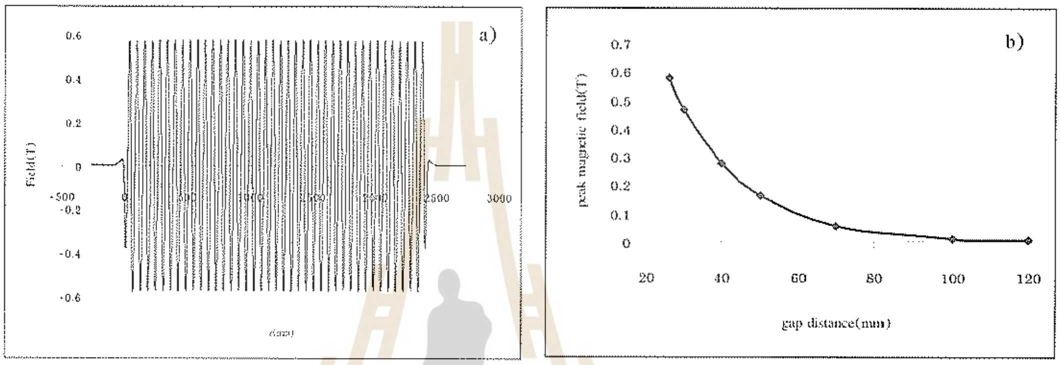

Figure 2: The simulated magnetic field of the U60 undulator (a) and undulator peak magnetic field as a function of undulator gap (b).

Measurment system of the SPS

Hall probe system of the SPS was installed in 2004. Hall was held on the test bench of 3010 mm longs. The test bench (shown in fig. 3a) consists of more than ten components accurate positioned by the Laser tracker during the installation (shown in fig. 3a and 3b). The Hall probe can be moved in 3-direction, z (longitudinal), x (horizontal) and y (vertical), independently. At present, it can measure only the vertical field. The movement in each direction is driven by the stepping motor and can be moved only one direction at a time. The x, y and z positions are measured by a linear encoder having a accuracy of 1 µm. The lengths of travel in x, y and z axis are 250, 250 and 2680 mm, respectively. All motion are controlled by LabVIEW programming on PC.

Hall probe measurements

A group3 Hall probe, is used at the SPS. Before measurement the probe was reset to zero by zero gauss chamber. Data collection of the field distribution was managed by the software on PC. The software controlling the movement of the Hall probe was set up for continuous scans for the optimal speed. The measured field data were saved every 1 mm and the probe position from the encoder are recorded along the longitudinal axis. The field distributions were measured at various undulator gap.

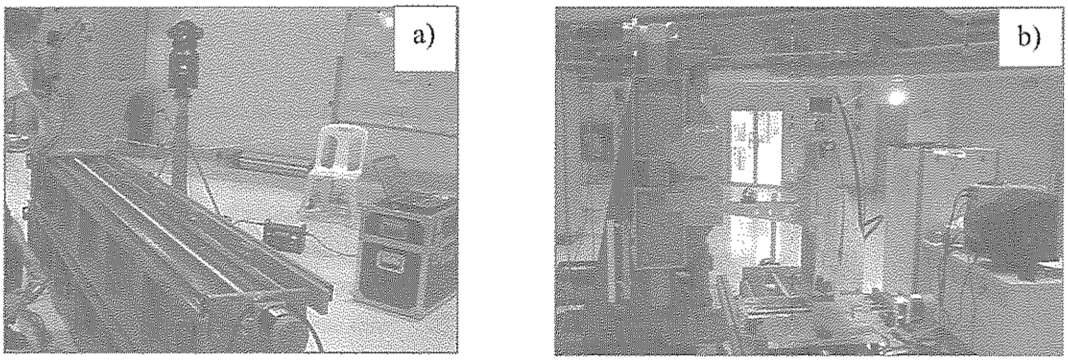

Figure 3: (color online). Show the Hall probe system and installation.

FIELD ERROR CALCULATIONS

The first and second field integral

A deflection angle of a relativistic electron moving in a periodic field, $B(z'')$, is given by

$$x'(z) = \frac{0.3}{E(\mathrm{GeV})} I(z) \tag{1}$$

where E is an electron energy in GeV and where the first field integral is defined as

$$I(z) = \int_{-\infty}^{z} B(z')\,\mathrm{d}z' \tag{2}$$

where B is the magnetic field. The trajectory of a relativistic electron is found as

$$x(z) = \frac{0.3}{E(\mathrm{GeV})} J(z) \tag{3}$$

where the second field integral is defined as

$$J(z) = \int_{-\infty}^{z} \int_{-\infty}^{z'} B(z'')\,\mathrm{d}z''\,\mathrm{d}z'\,. \tag{4}$$

Phase error (Phase shake)

The second parameter of the field error is phase error which defined as

$$\Delta\delta = \delta_{\mathrm{real}} - \delta_{\mathrm{ideal}} \tag{5}$$

where δ_{real} and δ_{ideal} are phase function in real and ideal case of an electron, respectively. They are given by

$$\delta(z) = \frac{2\pi}{\lambda_{\mathrm{s}}} \left(\frac{z}{2\gamma^2} + \int_{-\infty}^{z} \frac{x'^2}{2}\,\mathrm{d}z \right) \tag{6}$$

where x' is the angular deflection, λ_{s} is the resonance condition, defined as

$$\lambda_{\mathrm{s}} = \frac{\lambda_{\mathrm{u}}}{2n\gamma^2} \left(1 + \frac{K^2}{2} + \gamma^2\theta^2 \right)$$

where K is the wiggler strength, λ_{u} is the period length of the magnetic field, γ is the ratio between kinetic energy and rest energy of the electron, θ is observing angle from the axis and $n = 1, 2, 3, \ldots$ is integer.

Equation (5) means that the path length of an electron in each period will be deviated from an ideal case, if phase error is not zero. Nonzero phase error give rise to imperfect constructive interference of the synchrotron radiation emitted from each period of the undulator.

Error storage

Error storage is another method for representing the field error [12]. It is defined by the equation as

$$\mathrm{ES}_n = \sum_{m=1}^{n} \frac{|L_m| - \langle L \rangle}{\langle L \rangle} \tag{7}$$

where L_m is the first field integral at the m^{th} pole and $\langle L \rangle$ is the mean value of L_m.

Equation (7) tells how the field integral deviation is stored with an increasing pole number.

RESULTS AND DISCUSSION

The magnetic field

Figure 4 shows results of the measured vertical field, $B_y(0,0,z)$, of the U60 by Hall probe scanning at various undulator gap. These field measurement are used to calculate the parameters to estimate the field errors of the U60.

The field integral

The first and second field integrals are shown in Figure 5b) and 5c), respectively. Ideally, an electron is not deflected after passing through an undulator. That requires the longitudinally integrated vertical field, the first and second field integral, must vanishe. In addition, an electron enter on-axis must exit on-axis (the second field integral). However, the calculated angle and trajectories show that an electron is deviated from the axis, which resulted from nonzero field integrals.

Error storage

Figure 5d shows the error storage obtained from field distribution measurements at the different gap distance. The error storage, given equation (7), indicates that the accumulated field integral deviation is increasingly or decreasingly stored with an increasing pole number. The results in figure 5d show that the accumulated error of the of U60 increases with larger pole number.

Phase error

The results of phase error shown in Figure 5e are also calculated from field distribution measurements at the difference gap distances. The phase error, expressed in equation (5), describes the deviation of the real path length from the ideal undulator. So if the phase error is zero or small, the constructive interference of the photon radiated by an electron is excellent. The average of the RMS phases error for the first harmonic, at zero observing angle, in figure 5e are 2.5864, 2.5481, 2.1320 and 1.8463 degrees at the wiggler strengths of 2.9542, 1.9389, 1.4916 and 0.8820, respectively.

CONCLUSION

We have presented measurements and calculations of the U60 field characteristic. The magnetic measured field distribution using Hall probe has been used to calculate the field integrals, phase errors and error storages. The studies are carried out to predict the optical performance of the U60.

Acknowledgements

The author would like to thank, the National Synchrotron Research Center, Thailand for partial financial support, Prof. Helmut Wiedemann for advise on analysis and calculation.

---

* ชื่อไทย: ธนัญชัย ดาศรี
Email: `Thananchai_Dasri@hotmail.com`

[1] `http://www.nsrc.or.th/th/`.

[2] P. J. Duke, *Synchrotron Radiation: Production and Properties*, Oxford University Press, New York (2000).

[3] H. Winick (ed.), *Synchrotron Radiation Sources: A Primer*, World Scientific, Singapore (1994).

[4] H. Wiedemann, *Particle Accelerator Physics II: Nonlinear and Higher-Order Beam Dynamics*, Springer, Berlin (1995).

[5] P. Elleaume, *"Introduction to Insertion Devices"*, CAS - CERN Accelerator School 2005, Trieste (2 14 October 2005).

[6] P. Elleaume, *"Lecture on Insertion Devices"*, CAS - CERN Accelerator School 2003, Trieste (2 9 July 2003).

[7] R. P. Walker, *"Interference Effects in Undulator and Wiggler Radiation Sources"*, Nucl. Instrum. Methods Phys. Res. A **335** (1-2), 328-337 (1993).

[8] B. L. Bobbs *et al.*, *"In Search of a Meaningful Field-Error Specification for Wigglers"*, Nucl. Instrum. Methods Phys. Res. A **296** (1-3), 574-578 (1990).

[9] Yu. M. Nikitina and J. Pflüger, *"Influence of Magnetic Field Errors on the Spectrum of the PETRA*

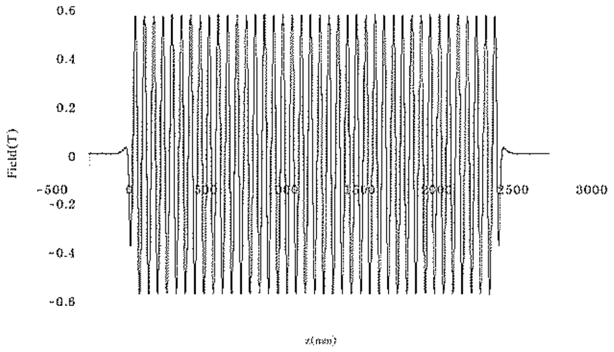

Figure 4: The measured vertical field of 0.5270 tesla peak field.

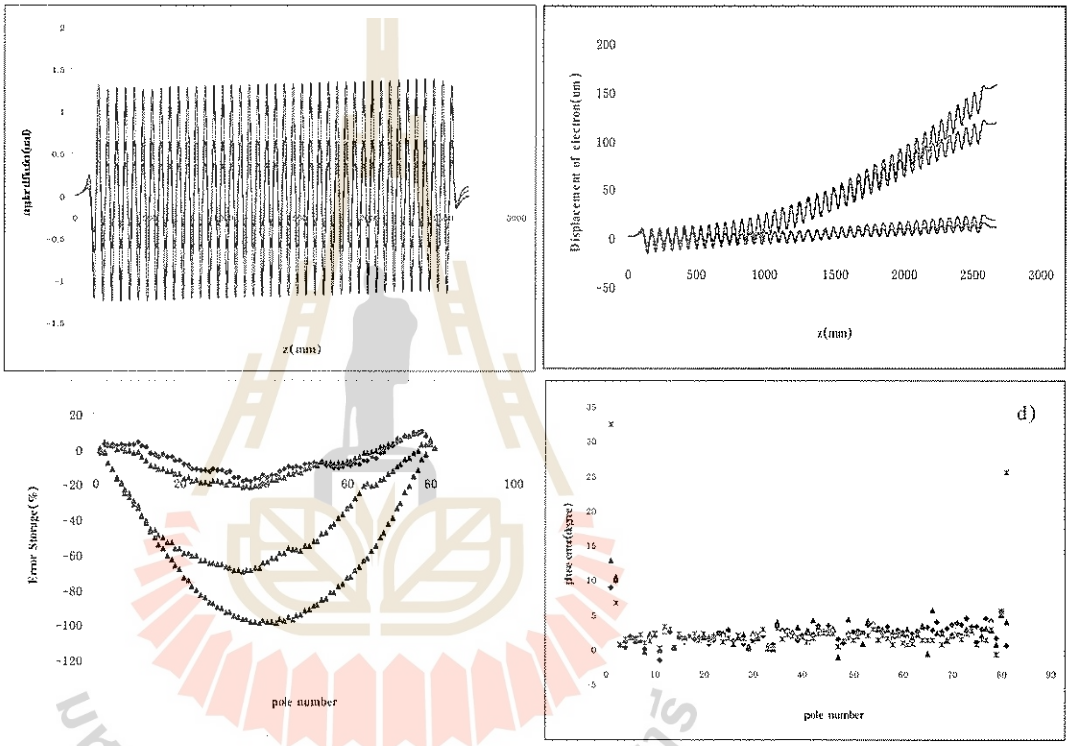

Figure 5: (color online). a) The first field integral, b) second field integral, c) Error storage and d) Phase error. The results are for the different undulator gaps, corresponding to the wiggler strength of 2.9542, 1.9389, 1.4916 and 0.8820, represented by dark blue, pink, orange and green line, respectively.

Undulator", Nucl. Instrum. Methods Phys. Res. A **359** (1-2), 89–92 (1995).

[10] A. Hiraya *et al.*, *"Analysis for Magnetic and Radiation Spectral Properties of Undulators at HISOR"*, in A. Luccio and W. MacKay (eds.), *Proceedings of the 1999 IEEE Particle Accelerator Conference, New York (27 March – 2 April 1999)*, Volume **4**, pp. 2689–2691.

[11] J. Qi-ka, *"Field Integrals Error of Undulator"*, Nucl. Instrum. Methods Phys. Res. A **428** (2–3), 589–592 (1999).

[12] Y. Tanaka *et al.*, *"Timing Control of an Intense Picosecond Pulse Laser to the SPring-8 Synchrotron Radiation Pulses"*, Rev. Sci. Instrum. **71**

(3), 1268–1274 (2000).

[13] A. Temnykh, *"Vibrating Wire and Flipping Coil Magnetic Measurement of a CESR-c 7-Pole Wiggler Magnet"*, in J. Chew, P. Lucas and S. Webber (eds.), *Proceedings of the 2003 IEEE Particle Accelerator Conference, Portland, Oregon U.S.A. (12–16 May 2003)*, Volume **2**, pp. 1026–1028.

[14] O. Chubar, P. Elleaume and J. Chavanne, *"A Three-Dimensional Magnetostatics Computer Code for Insertion Devices"*, J. Synchrotron Rad. **5** (3), 481–484 (1998). The RADIA code is freely available from: `http://www.esrf.eu/Accelerators/Groups/InsertionDevices/Software/Radia`

OH Masers Associated with Bipolar Molecular Outflows in Onsala1 Star-Forming Region[*]

ไฮดรอกซิลเมเซอร์ที่สัมพันธ์กับการเกิดลำก๊าซพวยพุ่งของโมเลกุล ในบริเวณ ON1

KITTYANEE ASANOK,[1,†] SUWIT NAMMAHACHAK,[1] BUSABA HUTAWARAKORN KRAMER,[2]
JIM COHEN,[3] ORRARUJEE MUANWONG,[1] and NIPON GASIPRONG[4]

[1] *Department of Physics, Faculty of Science, Khon Kaen University,*
Khon Kaen, 40002, Thailand
[2] *National Astronomical Research Institute of Thailand,*
Department of Physics Building, Chiang Mai University, Chiang Mai 50200, Thailand
[3] *University of Manchester, Jodrell Bank Observatory,*
Macclesfield, Cheshire SK11 9DL, United Kingdom
[4] *Department of Physics, Faculty of Science, Ubon Rajathanee University,*
Ubon Rajathanee, 34190, Thailand

The Multi-Element Radio Linked Interferometer Network (MERLIN) polarization measurements of the OH 1665-MHz masers emission from the bipolar outflow source ON1 are studied. The OH masers are distributed over a region 3.5 arcsec a side, which is elongated in a north-west-south-east (NW-SE) direction. The distribution is interpreted in terms of a disc surrounding the source of the outflow. The main velocities of OH masers are close to the central velocity (15 $\mathrm{km\,s^{-1}}$). Comparing the distribution of OH masers with previous work shows close matched in positions with those determined using the Very Large Array (VLA) of National Radio Astronomy Observatory (NRAO), plus 6 new maser features separated from the other masers. Analysis of the OH maser polarization reveals three Zeeman Pairs, with field strengths −0.97, −1.49 and −2.07 mG (directed toward us). The fields are strong enough to be important in the star formation process. Circular polarization of the OH masers in this source is very strong ($\sim 94\%$) while linear polarization is weak ($\sim 32\%$). The linear polarization vectors are predominantly either perpendicular or parallel to the HCO^+ outflow direction. Thus, the OH masers observed associated with bipolar molecular outflow.

การศึกษาโพลาไรเซชันของไฮดรอกซิลเมเซอร์ในบริเวณเกิดดาว ON1 ที่ความถี่ 1665 MHz โดยใช้ข้อมูลของ MERLIN ประเทศสหราชอาณาจักรพบว่า ไฮดรอกซิลเมเซอร์กระจายตัวจากทิศทางตะวันออกเฉียงเหนือไปทางตะวันตกเฉียงใต้ด้านละ 3.5 arcsec และมีรูปร่างคล้ายแผ่นดิสก์ล้อมรอบบริเวณเกิดลำก๊าซพวยพุ่ง ความเร็วของไฮดรอกซิลเมเซอร์ที่วัดได้ส่วนใหญ่ ให้ค่าใกล้เคียงกับความเร็วศูนย์กลางของ ON1 (15 กิโลเมตรต่อวินาที) เมื่อเปรียบเทียบข้อมูลการกระจายตัวของไฮดรอกซิลเมเซอร์กับผลงานที่ผู้อื่นได้ทำก่อนหน้านี้ พบว่าตำแหน่งที่ MERLIN วัดได้เกือบจะตรงกับตำแหน่งที่วัดได้โดย VLA ของ NRAO และพบไฮดรอกซิลเมเซอร์ที่แยกออกจากกลุ่มของเมเซอร์อีก 6 ลักษณะข้อมูล Zeeman Pairs ที่วัดได้มีจำนวน 3 คู่ ค่าสนามแม่เหล็กเป็น −0.97, −1.49 และ −2.07 mG ตามลำดับ ดังนั้นค่าสนามแม่เหล็กที่ได้นี้ เพียงพอและเป็นปัจจัยสำคัญต่อขั้นตอนการเกิดดาว ข้อมูลโพลาไรเซชันแบบวงกลมของไฮดรอกซิลเมเซอร์ให้ค่า $\sim 94\%$ ในขณะที่โพลาไรเซชันแบบเชิงเส้นให้ค่า $\sim 32\%$ โพลาไรเซชันแบบเชิงเส้นของไฮดรอกซิลเมเซอร์มีทิศทางทั้งขนานและตั้งฉากกับลำก๊าซพวยพุ่งของ HCO^+ ดังนั้นการเกิดลำก๊าซพวยพุ่งของโมเลกุลจึงมีความสัมพันธ์กับไฮดรอกซิลเมเซอร์

PACS numbers: 97.10.Bt, 97.10.Ld, 97.21.+a, 98.35.Ac, 98.38.Er, 98.58.Ec, 98.62.Ai
Keywords: magnetic fields, masers, polarization, stars: formation, ISM: individual: ON1, ISM: jets and outflows

---

[*] cf. Mon. Not. R. Astron. Soc. **371** (2), 619-625 (2006).

INTRODUCTION

Star formation process is an outstanding and largely unsolved problem in astrophysics. The role of the magnetic field is unclear but it is widely considered to be important at all stages of protostellar evolution, from cloud collapse to the ZAMS. In some hydromagnetic models, the magnetic field may help in removing angular momentum, therefore driving accretion and perhaps bipolar molecular outflows. The Zeeman splitting of components of the 18 cm OH masers lines provides a direct way of measuring the magnetic field in transverse and line-of-sight components. MERLIN at Jodrell Bank Observatory, United Kingdom has high sensitivity and resolution necessary for such spectral-line imaging (see for example [5]). Therefore, this research will concentrate on the process of star formation, in particular the physical properties of OH masers such as energy (in terms of intensity of signal), location, velocity and magnetic field using the reduced data at 1665 MHz from MERLIN. The data were reduced and mapped by Suwit Nammahachak (Ph.D. student at Department of Physics, Faculty of Science, Khon Kaen University, Thailand). Onsala 1 or ON1 which is a star-forming region is chosen for our study, having a well-defined bipolar molecular outflow [6, 7, 8].

METHODOLOGY

Reduced and mapped data of ON1 star-forming region are obtained from MERLIN at Jodrell Bank Observatory, University of Manchester, United Kingdom. The dates of observations were 1–2 March 1996. The data which have been mapped and analysed using the Astronomical Image Processing System (AIPS) from which we can obtain intensity, location and frequency of each maser. The results from AIPS are used to study the kinematics of masers by the following procedures. The intensity is used to identify masers on the map in order to obtain their distribution in the region. The frequency is then used to calculate the velocity with respect to the average group velocity using the principle of Doppler shift effect. In order to determine the strength of the magnetic field and to map the field structure, the peak signals of the left-hand and right-hand circularly polarized of the lines and splitting between them (in terms of frequency) are obtained. Such a splitting is the result of the Zeeman effect, hence the determination of the value of the magnetic field.

RESULTS AND DISCUSSION

OH Maser Distribution

The results of circularly polarised emission are summarized in Table 1, which show the velocity, position, position uncertainty, and peak flux density of each circularly polarised OH maser. The positions related to the zero-point at R.A.(J2000) = $20^{h}10^{m}09^{s}.23$, Dec.(J2000) = $31°31'36''.37$. Maser emissions are detected from 28 different spectral features. Nineteen features are seen in left circular polarisation (LCP) and nine features are seen in right circular polarisation (RCP). The velocity profiles of each feature in both RCP and LCP cover the velocity range of 22 km s^{-1} (from 6 km s^{-1} to 28 km s^{-1}) which does not include another group of OH maser emissions at the velocity between 0 km s^{-1} to 6 km s^{-1} as seen in Argon *et al.* [1]. The OH masers are distributed over a region of 3.5 arcsec a side, which is elongated in a north west and south east (NW-SE) direction. The elongation is approximately orthogonal to the projected direction of the bipolar outflow seen in HCO^{+} [8]. The distribution is interpreted in terms of a disc surrounding the source of the outflow. Comparing the distribution of OH masers with Argon *et al.* [1] which show good match of positions with VLA of NRAO and in the southern part from 1.5 to -1 arcsec in RA offset. With MERLIN resolution, six features of LCP are separated from other masers and have weak peak flux which are less than 1 Jy $beam^{-1}$. This suggests that MERLIN resolution can observe molecular positions better than the VLA while it has sensitivity less than the Very-Long-Baseline-Interferometry (VLBI).

OH Maser Kinematics

Some velocities distributions are similar to the model of velocity distributions of the 1665 MHz OH masers by Gray *et al.* [3] where the bluest velocities appear for masers in the north of the map, while the reddest velocities appear near the centre and in the southern part of map (see Figure 1). The main velocities of OH masers are near the central velocity (15 kms^{-1}). Thus, the OH masers are possibly slow moving with respect to the center of ON1.

Magnetic Field in ON1

Analysis of the OH maser polarization reveals three Zeeman Pairs, with field strengths ranging from −0.97, −1.49 and −2.07 mG (directed toward us). Comparing the magnetic pressure $B^2/2\pi$ with the kinetic energy density $\rho V^2/2$, for typical H_2 densities of 10^6 cm^{-3} and typical velocities of 3 $\mathrm{km\,s}^{-1}$ we find that the fields are strong enough to be dynamically important in the star formation process. Circular polarization of the OH masers in this source is very strong, ~ 94% while linear polarization is weaker, ~ 32% (see Table II).

Relation of Masers to Molecular Outflow

The linear polarization vectors are predominantly either perpendicular or parallel to the outflow direction. The linear polarization vectors imply that the transverse magnetic field directions are either parallel or perpendicular to the outflow, therefore, supporting the hydromagnetic model proposed by Uchida and Shibata [9]. ON1 has linear polarisations, both parallel and orthogonal to the outflow direction, while its maser distribution is orthogonal to the outflow direction. From previous MERLIN observations in NGC7538 [4], the linear polarisation vectors are the most organized, both parallel and orthogonal to the outflow especially in Infrared Sources 11 (IRS 11) which the result of the percentage of polarisation are likely ON1 (see Figure 2). Moreover, full polarisation measurements of the OH emission show systematic difference between IRS 1, IRS 9 and IRS 11 while they can trace a possible evolutionary sequence from oldest (IRS 1) to youngest (IRS 11). In this case, if compare between the polarisations of ON1 with IRS 11, ON1 will have the evolution in the young old. Thus plotting the diagram is a method to analyse the evolution sequence of star forming region. Cohen [2] suggested that the polarisation properties are age related with younger sources being more highly organized, having stronger polarisation and greater alignment with the outflow direction.

CONCLUSION

The OH masers are distributed over a region of 3.5 arcsec a side, which is elongated in a north-west-south-east (NW-SE) direction. The elongation is approximately orthogonal to the projected direction of the bipolar outflow seen in HCO^+. The distribution is interpreted in terms of a disc surrounding the source of the outflow. The main velocities of OH masers are near the central velocity (15 $\mathrm{km\,s}^{-1}$). Thus the OH masers are possibly slow moving with respect to the center of ON1. Comparing the distribution of OH masers with previous work shows close matched positions with those measured using the Very Large Array (VLA) of National Radio Astronomy Observatory (NRAO). We also detected 6 maser features that are separated from the other masers. This suggests that MERLIN resolution can observe molecular positions better than the VLA while it has resolution less than that of Very-Long-Baseline-Interferometry (VLBI). Analysis of the OH maser polarization reveals three Zeeman Pairs, with field strengths ranging from −0.97, −1.49 and −2.07 mG (directed toward us). Comparing the magnetic pressure $B^2/2\pi$ with the kinetic energy density $\rho V^2/2$, for typical H_2 densities of 10^6 cm^{-3} and typical velocities of 3 $\mathrm{km\ s}^{-1}$ we find that the fields are strong enough to be dynamically important in the star formation process. Circular polarization of the OH masers in this source is very strong, ~ 94% while linear polarization is

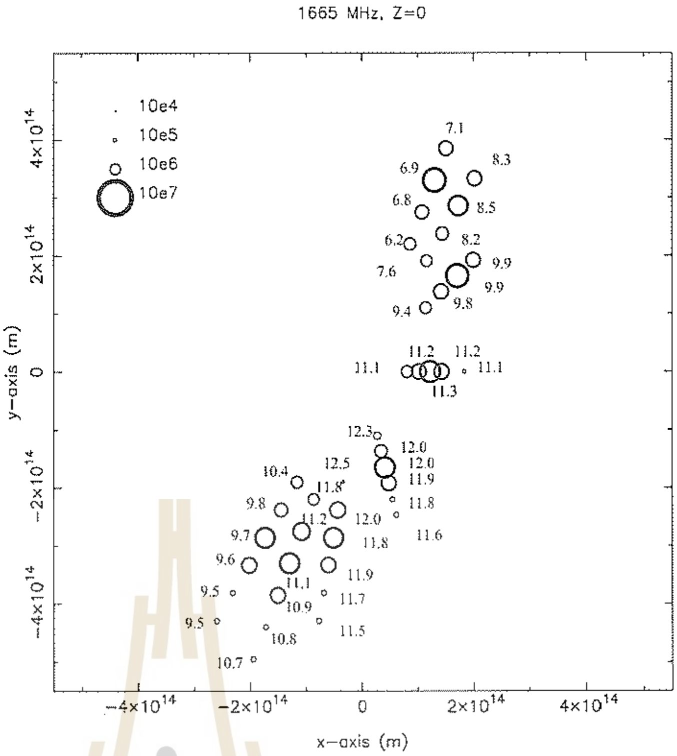

Figure 1: The distribution of model maser spots in the disc plane at 1665 MHz. Stokes *I* amplification factor is indicated by the size of the circles; numbers indicate the line-of-sight velocity in km s^{-1}. (Source: Figure 8 of Gray *et al.* [3])

weak, ~ 32%. The linear polarization vectors are predominantly either perpendicular or parallel to the outflow direction. The linear polarization vectors imply that the transverse magnetic field directions are either parallel or perpendicular to the outflow, therefore, supporting the hydromagnetic model proposed by Uchida and Shibata [9].

SUGGESTIONS

1. In this work the polarisation properties of the 1665 MHz OH masers have been studied. However, the polarisation study of other transitions of OH masers (e.g. 1612, 1667, and 1720 MHz) will help to confirm and complement to the result from this work.

2. Comparing the distribution of OH masers with Argon *et al.* [1] which show nearly match positions with VLA of NRAO. There are 6 features of masers which are separated from other masers and have weak peak flux being less than 1 Jy beam^{-1}. This suggests that MERLIN has sensitivity more than the VLA. The observations at higher sensitivity (such as VLBI) may be able to measure the polarisations and magnetic fields of the weak masers.

3. Observations of more samples of OH masers in Star Forming Regions (SFRs) will help to confirm the method of using polarisation and ordered of to identify the age of star-forming regions.

ACKNOWLEDGEMENT

One of the authors (Kitiyanee Asanok) would like to thank the advisor, Dr. Orrarujee Muanwong

Table I: OH maser features in ON1. Flux weighted mean velocities and positions are given for each feature in both polarization. The positions are given related to zero-point at R.A.(J2000) = $20^h10^m09^s.23$, Dec.(J2000) = $31°31'36''.37$.

Trnasition	Feature	Stokes I No.	Velocity[a] (km s^{-1})	ΔR.A.[b] (arcsec)	ΔDec.[b] (arcsec)	σ_{RA}[c] (arcsec)	σ_{Dec}[c] (arcsec)	Peak flux[d] (Jy $beam^{-1}$)	Comment
1665-LCP:									
	A	20	6.16	−2.046	−0.386	0.008	0.010	0.37	
	B	19	11.60	−1.628	−1.803	0.004	0.002	0.30	
	C1	18	11.83	−2.965	−0.722	0.003	0.002	0.70	Z_1 − 2.07 mG
	D	–	12.90	−1.962	−1.389	0.040	0.004	0.14	
	C2	–	12.97	−2.962	−0.729	0.011	0.011	0.27	Z_1
	E1	15	13.68	−1.962	−0.862	0.013	0.007	1.90	Z_2 − 0.97 mG
	E2	13	13.93	−1.962	−0.865	0.011	0.011	2.75	Z_2
	F1	–	14.19	−1.751	−1.915	0.002	0.005	0.60	
	G1	–	14.22	−1.850	−1.394	0.003	0.001	12.30	Z_3 − 1.49 mG
	H	–	14.29	−2.386	−1.180	0.004	0.004	5.77	
	F2	8	14.96	−1.737	−1.899	0.001	0.003	1.07	
	G2	7	14.97	−1.845	−1.396	0.002	0.001	18.64	Z_3
	I	6	14.98	−1.716	−0.884	0.010	0.006	0.57	
	J	9	14.98	−1.165	−1.572	0.037	0.009	0.29	
	K	5	15.02	−2.411	−0.893	0.009	0.003	0.22	
	L	4	15.04	−3.307	−1.606	0.007	0.010	0.20	
	M	3	15.23	−2.835	−0.676	0.011	0.009	0.75	
	N	2	16.37	−2.123	−1.800	0.018	0.004	0.37	
	O	1	16.37	−2.233	−1.297	0.015	0.004	6.63	
1665-RCP:									
	c1	–	11.75	−2.903	−0.767	0.019	0.029	0.59	Z_1
	c2	16	12.83	−2.903	−0.712	0.002	0.005	0.46	Z_1
	d	17	12.86	−1.997	−1.391	0.003	0.001	17.43	
	e1	–	13.36	−1.969	−0.851	0.019	0.015	0.98	Z_2
	p	14	13.63	−2.266	−1.287	0.003	0.008	3.47	
	g1	11	14.09	−1.846	−1.396	0.005	0.002	22.57	Z_3
	r	12	14.10	−2.776	−0.677	0.025	0.019	0.61	
	h	10	14.19	−2.388	−1.182	0.012	0.009	8.51	
	g2	–	14.82	−1.846	−1.397	0.006	0.007	0.59	Z_3

[a] Velocity with respect to the local standard of rest (LSR), assuming a rest frequency of 1665.402 MHz.

[b] R.A. and Dec. offset from zero-point at R.A.(J2000) = $20^h10^m09^s.23$, Dec.(J2000) = $31°31'36''.37$.

[c] The positional uncertainties in each feature are calculated from the standard deviation of the position of the components in that R.A. and Dec. of each feature.

[d] Peak flux density in Janskys per beam.

for her suggestion and supervision on my thesis. It is a great pleasure to work with Dr. Jim Cohen and Dr. Busaba Hutwarakorn Kramer. I would like to thank them for suggesting such as an interesting project and for helpful guidance and also thank Dr. Nipon Gasiprong for helping on my funding and thesis. Thanks also to Suwit Nammahachak for ON1's mapping and suggestions on my project. I would like to thank Department of Physics, Faculty of Science, Khon Kaen University for using facilities and also thank Jodrell Bank Observatory, United Kingdom for ON1's data. I gratefully ac-

Table II: The Stokes parameter flux (I,Q,U,V) and the polarization properties of OH maser features in ON1. The flux weighted mean velocities and positions are given for each feature.

No.	Vel. (km s^{-1})	$\Delta\alpha^{e}$ (arcsec)	$\Delta\delta^{e}$ (arcsec)	I (Jy b^{-1})	Q^{f} (Jy b^{-1})	U^{f} (Jy b^{-1})	V^{f} (Jy b^{-1})	P (Jy b^{-1})	χ (°)	m_L (%)	m_C (%)	m_T (%)
1	16.37	−2.233	−1.297	3.339	0.007	0.330	−3.181	0.330	–	9.9	−95.3	95.8
2	16.35	−2.124	−1.797	0.154	−0.011	0.014	−0.124	0.018	–	11.5	−80.4	81.3
3	15.23	−2.836	−0.676	0.367	0.005	−0.025	−0.363	0.025	–	6.9	−98.9	99.1
4	15.06	−3.284	−1.588	0.132	−0.017	−0.002	−0.027	0.017	–	12.8	−20.3	24.0
5	15.01	−2.408	−0.891	0.119	−0.013	0.008	−0.085	0.015	–	12.7	−71.2	72.3
6	14.99	−1.707	−0.883	0.224	0.006	0.016	−0.256	0.017	–	7.5	−114.4	114.7
7	14.97	−1.846	−1.396	9.561	−0.360	3.031	−8.973	3.052	48	31.9	−93.9	99.1
8	14.97	−1.741	−1.899	0.526	0.020	0.129	−0.505	0.131	–	24.8	−96.0	99.1
9	14.95	−1.127	−1.582	0.168	−0.018	0.014	−0.088	0.023	–	13.4	−52.6	54.3
10	14.23	−2.386	−1.181	7.295	−2.722	−4.162	1.656	4.973	−62	68.2	22.7	71.9
11	14.13	−1.847	−1.395	17.411	−13.061	−5.629	6.453	14.222	−78	81.7	37.1	89.7
12	14.06	−2.791	−0.683	0.362	−0.138	−0.045	0.158	0.145	−81	40.0	43.6	59.2
13	13.86	−1.972	−0.854	1.603	−0.538	0.542	−0.590	0.764	68	47.6	−36.8	60.2
14	13.64	−2.268	−1.286	1.828	0.142	0.196	1.832	0.242	28	13.2	100.2	101.1
15	13.56	−1.965	−0.862	1.225	−0.391	0.446	−0.521	0.594	65	48.4	−42.5	64.5
16	12.88	−2.919	−0.716	0.375	−0.002	0.008	0.092	0.008	–	2.2	24.5	24.6
17	12.86	−1.996	−1.391	8.847	−0.075	−0.622	9.372	0.626	−48	7.1	105.9	106.2
18	11.81	−2.943	−0.738	0.605	0.042	−0.016	−0.038	0.045	–	7.5	−6.2	9.7
19	11.60	−1.626	−1.805	0.122	−0.007	0.009	−0.131	0.011	–	8.9	−107.0	107.4
20	6.16	−2.041	−0.392	0.179	0.005	0.000	−0.153	0.005	–	2.6	−85.2	85.2

[e] Angular offsets on the sky of the maser from the zero point toward the east (R.A.) and north (Dec.).

[f] Peak flux intensity in Stokes I and use the position of the I peak to measure peak flux in Stokes Q, U and V respectively.

knowledge receipt of Thai Cooperative Research Network Scholarship (CRN) in Astronomy.

[†] ชื่อไทย: กิติยาณี อาษานอก
Email: `kitiyanee_asanok@yahoo.com`

[1] A. L. Argon, M. J. Reid and K. M. Menten, *"Interstellar Hydroxyl Masers in the Galaxy I. The VLA Survey"*, Astrophys. J. Suppl. Ser. **129** (1), 159–227 (2000).

[2] R. J. Cohen, *"Observing Magnetic Fields in Star-Forming Regions"*. In Dense Molecular Gas around Protostars and in Galactic Nuclei: European Workshop on Astronomical Molecules 2004, pp. 27–36, Y. Hagiwara *et al.* (Eds.), Springer, Dordrecht (2005). Reprinted from Astrophys. Space Sci. **295** (1–2), 27–36 (2005).

[3] M. D. Gray, B. Hutawarakorn and R. J. Cohen, *"A Model of Polarized OH Maser Emission in W75N"*, Mon. Not. R. Astron. Soc. **343** (4), 1067–1080 (2003).

[4] B. Hutawarakorn and R. J. Cohen, *"OH Masers, Molecular Outflows and Magnetic Fields in NGC 7538"*, Mon. Not. R. Astron. Soc. **345** (1), 175–185 (2003).

[5] B. Hutawarakorn, R. J. Cohen and G. C. Brebner, *"OH Masers and Magnetic Fields in the Bipolar Outflow Source W75N"*, Mon. Not. R. Astron. Soc. **330** (2), 349–364 (2002).

[6] M. S. Nanda Kumar, R. Bachiller and C. J. Davis, *"H_2 Emission around Massive Young Stellar Objects with Outflows"*, Astrophys. J. **576** (1), 313–322 (2002).

[7] M. S. Nanda Kumar, C. J. Davis and R. Bachiller, *"The Earliest Stages of Massive Star Formation: Near and Mid Infrared Observations"*, Astrophys. Space Sci. **287** (1–4), 191–194 (2003).

[8] M. S. Nanda Kumar, M. Tafalla and R. Bachiller,

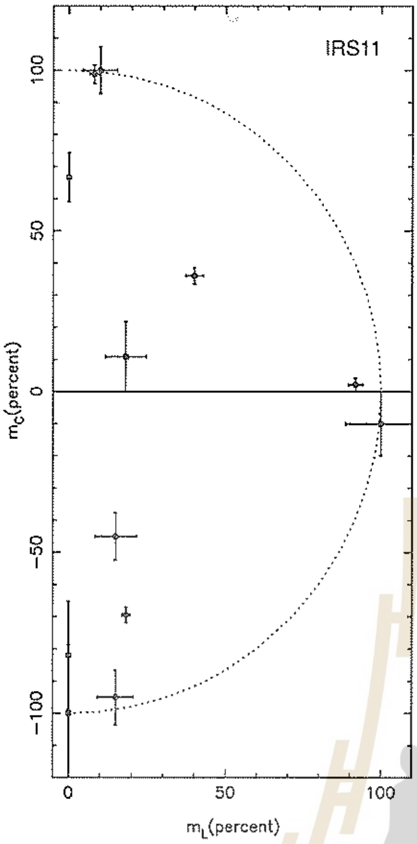

Figure 2: Percentage of linear versus circular polarization of each feature in NGC 7538. Circles, squares and triangles represent the 1665-, 1667- and 1720-MHz maser features, respectively. The degree of polarization increases from IRS 1 through IRS 9 to IRS 11. (Source: Figure 11(c) of Hutawarakorn and Cohen [4])

"The Structure of the Onsala 1 Star Forming Region", Astron. Astrophys. **426** (1), 195–200 (2004). [arXiv: `astro-ph/0406646`].

[9] Y. Uchida and K. Shibata, *"Magnetodynamical Acceleration of CO and Optical Bipolar Flows from the Region of Star Formation"*, Publ. Astron. Soc. Japan **37** (3), 515–535 (1985).

Electron Spin Resonance Study of Gd^{3+} in Zircon

การศึกษาอิเล็กตรอนสปินเรโซแนนซ์ของกาโดลิเนียมในเพทาย

ARAYA MUNGCHAMNANKIT,[1,*] PICHET LIMSUWAN,[1] and PONGTIP WINOTAI[2]

[1] *Department of Physics, Faculty of Science,*
King Mongkut's University of Technology Thonburi, Bangkok, 10140, Thailand
[2] *Department of Chemistry, Faculty of Science, Mahidol University,*
Bangkok, 10400, Thailand

This research work, the X-band ESR spectra of the untreated zircon at room temperature with the applied magnetic field directions approximately perpendicular to the [100] and [001] directions have been studied. The ESR spectra were generated from the microwave energy absorptions due to the transitions between the spin states of gadolinium ions (Gd^{3+}, $S = 7/2$), which were the impurity ions in the natural zircon. This effect can be proved by the study of fine structure of Gd^{3+}. Angular variation of peak positions reflected that the symmetry surrounding of Gd^{3+} is D_{2d}, hence the Gd^{3+} replaced for the Zr^{4+} in the lattice.

งานวิจัยนี้ได้ศึกษาสเปกตรัมของเพทายที่ยังไม่ผ่านกระบวนการให้ความร้อนด้วยเครื่องอิเล็กตรอนสปินเรโซแนนซ์ในย่านความถี่ไมโครเวฟ ณ อุณหภูมิห้อง โดยให้ทิศทาง [100] และ [001] ของผลึกเพทายทำมุมตั้งฉากโดยประมาณกับทิศทางของสนามแม่เหล็กภายนอก จากการวิเคราะห์พบว่า สเปกตรัมที่ได้จากการดูดกลืนพลังงานคลื่นแม่เหล็กไฟฟ้าในย่านความถี่คลื่นไมโครเวฟทำให้เกิดการเปลี่ยนสถานะของสปินของกาโดลิเนียมไอออนที่เป็นไอออนมลทินในเพทายธรรมชาติ ซึ่งยืนยันได้จากจำนวนของสัญญาณที่มีความเข้มสูงอันเนื่องมาจากอิเล็กตรอนสปินของกาโดลิเนียมไอออน (Gd^{3+}, $S = 7/2$) เมื่อสังเกตตำแหน่งที่เกิดสัญญาณโดยการหมุนผลึกพบว่ากาโดลิเนียมจะมีลักษณะสมมาตรแบบ D_{2d} ดังนั้นสรุปได้ว่ากาโดลิเนียมไอออนจะไปแทนที่เซอร์โคเนียมไอออน

PACS numbers: 61.72.Hh, 61.72.Ji
Keywords: Electron Spin Resonance, Gadolinium, Zircon

INTRODUCTION

Zircon is found in igneous rocks and sediments. It is a host mineral for radioactive elements such as uranium and thorium in the earth's crust and is a natural candidate for usage as a nuclear waste storage material. It has a wide variety of impurity ions, rare-earth ions and several other transition ions. Zircon is used as a gemstone because of its good optical quality and resistance to chemical attack [1]. It has a high refractive index (about 1.933–1.992) which responsible for its diamond-like appearance. Zircon has a specific gravity about 4.7 and a hardness of 7.5 on the Mohs' scale.

Zircon is a crystal of zirconium silicate having an empirical formula of $ZrSiO_4$ and molecular weight of 183.28. $ZrSiO_4$ comprises an arrangement of SiO_4 tetrahedrons and ZrO_8 dodecahedron; two different arrangements corresponding to two distinct phases are observed depending on the pressure. $ZrSiO_4$ has a tetragonal body-centered Bravias lattice with 12 atoms in the unit cell (Fig. 1). The space group is $I4_1/amd$ (D_{4h}^{19}) and the unit cell contains four SiO_4^{-4} and four ZrO_8^{-12} groups. The four groups within each set have the same geometry and different orientations. The SiO_4^{-4} groups are distorted tetrahedral elongated along a 2-fold z-axis parallel to the c crystallographic axis and their symmetry is D_{2d} [2].

METHODOLOGY

An ESR spectrum is due to electronic transitions between electronic-spin levels which are hard to calculate from the total Hamiltonian of an atom surrounded by neighbor atoms, especially in low site symmetry. A solution of the problem lie in the

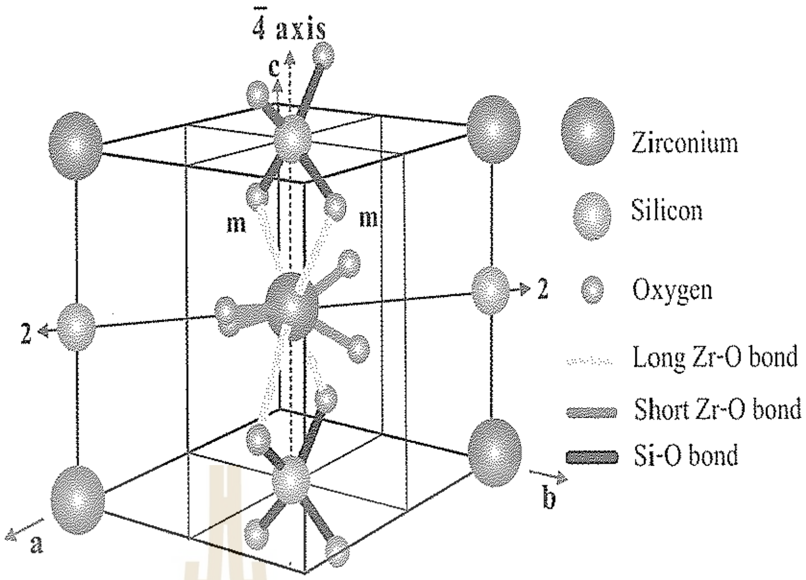

Figure 1: (color online). Portion of the zircon unit cell showing interconnection of SiO_4^{-4} tetrahedral and ZrO_8 dodecahedron along the $\bar{4}$ axis [3].

use of a phenomenological Hamiltonian called the spin Hamiltonian (SH). It is related to an effective spin S for the ground state such that the number of level is $2S+1$. The require spin Hamiltonian [4] may be written as

$$H = \beta\vec{B}\cdot\mathbf{g}\cdot\vec{S} + \sum_{k}\sum_{q=-k}^{k} B_k^q O_k^q + \vec{S}\cdot\mathsf{A}\cdot\vec{I} + \vec{I}\cdot\mathsf{P}\cdot\vec{I}. \tag{1}$$

Where the first term correspond to the Zeeman interaction due to the external applied magnetic field. The Zeeman term, β, $\vec{B}$, $\mathbf{g}$ and $\vec{S}$ are the Bohr magneton, magnetic field, gyromagnetic tensor, the spin operators S_x, S_y and S_z respectively.

The second term is related to the fine structure interaction and reflects the local symmetry of the crystal, this term is called zero field splitting term. The $O_k^{\pm q}$ are Stevens's operators and $B_k^{\pm q}$ is associated real Stevens constant. Operators with odd k value are not considered because they are not invariant with time reversal. The summation of $\sum_{k}\sum_{q=-k}^{k} B_k^q O_k^q$ term is limited by the electronic configuration of the transition metal ion. The required k value is equal to 2ℓ, where ℓ is the individual electron's angular momentum number. For example, the transition metal ion in f-block ($\ell = 3$) hence the highest order of k is 6. The superscript q is reflected to the symmetry, the presence of $B_k^{\pm q}$ will be depended on the appreciable symmetry.

The third term is hyperfine interaction due to the interaction between electron spin and nuclear spin with spin $\vec{I}$. A and $\vec{I}$ are the nuclear spin tensor and the nuclear-spin operator in the $(2I+1)$-dimension space, respectively.

The last term is the nuclear quadrupole interaction, where P are nuclear quadrupole tensor [5].

It has been known that crystalline electric fields interact weakly with the $^8S_{7/2}$ ground state of Gd^{3+}. The crystal field splitting for Gd^{3+} is generally smaller than that produced by the Zeeman interaction in X-band ESR experiments. The ESR spectrum consists of seven anisotropic lines described by a spin Hamiltonian incorporating both crystal field and Zeeman operators [6].

$$H = \beta\vec{S}\cdot\mathbf{g}\cdot\vec{B} + B_2^0 O_2^0 + B_4^0 O_4^0$$

$$+ B_4^4 O_4^4 + B_6^0 O_6^0 + B_6^4 O_6^4. \qquad (2)$$

A chosen natural zircon sample of dimension about $2 \times 2 \times 5$ mm^3 was cleaned thoroughly with acid and solvent to removed stains and other impurities on its surface. The ESR spectra of the natural zircon crystal were measured at room temperature by the ESR spectrometer in the microwave range of X-band ($\sim$ 9.86 GHz). The sample was mounted on a glass sample holder which could rotate about its axis. The ESR spectra were measured with the c-axis of the crystal both perpendicular and parallel to the applied magnetic field and were recorded in the range of 0 to 180 degrees for every 15 degrees of rotation angle.

RESULTS, DISCUSSION AND CONCLUSION

The rotation patterns of ESR peak positions in the ESR spectra with the different applied magnetic field directions will reflect the impurity ion site symmetry.

Since most of the ESR spectra are generally very complicated and some of them are not clearly resolved, then it is not easy to comprehend the ESR information. However at one distinctive angle of the magnetic field direction perpendicular to the [100] and [001] direction, ESR spectrum in Fig. 2 and 3 clearly exhibits seven peaks of fine structure that are symmetric relative to the central resonant field ($B = 354.31$ mT, 333.75 mT).

The spectrum is generated only from the microwave-energy transitions between the states within the paramagnetic spin system of $S = 7/2$ and the ESR spectra shown in Fig. 1 indicated that the applied magnetic field is more or less parallel to the principal direction. This direction is theoretically taken as an axis of quantization (or z-axis) which coincides with the c-axis of zircon lattice. Therefore, whenever the principal direction (or z-axis) of ESR system is identified, ESR spectra analysis will become more convenient to understand by using the concept of transformation (i.e. rotation). Applying an external magnetic field parallel to the principal direction will result in the ESR spectra being symmetric with respect to the central peak and having the maximum separation between the adjacent peaks. The angular variation plot of ESR spectra as shown in Fig. 4 and 5 reflects that the crystal field symmetry of the surroundings around the paramagnetic ion is D_{2d}, i.e. the point-symmetry at the Zr^{4+} site.

- ชื่อไทย: อารยา มุ่งชำนาญกิจ
Email: `opticslaser@yahoo.com`

[1] R. Mittal *et al.*, *"Measurement of Phonon Dispersion Relation in Zircon"*, Physica B **241–243**, 403–405 (1998).

[2] R. Terki, G. Bertrand and H. Aourag, *"Full Potential Investigations of Structural and Electronic Properties of* $ZrSiO_4$*"*, Microelectronic Eng. **81** (2–4), 514–523 (2005).

[3] W. C. Tennant *et al.*, *"Point Defects in Crystalline Zircon (Zirconium Silicate),* $ZrSiO_4$*: Electron Paramagnetic Resonance Studies"*, Phys. Chem. Minerals **31** (4), 203–223 (2004).

[4] A. Abraham and B. I. Bleaney, *Electron Paramagnetic Resonance of Transition Ions*, Clarendon Press, Oxford, England (1970).

[5] G. Morin and D. Bonnin, *"Modeling EPR Powder Spectra Using Numerical Diagonalization of the Spin Hamiltonian"*, J. Magn. Reson. **136** (2), 176–199 (1999).

[6] M. M. Abraham *et al.*, *"Ground-State Splitting of Trivalent* Gd *and* Cm *in* $ZrSiO_4$, $HfSiO_4$, *and* $ThSiO_4$, *Determined by ESR"*, J. Chem. Phys. **50** (5), 2057–2062 (1969).

Proceedings of the First National Symposium on Physics Graduate Research (1^{st} NSPG)
29 June – 1 July 2006, Chulabhorn Dam, Khon San, Chaiyaphum, Thailand

Impurities in Natural Diamond Observed by ESR Spectroscopy

CHITTRA KEDKEAW,[1,*] SUPANEE LIMSUWAN,[1] and PONGTIP WINOTAI[2]

[1]*Department of Physics, Faculty of Science,*
King Mongkut's University of Technology Thonburi, Bangkok, 10140, Thailand
[2]*Department of Chemistry, Faculty of Science, Mahidol University,*
Bangkok, 10400, Thailand

Characterization of different types of natural diamonds with Electron Spin Resonance (ESR) spectroscopy reveals absorption spectrum. The ESR spectra exhibit the detail of impurities and point defect. In natural diamond, nitrogen is major impurity. The P1 center is one of paramagnetic center in natural type I diamonds. The ESR spectra of this center consists three strong lines. These lines, generated from a coupling between the electron spin ($s = 1/2$) and the nuclear spin ($I = 1$) of the nitrogen atom, exhibited the hyperfine splitting phenomena. In addition, the position of isolated substitutional nitrogen (P1 center) was at $(0, 0, 0)$ of unit cell. Because the ESR spectra obtained at $\phi = 0$, 90 and 180 degree were the same line shape.

ลักษณะความแตกต่างของเพชรธรรมชาติที่วัดจากเครื่อง ESR จะแสดงออกมาในรูปของสเปกตรัมการดูดกลืน สเปกตรัม ESR จะสามารถบอกรายละเอียดเกี่ยวกับธาตุมลทินและจุดบกพร่องในผลึกเพชรได้ ในเพชรธรรมชาติจะพบไนโตรเจนเป็นธาตุมลทินอยู่มากที่สุด และมีศูนย์กลางที่เรียกว่า P1 ซึ่งเป็นศูนย์กลางที่พบในการวัดด้วยเครื่อง ESR สำหรับเพชรในกลุ่มที่ I ในศูนย์กลาง P1 นี้จะให้สัญญาณ ESR ที่เห็นได้ชัดเจนทั้งหมด 3 พีค โดยพีคเหล่านี้เกิดจากการทำอันตรกิริยาระหว่าง อิเล็กตรอนสปิน ($s = 1/2$) และนิวเคลียร์สปิน ($I = 1$) ของไนโตรเจนอะตอม ที่แสดงออกมาในรูปของไฮเปอร์ฟาย นอกจากนี้ ตำแหน่งของอะตอมไนโตรเจนเดี่ยวที่แทรกตัวอยู่ในศูนย์กลาง P1 พบว่าจะอยู่ที่ตำแหน่ง $(0, 0, 0)$ ในยูนิตเซลล์ เนื่องจากสเปกตรัม ESR ที่มุม $\phi = 0$, 90 และ 180 องศา มีลักษณะสเปกตรัมเป็นสามพีคเหมือนกัน

PACS numbers: 71.70.Ch, 71.70.Ej, 73.20.Hb
Keywords: ESR, Natural Diamond, Nitrogen Impurity, Hyperfine Structure

INTRODUCTION

Diamonds are specifically gems, which is very popular and highly expensive due to its scarcity, beauty, and durability. Diamond can be highly valued though it is small in size. According to these factors, diamond has been made and known as precious object for a long time. Generally, clarity, color, cut, and carat or quality indicate value or price of diamond.

The value of a diamond is determined by what are commonly referred to as the 4Cs. Color is one of four Cs and is used throughout the world to classify the rarity of diamonds. Colored diamonds contain impurities or structural defects that cause the coloration, while pure or nearly pure diamonds are transparent and colorless. Most diamond impurities replace a carbon atom in the crystal lattice. The most common impurity in diamond crystal is nitrogen in which it causes a slight to strong yellow coloration depending upon the type and concentration of nitrogen present. The defects (i.e. substitutional impurities) can be detected by different types of spectroscopy, including ESR, photoluminescence in ultraviolet light, and absorption of infrared light. The resulting absorption spectrum can then be analyzed, identified, and used to separate natural from synthetic or enhanced diamonds. The nitrogen can comprise up to 1% of a diamond by weight. Nitrogen as a diamond impurity was first identified in 1959 by Kaiser and Bond of Bell Telephone [1]. In this work, we measured natural type I diamonds by ESR spectroscopy. This technique was employed for natural diamond crystal or powder measurement. Because the ESR technique can specify impurities position in crystal lattice [1, 2, 3].

Diamonds typically crystallize in the face-centered cubic crystal system. The unit cell of diamond has two atom basis at $(0, 0, 0)$ and $(1/4, 1/4, 1/4)$. But in natural diamond, the tetrahedral or octahedral are normally formed. The group symmetry of natural diamond is tetrahedral, T_d. The tetrahedral arrangement of atoms in a diamond crystal is the source of many of diamond's properties. In this research work, ESR spectra of diamond were described based on basic quantum mechanics.

EXPERIMENTAL

The measured samples were natural type I diamonds. The samples were not cut and polished its surface. Due to the polish make to deteriorate plane of crystal samples. The good samples were cubic shape. We were cleaned thoroughly with acid and solvent to remove stains and other impurities on its surface. The ESR spectra of natural diamond crystal were measured at room temperature by ESR spectroscopy in microwave range of X-band (9.34 GHz).

Subsequently it was mounted on a sample holder with the c-axis [001] perpendicular to magnetic field direction and was inserted into a goniometer to control the orientation of the crystal axis with respect to the external applied magnetic field direction, as shown in Figure 1. From Figure 1, θ is the angle between magnetic field direction and x-axis and ϕ is the angle between projection of magnetic field on xy plane and x-axis. In this paper, the magnetic fields were along z-axis, and hence θ and ϕ are zero. The magnetic field was varied from 3440 to 3560 Gauss. Then, the ESR spectra were measured at every 90 degree of rotation phi angle (ϕ) of diamond about c-axis from 0–180 degree.

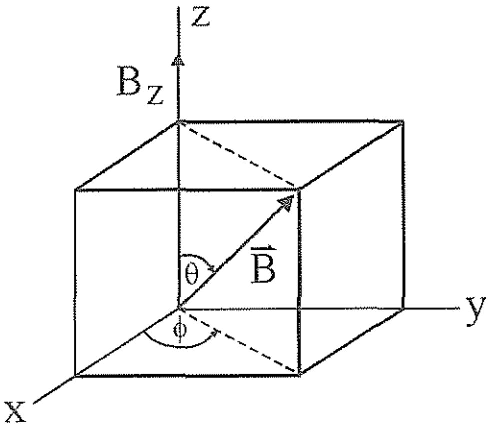

Figure 1: Direction of magnetic field.

RESULTS AND DISCUSSION

The result of ESR spectra of one diamond sample is shown in Figure 2, when the magnetic field was applied in the direction perpendicular to c-axis. There are three strong lines. We can interpret these spectra by considering substitutional nitrogen in diamond. Each one of nitrogen atom replaces a carbon atom to form covalent bond with carbon atom (C–N bond) and one unpaired electron was remained in C–N bond. In nature, substitutional nitrogen comprise of nearly 100% ^{14}N, with nuclear spin, $I = 1$ [2, 3, 4]. When we applied magnetic field into atom, the single unpaired electron energy level of nitrogen atom splitted into two energy levels [5], spin up $(+1/2)$ and spin down$(-1/2)$, as shown in Figure 3. The nuclear spin ($I = 1$ for ^{14}N) is interaction with electron spin ($s = 1/2$) which the energy levels were splitted six level. The energy level of electrons splitted by interaction with nuclear spin, was called the nuclear hyperfine interaction. The transition between sublevels is under selection rule ($\Delta m_s = \pm 1$, $\Delta m_I = 0$) as shown in Figure 3.

We rotated crystal sample about c-axis of crystal through phi angle from 0 to 90 and 180 degree. The results of ESR spectra are shown in Figure 4. It is seen that the ESR spectra at phi 0, 90 and 180 degree are exactly the same line shapes with three strong lines, due to the symmetry of diamond crystal is tetrahedral and unit cell is faced-center cubic. Moreover, when we rotate the crystal sample every 90 degree in which the angle between position of substitutional nitrogen and direction of magnetic field is the same.

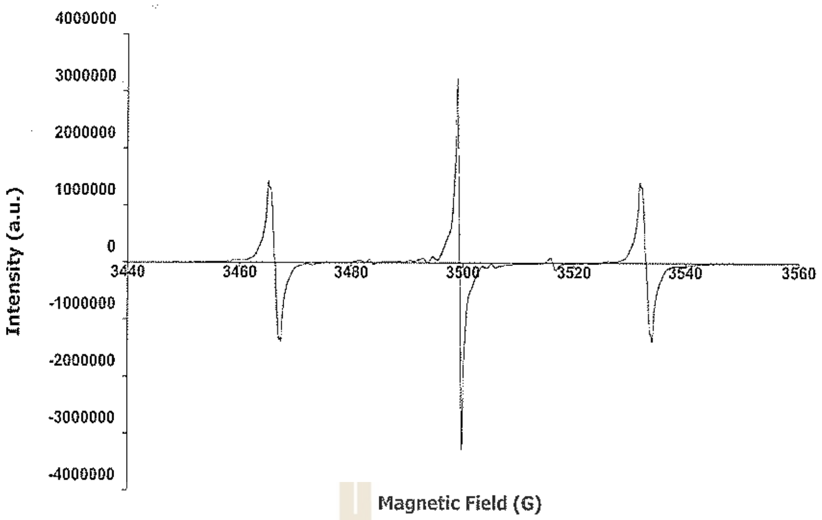

Figure 2: ESR spectra at $\theta = 0$ and $\phi = 0$ degree.

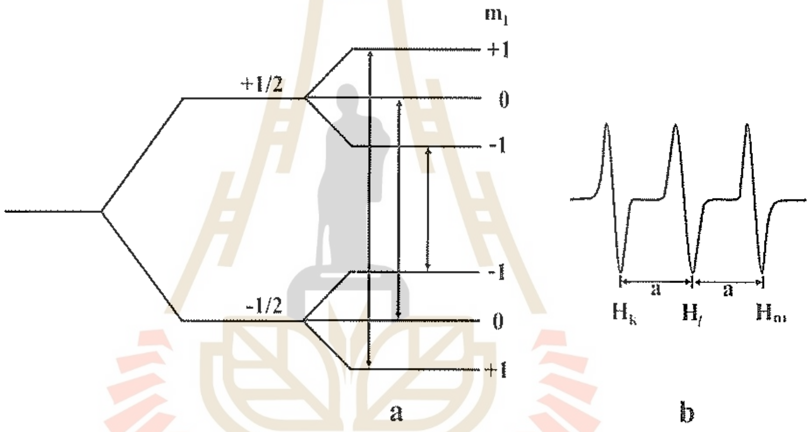

Figure 3: Hyperfine splitting for $s = 1/2$ and $I = 1$.

CONCLUSION

The characterization of paramagnetic center in diamond has been studied by ESR spectroscopy. The results of ESR spectra obtained were three lines at phi angles of $\phi = 0$, 90 and 180 degrees. These peaks, generated from a coupling between the electron spin ($s = 1/2$) and the nuclear spin ($I = 1$) of the nitrogen atom, exhibited the hyperfine splitting phenomena which prove the nitrogen impurity in the diamond of type I. Since the ESR spectra for all phi angles is comparably similar due to the angles between subtitutional nitrogen and magnetic field were the similarity.

---

* ชื่อไทย: จิตรา เกตุแก้ว
Email: `chittra193@hotmail.com`

[1] W. Kaiser and W. L. Bond, *"Nitrogen, A Major Impurity in Common Type I Diamond"*, Phys. Rev. **115** (4), 857–863 (1959).

[2] P. E. Klingsporn, M. D. Bell and W. J. Leivo,

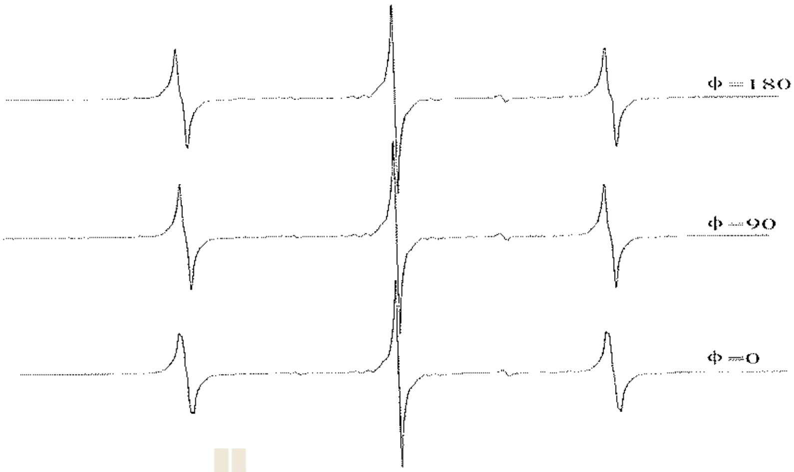

Figure 4: Comparison of ESR spectra at $\phi = 0$, 90 and 180 degree.

"Analysis of an Electron Spin Resonance Spectrum in Natural Diamonds", J. Appl. Phys. **41** (7), 2977–2980 (1970).

[3] J. H. N. Loubser and J. A. van Wyk, *"Electron Spin Resonance in the Study of Diamond"*, Rep. Prog. Phys. **41** (8), 1201–1248 (1978).

[4] P. R. Briddon and R. Jones, *"Theory of Impurities in Diamond"*, Physica B **185** (1–4), 179–189 (1993).

[5] J. E. Wertz and J. R. Bolton, *Electron Spin Resonance: Elementary Theory and Practical Applications*, Chapman & Hall, New York (1986).

1st NSPG

Proceedings of the First National Symposium on Physics Graduate Research (1st NSPG)
29 June – 1 July 2006, Chulabhorn Dam, Khon San, Chaiyaphum, Thailand

Effect of Annealing Ambient on Structural, Electrical and Optical Properties of ITO Films

อิทธิพลของบรรยากาศการอบฟิล์มที่มีผลต่อสมบัติทางโครงสร้างทางไฟฟ้าและทางแสงของฟิล์มอินเดียมทินออกไซด์

Kamon Aiempanakit,[1],* Sayan Phutwat,[1]
Supattanapong Dumrongrattana,[1] and Pattana Rakkwamsuk[2]
[1]Department of Physics, Faculty of Science,
King Mongkut's University of Technology Thonburi, Bangkok, 10140, Thailand
[2]Division of Materials Technology, School of Energy and Materials,
King Mongkut's University of Technology Thonburi, Bangkok, 10140, Thailand

Indium tin oxide (ITO) films have been deposited on glass substrate without heating by DC magnetron sputtering using an In_2O_3–SnO_2 (90–10 wt%) target. The various oxygen gas flow rates (0–2.0 sccm) of ITO films coating changed the crystal orientation to (222) peak. The ITO films prepared, have been compared of structural, electrical and optical properties for as-deposited, annealed in air, and annealed in vacuum (2×10^{-3} mbar) at 300 °C for 1 hour. After annealed, the ITO films increased their crystalline structure, as revealed by XRD analysis. The ITO film has a lowest resistivity of 2.89×10^{-4} Ω cm after annealed in vacuum, and the film has a lower transmission in NIR than the films which annealed in air, or as-deposited.

ฟิล์มอินเดียมทินออกไซด์ถูกเคลือบลงบนกระจกโดยไม่มีการให้ความร้อนด้วยวิธีดีซีแมกนีตรอนสปัตเตอริง ซึ่งใช้เป้าอินเดียมออกไซด์-ทินออกไซด์ (90–10 เปอร์เซ็นต์โดยน้ำหนัก) การป้อนก๊าซออกซิเจนในช่วง 0–2.0 sccm ของการเคลือบฟิล์มอินเดียมทินออกไซด์ จะส่งผลต่อการเปลี่ยนโครงสร้างการจัดเรียงตัวของผลึก โดยเฉพาะพีคที่ระนาบ (222) ฟิล์มอินเดียมทินออกไซด์หลังเคลือบโดยไม่มีการอบฟิล์ม อบฟิล์มในอากาศ และอบฟิล์มในสุญญากาศ (2×10^{-3} mbar) จะถูกนำมาเปรียบเทียบสมบัติทางโครงสร้าง สมบัติทางไฟฟ้า และสมบัติทางแสง หลังการอบฟิล์ม ฟิล์มอินเดียมทินออกไซด์จะมีการปรับโครงสร้างให้มีความเป็นผลึกสูงขึ้นซึ่งแสดงให้เห็นจากการวิเคราะห์ด้วยการเลี้ยวเบนรังสีเอ็กซ์ ฟิล์มอินเดียมทินออกไซด์จะมีค่าสภาพต้านทานไฟฟ้าต่ำสุดเท่ากับ 2.89×10^{-4} Ω cm หลังการอบฟิล์มในสุญญากาศ ฟิล์มที่ได้นี้จะมีค่าการส่องผ่านในช่วงรังสีอินฟราเรดที่ต่ำกว่าฟิล์มที่อบในอากาศและฟิล์มที่ไม่ผ่านการอบ

PACS numbers: 78.66.-w, 81.40.Ef, 81.15.Cd
Keywords: ITO Film, Annealing, DC Magnetron Sputtering

INTRODUCTION

Indium tin oxide (ITO) thin films have been widely used in many applications for optoelectronic device such as gas sensors [1, 2], heterojunction solar cell [3], electrode in a dry-sensitized solar cell [4], cathode in transparent organic light-emitting diode [5], ferroelectric photoconductor storage devices [6], and some other applications for architectural and automotive glass (low-e coatings) [7]. Because ITO thin films have a good electrical conduction and high transparence in visible region, which in fact ITO is an n-type semiconductor with a wide band gap ($E_g \approx 4$ eV) [8]. High quality ITO thin films have been prepared by various deposition methods such as sputtering [9, 10, 11, 12, 13], sol-gel [14], chemical vapor deposition (CVD) [15], and electron beam evaporation [16]. Due to a high sputtering rate and good film performance, DC-magnetron sputtering is widely used. In this work, we deposited ITO thin films on glass substrate by DC-magnetron sputtering without substrate extra heating and investigated the effect of annealing in air and in vacuum to determine the effect of changes in structural, electrical and optical properties.

EXPERIMENTAL DETAILS

The target used in this work was a 90 wt% In_2O_3 and 10 wt% SnO_2 (purity 99.99% diameter 3″ and thickness 0.25″). The glass substrate was ultrasonically cleaned in acetone, rinse in deionized water and allowed to dry in air before deposition.

The sputtering was performed in a mixed Ar–O_2 (purity 99.99% and 99.99%) which was separately controlled by mass flow controllers. The gas flow rate of argon was fixed at 50 sccm and oxygen was varied in the range of 0–2.0 sccm. The distance between the ITO target and the glass substrate was 8.6 cm, and the DC power was kept constant at 50 W. A turbo-molecular pump coupled with a rotary pump was used to achieve a base pressure of 6×10^{-6} mbar before introducing gas mixtures and working pressure of about 5×10^{-3} mbar. The films prepared at room temperature were then annealed at 300 °C in different ambient conditions, one in air and the other in vacuum (2×10^{-3} mbar) for 1 h.

The films thickness was measured with a spectroscopic ellipsometry. In this work, the measurements were performed on the films having the thickness about 230 nm. The x-ray diffractometer was used to study the crystallinity and crystal orientation of ITO thin films. The optical transmission spectra of films in UV-Vis-NIR region were recorded by a spectrophotometer. The electrical resistivity was measured by four point-probes in van der Pauw configuration.

RESULTS AND DISCUSSION

The effect of oxygen gas flow

Fig. 1 shows the XRD patterns of ITO films prepared at DC power of 50 W, argon gas flow 50 sccm and time coated 600 s (230 nm thick) at room temperature for various oxygen gas flow in the range of 0–2.0 sccm. It could be seen that the intensity ratio of (222)/(400) peak increased with increasing the oxygen gas flow rate. However, only the small amount of ITO films showed crystalline structure.

Fig. 2 shows transmission spectra of ITO thin film at various oxygen gas flow rates prepared at DC power of 50 W, argon gas flow rate 50 sccm and time coated 600 s (230 nm thick) at room temperature in the range of 190 nm to 2100 nm. It could be seen that the films had high transparence in visible region (78%) and near infrared region. The transmission at ultraviolet region of ITO films rapidly decreased due to absorption at the energy band gap (E_g).

The effect of annealing ambient

A study of the effect of annealing ambient we prepared the ITO films at DC power of 50 W, gas flow rates of argon and oxygen were 50 and 0.5 sccm, respectively and time coated 600 s (230 nm thick) at room temperature. Fig. 3 shows the XRD patterns for specimens of as-deposited, annealed in air and annealed in vacuum at 300 °C for 1 h. It could be seen the XRD patterns of ITO films became crystalline after annealing. The dominate intensity of the four peak, (222), (400), (440) and (622), were significantly affected by annealing. The intensity ratio of (222)/(400) peak for specimen after annealing in air is higher than annealing in vacuum.

Fig. 4 show the electrical resistivity of ITO prepared at 50 W, gas flow rates of argon and oxygen were 50 and 0.5 sccm, respectively. The resistivity decreased from specimens as-deposited, annealed in air, and annealed in vacuum ($\sim 2 \times 10^{-3}$ mbar), respectively. The specimens annealed both in vacuum and in air show higher crystallinity, but the one annealed in air should be oxidized to form stoichiometric oxide with high resistivity, while the one annealed in vacuum, no oxygen, should have more oxygen vacancies that provide the film with lower resistivity [17].

Fig. 5 show Transmission spectra of ITO for specimens as-deposited, annealed in air, and annealed in vacuum at 300 °C for 1 h. The transmission in visible range were high in both annealed cases, but the transmission in the near infrared range of the specimen annealed in vacuum was lower than annealed in air and as-deposited. Consider transmission at ultraviolet range of all films,

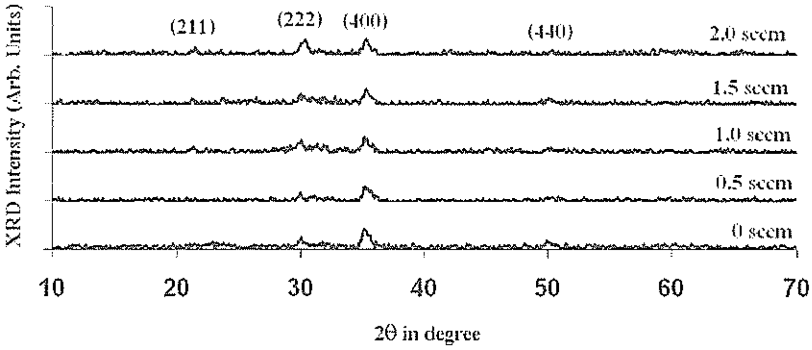

Figure 1: XRD pattern of as-deposited ITO films at various oxygen gas flow rates.

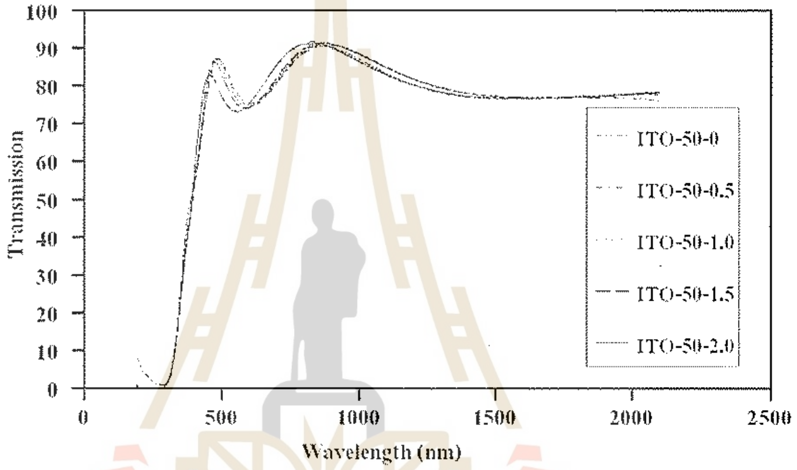

Figure 2: Transmission spectra of ITO thin film at various oxygen gas flow rates.

the edge of absorption was shift to the lower wavelength for annealed in vacuum, annealed in air and as-deposited, respectively. The change of the band gap energy of films after annealing has been reported as a Moss–Burstein shift [18].

CONCLUSIONS

The sputtering of ITO with fixed argon flow rates of 50 sccm and varied oxygen flow rates of 0–2 sccm. The as-deposited film on glass substrate form small amount of crystalline structure with preferred orientation in (400) plane in case of no oxygen flow rate, but the orientation changed to (222) plane when oxygen flow rate increased. The ITO film with oxygen flow rate 0.5 sccm, after annealed at 300 °C for 1 hour, both in air and in vacuum, showed that the film crystallinity increased. The one annealed in vacuum showed lower intensity ratio of (222)/(400) than annealed in air due to more oxygen vacancies and resulted in lower resistivity. This lower resistivity of vacuum annealing provided lower infrared transmission due to heat mirror effect of lower resistivity.

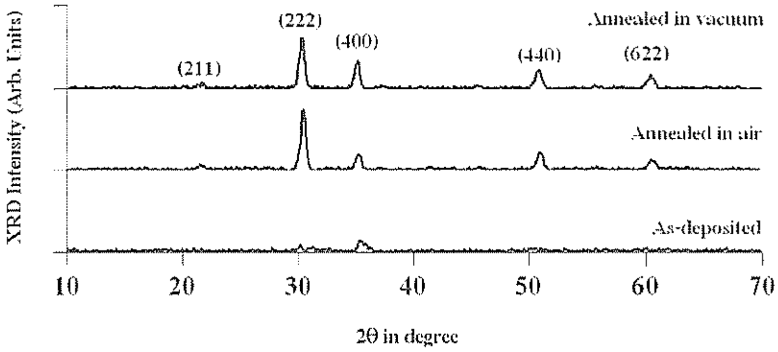

Figure 3: XRD pattern of ITO films prepared at 50 W, O_2 flow rate 0.5 sccm for specimens as-deposited, annealed in air, and annealed in vacuum at 300 °C for 1 h.

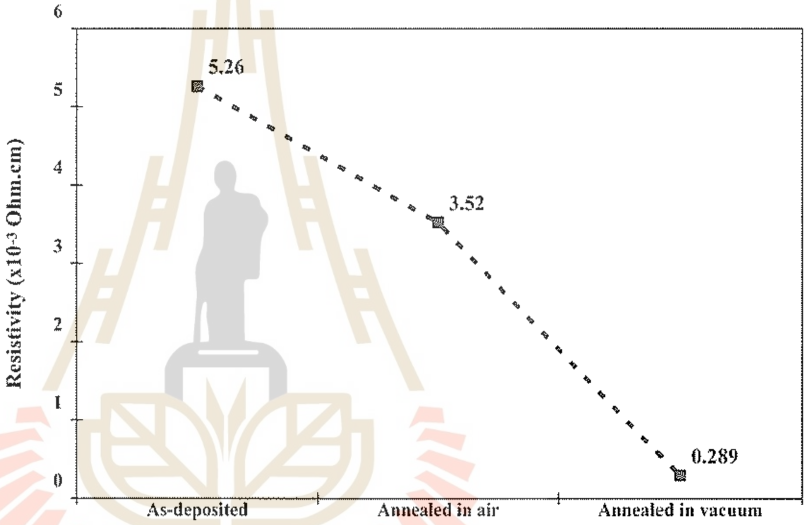

Figure 4: Electrical resistivity of ITO prepared at 50 W, O_2 flow rates 0.5 sccm for specimens as-deposited, annealed in air, and annealed in vacuum at 300 °C for 1 h.

---

[*] ชื่อไทย: กมล เอี่ยมพนากิจ
Email: `Kamon_KMUTT@hotmail.com`

[1] V. S. Vaishnav, P. D. Patel and N. G. Patel, *"Preparation and Characterization of Indium Tin Oxide Thin Films for Their Application as Gas Sensors"*, Thin Solid Films **487** (1–2), 277–282 (2005).

[2] V. S. Vaishnav, P. D. Patel and N. G. Patel, *"Indium Tin Oxide Thin Film Gas Sensors for Detection of Ethanol Vapours"*, Thin Solid Films **490** (1), 94–100 (2005).

[3] L. Zhao *et al.*, *"Indium Tin Oxide Thin Films by Bias Magnetron RF Sputtering for Heterojunction Solar Cells Application"*, Appl. Surf. Sci. **252** (2), 385–392 (2005).

[4] T. Hino, Y. Ogawa and N. Kuramoto, *"Preparation of Functionalized and Non-Functionalized Fullerene Thin Films on ITO Glasses and the Application to a Counter Electrode in a Dye-*

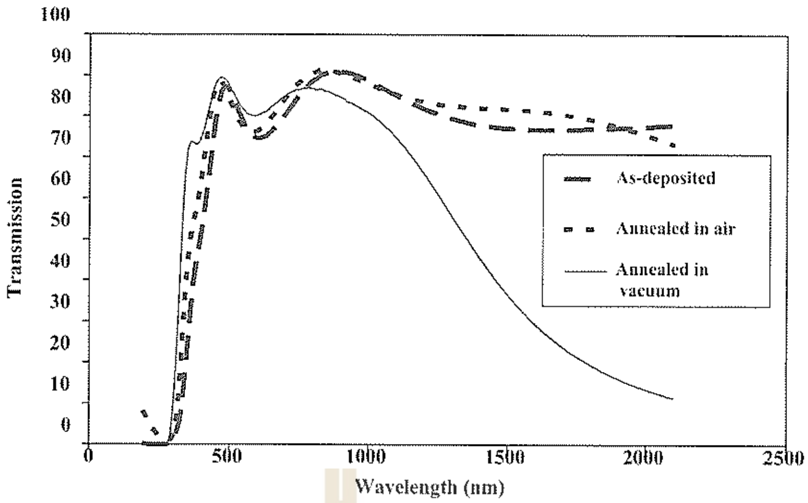

Figure 5: Transmission spectra of ITO prepared at 50 W, O_2 flow rate 0.5 sccm for specimens as-deposited, annealed in air, and annealed in vacuum at 300 °C for 1 h.

Sensitized Solar Cell", Carbon **44** (5), 880–887 (2006).

[5] C.-H. Chung *et al.*, *"Radio Frequency Magnetron Sputter-Deposited Indium Tin Oxide for Use as a Cathode in Transparent Organic Light-Emitting Diode"*, Thin Solid Films **491** (1–2), 294–297 (2005).

[6] D. Dimos *et al.*, *"Photoinduced Hysteresis Changes and Optical Storage in* (Pb, La)(Zr, Ti)O_3 *Thin Films and Ceramics"*, J. Appl. Phys. **76** (7), 4305–4315 (1994).

[7] K. H. Choi *et al.*, "ITO/Ag/ITO *Multilayer Films for the Application of a Very Low Resistance Transparent Electrode"*, Thin Solid Films **341** (1–2), 152–155 (1999).

[8] S. Laux *et al.*, *"Room-Temperature Deposition of Indium Tin Oxide Thin Films with Plasma Ion-Assisted Evaporation"*, Thin Solid Films **335** (1–2), 1–5 (1998).

[9] L.-J. Meng and M. P. dos Santos, *"Structure Effect on Electrical Properties of* ITO *Films Prepared by RF Reactive Magnetron Sputtering"*, Thin Solid Films **289** (1–2), 65–69 (1996).

[10] J.-O. Park *et al.*, *"Crystallization of Indium Tin Oxide Thin Films Prepared by RF-Magnetron Sputtering without External Heating"*, Thin Solid Films **474** (1–2), 127–132 (2005).

[11] K. Sreenivas *et al.*, *"Preparation and Characterization of RF Sputtered Indium Tin Oxide Films"*, J. Appl. Phys. **57** (2), 384–392 (1985).

[12] Y. S. Jung and S. S. Lee, *"Development of Indium Tin Oxide Film Texture During DC Magnetron Sputtering Deposition"*, J. Crystal Growth **259** (4), 343-351 (2003).

[13] M. Bender *et al.*, *"Dependence of Oxygen Flow on Optical and Electrical Properties of DC-Magnetron Sputtered* ITO *Films"*, Thin Solid Films **326** (1–2), 72–77 (1998).

[14] S. Kundu and P. K. Biswas, *"Synthesis and Photoluminescence Property of Nanostructured Sol-Gel Indium Tin Oxide Film on Glass"*, Chem. Phys. Lett. **414** (1–3), 107–110 (2005).

[15] T. Maruyama and K. Fukui, *"Indium-Tin Oxide Thin Films Prepared by Chemical Vapor Deposition"*, J. Appl. Phys. **70** (7), 3848–3851 (1991).

[16] H. R. Fallah *et al.*, *"The Effect of Deposition Rate on Electrical, Optical and Structural Properties of Tin-Doped Indium Oxide (*ITO*) Films on Glass at Low Substrate Temperature"*, Physica B **373** (2), 274–279 (2006).

[17] D.-F. Lii *et al.*, *"Effects of Annealing on the Properties of Indium-Tin Oxide Films Prepared by Ion Beam Sputtering"*, Surf. Coat. Technol. **192** (1), 106–111 (2005).

[18] B. E. Sernelius *et al.*, *"Band-Gap Tailoring of* ZnO *by Means of Heavy* Al *Doping"*, Phys. Rev. B **37** (17), 10244–10248 (1988).

Proceedings of the First National Symposium on Physics Graduate Research (1st NSPG)
29 June – 1 July 2006, Chulabhorn Dam, Khon San, Chaiyaphum, Thailand

A Spectroscopic Ellipsometry Study of TiO_2 Thin Films Prepared by Ion-Assisted Electron-Beam Evaporation

PITAK EIAMCHAI,[1,*] PICHET LIMSUWAN,[1] and PONGPAN CHINDAUDOM[2]
[1]*Department of Physics, Faculty of Science,*
King Mongkut's University of Technology Thonburi, Bangkok, 10140, Thailand
[2]*Optical Coating Laboratory, National Electronics and Computer Technology Center,*
Pathumthani, 12120, Thailand

(Dated: March 5, 2007)

Titanium dioxide has been extensively studied for optically active transmission films due to its high index of refraction and transparency across the visible range. Film characterization based on variable-angle spectroscopic ellipsometry (VASE) is desirable in order to understand physical and optical characteristics of the films. A number of thin film samples were deposited by ion-assisted electron-beam evaporation, and eventually annealed in air atmosphere. The crystalline structures of as-deposited (ASD) and annealed films were deduced by VASE, and supported by X-ray diffractometry (XRD). The optical properties of the films were examined by VASE. Several SE models, categorized by physical and optical models, were proposed based on the 'simpler-better' rule. Curve-fits were generated and compared to experimental data using regression analysis.

การศึกษาฟิล์มบางแสงไททาเนียมไดออกไซด์ได้รับความสนใจ เนื่องเพราะค่าดัชนีหักเหสูงและมีความใสในช่วงตามองเห็น การวิเคราะห์โครงสร้างฟิล์มโดยวิธีอิลิพโซเมทรี (VASE) สามารถนำไปสู่ความเข้าใจในสมบัติทางโครงสร้างและทางแสงของเนื้อฟิล์มได้ ตัวอย่างของฟิล์มถูกเตรียมขึ้นโดยวิธีการระเหยสารชนิดใช้ไอออนช่วย แล้วจึงนำไปอบในบรรยากาศ โครงสร้างผลึกของฟิล์มก่อนและหลังอบสามารถวิเคราะห์ได้ด้วย วิธี VASE และวิธี XRD สมบัติทางแสงของฟิล์ม สามารถวิเคราะห์ได้ด้วยอิลิพโซเมทรี รูปแบบการหาโมเดลถูกแบ่งเป็นสองกลุ่มคือโมเดลทางโครงสร้างและโมเดลทางแสง

PACS numbers: 68.55.Jk, 68.60.-p, 78.20.-e
Keywords: TiO_2, Evaporation, Spectroscopic Ellipsometry.

INTRODUCTION

Titanium dioxide thin film has been widely studied for optical applications due to its high index of refraction and transparency [1, 2]. The electron-beam evaporation is one of the preferred methods for TiO_2 film deposition to achieve high-quality optical thin films [1]. Limit controls of the deposition process may however yield inhomogeneous transparent films that are in need of annealing for encouraging results [1, 2].

Although TiO_2 is recognized of having three phases (anatase, rutile and brookite), only amorphous, anatase and rutile films have been extensively observed. Post-deposition annealing is the key factor to modify microstructure of amorphous TiO_2 films [2]. Therefore, film characterization by VASE is therefore appreciated in order to understand the effects of annealing to physical and optical properties of the films.

FILM CHARACTERIZATION

The TiO_2 thin films were prepared by ion-assisted electron-beam evaporation with operating pressure of $\sim 5.0 \times 10^{-5}$ Torr in oxygen atmosphere. The 99.99% pure TiO_2 tablets were used as a source, while pure oxygen was being supplied into the chamber via a cold-cathode ion source. The substrates were polished Si wafers (100) and micro slides, maintained at 250 °C. The nominal film thickness was configured at 200 nm at 2.0 Å/s deposition rate. After deposition, the cooled-down film samples were annealed and allowed to cool overnight and stored in air atmosphere. .

The physical structure and optical constants of the films were determined by J. A. Woolam variable-angle spectroscopic ellipsometer. The proposed physical model corresponding to each film sample was generated based on appropriate generalized oscillator for the optical dispersion, and eventually curve-fitted with the experimental data. The goal is, by a regression algorithm for the ellipsometry equation, to minimize the mean square error function:

$$\mathrm{MSE} = \sqrt{\frac{1}{2N-M}\sum_{i=1}^{N}\left[\left(\frac{\Psi_i^{\mathrm{mod}}-\Psi_i^{\mathrm{exp}}}{\sigma_{\Psi,i}^{\mathrm{exp}}}\right)^2+\left(\frac{\Delta_i^{\mathrm{mod}}-\Delta_i^{\mathrm{exp}}}{\sigma_{\Delta,i}^{\mathrm{exp}}}\right)^2\right]} \tag{1}$$

where N is the number of measured Ψ and Δ pairs, M is the total number of variable parameters and σ is the standard deviations. The *'mod'* means the theoretical calculation, and the *'exp'* means the experimentally measured data.

The film crystalline structures were also examined by a Bruker X-ray diffractometer operating with Cu-K$_{\alpha 1}$. The XRD results were to be analyzed in comparison with the VASE results.

Physical Modeling

A physical model was constructed in order to describe physically possible TiO_2 films. The films, assumed to be ideally homogeneous, were first described by a single-layer model (Figure 1a). The second proposal was a double-layer film with a dense TiO_2 layer and a surface roughness atop (Figure 1b), based on the island film formation. Generally, inhomogeneity was particularly considered for the island film growth which optically represented a mixture of dense material and void [3]. Therefore, the third proposal was to include a heterogeneous mixture layer of TiO_2 and excessive material (Figure 1c). The additional mixture would be identified as a voided layer, using the Bruggeman effective medium approximation (BEMA) for the estimated percentage of the mixture.

These three proposed physical models were then curve-fitted in comparison with experimental data (Figure 2). Even though the single-layer and double-layer models offered reasonable curve-fits in low photon energy range, they failed to describe the fits in high photon energy range. Obviously, the triple-layer physical model proposed the best curve-fits.

Optical Modeling

The Cauchy (CH) dispersion is a simple formulation to describe the refractive index and the Urbach absorption formulation was introduced for the extinction coefficient. The Cauchy dispersion is therefore represented by [4]:

$$n(\lambda) = A_n + \frac{B_n}{\lambda^2} + \frac{C_n}{\lambda^4}\,, \tag{2a}$$

$$k(E) = \frac{a}{E}\exp\left(\frac{E-E_g}{E_1}\right)\,, \tag{2b}$$

$$E = \frac{hc}{\lambda}\,, \tag{2c}$$

where A_n, B_n, C_n, E_g and E_1 are the Cauchy parameters. This optical model is generally suitable in visible and infrared regions. However, it cannot well describe optical dispersion in the UV region, for which it is a model of choice for insulator and dielectrics.

The Lorentz oscillator was considered in an attempt to describe the optical constants for semiconductor, by using a classical spring-mass system of dipole oscillation. Recalling that the Lorentzian dielectric function: $\tilde{\varepsilon} = (n - \mathrm{i}k)^2 = \varepsilon_1 + \mathrm{i}\varepsilon_2$, the refractive index can be ideally obtained as [5]:

$$n(E) = \sqrt{\frac{1}{2}\left[(\varepsilon_1^2+\varepsilon_2^2)^2+\varepsilon_1\right]}\,, \tag{3a}$$

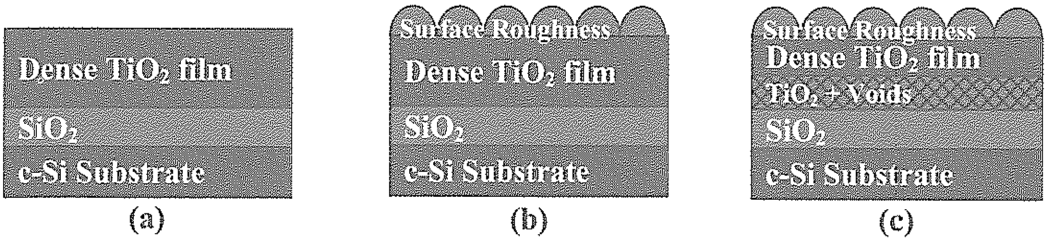

Figure 1: (color online). Schematic representation of the proposed (a) single-layer, (b) double-layer and (c) triple-layer physical models for the SE-modeling procedure.

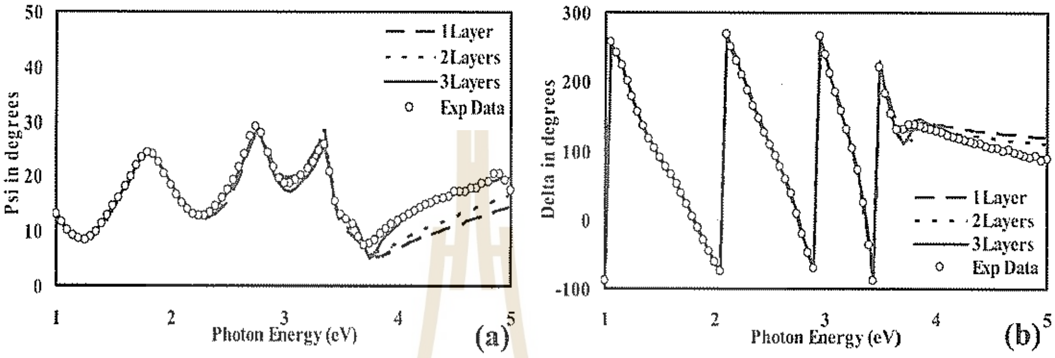

Figure 2: (color online). Illustration of generated and experimental data, curve-fitted with three physical models: (a) fittings on Ψ, (b) fittings on Δ at 70° incident angle.

$$k(E) = \sqrt{\frac{1}{2}\left[\left(\varepsilon_1^2+\varepsilon_2^2\right)^2-\varepsilon_1\right]}\,. \qquad (3b)$$

The Lorentz oscillator is an ideal formulation to classically describe dipole oscillation in an atom. For semiconductor TiO_2, quantum-size effect and band gaps are essentially important. Therefore, the Tauc–Lorentz (TL) dispersion has been proposed by combining the Tauc band edge with the classical Lorentz broadening function:

$$\varepsilon_2(E) = \begin{cases} \left[\dfrac{AE_0C\left(E-E_g\right)^2}{\left(E^2-E_0^2\right)^2+C^2E^2}\right]\dfrac{1}{E}\,, & E > E_g\,, \\ 0\,, & E \leqslant E_g\,, \end{cases} \qquad (4)$$

where A is the amplitude, E_0 is the peak transition energy, C is the broadening constant, and E_g is the band gap. Applying the Kramers–Kronig relations, then ε_1 can be derived:

$$\varepsilon_1(E) = \varepsilon_1(\infty) + \frac{2}{\pi}\,\mathrm{P}\int_{E_g}^{\infty}\frac{\xi\,\varepsilon_2(\xi)}{\xi^2-E^2}\,\mathrm{d}\xi\,. \qquad (5)$$

The TL optical model, however, has explicit restriction of ε_2 to be zero for energies less than the band gap. The Cody–Lorentz (CL) dispersion was proposed to offer a contribution above the band edge, by parameterizing transition energy in the transparent and interband transition regions. This gives [6, 7]:

$$\varepsilon_2(E) = \begin{cases} \left(\dfrac{E_1}{E}\right) \exp\left(\dfrac{E - E_t}{E_\mu}\right) , & 0 < E \leqslant E_t , \\ G(E) \left[\dfrac{AE_0\Gamma E}{\left(E^2 - E_0^2\right)^2 + \Gamma^2 E^2}\right] , & E > E_t , \end{cases} \tag{6}$$

where E_t is a transition energy between the Urbach tail and band-to-band transitions, E_μ represents the extent of broadening, $G(E)$ represents the joint density-of-states, and E_p is a transition energy for the absorption onset.

Examples of illustrations of the generated and experimental data are shown in Figure 3 for the optical model comparison, where the CL optical model offered the best curve-fits.

RESULTS AND DISCUSSION

Based on the film characterization, the ASD film was initially represented by a double-layer model, whose its refractive index was close to that of anatase. After annealing at 300 °C, the film could only be represented by a triple-layer model, with a significant drop of the refractive index. That is, the ASD film was actually a metallic sub-oxide TiO_x film. Annealing in air atmosphere, however, resulted in oxygen diffusion into the dense film layer, possibly at interstitial vacancy. During annealing, oxygen molecules may have incorporated with the material to form an amorphous TiO_2 structure.

Further increase in annealing temperatures up to 500 °C resulted in a slight decrease in the BEMA layer, and a slight increase in the dense film layer (Figure 4). The increase in the refractive index means that the amorphous-to-anatase phase transition has been detected. From Figure 5b, the 500 °C annealed-film demonstrated an index increase very close to that of anatase, corresponding to several reports [8].

Annealing treatment at 600 °C and 700 °C resulted in yet again a decrease in the refractive index, while the film's physical model continued to have an increasing BEMA layer thickness and a decreasing dense TiO_2 layer thickness (Figure 4). The film began to deteriorate and became apparently swollen. The peeled-off film layer logically resulted in decrease in the refractive index. Altogether, this leads to increasing total film thickness, in which it corresponds to previous work [8].

From Figure 4b, the XRD patterns showed phase variation from annealing. The ASD film was supposedly amorphous, whereas annealed film at 300 °C–400 °C illustrated a slight increase in anatase phase. Annealing temperature at 500 °C, however, caused phase transitions from amorphous or anatase to rutile phase. At 700 °C, $R(101)$ was considered the preferred orientation, while $R(110)$ has a comparable intensity. Annealing at 500 °C–600 °C is possibly the critical phase-transition temperature for anatase-to-rutile structure.

Evidently, the XRD measurements on the film support the film characterization from VASE analysis. The ASD film, with amorphous phase and high refractive index, is said to be a metallic TiO_x film, possibly caused by less chemical reaction between TiO_2 evaporants and reactive oxygen ions.

CONCLUSION

The ASD TiO_2 films were found to be an inhomogeneous, double-layer, sub-oxide film. The film characterization demonstrated that the double-layer film became the triple-layer film immedi-

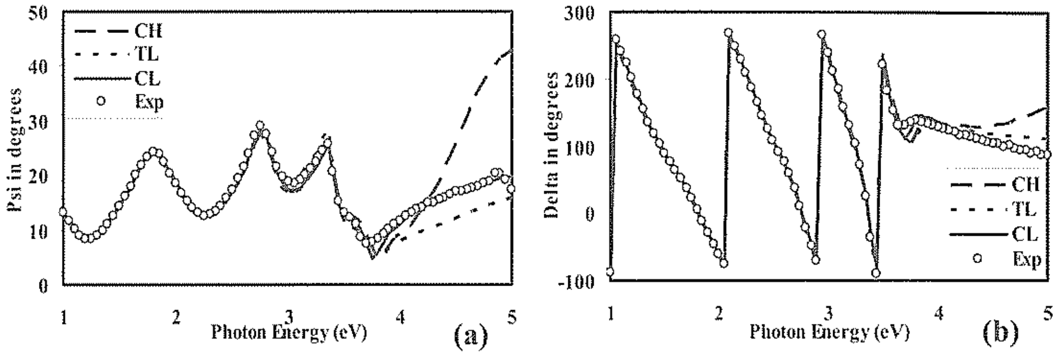

Figure 3: (color online). Illustration of generated and experimental data fitted with three optical-models: fittings on (a) Ψ, and (b) Δ at 70° incident angle.

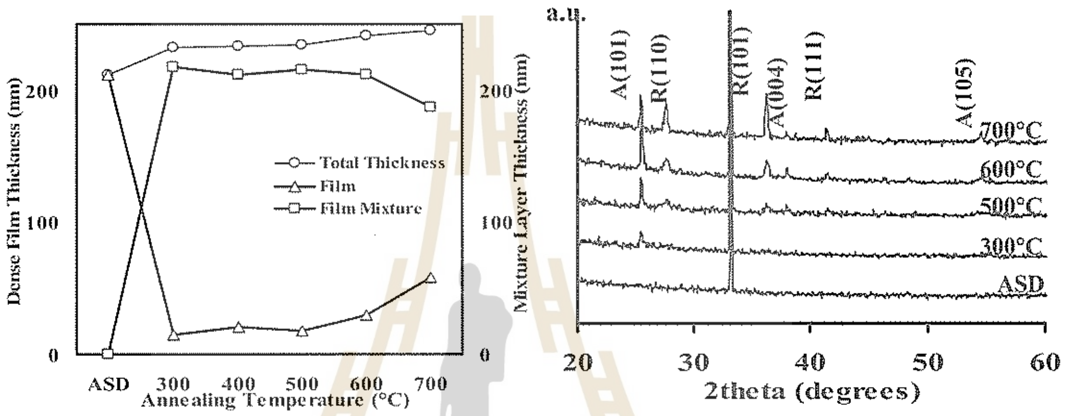

Figure 4: (color online). (a) Illustrations of sub-layer thickness evolution and (b) X-ray diffraction patterns of the TiO_2 film sample, prior and after annealing.

ately after annealing. The mixture of TiO_2 and voids became significant. Furthermore, annealing temperatures caused an increase in the dense film layer, and a decrease in the voided layer. The total film thickness increased with increasing annealing temperatures and resulted in the swelling. At 700 °C, the films suffered from deformity and failed to maintain their optical characteristics.

All in all, the VASE measurements, integrating with the XRD measurements, can extensively characterize the films' physical and optical properties, whereas the VASE analysis is more practical and informative. The developed SE-modeling procedure is supposedly capable of characterizing TiO_2 thin films prepared by either sputtering or evaporation processes. Ideally, SE analysis can also characterize other metal-oxide thin films, using similar physical model approaches and optical model considerations.

This study was technically supported by the National Electronics and Computer Technology Center (NECTEC), and the Department of Chemistry, Mahidol University.

---

[*] ชื่อไทย: พิทักษ์ เอี่ยมชัย
Email: `opticslaser@yahoo.com`

[1] M. J. Colgan *et al.*, *"Effects of Annealing on Titanium Dioxide Structured Films"*, Thin Solid Films **466** (1-2), 92-96 (2004).

[2] Y.-Q. Hou *et al.*, *"Influence of Annealing Temperature on the Properties of Titanium Oxide Thin*

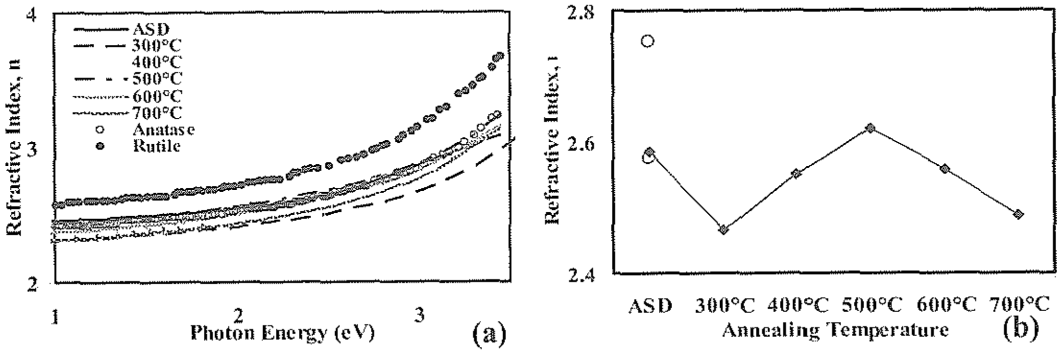

Figure 5: (color online). (a) Variation of the refractive index as a function of photon energy and (b) the effective refractive index, n_{550}, from the film sample prior and after annealing.

Film", Appl. Surf. Sci **218** (1–4), 98–106 (2003).

[3] A. Amassian, P. Desjardins and L. Martinu, *"Study of* TiO_2 *Film Growth Mechanisms in Low-Pressure Plasma by In Situ Real-Time Spectroscopic Ellipsometry"*, Thin Solid Films **447–448**, 40–45 (2004).

[4] D. Franta, I. Ohlídal and D. Petrýdes, *"Optical Characterization of* TiO_2 *Thin Films by the Combined Method of Spectroscopic Ellipsometry and Spectroscopic Photometry"*, Vacuum **80** (1–3), 159–162 (2005).

[5] H. G. Tompkins and W. A. McGahan, *Spectroscopic Ellipsometry and Reflectometry: A User's Guide*, Wiley, New York (1999).

[6] J. Price *et al.*, *"Spectroscopic Ellipsometry Characterization of* $Hf_xSi_yO_z$ *Films Using the Cody-Lorentz Parameterized Model"*, Appl. Phys. Lett. **85** (10), 1701–1703 (2004).

[7] A. S. Ferlauto *et al.*, *"Analytical Model for the Optical Functions of Amorphous Semiconductors and Its Applications for Thin Film Solar Cells"*, Thin Solid Films **455–456**, 388–392 (2004).

[8] L. Sun and P. Hou, *"Spectroscopic Ellipsometry Study on E-beam Deposited Titanium Dioxide Films"*, Thin Solid Films **455–456**, 525–529 (2004).

Proceedings of the First National Symposium on Physics Graduate Research (1st NSPG)
29 June – 1 July 2006, Chulabhorn Dam, Khon San, Chaiyaphum, Thailand

Pentaquark Production in Neutron–Proton Collisions

การเกิดเพนตะควาร์กในการชนของนิวตรอนและโปรตอน

Ayut Limphirat,* Khanchai Khosonthongkee, Chinorat Kobdaj, and Yupeng Yan
School of Physics, Institute of Science, Suranaree University of Technology,
Nakhon Ratchasima, 30000, Thailand

The production of the pentaquark Θ^+ in the $np \rightarrow \Lambda^0 nK^+$ reaction is simulated in the UrQMD model. A narrow peak around 1540 MeV is found in the nK^+ invariant mass spectrum. Our study leads to positive results towards the existence of the pentaquark Θ^+.

กระบวนการเกิดเพนตะควาร์ก Θ^+ ในปฏิกิริยา $np \rightarrow \Lambda^0 nK^+$ ได้ถูกจำลองโดยใช้แบบจำลอง UrQMD พบว่ามีพีคแคบๆ รอบมวล 1540 MeV ในสเปกตรัมมวลยืนยงของ nK^+ การศึกษานี้เป็นหลักฐานยืนยันการเกิดเพนตะควาร์ก Θ^+

PACS numbers: 12.38.-t, 13.75.Cs, 13.85.Hd
Keywords: Quark, Pentaquark, Exotic Baryon, UrQMD

INTRODUCTION

Normal hadrons are classified into two groups, that are, mesons, quark–antiquark pairs ($q\bar{q}$) and baryons, three quarks system (qqq). A large number of such particles have been confirmed in experiments. As presently understood, QCD does not forbid the existence of multiquark states other than quark–antiquark and three-quark systems as long as they form color singlets. Multiquark states other than quark–antiquark and three-quark systems are called exotic hadrons, exotic mesons (i.e. $q\bar{q}q$, $q\bar{q}q\bar{q}$) and exotic baryons (i.e. $qqqq\bar{q}$).

The exotic baryon known as "pentaquark" ($qqqq\bar{q}$) has attracted strong interests both in theoretical and experimental sectors. The first prediction is suggested in 1997 by Diakonov, Petrov and Polyakov using the chiral quark soliton model. It was predicted that the exotic baryon posses spin 1/2, isospin 0, strangeness +1 and has a relative low mass of about 1530 MeV with total width less than 15 MeV [1]. The LEPS Collaboration at SPring-8 reported in 2003 [2] the first evidence of the lightest pentaquark, called Θ^+, in $\gamma n \rightarrow K^- K^+ n$ reaction. The existence of the pentaquark Θ^+ was later confirmed by the CLAS, SAPHIR, DIANA and HERMES Collaborations. Θ^+ is considered to be an $uudd\bar{s}$ state with strangeness ($S = +1$), baryon number ($B = +1$), charge ($Q = +1$) and mass of around 1540 MeV [3–6].

In experiments, the Θ^+ is observed as a narrow peak in nK^+ invariant mass spectrum. The definition of invariant mass is

$$M(nK^+) = \sqrt{(E_n + E_{K^+})^2 - (\vec{p}_n + \vec{p}_{K^-})^2} \quad (1)$$

where $M(nK^+)$, E and $\vec{p}$ are the mass of Θ^+, energy and momentum respectively. Shown in Fig. 1 is the diagram of the reaction $\gamma d \rightarrow K^+ K^- pn$ in the CLAS experiment [3], where the collision between the photon, γ, and the neutron, n, in the deuteron target produces K^- and Θ^+ which decays to nK^+. Displayed in Fig. 2 is the final nK^+ invariant mass spectrum, $M(nK^+)$, of CLAS experiment.

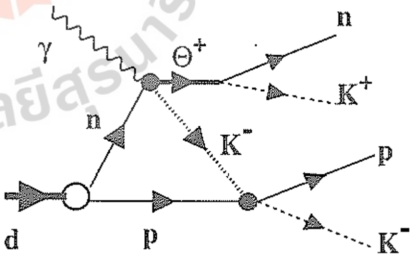

Figure 1: Diagram of the reaction $\gamma d \rightarrow K^+ K^- pn$ at CLAS experiment [3] and the decay of the pentaquark Θ^+ to nK^+.

The first round of observations of pentaquark

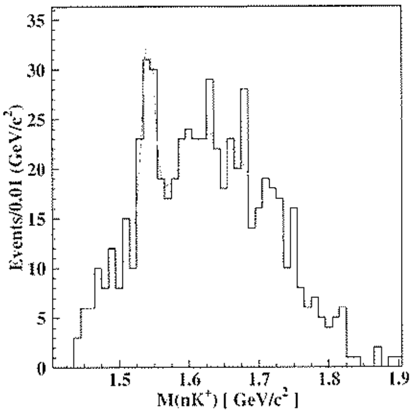

Figure 2: Invariant mass of the nK$^+$ spectrum shows a sharp peak at the mass of 1542 MeV [3].

candidates looked on the one hand very promising, but on the other hand all suffered from the low statistical significance. Moreover, there is a list of experiments which did not find any narrow structure in the region of interest. These results come from either electron–positron collisions [7] or high energy reactions using a hadron beam [8, 9]. Very recently a series of high statistic experiments and refined analysis have been started to clarify the situation. The actual result is still confusing.

The pentaquark Θ^+ may be produced in non-strange particle reactions [10] such as γN, NN and πN collisions. However, up to now, most experiments have studied only the γN reaction. It is interesting to study the existence of the Θ^+ in the NN reaction. Because of theoretical calculation [11] shows that the maximum cross section σ for the NN collision is around the center of mass energy of 3.0 GeV. In this work, the np $\rightarrow$ Λ^0nK$^+$ reactions are simulated by using the Ultra-relativistic Quantum Molecular Dynamics model (UrQMD) to check the existence of nK$^+$ resonances system.

THE UrQMD MODEL

The Ultra-relativistic Quantum Molecular Dynamics (UrQMD) model has been developed over ten years by hundreds of physicists since it was initiated by Frankfurt Heavy-Ion Group, Institute for Theoretical Physics, Frankfurt University. The main goals are to gain understandings, within a single transport model, of the following physical phenomena such as: creation of dense hadronic matter at high temperatures; properties of nuclear matter, delta and resonance matter; creation of mesonic matter and of anti-matter; creation and transport of rare particles in hadronic matter; creation, modification and destruction of strangeness in matter; emission of electromagnetic probes. The model describe the relativistic heavy ion collisions in the energy range from AGS (Alternating Gradient Synchrotron, Brookhaven) up to SPS (Super Proton Synchrotron, CERN) and RHIC (Relativistic Heavy Ion Collider, Brookhaven).

In the UrQMD model [12, 13], the projectile and target baryon are expressed in terms of Gaussian shaped density distributions,

$$\varphi_j(\vec{x}_j, t) = \left(\frac{2\alpha}{\pi}\right)^{3/4} \exp\left\{-\alpha\left[\vec{x}_j - \vec{r}_j(t)\right]^2 + \frac{\mathrm{i}}{\hbar}\vec{p}_j(t)\cdot\vec{x}_j\right\}. \qquad (2)$$

The wave function of projectile and target are just the product of wave function from each single baryon Gaussian,

$$\Phi = \prod_j \varphi_j(\vec{x}_j, \vec{p}_j, t). \qquad (3)$$

The interactions employed are Skyrme potential, Yukawa potential, Pauli potential and Coulomb potential. The UrQMD Hamiltonian take the form

$$H_{\mathrm{UrQMD}} = \sum_{j=1}^{N} E_j^{\mathrm{kin}} + \frac{1}{2}\sum_{j=1}^{N}\sum_{k=1}^{N}\left(E_{jk}^{\mathrm{Sk2}} + E_{jk}^{\mathrm{Yukawa}} + E_{jk}^{\mathrm{Coulomb}} + E_{jk}^{\mathrm{Pauli}}\right) + \frac{1}{6}\sum_{j=1}^{N}\sum_{k=1}^{N}\sum_{l=1}^{N} E_{jkl}^{\mathrm{Sk3}} \qquad (4)$$

where E_j^{kin}, E_{jk}^{Sk2}, E_{jk}^{Yukawa}, $E_{jk}^{\mathrm{Coulomb}}$, E_{jk}^{Pauli} and E_{jkl}^{Sk3} are kinetic energy, two body Skyrme, Yukawa, Coulomb, Pauli and three body Skyrme potential energy respectively.

In heavy ion collisions, a large number of particles are produced. The UrQMD model has capability to identify 55 different baryon species (including nucleon, delta, hyperon and their resonances) and 32 different meson species (including strange meson and its resonances). Their antiparticles and isospin-projected states can also be determined.

RESULTS AND DISCUSSION

The np → Λ^0nK^+ reactions are simulated in the UrQMD model. The first step work is the simulations of np → Λ^0nK^+ reactions for 1 million events at each center-of-mass-energy $\sqrt{s}$ which varies from 2.7 GeV to 3.2 GeV with a step 0.1 GeV. The invariant masses of nK^+ system are calculated by using Eq. (1). The number of events with Λ^0nK^+ in final state are counted as frequency count with the corresponding invariant mass range of 20 MeV.

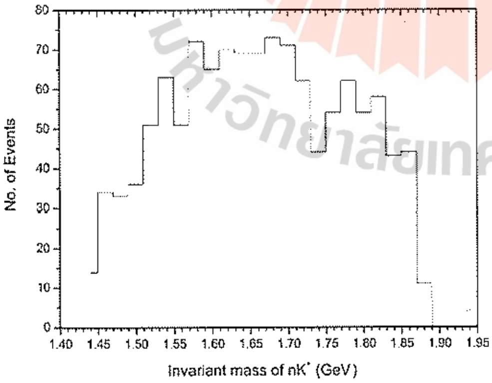

Figure 3: nK^+ invariant mass in the np → Λ^0nK^+ reaction at $\sqrt{s} = 3.0$ GeV for 1 million events.

Presented in Fig. 3 is the nK^+ invariant mass spectrum in the np → Λ^0nK^+ reaction at $\sqrt{s}$ = 3.0 GeV for 1 million events, which clearly shows a narrow peak around 1540 MeV while the others center-of-mass-energy are not found.

One may argue that the resonance peak may be the pentaquark Θ^+. To confirm the evidence of Θ^+ in np → Λ^0nK^+ reaction at $\sqrt{s}$ = 3.0 GeV, we have also simulated the reaction np → Λ^0nK^+ for 2, 3 and 4 millions events. Fig. 4, 5 and 6 show the nK^+ invariant mass spectra in the np → Λ^0nK^+ reaction for 2, 3 and 4 million events, respectively.

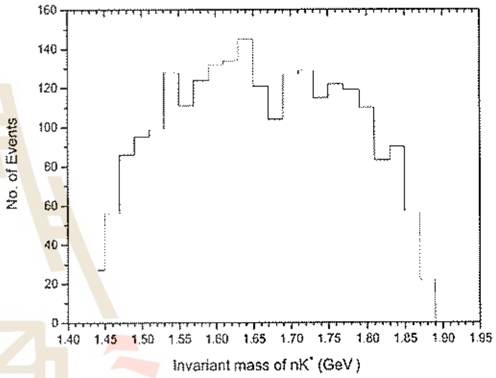

Figure 4: nK^+ invariant mass in the np → Λ^0nK^+ reaction at $\sqrt{s} = 3.0$ GeV for 2 million events.

It is found that with higher statistics the narrow peak around 1540 MeV in the nK^+ invariant mass spectrum is still seen clearly.

CONCLUSION

The simulation of the np → Λ^0nK^+ reactions using the UrQMD model at $\sqrt{s}$ = 3.0 GeV for 1 to 4 million events shows that there exits a narrow peak around 1540 MeV in the nK^+ invariant mass spectra. The narrow peak may be interpreted as the pentaquark $\Theta^+(1540)$ with the quark configuration $uudd\bar{s}$.

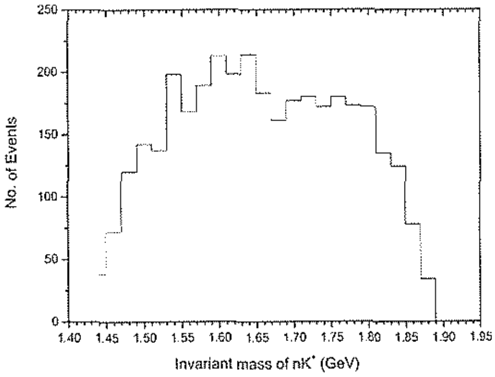

Figure 5: nK^+ invariant mass in the $np \to \Lambda^0 nK^+$ reaction at $\sqrt{s} = 3.0$ GeV for 3 million events.

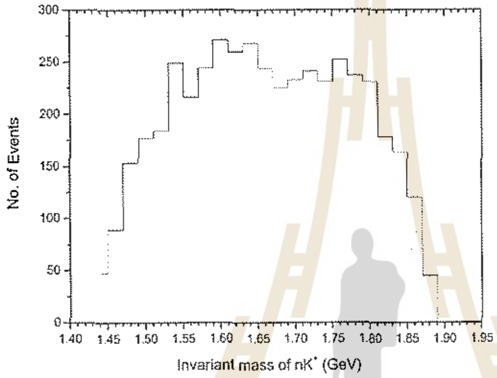

Figure 6: nK^+ invariant mass in the $np \to \Lambda^0 nK^+$ reaction at $\sqrt{s} = 3.0$ GeV for 4 million events.

Acknowledgements

This work is supported in part by the National Research Council of Thailand (NRCT) under Grant No. 1.CH5/2549.

---

* ชื่อไทย: อายุทธ ลิ้มพิรัตน์
Email: `limphirat@yahoo.com`

[1] D. Diakonov, V. Petrov and M. Polyakov, *"Exotic Anti-Decuplet of Baryons: Prediction from Chiral Solitons"*, Z. Phys. A **359** (3), 305–314 (1997). [arXiv: `hep-ph/9703373`].

[2] T. Nakano *et al.* (LEPS Collaboration), *"Evidence for a Narrow $S = +1$ Baryon Resonance in Photoproduction from the Neutron"*, Phys. Rev. Lett. **91** (1), 012002 (2003). [arXiv: `hep-ex/0301020`].

[3] S. Stepanyan *et al.* (CLAS Collaboration), *"Observation of an Exotic $S = +1$ Baryon in Exclusive Photoproduction from the Deuteron"*, Phys. Rev. Lett. **91** (25), 252001 (2003). [arXiv: `hep-ex/0307018`].

[4] J. Barth *et al.* (SAPHIR Collaboration), *"Evidence for the Positive-Strangeness Pentaquark Θ^+ in Photoproduction with the SAPHIR detector at ELSA"*, Phys. Lett. B **572** (3–4), 127–132 (2003). [arXiv: `hep-ex/0307083`].

[5] V. V. Barmin *et al.* (DIANA Collaboration), *"Observation of a Baryon Resonance with Positive Strangeness in K^+ Collisions with Xe Nuclei"*, Phys. At. Nucl. **66** (9), 1715–1718 (2003). [arXiv: `hep-ex/0304040`].

[6] A. Airapetian *et al.* (HERMES Collaboration), *"Evidence for a Narrow $|S| = 1$ Baryon State at a Mass of 1528 MeV in Quasi-Real Photoproduction"*, Phys. Lett. B **585** (3–4), 213–222 (2004). [arXiv: `hep-ex/0312044`].

[7] J. Z. Bai *et al.* (BES Collaboration), *"Search for the Pentaquark State in $\psi(2S)$ and J/ψ Decays to $K^0_S pK^-\bar{n}$ and $K^0_S \bar{p}K^+ n$"*, Phys. Rev. D **70** (1), 012004 (2004). [arXiv: `hep-ex/0402012`].

[8] I. Abt *et al.* (HERA-B Collaboration), *"Limits for the Central Production of Θ^+ and Ξ^- Pentaquarks in 920-GeV pA Collisions"*, Phys. Rev. Lett. **93** (21), 212003 (2004). [arXiv: `hep-ex/0408048`].

[9] Yu. M. Antipov *et al.* (SPHINX Collaboration), *"Search for $\Theta(1540)^+$ in the Exclusive Proton-Induced Reaction $p + C(N) \to \Theta^+\bar{K}^0 + C(N)$ at the Energy of 70 GeV"*, Eur. Phys. J. A **21** (3), 455–468 (2004). [arXiv: `hep-ex/0407026`].

[10] K. H. Hicks, *"Experimental Search for Pentaquarks"*, Prog. Part. Nucl. Phys. **55** (2), 647–676 (2005). [arXiv: `hep-ex/0504027`].

[11] S.-I. Nam, A. Hosaka and H.-Ch. Kim, *"Production of the Pentaquark Θ^+ in np Scattering"*, Phys. Rev. D **70** (11), 114027 (2004). [arXiv: `hep-ph/0402138`].

[12] S. A. Bass *et al.*, *"Microscopic Models for Ultrarelativistic Heavy Ion Collisions"*, Prog. Part. Nucl. Phys. **41**, 255–369 (1998). [arXiv: `nucl-th/9803035`].

[13] M. Bleicher *et al.*, *"Relativistic Hadron-Hadron Collisions in the Ultra-Relativistic Quantum Molecular Dynamics Model (UrQMD)"*, J. Phys. G **25** (9), 1859–1896 (1999). [arXiv: `hep-ph/9909407`].

Israel Junction Conditions on Hypersurface from Variational Principle Approach

เงื่อนไขการเชื่อมต่ออิสราเอลบนพื้นผิวมิติเกินจากการใช้หลักการแปรผัน

CHAKKRIT KAEONIKHOM*
Fundamental Physics & Cosmology Research Unit,
The Tah Poe Academia Institute (TPTP), Department of Physics,
Naresuan University, Phitsanulok 65000, Thailand

Einstein's field equation can be derived using variational with boundary term that vanishes at infinity. In case of bounded spacetime, we can include boundary terms into gravitational action. The result is Israel junction conditions on a hypersurface. The method has been widely applied to braneworld gravity and braneworld cosmology.

สมการสนามของไอน์สไตน์เป็นกฎที่สำคัญข้อหนึ่งในทฤษฎีสัมพัทธภาพทั่วไป สามารถถูกหาได้โดยใช้วิธีการแปรผัน โดยเลือกให้พจน์ที่ขอบเขตเป็นศูนย์ที่อนันต์ ในรายงานนี้ กาลอวกาศของเรามีขอบเขต เราสามารถเพิ่มพจน์ที่ขอบเขตให้กับแอคชันความโน้มถ่วงได้ อันนำมาซึ่งเงื่อนไขการเชื่อมต่ออิสราเอลบนพื้นผิวมิติเกิน วิธีการนี้ถูกประยุกต์ใช้อย่างแพร่หลายในทฤษฎีความโน้มถ่วงแบบกพแผ่นและจักรวาลวิทยาแบบกพแผ่น

PACS numbers: 04.20.Fy
Keywords: Israel junction conditions, variational principle, gravitational action, hypersurface.

INTRODUCTION

Among several variational principles used in general relativity, the most common one is to use the Einstein–Hilbert action which an integral over the invariant four-volume to the Ricci scalar (curvature scalar). The structure of the variation can be split into two parts: one yields Einstein's field equation in vacuum (excluding matter term), and another, with a four-divergence form resulting a surface term known as the Gibbons–Hawking boundary term. In general, surface terms are neglected in derivation of field equation from an action. But in this case, our manifold (spacetime) is bounded. An action considered here is the Einstein–Hilbert action with surface term. When our manifold is bounded, it automatically splits into two parts. They are called a bulk and a hypersurface. Variation of surface terms is done with respect to an induced metric on hypersurface, not the metric on the manifold. The result leads to the Israel junction conditions, if matter action is included on hypersurface.

METHODOLOGY

We start by reviewing the standard derivation of Einstein's field equation from the Einstein–Hilbert action.

$$S_{\mathrm{EH}} = \frac{1}{2\kappa}\int_{\mathcal{M}} \sqrt{-g}\, R \, \mathrm{d}^4x, \tag{1}$$

where $\mathcal{M}$ denotes the manifold, g is a determinant of the metric $g_{\mu\nu}$ which has a signature of $(-,+,+,+)$ in our convention, R is the Ricci scalar and $\kappa = 8\pi G$. Varying this action with respect to the metric, we get

$$\delta S_{\mathrm{EH}} = \frac{1}{2\kappa}\int_{\mathcal{M}} \sqrt{-g}\, G_{\mu\nu}\, \delta g^{\mu\nu} \, \mathrm{d}^4x + \delta S_{\mathrm{S}}, \tag{2}$$

where $G_{\mu\nu}$ is the Einstein tensor and δS_{S} is a surface term. It has the following form

$$S_{\mathrm{S}} = -\frac{1}{\kappa}\int_{\Sigma} \sqrt{-h}\, K \, \mathrm{d}^3x. \tag{3}$$

Σ denotes the hypersurface or our boundary of the manifold, h is the determinant of the induced metric on Σ and K is the trace of the extrinsic curvature of that boundary. We can define the energy–momentum tensor in the usual way,

$$T_{\mu\nu} = -\frac{2}{\sqrt{-g}}\frac{\delta S_{\mathrm{M}}}{\delta g^{\mu\nu}},$$

where $S_{\rm M}$ denotes the matter action. The full action is $S = S_{\rm EH} + S_{\rm M}$, which does not lead to the Einstein's field equation since our manifold is assumed to be a restrictive spacetime. The surface term therefore cannot be set to zero. In the derivation of gravitational action, the metric and induced metric do not vary on the boundary such that $\delta g_{\mu\nu} = 0$ and $\delta h_{ab} = 0$. (Here we use Greek indices $(\mu, \nu, \ldots)$ which run from 0 to 3 to denote coordinates on the manifold, and Latin indices $(a, b, \ldots)$ which run from 1 to 3 to denote coordinates on Σ.) We generalize the equation (2) by naming the first term as the variation of gravitational action, and get the result

$$S_{\rm Gravity} = \frac{1}{2\kappa}\left[\int_{\mathcal{M}} \sqrt{-g}\; R \;{\rm d}^4x + 2\int_{\Sigma} \sqrt{-h}\; K \;{\rm d}^3x\right]. \qquad (4)$$

This action is used to derive of Israel condition. Hereafter, we will not fix the metric and the induced metric on Σ for this derivation. The variation then gives three terms as follows,

$$\delta S_{\rm Gravity} = \frac{1}{2\kappa}\left[\int_{\mathcal{M}} \sqrt{-g}\; G_{\mu\nu}\,\delta g^{\mu\nu}\;{\rm d}^4x + 2\int_{\Sigma} \sqrt{-h}\,\left(K_{ab} - h_{ab}K\right)\delta h^{ab}\;{\rm d}^3x + \int_{\Sigma} \sqrt{-h}\;{\rm D}_b\!\left(h^b{}_a\,\delta n^a\right){\rm d}^3x\right]. \qquad (5)$$

${\rm D}_b$ in the last term denotes a covariant derivative associated with the hypersurface Σ, and n^a is the normal unit vector to Σ, whose normalization condition is $n_a n^a = -1$ for Σ is spacelike [3]. The last term in the equation (5) is a divergence term. It vanishes by using Stoke's theorem with a boundary on Σ at infinity. Finally, the variation of gravitational action is

$$\delta S_{\rm Gravity} = \frac{1}{2\kappa}\left[\int_{\mathcal{M}} \sqrt{-g}\; G_{\mu\nu}\,\delta g^{\mu\nu}\;{\rm d}^4x + \int_{\Sigma} \sqrt{-h}\,\left(K_{ab} - h_{ab}K\right)\delta h^{ab}\;{\rm d}^3x\right]. \qquad (6)$$

The energy-momentum tensor,

$$t_{ab} = \frac{2}{\sqrt{-h}}\,\frac{\delta S_{\rm Mat}}{\delta h^{ab}},$$

is included on Σ by adding an action for matter, $S_{\rm Mat}$, in the gravitational action. The Einstein tensor, $G_{\mu\nu}$ in the bulk vanishes because t_{ab} is only included on Σ. Therefore, the total action, $S_{\rm Gravity} = S_{\rm EH} + S_{\rm S} + S_{\rm Mat}$ gives the *Israel junction conditions*

$$K_{ab} - h_{ab}K = -8\pi G\, t_{ab}. \qquad (7)$$

The energy-momentum tensor on a hypersurface does not necessarily conserve because energy can flow from the hypersurface to the bulk. This can be seen by taking the divergence of the Israel junction conditions:

$${\rm D}_a t^{ab} = -\frac{1}{8\pi G}\left[{\rm D}_a K^{ab} - {\rm D}_a\!\left(h^{ab}K\right)\right]. \qquad (8)$$

The right side can be evaluated using Gauss-Codacci relations [2], giving

$$\begin{aligned} {\rm D}_a t^{ab} &= -\frac{1}{8\pi G}\, R_{cd}\, n^c h^{db} \\ &= -T_{cd}\, n^c h^{db}, \end{aligned} \qquad (9)$$

where T_{cd} is the bulk energy-momentum tensor. This equation describes conservation of energy when T_{cd} moves from the bulk to the boundary.

CONCLUSION

Usually, in deriving the Einstein's field equation using the variational principle, we use a boundary term that vanishes at infinity. But because of an attempt to explain bounded manifolds or spacetimes, e.g. black holes, a boundary term cannot be set zero. By varying this term, the Israel junction condition on a hypersurface is obtained. It acts as a connection between the events inside and on the boundary. There is wide application of the Israel junction condition to cosmology, and to the idea of Braneworld gravity and Braneworld cosmology.

Acknowledgements

I would like to thank Daris Samart and Burin Gumjudpai for useful discussions and checking some calculations. English proofreading is done by Kiattisak Thepsuriya.

---

* ชื่อไทย: จักรกฤษ แก้วนิคม
Email: `chain_ckk@hotmail.com`

[1] S. M. Carroll, *Spacetime and Geometry: An Introduction to General Relativity*, Addison Wesley (2003).

[2] R. M. Wald, *General Relativity*, University of Chicago Press (1984).

[3] E. Poisson, *A Relativist's Toolkit: The Mathematics of Black-Hole Mechanics*, Cambridge University Press (2004).

[4] Yu. V. Shtanov, *"On Brane-World Cosmology"*, arXiv: `hep-th/0005193`

[5] H. A. Chamblin and H. S. Reall, *"Dynamic Dilatonic Domain Walls"*, Nucl. Phys. B **562** (1–2), 133–157 (1999). [arXiv: `hep-th/9903225`].

[6] T. P. Sotiriou and S. Liberati, *"Field Equations from a Surface Term"*, Phys. Rev. D **74** (4), 044016 (2006). [arXiv: `gr-qc/0603096`].

1st NSPG
Proceedings of the First National Symposium on Physics Graduate Research (1st NSPG)
29 June – 1 July 2006, Chulabhorn Dam, Khon San, Chaiyaphum, Thailand

Cosmological Dynamics from Modified $f(R)$ Gravity in Einstein Frame*

พลวัตรเชิงจักรวาลวิทยาจากการปรับแต่งความโน้มถ่วงแบบ $f(R)$ ในกรอบไอน์สไตน์

DARIS SAMART†
Fundamental Physics & Cosmology Research Unit,
The Tah Poe Academia Institute (TPTP), Department of Physics,
Naresuan University, Phitsanulok 65000, Thailand

In this paper, we investigate and analyze the cosmological dynamics of the universe which is an effect of modified $f(R)$ gravity emerging at cosmological scale. We choose Einstein frame as a physical frame. We consider phase portraits at present and late time of the universe from modified $f(R)$ model gravity. This result yields an acceleration phase of the universe without existence of dark energy.

งานวิจัยชิ้นนี้ เราได้สำรวจและวิเคราะห์พลวัตรเชิงจักรวาลวิทยาของเอกภพ โดยที่ผลของการปรับแต่งความโน้มถ่วงแบบ $f(R)$ จะปรากฏขึ้นที่ระดับระยะทางเชิงจักรวาลวิทยา เราเลือกกรอบของ ไอน์สไตน์ เป็นกรอบทางกายภาพ และพิจารณาเฟสของแผนภาพที่ช่วงปัจจุบัน และช่วงปลายของเอกภพจากแบบจำลองการปรับแต่งความโน้มถ่วงแบบ $f(R)$ ผลที่ได้คือเอกภพมีช่วงการขยายตัวออกแบบเร่งโดยไม่จำเป็นต้องอาศัยพลังงานมืด

PACS numbers: 04.50.+h, 98.80.-k
Keywords: alternative theory of gravity, accelerating universe, cosmological dynamics, conformal transformation, Einstein frame.

INTRODUCTION

The alternative explanation to solve Dark Energy problem is modification of Einstein gravity theory to be source of acceleration universe. Carroll *et al.* [1] purposed of modified model of gravity by adding inverse power of Ricci scalar into Einstein–Hilbert action giving deviation from general relativity at small curvature and causing acceleration at large scale. This happens either with de Sitter and anti de Sitter solutions in vacuum case which provides purely gravitation driven accelerating universe and good agreement for testing in current cosmological observation data. The modified $f(R)$ gravity model is very interesting because it was shown it can be derived from string/M-theory [3]. Many works on various aspects and extends this model. We will consider cosmological dynamics of modified gravity like [1, 2], but we use metric variation formalisms in Einstein frame phase portraits diagrams. We consider this scenario in Einstein frame as the physical frame and this frame gives us to self gravity of scalar field effective potential $V(\phi)$ [4, 5, 6].

METHODOLOGY

In this section we review the conformal transformation method follow [4, 5, 6]. The action for $f(R)$ gravity of Jordan frame without matter field can be written in form,

$$S_J = \frac{1}{2\kappa^2}\int f(R)\,\sqrt{-g}\,\mathrm{d}^4x \qquad (1)$$

where $\kappa^2 = 8\pi G$. The field equation from (1) in Jordan frame gives us the fourth order and very complicate to solve [1, 2]. We choose Einstein frame as physical frame for it is simplicity. We define the conformal transformation between Jordan and Einstein frame as [13]

$${}^{\mathrm{E}}g_{ab} = \mathrm{e}^{\phi} g_{ab}. \qquad (2)$$

where $\phi \equiv \ln f'(R)$. We obtain action in Einstein frame by use conformal transformation in (2) i.e.

---

* cf. arXiv: `astro-ph/0606612`.

$g_{ab} \rightarrow e^{\phi} g_{ab}$ [3, 4, 5, 6]

$$S_{\mathrm{E}} = \frac{1}{2\kappa^2} \int \Big[{}^{\mathrm{E}}R - \frac{3}{2} \nabla_a \phi \nabla^a \phi - V(\phi) \Big] \sqrt{-{}^{\mathrm{E}}g}\, \mathrm{d}^4 x \qquad (3)$$

where $V(\phi)$ is effective potential which depends on choice of $f(R)$ models determined by $V = [Rf'(R) - f(R)]/[f'(R)]^2$ where $f'(R) \equiv \mathrm{d}f(R)/\mathrm{d}R$. We vary action (3) with respect to ${}^{\mathrm{E}}g^{ab}$, we get

$${}^{\mathrm{E}}R_{ab} - \frac{1}{2}\, {}^{\mathrm{E}}g_{ab}\, {}^{\mathrm{E}}R = 3 \nabla_a \phi \nabla_b \phi - {}^{\mathrm{E}}g_{ab} \left[\frac{3}{2} g^{cd} \nabla_c \phi \nabla_d \phi + V(\phi) \right] \qquad (4)$$

and when varying respect to ϕ, we get the Klein–Gordon equation

$$\nabla_a \nabla^a \phi + \frac{V_\phi}{3} = 0 \qquad (5)$$

where $V_\phi \equiv \mathrm{d}V/\mathrm{d}\phi$. Now we consider present universe based on FRW metric which is spatially flat,

$$\mathrm{d}s^2 = -\mathrm{d}t^2 + a^2(t) \left[\mathrm{d}x^2 + \mathrm{d}y^2 + \mathrm{d}z^2 \right]. \qquad (6)$$

where $a(t)$ is scale factor of universe.

Now we calculate the modified Friedman equation in Einstein frame from line element (6), the $(0,0)$ component of field equation (4) the Friedman equation and the Klein–Gordon equation become

$$H^2 = \frac{1}{4} \dot{\phi}^2 + \frac{V(\phi)}{6} \qquad (7)$$

$$\ddot{\phi} + 3H\dot{\phi} + \frac{V_\phi}{3} = 0. \qquad (8)$$

where $H \equiv \dot{a}/a$ is Hubble parameter and $\dot{a} \equiv \mathrm{d}a/\mathrm{d}t$. We also obtain the time derivative of Hubble parameter by using (7) and (8)

$$\dot{H} = -\frac{3}{4} \dot{\phi}^2. \qquad (9)$$

Next section we will consider cosmological dynamics in phase portrait in some particular types of $f(R)$ gravity model.

We consider scalar field dominate the late universe. The acceleration can happen when the field at late time moves very slow. Therefore we can use the slow-roll approximation in this phase [8] i.e. $\ddot{\phi} \approx 0$ and $\dot{\phi}^2 \ll V$. Using the slow-roll approximation condition directly to the Friedman equation in equation of motion of scalar field (8), we get the late time trajectory of scalar field evolving to approach an asymptotic attractor solution in phase space as [14]

$$\dot{\phi} \simeq -\frac{V_\phi}{9H}. \qquad (10)$$

We define a new variables as

$$X = \phi, \quad Y = \dot{\phi}, \quad Z = V(\phi). \qquad (11)$$

Using new variables in (11) substitute into (8) and (9) we obtain autonomous system,

$$Y = \dot{\phi} \qquad (12)$$

$$\dot{H} = -\frac{3}{4} Y \qquad (13)$$

$$\dot{Y} = -3HY - \frac{1}{3} \frac{\mathrm{d}Z}{\mathrm{d}X}. \qquad (14)$$

Next we will investigate and analyze the phase space portraits for some types of the effective potential $V(\phi)$ which depends on choices of $f(R)$ models of gravity. By using autonomous system of equations in (12), (13) and (14).

RESULTS, DISCUSSION AND CONCLUSION

1. The $f(R) = R - \mu^{2(n+1)}/R^n$ model was proposed by [1, 2] (for $n = 1$). In this model the effective potential (at the late time, R is very small) in Einstein frame is [7]

$$V(\phi) \simeq \frac{2}{\mu^2} e^{-(3/2)\phi}. \qquad (15)$$

This potential in our approximation look like the power law inflation, which gives scale factor increase proportion to $a \sim t^{4/3}$. We note that potential increases when curvature is minimum and

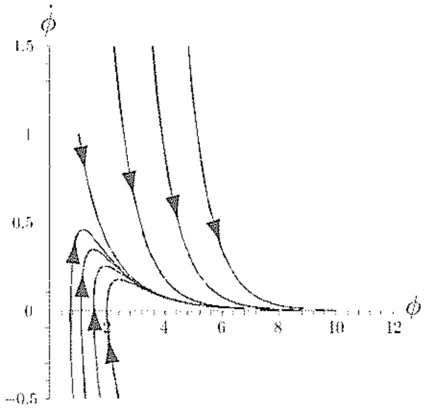

Figure 1: The phase portrait of $\dot{\phi}$ vs ϕ in the modified $1/R$ gravity model, when $\mu = 1$.

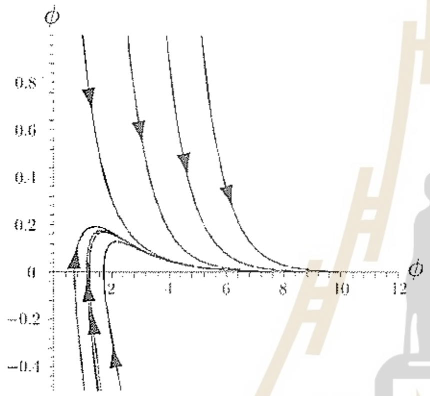

Figure 2: The phase portrait of $\dot{\phi}$ vs ϕ in the modified $\ln R$ gravity model, when $\alpha = 1$.

therefore the universe begins to have the power law expansion. We also consider phase space portrait of scalar fields of modified $1/R$ gravity model, which presents attractor in phase plane as Figure 1.

2. The $f(R) = R + \alpha \ln(R/\gamma^2)$ model was purposed by [9]. The effective potential in (at the late time, R is very small) Einstein frame is [9]

$$V(\phi) \simeq \alpha \, e^{-2\phi} \phi. \tag{16}$$

We note that when the curvature rolls slow down until reaching local minimum ($R \neq 0$) the curvature stay here. This may correspond to the present accelerating universe [9]. This potential can be shown to have $w \to -1$ (where w is the equation of state) by fine-tuning parameters. We also consider phase space portrait of scalar fields of modified $\ln R$ gravity model, which has attractor in phase plane as Figure 2.

Let we discuss from above phase space portraits both $1/R$ and $\ln R$ gravity model, both models give late time attractor. These results mean our universe is in accelerating expansion. The evolution when scalar field is at some given point on the potential has to be independent of any initial conditions. It is surprised our analysis in Einstein frame gives similar result as in [11, 12] which chooses Jordan frame as physical frame. They was shown that $1/R$ model gravity has late time attractor on phase space portrait. Both Jordan and Einstein frame are analyzed similarly $1/R$ gravity model. We still can not tell which one is physical frame. This work is still ongoing.

Acknowledgement

I would like to thanks Itzadah Thongkool for helpful discussion and critical comments, Kiattisak Thepsuriya for proofreading and calculation, Sarayut Pantian for very helpful and support for numerical results, Chakkrit Kaeonikhom for a nice graphics and finally thanks Burin Gumjudpai for a useful discussion, critical comments and financial support.

[†] ชื่อไทย: คริศ สามารถ
Email: `jod_daris@yahoo.com`

[1] S. M. Carroll *et al.*, *"Is Cosmic Speed-Up Due to New Gravitational Physics?"*, Phys. Rev. D **70** (4), 043528 (2004). [arXiv: `astro-ph/0306438`].

[2] S. Capozziello, S. Carloni and A. Troisi, *"Quintessence without Scalar Fields"*. In *Recent Research Developments in Astronomy & Astrophysics*, Vol. 1, Part II, pp. 625–670, S. G. Pandalai (Ed.), Research Signpost, Kerala, India (2003). [arXiv: `astro-ph/0303041`].

[3] S. Nojiri and S. D. Odintsov, *"Where New Gravitational Physics Comes from: M-Theory?"*,

Phys. Lett. B **576** (1–2), 5–11 (2003). [arXiv: `hep-th/0307071`].

[4] G. Magnano and L. M. Sokołowski, *"Physical Equivalence Between Nonlinear Gravity Theories and a General-Relativistic Self-Gravitating Scalar Field"*, Phys. Rev. D **50** (8), 5039–5059 (1994). [arXiv: `gr-qc/9312008`].

[5] G. Magnano, *"Are There Metric Theories of Gravity Other Than General Relativity?"*. In *Proceedings of the 11th Italian Conference on General Relativity and Gravitational Physics*, Trieste, Italy, 26–30 September, 1994, pp. 213–234, M. Carfora *et al.* (Eds.), World Scientific, Singapore (1996). [arXiv: `gr-qc/9511027`]..

[6] P. Teyssandier and Ph. Tourrenc, *"The Cauchy Problem for the $R+R^2$ Theories of Gravity without Torsion"*, J. Math. Phys. **24** (12), 2793–2799 (1983).

[7] S. Nojiri and S. D. Odintsov, *"Modified Gravity with Negative and Positive Powers of Curvature: Unification of Inflation and Cosmic Acceleration"*, Phys. Rev. D **68** (12), 123512 (2003). [arXiv: `hep-th/0307288`].

[8] B. Gumjudpai, *"Brane-Cosmology Dynamics with Induced Gravity"*, Gen. Rel. Grav. **36** (4), 747–766 (2004). [arXiv: `gr-qc/0308046`].

[9] S. Nojiri and S. D. Odintsov, *"Modified Gravity with* $\ln R$ *Terms and Cosmic Acceleration"*, Gen. Rel. Grav. **36** (8), 1765–1780 (2004). [arXiv: `hep-th/0308176`].

[10] A. R. Liddle and D. H. Lyth, *Cosmological Inflation and Large-Scale Structure*, Cambride University Press (2000).

[11] D. A. Easson *et al.*, *"Cosmological Constraints on a Classical Limit of Quantum Gravity"*, Phys. Rev. D **72** (4), 043504 (2005). [arXiv: `astro-ph/0506392`].

[12] D. A. Easson, *"Modified Gravitational Theories and Cosmic Acceleration"*, Int. J. Mod. Phys. A **19** (31), 5343–5350 (2004). [arXiv: `astro-ph/0411209`].

[13] For convenient to find conformal factor e^{φ}, we use Palatini formalisms varying action with respect $\Gamma^{c}{}_{ab}$.

[14] For detail of slow-roll approximation and relate topics see [10].

1st NSPG
Proceedings of the First National Symposium on Physics Graduate Research (1st NSPG)
29 June – 1 July 2006, Chulabhorn Dam, Khon San, Chaiyaphum, Thailand

Sigma Meson Production in Heavy Ion Collisions at Intermediate Energies
การเกิดอนุภาคซิกมาเมซอนในการชนของไอออนหนักที่พลังงานปานกลาง

PORNRAD SRISAWAD,[1,*] YU-MING ZHENG,[2] CHRISTIAN FUCHS,[3]
AMAND FAESSLER,[3] YUPENG YAN,[1] and CHINORAT KOBDAJ[1]

[1]*School of Physics, Institute of Science, Suranaree University of Technology,*
Nakhon Ratchasima, 30000, Thailand
[2]*China Institute of Atomic Energy, P. O. Box 275(18),*
Beijing, 102413, P. R. China
[3]*Institut für Theoretische Physik, Eberhard Karls Universität Tübingen,*
D-72076 Tübingen, Germany

The production of the sigma meson is investigated in the Quantum Molecular Dynamics (QMD) transport model for the p + A reactions with the nuclei A being (^{12}C, ^{40}Ca and ^{208}Pb) at the incident proton energies $T_p = 0.85$ and 1.50 GeV. The QMD simulation results indicates a distinctive A dependence of the sigma production, that is, the increase of A is followed by an increase of the production cross sections. It is also found that the σ meson production in heavy-ion collisions is strongly medium-dependent, and the produced σ mesons decaying in a denser medium experience a stronger mass shift towards lower masses. This mass shift is an experimentally accessible observable in the final state pion pairs which did not suffer reabsorption and rescattering by the surrounding nucleons. It may be pointed out that the ratio of measured sigma mesons from various reactions opens the possibility to address experimentally the mass shift of the σ in a dense nucleus environment.

การเกิดอนุภาคซิกมาเมซอน ได้ถูกศึกษาในทางทฤษฎี โดยใช้แบบจำลองพลศาสตร์โมเลกุลควอนตัม (QMD) ของปฏิกิริยาโปรตอนชนนิวคลีออน โดยพิจารณาปฏิกิริยานิวคลีออนของ คาร์บอน-12 , แคลเซียม-40, และตะกั่ว-208 โดยที่โปรตอนมีพลังงานเข้าชน 0.85 และ 1.5 จิกะอิเล็กตรอนโวลท์ ผลการศึกษา QMD พบว่าการเกิดซิกมามีลักษณะเฉพาะขึ้นอยู่กับนิวคลีออน ถ้านิวคลีออนเพิ่มขึ้น ค่าภาคตัดขวางมีค่าเพิ่มขึ้น และพบว่าการเกิดซิกมาในการชนของไอออนหนักขึ้นอยู่กับตัวกลางอย่างมาก และการสลายตัวในตัวกลางที่หนาแน่นกว่าจะมีการเปลี่ยนมวลไปในทางที่ต่ำลง ค่ามวลเปลี่ยน สังเกตได้ในสถานะสุดท้ายของคู่ไพออน ซึ่งไม่ถูกดูดกลืนครั้งที่สอง และไม่ถูกกระเจิงครั้งที่ 2 โดยนิวคลีออนที่อยู่รายรอบ อัตราส่วนของซิกมาเมซอนที่วัดได้จากหลายปฏิกิริยาเป็นสิ่งที่นำไปสู่การทดลองมวลเปลี่ยนของซิกมาในสิ่งแวดล้อมของนิวเคลียสที่หนาแน่น

PACS numbers: 25.75.-q, 25.40.Ve
Keywords: Heavy-Ion Collision, Quantum Molecular Dynamics, Nuclear Medium, Meson Production

INTRODUCTION

The experimental situation for the σ meson, which is responsible for the mid-range nucleon-nucleon attraction [1] and pays an important role in the Quantum Hadrodynamics (QHD) [2, 3] and the nonlinear sigma model [4], is not so clear. What we know well is that the σ meson is a broad scalar resonance and that it mainly decays into two pions in free space. The pole mass of the σ meson has not been precisely determined so far. Therefore, the σ meson is very difficult to identify from the experimental side. The σ meson production has not yet been measured in heavy ion reactions.

Recently theoretical studies show that the σ mass (m_σ) and width (Γ_σ) decrease dramatically with increasing of the nuclear density (ρ) [5]. This means that the sigma meson may exist in a dense nuclear environment. There are also number of experimental efforts to explore the existence of the sigma meson by pion and photon induced reactions on nuclei [6–12].

The sigma meson can not be detected directly in an experimental setup, but there are indications towards its existence through the information collected from two pions that are measured in coincidence. In the Quantum Molecular Dynamics (QMD) simulations every sigma and pion that are created are stored in some arrays and their evolutions are followed through the end of the reaction. So we are able to get the whole number of σ meson and $\pi\pi$ pairs that are a direct product of the sigma decay. The primary interest is directed to the study of the σ meson dynamics in nuclear matter. The simulations are examined on nuclei in order to determine the effects of medium modifications on the $\pi\pi$-system. The total σ meson distributions span the total energy interval available to the $(\mathrm{p}, \pi\pi)$ reaction, which ranges from $2m_\pi \leqslant M_{\pi\pi} \leqslant 0.70$ GeV. The properties of the sigma meson are highlighted by means of invariant mass, density, decay time, cross section, etc.

The results of the QMD model for the description of the sigma meson production in $\mathrm{p}+A$ reactions with A being nuclei ^{12}C, ^{40}Ca and ^{208}Pb at incident proton energies $E_\mathrm{p} = 1.50$ GeV seem to confirm the importance of the 2π final state interaction in the scalar–isoscalar σ channel.

QUANTUM MOLECULAR DYNAMICS MODEL

It is known that the classical molecular dynamics is a N-body theory, all information about the system is contained in the solution of the N body Liouville equation [13]. Important quantum features are included in the QMD approach [14–19]: collisions among nucleons are Pauli blocked when the scattered nucleons would enter already occupied or partially occupied phase space regions. Furthermore, the scattering amplitude does not relate the scattering angle with the impact parameter in an unique way: the square of the scattering amplitude is identified as a probability distribution.

In the QMD model each nucleon is represented by a coherent state of the form (we set $\hbar, c = 1$)

$$\psi(\vec{r}, \vec{p}_0, t) = \frac{1}{(2\pi L)^{3/4}} \exp\left[\mathrm{i}\vec{p}_0 \cdot (\vec{r} - \vec{r}_0)\right] \exp\left[-\frac{(\vec{r} - \vec{r}_0)^2}{4L}\right] \tag{1}$$

where $\vec{r}_0$ is the time dependent center of the Gaussian wave packet in coordinate space. The width L is kept constant, which means that one does not allow the spreading of the wave function. Otherwise, the whole nucleus would spread in coordinate space as a function of time. L is set to be $L = 1.08$ fm^2 corresponding to a root mean square radius of the nucleons of 1.8 fm. To keep the formulation as close as possible to the classical transport theory, one uses Wigner density instead of working with wave function.

The Wigner transformation of the coherent states is Gaussians in momentum and coordinate space. Then, the Wigner density reads

$$\begin{aligned} f(\vec{r}, \vec{p}, t) &= \frac{1}{(2\pi)^3} \int \mathrm{e}^{-\mathrm{i}\vec{p}\cdot\vec{r}_{12}}\, \psi\!\left(\frac{\vec{r}+\vec{r}_{12}}{2}, t\right) \psi^*\!\left(\frac{\vec{r}-\vec{r}_{12}}{2}, t\right) \mathrm{d}^3\vec{r}_{12} \\ &= \frac{1}{\pi^3} \exp\left\{-\left[\frac{(\vec{r}-\vec{r}_0)^2}{2L} - (\vec{p}-\vec{p}_0)^2 \cdot 2L\right]\right\}. \end{aligned} \tag{2}$$

The N body Wigner density is the direct product of the Wigner densities of N coherent states

$$f^N(\vec{r}_1, \ldots, \vec{r}_N; \vec{p}_1, \ldots, \vec{p}_N; t) = \prod_{i=1}^{N} \frac{1}{\pi^3} \exp\left\{-\left[\frac{(\vec{r}_i - \vec{r}_{i0})^2}{2L} - (\vec{p}_i - \vec{p}_{i0})^2 \cdot 2L\right]\right\}. \tag{3}$$

The Wigner representation of our Gaussian wave packets obeys the uncertainty relation $\Delta r_x \Delta p_x = \hbar/2$. The density in coordinate space is given by the momentum integral over the Wigner density,

$$\begin{aligned}\rho(\vec{r},t) &= \sum_{i=1}^{N} \delta(\vec{r}-\vec{r}_i) \int f^N(\vec{r}_1,\ldots,\vec{r}_N;\vec{p}_1,\ldots,\vec{p}_N;t)\,\mathrm{d}^3\vec{p}_1\ldots\mathrm{d}^3\vec{p}_N\mathrm{d}^3\vec{r}_1\ldots\mathrm{d}^3\vec{r}_N \\ &= \sum_{i}^{N} \frac{1}{(2\pi L)^{3/2}} \exp\left[-\frac{(\vec{r}-\vec{r}_{i0})^2}{2L}\right] . \end{aligned} \tag{4}$$

To initialize the ground state of nucleus A, one first determine the position of the nucleons in a sphere of the radius $r = 1.12A^{1/3}$ by drawing random numbers but rejecting those which would position the centers of two nucleons closer than $r_{\min} = 1.5$ fm. The next step is to determine the local potential $U(r)$ generated by all the other nucleons at the centers of the Gaussians. The local Fermi momentum is determined by the relation $p_{\mathrm{F}}(r_{i0}) = \sqrt{2mU(r_{i0})}$, where $U(r_{i0})$ is the potential energy of particle i. Finally the momenta of all particles are chosen randomly between zero and the local Fermi momentum. We then reject all random numbers which yield two particles closer in phase space than $(r_i - r_j)^2(p_i - p_j)^2 = d_{\min}$.

Nuclei which have been successfully initialized are then boosted towards each other with the proper center of mass velocity using relativistic kinematics. Because we keep the width of the Gaussians fixed, the time evolution of the N-body distribution is determined by the motion of the centroids of the Gaussians $(\vec{r}_{i0}, \vec{p}_{i0})$, which are propagated by the Poisson brackets

$$\dot{\vec{p}}_{i0} = \{\vec{r}_{i0}, H\} \quad \text{and} \quad \dot{\vec{r}}_{i0} = \{\vec{p}_{i0}, H\} . \tag{5}$$

H is the nuclear Hamiltonian

$$\begin{aligned} H &= \sum_i \sqrt{\vec{p}_{i0}^{\,2} + m_i^2} \\ &+ \frac{1}{2} \sum_{i \neq j} \left(U_{ij}^{\mathrm{str}} + U_{ij}^{\mathrm{cou}}\right) . \end{aligned} \tag{6}$$

Here U_{ij}^{cou} is the Coulomb interaction. U_{ij}^{str} the nuclear mean field.

The sigma meson is produced via the decay of nucleon resonances N* (N* → Nσ). The N*'s can be created via NB$_1$ → B$_2$N* (B$_i$ stands N or Δ) and πN → N*. In the N* → Nππ decay the pion pair can occur in an isospin singlet s-wave state $(\pi\pi)^{I=0}_{s\text{-wave}}$ with corresponding branching ratio. This state has the same quantum numbers as the σ-meson and is therefore identified with the σ-meson. The σ-mass is randomly chosen according to the Breit–Wigner distribution

$$\mathrm{d}W_\sigma(\mu) = \alpha\, \frac{\mu\Gamma_\sigma^2\,\mathrm{d}\mu}{(\mu - m_\sigma)^2 + \mu\Gamma_\sigma} , \tag{7}$$

where m_σ is the pole mass and μ the running mass of the σ-meson, Γ_σ is the σ-width. The normalization constant α is determined by the available phase space, i.e. the mass of the decaying N* resonance:

$$\frac{1}{\alpha} = \int_{2m_\pi}^{m_{\mathrm{R}} - m_{\mathrm{N}}} \mathrm{d}W_\sigma(\mu) , \tag{8}$$

where m_{R} is the resonance mass and m_{N} is the nucleon mass. Here one can see that the σ-meson can be assigned a value between the two-pion-threshold and the resonance minus nucleon mass. The resonance decays according to the formula:

$$N(t) = N(0)\, \mathrm{e}^{-\Delta t \Gamma/\gamma} . \tag{9}$$

RESULTS AND DISCUSSIONS

For the elementary (p, ππ) reaction which couple pions to the sigma meson, we take nucleons and resonances Δ(1232), N*(1440), N*(1520), N*(1650) and N*(1680) into account. The σ meson is a very broad resonance, its life time is very small. The sigma meson creates during the collision, propagates inside the nucleus and decays after a short time inside the nucleus. The sigma meson can not be detected directly in an experimental setup, but there are indications towards its existence through the information collected from two pions that are measured in coincidence. In the QMD simulations every sigma and pion that are created are stored in some arrays and their evolutions are followed through the end of the reaction. So we are able to get the whole number of σ meson and $\pi\pi$ that are a direct product of the sigma decay.

The solid curves and dot-dashed curves in the top of Fig. 1 are the produced sigma mesons in ^{12}C without and with medium modifications, respectively. We can see the results of the invariant mass distribution of sigma meson production. There is an appreciable shift of strength to the low invariant mass region due to the medium modifications. The density dependence of the σ mass shifts the curve to the lower mass region when medium effect is taken into account. The dashed curves and dot curves in the figure are the measured sigma mesons without and with medium modifications, respectively. We can also see the same results for the shift of strength to the lower invariant mass region due to the medium modifications. In the second and third rows of Fig. 1 one shows the same results for ^{40}Ca and ^{208}Pb, respectively. The data points display a distinctive A dependence: the increase of A is followed by increase of the production cross sections.

Shown in Fig. 2 are the ratios of the sigma cross sections in various reactions. It is found from the larger values of the sigma production ratios $\sigma(\mathrm{p}+\mathrm{Pb})/\sigma(\mathrm{p}+\mathrm{Ca})$ and $\sigma(\mathrm{p}+\mathrm{Pb})/\sigma(\mathrm{p}+\mathrm{C})$ that the σ meson production in $\mathrm{p}+A$ collisions is strongly medium-dependent. Without additional medium effects the ratio is almost constant as a function of the invariant σ-mass when the shift of the σ mass is taken into account.

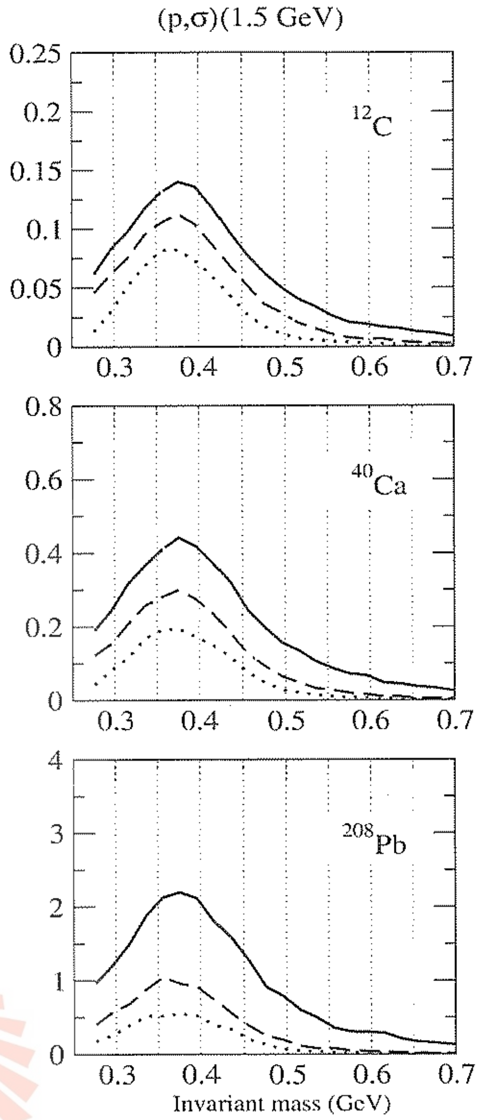

Figure 1: (color online). The invariant-mass distribution of the sigma mesons produced in the $\mathrm{p}+A$ reactions with A being nuclei (^{12}C, ^{40}Ca and ^{208}Pb) at the incident energies 1.5 GeV. Solid lines: produced σ without medium modifications of the σ meson; dashed lines: measured σ without medium modifications of the σ meson; dot and dashed lines: produced σ with medium modifications of the σ meson; and dot lines: measured σ with medium modifications of the σ meson.

The ratios for the measured sigma show a significant enhancement at low invariant masses if the medium modification is considered. It indicates that the produced σ mesons decaying in a denser medium experience a stronger mass shift towards lower masses since the medium is more dense in a heavier nucleus. It should be stressed that this mass shift is an experimentally accessible observable in the final state pion pairs which did not suffer reabsorption and rescattering by the surrounding nucleons. The ratio of measured sigma mesons from various reactions opens the possibility to address experimentally the mass shift of the σ in a

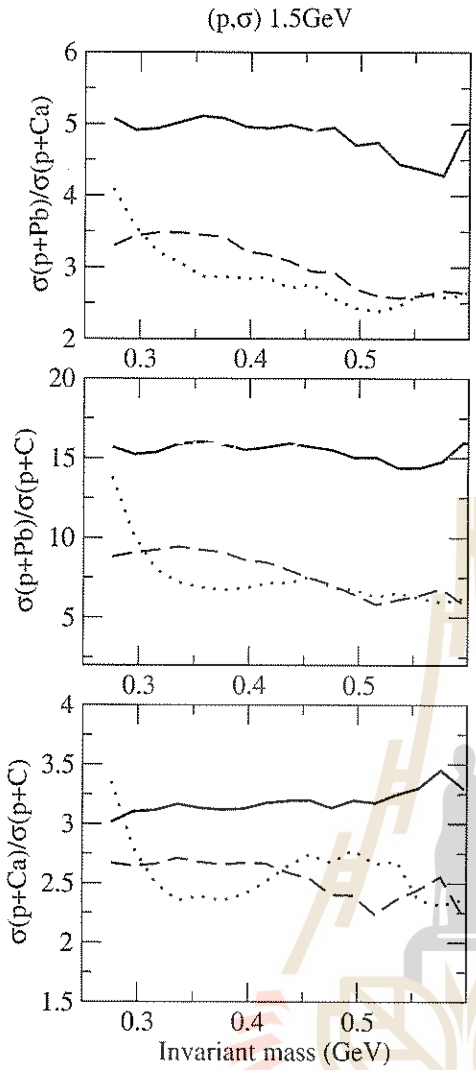

Figure 2: (color online). Ratios of the sigma cross sections in various collisions. Solid lines: produced σ without medium modifications of the σ meson; dashed lines: measured σ without medium modifications of the σ meson; dot and dashed lines: produced σ with medium modifications of the σ meson; dot lines: measured σ with medium modifications of the σ meson.

dense nucleus environment.

ACKNOWLEDGMENTS

This work was supported in part by the National Research Council of Thailand (NRCT) under Grant No. 1.CH5/2549, by the Deutsche Forschungsgemeinschaft (DFG) under Grant No. 446CHV-113/91/1-3, and by the National Natural Science Foundation of China (NSFC) under Grant Nos. 10435080, 10575075 and 10447006.

---

* ชื่อไทย: พรรัตน์ ศรีสวัสดิ์
Email: `pornrads@nu.ac.th`

[1] R. Machleidt, K. Holinde and Ch. Elster, *"The Bonn Meson-Exchange Model for the Nucleon-Nucleon Interaction"*, Phys. Rep. **149** (1), 1–89 (1987).

[2] J. D. Walecka, *"A Theory of Highly Condensed Matter"*, Ann. Phys. (N.Y.) **83** (2), 491–529 (1974).

[3] J. Boguta and A. R. Bodmer, *"Relativistic Calculation of Nuclear Matter and the Nuclear Surface"*, Nucl. Phys. A **292** (3), 413–428 (1977).

[4] N. Petropoulos, *"Linear Sigma Model at Finite Temperature"*, arXiv: `hep-ph/0402136`.

[5] M. J. Vicente Vacas and E. Oset, *"Sigma Meson Mass and Width at Finite Density"*, arXiv: `nucl-th/0204055`.

[6] F. Bonutti *et al.* (CHAOS Collaboration), *"A Dependence of the* $(\pi^+, \pi^+\pi^\pm)$ *Reaction near the* $2m_\pi$ *Threshold"*, Phys. Rev. Lett. **77** (4), 603–606 (1996).

[7] F. Bonutti *et al.* (CHAOS Collaboration), *"*$\pi\pi$ *Pairs in Nuclei and the* σ *Meson"*, Phys. Rev. C **60** (1), 018201 (1999).

[8] F. Bonutti *et al.* (CHAOS Collaboration), *"The* $\pi\pi$ *Interaction in Nuclear Matter from a Study of the* $\pi^+A \to \pi^+\pi^\pm A'$ *Reactions"*, Nucl. Phys. A **677** (1–4), 213–240 (2000). [arXiv: `nucl-ex/0007017`].

[9] P. Camerini *et al.*, *"Threshold Behaviour of the* $\pi^+\pi^-$ *Invariant Mass in Nuclei"*, Nucl. Phys. A **552** (4), 451–468 (1993).

[10] A. Starostin *et al.* (Crystal Ball Collaboration), *"Measurement of* $\pi^0\pi^0$ *Production in the Nuclear Medium by* π^- *Interactions at* 0.408 GeV/c^2*"*, Phys. Rev. Lett. **85** (26), 5539–5542 (2000).

[11] J. G. Messchendorp *et al.*, *"In-Medium Modifications of the* $\pi\pi$ *Interaction in Photon-Induced Reactions"*, Phys. Rev. Lett. **89** (22), 222302 (2002). [arXiv: `nucl-ex/0205009`].

[12] M. Wolf *et al.*, *"Photoproduction of Neutral Pion Pairs from the Proton"*, Eur. Phys. J. A **9** (1), 5–8 (2000).

[13] A. R. Bodmer and C. N. Panos, *"Classical Mi-*

croscopic Calculations of High-Energy Collisions of Heavy Ions", Phys. Rev. C **15** (4), 1342–1358 (1977).

[14] J. Aichelin, *"Quantum Molecular Dynamics—A Dynamical Microscopic n-Body Approach to Investigate Fragment Formation and the Nuclear Equation of State in Heavy Ion Collisions"*, Phys. Rep. **202** (5–6), 233–360 (1991).

[15] C. Fuchs *et al.*, *"Probing the Nuclear Equation of State by* K^+ *Production in Heavy-Ion Collisions"*, Phys. Rev. Lett. **86** (10), 1974–1977 (2001). [arXiv: `nucl-th/0011102`].

[16] C. Fuchs, *"Kaon Production in Heavy Ion Reactions at Intermediate Energies"*, Prog. Part. Nucl. Phys. **56** (1), 1–103 (2006). [arXiv: `nucl-th/0507017`].

[17] Y.-M. Zheng, B.-H. Sa and X.-Z. Zhang, *"Dynamical Features of Medium Energy Heavy Ion Collision Processes"*, Chinese Phys. Lett. **6** (3), 117–121 (1989).

[18] Y.-M. Zheng *et al.*, *"Covariant Kaon Dynamics and Kaon Flow in Heavy Ion Collisions"*, Phys. Rev. C **69** (3), 034907 (2004). [arXiv: `nucl-th/0211088`].

[19] Y.-M. Zheng *et al.*, *"Influence of Chiral Mean Field on Kaon In-plane Flow in Heavy Ion Collisions"*, Commun. Theor. Phys. **41** (5), 746–750 (2004).

Schwinger's Quantum Dynamical Principle and Quantization Problem of Gauge Theories

หลักพลวัตเชิงควอนตัมของชวิงเงอร์และปัญหาการควอนไทซ์ทฤษฎีเกจ

SUPPIYA SIRANAN*
School of Physics, Institute of Science, Suranaree University of Technology,
Nakhon Ratchasima, 30000, Thailand

Schwinger's quantum dynamical principle is used to derive, by an entirely algebraic approach, gauge transformations of the full vacuum-to-vacuum transition amplitude (generating functional) from the celebrated Coulomb gauge to arbitrary covariant gauges for the Abelian gauge theory (quantum electrodynamics) without recourse to Feynman path-integral method.

หลักพลวัตควอนตัมของชวิงเงอร์ ได้ถูกนำมาใช้คำนวณ การแปลงเกจของแอมพลิจูดการเปลี่ยนสถานะ สุญญากาศไปสุญญากาศ (เจเนอเรติงฟังก์ชันนัล) แบบพีชคณิตล้วนๆ จากเกจแบบคูลอมบ์ไปสู่เกจแบบโควาเรียนท์อื่นๆ สำหรับทฤษฎีเกจแบบอาบีเลียน (พลศาสตร์ไฟฟ้าควอนตัม) โดยไม่ต้องอาศัยวิธีปริพันธ์เชิงวิถีของไฟน์แมน

PACS numbers: 11.15.-q, 11.15.Bt,11.15.Tk, 12.20.-m
Keywords: quantum dynamical principle, gauge transformations, Coulomb gauge

INTRODUCTION

When the quantum state $|b, t_i\rangle$ at time t_i evolves to another quantum state $|a, t_f\rangle$ at time t_f ($t_f > t_i$), the transition amplitude is $\langle a, t_f | b, t_i\rangle$. We are interested in studying the variations of $\langle a, t_f | b, t_i\rangle$ with respect to some parameter λ such as masses, coupling constants, external sources and so on.

Schwinger's quantum dynamical principle is

$$\delta\langle a, t_f | b, t_i\rangle = -\frac{i}{\hbar}\int_{t_i}^{t_f} dt\,\langle a, t_f | \delta H | b, t_i\rangle \tag{1}$$

where $H = H\big(q(t), p(t), t; \lambda\big)$ is the Hamiltonian in the Heisenberg representation [1]. δH in (1) refers to the change of $H\big(q(t), p(t), t; \lambda\big)$, with respect to the parameter λ, when q, p and t are fixed.

For some variations, we may replace the Hamiltonian by minus Lagrangian, $H \rightarrow -L$,

$$\delta\langle a, t_f | b, t_i\rangle = \frac{i}{\hbar}\,\langle a, t_f | \,\delta S\, | b, t_i\rangle\,. \tag{2}$$

Also known as quantum action principle or Schwinger's action principle [2, 3].

The aim of this paper is to derived the expression for the vacuum-to-vacuum transition amplitude (or vacuum persistence amplitude) in quantum electrodynamics (QED)

$$\langle 0_+ | 0_-\rangle = \lim_{\substack{t_i \to -\infty \\ t_f \to +\infty}} \langle \text{vac}, t_f | \text{vac}, t_i\rangle \tag{3}$$

and solved the quantization problem of gauge theories. The simplicity and the power of this method is evident and it is expected to be applicable to non-Abelian gauge theories as well as to supersymmetric gauge theories.

DERIVATION

QED in Coulomb Gauge

The Lagrangian density for QED with external (c-number) sources is

$$\begin{aligned}\mathscr{L} = -\frac{1}{4}F_{\mu\nu}F^{\mu\nu} - \frac{1}{2}\bar{\psi}\gamma^\mu\frac{\overleftrightarrow{\partial}_\mu}{i}\psi - m_0\bar{\psi}\psi \\ + \mathscr{L}_I + \mathscr{L}_S\end{aligned} \tag{4}$$

where $F_{\mu\nu} = \partial_\mu A_\nu - \partial_\nu A_\mu$ [8],

$$\mathscr{L}_I = e_0\bar{\psi}\gamma^\alpha\psi A_\alpha \tag{5}$$

is the interaction Lagrangian,

$$\mathscr{L}_S = \bar{\eta}\psi + \bar{\psi}\eta + A_\mu J^\mu \tag{6}$$

is the external source terms, and J^μ is an external source for the Maxwell (gauge) field A^μ, while η and $\bar{\eta}$ are the Grassmannian external sources for Dirac (matter) fields ψ and $\bar{\psi}$ respectively.

To obtain the expression for the vacuum-to-vacuum transition amplitude $\langle 0_+|0_-\rangle$, as the generator of all the propagators (Green functions) of the theory in the presence of the external sources, we work explicitly in the celebrated Coulomb gauge (as a physical gauge, where the physical components are clear at the outset) by imposing the constraint

$$\vec{\nabla}\cdot\vec{A} = \partial_k A^k = 0, \quad k = 1,2,3. \tag{7}$$

This constraint allows us to solve A^3 in terms of A^1 and A^2 [4]:

$$A^3 = -(\partial_3)^{-1}\partial_\mathsf{a} A^\mathsf{a}, \quad \mathsf{a} = 1,2, \tag{8}$$

or

$$A^k = \left(\delta^{k\mathsf{a}} - \delta^{k3}\frac{\partial_\mathsf{a}}{\partial_3}\right) A^\mathsf{a}, \tag{9}$$

and treat A^0, A^1, A^2 (not A^3), and ψ as dynamical variables (later we will see that A^0 is a dependent field). The field equations are

$$\left[\gamma^\mu\left(\frac{\partial_\mu}{\mathrm{i}} - e_0 A_\mu\right) + m_0\right]\psi = \eta\,, \tag{10a}$$

$$\overline{\psi}\left[-\gamma^\mu\left(\frac{\overleftarrow{\partial}_\mu}{\mathrm{i}} - e_0 A_\mu\right) + m_0\right] = \overline{\eta} \tag{10b}$$

and

$$-\partial_\mu F^{\mu\nu} = \left(g^{\nu\alpha} - g^{\nu i}\frac{\partial_i\partial^\alpha}{\nabla^2}\right)\left(e_0\overline{\psi}\gamma_\alpha\psi + J_\alpha\right). \tag{10c}$$

It should be noted that equations (10a) and (10b) lead to

$$\partial_\mu(\overline{\psi}\gamma^\mu\psi) = \mathrm{i}\left(\overline{\psi}\eta - \overline{\eta}\psi\right) \tag{11}$$

and the Dirac current is conserved in the absence of the Grassmannian external sources η and $\overline{\eta}$, while J_α need not be conserved because $\partial_\nu\partial_\mu F^{\mu\nu} = 0$ is automatically satisfied for all J_α [4]. No restriction is set on J_α (such as $\partial^\alpha J_\alpha = 0$), until the entire analysis is completed, we may vary the components of J_α independently to generate the full photon propagator if we know the expression of the vacuum-to-vacuum transition amplitude (generating functional) [5].

From (10c), we obtain

$$-\Box A^\mu = \left(g^{\mu\alpha} - g^{\alpha i}\frac{\partial_i\partial^\mu}{\nabla^2}\right) g_{\alpha\beta}\left(g^{\beta\sigma} - g^{\beta k}\frac{\partial_k\partial^\sigma}{\nabla^2}\right)\left(e_0\overline{\psi}\gamma_\sigma\psi + J_\sigma\right) \tag{12a}$$

or

$$-\Box F^{\mu\nu} = \left(g^{\nu\alpha}\partial^\mu - g^{\mu\alpha}\partial^\nu\right) g_{\alpha\beta}\left(g^{\beta\sigma} - g^{\beta k}\frac{\partial_k\partial^\sigma}{\nabla^2}\right)\left(e_0\overline{\psi}\gamma_\sigma\psi + J_\sigma\right). \tag{12b}$$

Schwinger's quantum dynamical principle reads

$$\langle 0_+|0_-\rangle\frac{\overleftarrow{\delta}}{\mathrm{i}\delta\eta(x)} = -\frac{\delta}{\mathrm{i}\delta\eta(x)}\langle 0_+|0_-\rangle = \langle 0_+|\overline{\psi}(x)|0_-\rangle \tag{13a}$$

and

$$\frac{\delta}{\mathrm{i}\delta\overline{\eta}(x)}\langle 0_+|0_-\rangle = -\langle 0_+|0_-\rangle\frac{\overleftarrow{\delta}}{\mathrm{i}\delta\overline{\eta}(x)} = \langle 0_+|\psi(x)|0_-\rangle\,, \tag{13b}$$

while for non-Grassmannian source, variations of the components of J^μ may be carried out independently, we have

$$\frac{\delta}{\mathrm{i}\delta J^\mu(x)}\langle 0_+|0_-\rangle = \langle 0_+|0_-\rangle\frac{\overleftarrow{\delta}}{\mathrm{i}\delta J^\mu(x)} = \langle 0_+|A_\mu(x)|0_-\rangle \tag{13c}$$

and

$$-\mathrm{i}\frac{\partial}{\partial e_0}\langle 0_+|0_-\rangle = \int_{\sigma_i}^{\sigma_f}(\mathrm{d}x)\left\langle 0_+\left|\left(\overline{\psi}(x)\gamma^\alpha\psi(x)A_\alpha(x)\right)_+\right|0_-\right\rangle$$

$$= \int_{\sigma_i}^{\sigma_f}(\mathrm{d}x)\,\frac{\delta}{\mathrm{i}\delta\eta(x)}\gamma^\alpha\frac{\delta}{\mathrm{i}\delta\overline{\eta}(x)}\,\frac{\delta}{\mathrm{i}\delta J^\alpha(x)}\,\langle 0_+|0_-\rangle \tag{13d}$$

where $(\ldots)_+$ denotes the time-ordered product. Although A^0 and A^3 are dependent fields, but ψ and $\overline{\psi}$ are not dependent fields, equations (13c) and (13d) hold true [6] since the functional derivatives in (13c) and (13d) is defined with the independent fields and their conjugate momenta fixed.

Let $\langle 0_+|0_-\rangle_0$ denotes the vacuum-to-vacuum transition amplitude in the presence of the external sources with e_0 set equal to zero, $\langle 0_+|0_-\rangle_0 = \langle 0_+|0_-\rangle\big|_{e_0=0}$, and satisfies

$$\left[\gamma^\mu\frac{\partial_\mu}{\mathrm{i}} + m_0\right]\frac{\delta}{\mathrm{i}\delta\overline{\eta}(x)}\langle 0_+|0_-\rangle_0 = \eta(x)\,\langle 0_+|0_-\rangle_0 \tag{14a}$$

$$\langle 0_+|0_-\rangle_0\,\frac{\overleftarrow{\delta}}{\mathrm{i}\delta\eta(x)}\left[-\gamma^\mu\frac{\overleftarrow{\partial}_\mu}{\mathrm{i}} + m_0\right] = \overline{\eta}(x)\,\langle 0_+|0_-\rangle_0 \tag{14b}$$

and

$$-\partial_\mu\left[\partial^\mu\frac{\delta}{\mathrm{i}\delta J_\nu(x)} - \partial^\nu\frac{\delta}{\mathrm{i}\delta J_\mu(x)}\right]\langle 0_+|0_-\rangle_0 = \left(g^{\nu\alpha} - g^{\nu i}\frac{\partial_i\partial^\alpha}{\nabla^2}\right)J_\alpha(x)\,\langle 0_+|0_-\rangle_0 \tag{14c}$$

or

$$-\Box\frac{\delta}{\mathrm{i}\delta J_\mu(x)}\langle 0_+|0_-\rangle_0 = \left(g^{\mu\alpha} - g^{\alpha i}\frac{\partial_i\partial^\mu}{\nabla^2}\right)g_{\alpha\beta}\left(g^{\beta\sigma} - g^{\beta k}\frac{\partial_k\partial^\sigma}{\nabla^2}\right)J_\sigma(x)\,\langle 0_+|0_-\rangle_0\,. \tag{14d}$$

From (14a)–(14d), together with the normalization $\langle 0_+|0_-\rangle\big|_{\eta=\overline{\eta}=J=0} = 1$, we obtain

$$\langle 0_+|0_-\rangle_0 = \exp\left[\mathrm{i}\int(\mathrm{d}x)(\mathrm{d}x')\,\overline{\eta}(x)\,S_+(x,x')\,\eta(x')\right]$$

$$\times\exp\left[\frac{\mathrm{i}}{2}\int(\mathrm{d}y)(\mathrm{d}y')\,J_\mu(y)\,D^{\mu\nu}_{\mathrm{C}+}(y,y')\,J_\nu(y')\right] \tag{15}$$

where

$$S_+(x,x') = \int\frac{(\mathrm{d}p)}{(2\pi)^4}\,\mathrm{e}^{\mathrm{i}p(x-x')}\,\frac{-\gamma p + m_0}{p^2 + m_0^2 - \mathrm{i}\epsilon} \tag{16a}$$

and

$$D^{\mu\nu}_{\mathrm{C}+}(y,y') = \int\frac{(\mathrm{d}q)}{(2\pi)^4}\,\mathrm{e}^{\mathrm{i}q(y-y')}\left(g^{\mu\alpha} - g^{\alpha i}\frac{q_i q^\mu}{\vec{q}^{\,2}}\right)g_{\alpha\beta}\left(g^{\beta\nu} - g^{\beta k}\frac{q_k q^\nu}{\vec{q}^{\,2}}\right)\frac{1}{q^2 - \mathrm{i}\epsilon} \tag{16b}$$

are the free electron propagator and the free photon propagator in the Coulomb gauge, respectively.

Equation (13d) may be integrated to give

$$\langle 0_+|0_-\rangle = \exp\left[\mathrm{i}e_0\int(\mathrm{d}z)\,\frac{\delta}{\mathrm{i}\delta\eta(z)}\gamma^\alpha\frac{\delta}{\mathrm{i}\delta\overline{\eta}(z)}\,\frac{\delta}{\mathrm{i}\delta J^\alpha(z)}\right]\langle 0_+|0_-\rangle_0 \equiv Z_{\mathrm{C}}[\eta,\overline{\eta},J]\,. \tag{17}$$

The full electron propagator $S(x,x';J)$ and the full Coulomb-gauge photon propagator $D^{\mu\nu}_{\mathrm{C}}(y,y';J)$, in the absence of external Grassmannian sources η, $\overline{\eta}$, may be easily generated by taking functional differentiations [5]:

$$S(x,x';J) = \mathrm{i}\left[\frac{1}{Z_{\mathrm{C}}[\eta,\overline{\eta},J]}\,\frac{\delta}{\mathrm{i}\delta\eta(x')}\,\frac{\delta}{\mathrm{i}\delta\overline{\eta}(x)}Z_{\mathrm{C}}[\eta,\overline{\eta},J]\right]_{\eta=\overline{\eta}=0} \tag{18a}$$

and

$$D^{\mu\nu}_{\mathrm{C}}(y,y';J) = \mathrm{i}\left[\frac{\delta}{\mathrm{i}\delta J_\mu(y)}\,\frac{\delta}{\mathrm{i}\delta J_\nu(y')}\ln Z_{\mathrm{C}}[\eta,\overline{\eta},J]\right]_{\eta=\overline{\eta}=0}. \tag{18b}$$

Quantization Problems of Gauge Field in QED

For gauge theories, the dependent fields A^3 and A^0 have no canonical momenta ($\Pi^3 = 0$ and $\Pi^0 = 0$) and hence we cannot quantize gauge field A^μ by using the naïve (equal-time) commutation relation:

$$\left[A^\mu(x),\Pi^\nu(x')\right]\Big|_{x^0=x'^0} \overset{?}{=} \mathrm{i}g^{\mu\nu}\delta^3(\vec{x}-\vec{x}'). \tag{19}$$

We have to quantize only independent fields A^1 and A^2, the (equal-time) commutation relation for the physical degree of freedom A^1 and A^2 is

$$\left[A^{\mathrm{a}}(x),\Pi^{\mathrm{b}}(x')\right]\Big|_{x^0=x'^0} = \mathrm{i}\delta^{\mathrm{ab}}\delta^3(\vec{x}-\vec{x}'), \tag{20}$$

$\mathrm{a},\mathrm{b} = 1,2$, where $\Pi^\mu(x)$ is the canonical conjugate momenta to $A^\mu(x)$ defined by

$$\Pi^\mu(x) \equiv \frac{\delta S}{\delta \dot{A}_\mu(x)} = -F^{0\mu}(x) + g^{\mu k}\frac{\partial_k}{\partial_3}F^{03}(x). \tag{21}$$

It is easily to show that the correct (equal-time) commutation relation is

$$\left[A^\mu(x),\Pi^\nu(x')\right]\Big|_{x^0=x'^0} = \mathrm{i}g^{\mu i}g^{\nu k}\left(\delta^{ik} - \delta^{i3}\frac{\partial_k}{\partial_3}\right)\delta^3(\vec{x}-\vec{x}'), \tag{22}$$

not (19).

From (10c) and (21) we may also write:

$$\begin{aligned} F^{\mu\nu}(x) &= \left(g^{\mu0}g^{\nu\sigma} - g^{\nu0}g^{\mu\sigma}\right)g_{\sigma\beta}\left(g^{\beta\alpha} - g^{\beta k}\frac{\partial_k\partial^\alpha}{\nabla^2}\right)\Pi_\alpha(x) \\ &\quad - \left(g^{\mu0}g^{\nu k} - g^{\nu0}g^{\mu k}\right)\frac{\partial_k}{\nabla^2}\left[e_0\overline{\psi}(x)\gamma^0\psi(x) + J^0(x)\right] \\ &\quad + \frac{1}{2}\left(\delta^\mu{}_k\delta^\nu{}_l - \delta^\nu{}_k\delta^\mu{}_l\right)F^{kl}(x), \end{aligned} \tag{23}$$

which then leads to the (equal-time) commutation relations

$$\left[A^\mu(x),F^{\alpha\beta}(x')\right]\Big|_{x^0=x'^0} = \mathrm{i}g^{\mu i}\left(g^{\alpha0}g^{\beta k} - g^{\beta0}g^{\alpha k}\right)\delta^{ik}_\perp(\vec{x}-\vec{x}') \tag{24}$$

and

$$\begin{aligned} \left[F^{\mu\nu}(x),F^{\alpha\beta}(x')\right]\Big|_{x^0=x'^0} &= \mathrm{i}\Big[\left(g^{\alpha0}g^{\beta k} - g^{\beta0}g^{\alpha k}\right)\left(g^{\nu i}\partial^\mu - g^{\mu i}\partial^\nu\right) \\ &\quad - \left(g^{\mu0}g^{\nu k} - g^{\nu0}g^{\mu k}\right)\left(g^{\beta i}\partial^\alpha - g^{\alpha i}\partial^\beta\right)\Big]\,\delta^{ik}_\perp(\vec{x}-\vec{x}') \end{aligned} \tag{25}$$

in terms of the transverse delta function

$$\delta^{ik}_\perp(\vec{x}-\vec{x}') \equiv \left(\delta^{ik} - \frac{\partial^i\partial^k}{\nabla^2}\right)\delta^3(\vec{x}-\vec{x}'). \tag{26}$$

Gauge Transformations

We note that the Lagrangian density $\mathscr{L}$ in (4), without the external source terms $\mathscr{L}_{\mathrm{S}}$ is invariant under simultaneous local gauge transformations:

$$\psi(x) \longrightarrow \psi'(x) \equiv \mathrm{e}^{\mathrm{i}e_0\lambda(x)}\,\psi(x) \tag{27a}$$

$$\overline{\psi}(x) \longrightarrow \overline{\psi}'(x) \equiv \overline{\psi}(x)\,\mathrm{e}^{-\mathrm{i}e_0\lambda(x)} \tag{27b}$$

and

$$A^{\mu}(x) \longrightarrow A'^{\mu}(x) \equiv A^{\mu}(x) + \partial^{\mu}\lambda(x)\,. \tag{27c}$$

We introduce the generating functional in arbitrary covariant gauges

$$Z[\rho,\overline{\rho},K;G] = \exp\left[\mathrm{i}e_0\int(\mathrm{d}z)\,\frac{\delta}{\mathrm{i}\delta\rho(z)}\gamma^{\alpha}\frac{\delta}{\mathrm{i}\delta\overline{\rho}(z)}\,\frac{\delta}{\mathrm{i}\delta K^{\alpha}(z)}\right]$$
$$\exp\left[\mathrm{i}\int(\mathrm{d}x)(\mathrm{d}x')\,\overline{\rho}(x)\,S_{+}(x-x')\,\rho(x')\right]$$
$$\times\exp\left[\frac{\mathrm{i}}{2}\int(\mathrm{d}y)(\mathrm{d}y')\,K_{\mu}(y)\,D^{\mu\nu}_{G+}(y-y')\,K_{\nu}(y')\right] \tag{28}$$

where the free photon propagator in arbitrary covariant gauges is

$$D^{\mu\nu}_{G+}(y-y') = \int\frac{(\mathrm{d}q)}{(2\pi)^4}\,\mathrm{e}^{\mathrm{i}q(y-y')}\left[\left(g^{\mu\nu}-\frac{q^{\mu}q^{\nu}}{q^2}\right)\frac{1}{q^2-\mathrm{i}\epsilon}+q^{\mu}q^{\nu}G(q^2)\right] \tag{29}$$

and $G(q^2)$ is arbitrary.

Manoukian and Siranan [7] show that

$$Z_{\mathrm{C}}[\eta,\overline{\eta},J] = \left[\mathrm{e}^{\mathrm{i}\widehat{W}'}Z[\rho,\overline{\rho},K;G]\right]_{\rho=0,\overline{\rho}=0,K=0} \tag{30}$$

where

$$\widehat{W}' = \int(\mathrm{d}x)\left\{\overline{\eta}(x)\exp\left[-\mathrm{i}e_0\widehat{a}^{\xi}\frac{\delta}{\mathrm{i}\delta K^{\xi}(x)}\right]\frac{\delta}{\mathrm{i}\delta\overline{\rho}(x)}+\frac{\delta}{\mathrm{i}\delta\rho(x)}\exp\left[\mathrm{i}e_0\widehat{a}^{\xi}\frac{\delta}{\mathrm{i}\delta K^{\xi}(x)}\right]\eta(x)\right.$$
$$\left.+\left[(g^{\xi\sigma}-\widehat{a}^{\xi}\partial^{\sigma})J_{\sigma}(x)\right]\frac{\delta}{\mathrm{i}\delta K^{\xi}(x)}\right\} \tag{31}$$

and

$$\widehat{a}^{\xi} = g^{\xi k}\frac{\partial_k}{\nabla^2} \tag{32}$$

relating the Coulomb gauge to arbitrary covariant gauges. Gauge transformations of all the propagators (Green functions) may be explicitly carried out from (30)–(31) and this expression is consistent with earlier derivations [5] by different methods.

CONCLUDING REMARKS

Schwinger's quantum dynamical principle leads systematically to the expression for the vacuum-to-vacuum transition amplitude $\langle 0_+ | 0_- \rangle$ and solves the quantization problem of gauge fields with no much effort, without the recourse to Feynman's path integrals. Of course, the path integrals may be formally derived from the quantum dynamical principle (cf. [1, 3, 6]).

The extensions to non-Abelian gauge theory and supersymmetric gauge theories will be attempted in a forthcoming report.

Acknowledgements

I would like to thank my thesis advisor Prof. Dr. Edouard Berge Manoukian for discussions. The financial support from the "Royal Golden Jubilee Ph.D. Program" by the Thailand Research Fund (Grant No. PHD/0193/2543) is acknowledged.

---

* ชื่อไทย: ศุภปิยะ สิระนันท์
Email: `suppiya007@yahoo.com`

[1] E. B. Manoukian, *Quantum Physics: A Wide Spectrum*, Springer, Dordrecht (2006).

[2] S. S. Schweber, *"The Sources of Schwinger's Green's Functions"*, Proc. Natl. Acad. Sci. USA **102** (22), 7783–7788 (2005).

[3] K. A Milton (ed.), *A Quantum Legacy: Seminal Papers of Julian Schwinger*, World Scientific, Singapore (2000).

[4] E. S. Fradkin and I. V. Tyutin, *"S Matrix for Yang–Mills and Gravitational Fields"*, Phys. Rev. D **2** (12), 2841–2857 (1970).

[5] B. Zumino, *"Gauge Properties of Propagators in Quantum Electrodynamics"*, J. Math. Phys. **1** (1), 1–7 (1960).

[6] C. S. Lam, *"Feynman Rules and Feynman Integrals for System with Higher-Spin Fields"*, Nuovo Cimento **38** (4), 1755–1764 (1965).

[7] E. B. Manoukian and S. Siranan, *"Action Principle and Algebraic Approach to Gauge Transformations in Gauge Theories"*, Int. J. Theor. Phys. **44** (1), 53–62 (2005). And references therein.

[8] We work in the natural unit $\hbar = c = 1$ with Lorentz signature $(-,+,+,+)$ and use Einstein's summation convention where all Greek indices (α, β, μ, ν, σ, ξ) run from 0 to 3, but the Latin (italic) indices (i, k) run from 1 to 3, except the indices a and b run from 1 to 2.

The Conceptual Understanding of Light Refraction of Thai Science Students and High School Physics Teachers

การสำรวจความเข้าใจเรื่องการหักเหของแสงของนักศึกษาคณะวิทยาศาสตร์ มหาวิทยาลัยเชียงใหม่ และครูฟิสิกส์ระดับมัธยมศึกษา

Kreetha Keawkhong,[1,*] Narumon Emarat,[2] Kwan Arayathanitkul,[2]
Chernchok Soankwan,[2] and Ratchapak Chitaree[2]

[1] *Institute for Innovation and Development of Learning Process,*
Mahidol University, Bangkok, 10400, Thailand
[2] *Department of Physics, Faculty of Science, Mahidol University,*
Bangkok, 10400, Thailand

This research shows the results of an investigation in conceptual understanding of light refraction of 37 science students and 63 high school physics teachers. This is done by using the conceptual test which comprises of a series of open-ended questions. The results from the investigation show that the tendency of students misunderstandings in light reflection are the same as that of high school physics teachers. Moreover, some of them can not apply the refraction principle for light phenomena. The results of this research are useful for the improvement of science teaching, especially in physics. They can be used as a guide to design the apparatus and the appropriate learning process of refraction of light.

งานวิจัยนี้แสดงผลการสำรวจความเข้าใจของนักศึกษาคณะวิทยาศาสตร์ ระดับปริญญาตรีชั้นปีที่หนึ่ง จำนวน 37 คน และครูฟิสิกส์ระดับมัธยมศึกษาจำนวน 63 คน เกี่ยวกับเรื่องการหักเหของแสง โดยใช้แบบทดสอบที่มีชุดคำถามเป็นแบบปลายเปิด ซึ่งแต่ละชุดนั้นสามารถที่จะบอกได้ว่า นักศึกษามีความเข้าใจหรือไม่เข้าใจในความรู้พื้นฐานใดในเรื่องการหักเหของแสง จากผลการวิจัยพบว่า นักศึกษาและครูสอนฟิสิกส์ มีความเข้าใจที่ผิดในหลักการของการหักเหของแสง อยู่ในแนวโน้มที่ใกล้เคียงกัน นอกจากนั้น จากการสำรวจยังทำให้พบว่า นักศึกษาและครูฟิสิกส์บางท่าน ยังไม่สามารถนำความรู้ และหลักการของการหักเหของแสง มาประยุกต์ใช้ในการอธิบายปรากฏการณ์ธรรมชาติของแสงได้ แต่อย่างไรก็ตาม ผลของงานวิจัยนี้เป็นสิ่งที่แสดงให้เห็นว่า ทั้งนักศึกษาและครูฟิสิกส์ ยังมีสิ่งที่เข้าใจผิดในเนื้อหา และหลักการการหักเหของแสงอยู่ ดังนั้น ผลการทดลองนี้จึงมีความสำคัญในการช่วยพัฒนาการสอนวิทยาศาสตร์อย่างยิ่ง ผลของการวิจัยนี้สามารถทำให้ผู้วิจัยตระหนัก และพบหนทางที่จะออกแบบอุปกรณ์ และกระบวนการเรียนการสอนที่เหมาะสม ในการเรียนการสอนฟิสิกส์ เพื่อให้นักศึกษา มีความเข้าใจที่ถูกต้องในเรื่องการหักเหของแสงต่อไป

PACS numbers: 13.85.Hd, 24.10.Jv, 24.85.+p
Keywords: Investigation, Light Refraction, Concepts.

INTRODUCTION

About 30 years ago, physics lecturers found that their students had misunderstanding in some physics principles; therefore they try to help their students to have better understanding by using new methods. Light was one of physics topics which many students had confusion. They were many researches that investigated light misconception of students such as "Children observation, ideas, and the development of classroom theories about light (Brick house , N.W.1994)", "Student Difficulties in understanding Image Formation by plane mirror (McDermott,1986)". All of researches found that college students can not connect physics principle to science phenomena. This paper is the beginning of research which helps Thai students to improve their thinking skills in light refraction concepts. The first step of this research is to probe understanding in light refraction concepts of students and teachers in order to find out the appropriate methods for change misconceptions.

Light conceptual test is used for probe an understanding of students in light concepts. They were many researchers who used this test before. This research uses some conceptual questions about refraction from some researches and constructs some questions from teaching experience to test 63 Thai physics teacher and 37 the first year science student.

METHODOLOGY

The first step of this research is to investigate the works that have done before. Beside, I use some wrong student ideas about refraction to design the question series. They are 3 questions for refraction conceptual test.

The first question is about studies students' idea of refraction and how students perceive water as a medium for refraction. This question is chosen from *"Malaysian School Children Misconceptions of Light"* by Siti Hendon Binti Sheikh Abdullah and Khalijah Binti Mohd Salleh [1].

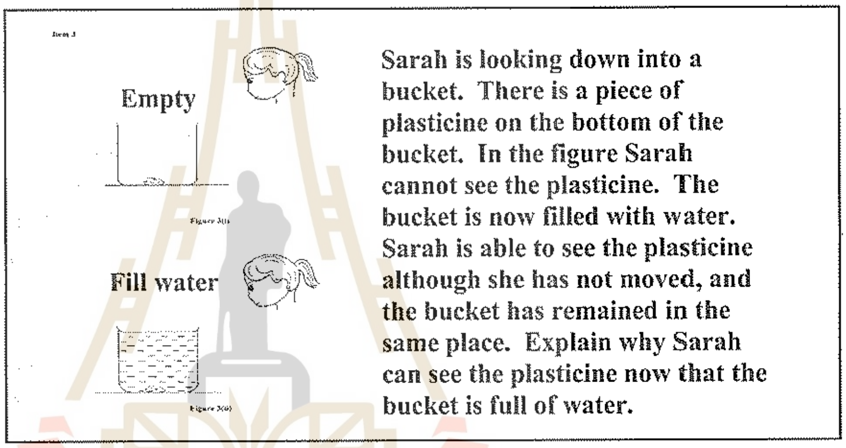

Sarah is looking down into a bucket. There is a piece of plasticine on the bottom of the bucket. In the figure Sarah cannot see the plasticine. The bucket is now filled with water. Sarah is able to see the plasticine although she has not moved, and the bucket has remained in the same place. Explain why Sarah can see the plasticine now that the bucket is full of water.

The second question is about refraction index concepts. This question probe students' idea of relation between refraction index and the angle of light beams when they pass through the different medium. It is chosen from *"Action Research and the Light and Optics Conceptual Evaluation"* that developed by David Sokoloff [2].

Questions 2.1–2.5 refer to a very narrow beam of light (for example, a laser beam) that can be represented by a single ray. The light is initially traveling from left to right in a transparent medium of index of refraction n_1, and incident on a second transparent medium of index of refraction n_2. The reflected and refracted rays are as shown in the diagrams below. (If either is missing, it means there is no reflected or no refracted ray.) Answer each of the questions below with one of the following choices, **A** through **F**.

A. Only if $n_2 > n_1$,
B. Only if $n_2 = n_1$,
C. Only if $n_2 < n_1$,
D. Can happen with A or C.
E. Never possible.
F. Always possible regardless of the relative sizes of the indexes of refraction.

2.1 For which condition A through F could the rays be as shown in the figure?

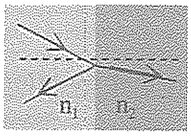

2.2 For which condition A through F could the rays be as shown in the figure?

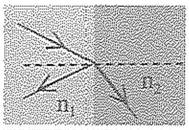

2.3 For which condition A through F could the rays be as shown in the figure?

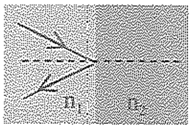

2.4 For which condition A through F could the rays be as shown in the figure?

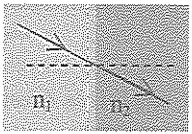

2.5 For which condition A through F could the rays be as shown in the figure?

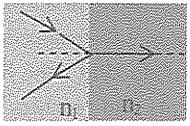

The third question is about refraction index and refraction angle of different light wavelengths. This question comes from my physics teaching experience. My student believe that refraction index in any mediums have only one value. In fact, it depends on a light wave length.

Questions 3.1–3.2 are the experiments that used laser beam to pass through air and water at the same angle. The figure 1 use blue laser, figure 2 use red laser and figure 3 use green laser. All of experiments, the medium (water) and vessel are the same.

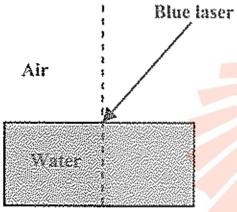

Figure: 1

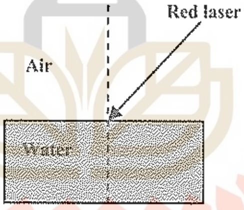

Figure: 2

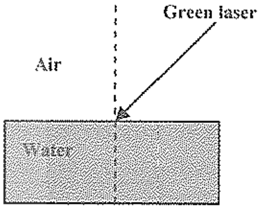

Figure: 3

3.1) Order the refraction angle of each experiments from large to small.

3.2) Are the refraction index of each experiments the same? Give the reason.

All questions are used to test the refraction concepts of 37 the first year science students at Chaingmai University and 63 high school physics teacher of Thailand for 15 minutes. The data of each group is analyzed and compared the tendency.

RESULTS, DISCUSSION AND CONCLUSION

The first question:

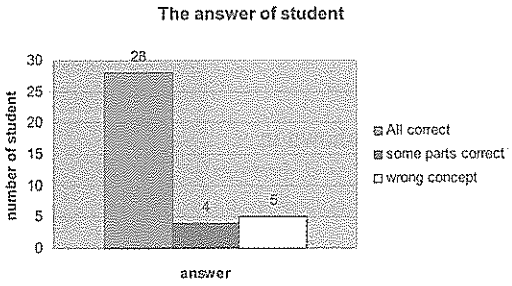

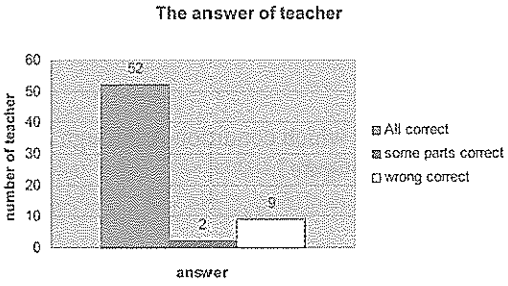

Although this question is very basic but it still has wrong answer. The students who had correct answer are 76% and 83% for teacher. Both student and teacher who had wrong answer are closely, 13% and 14% respectively. Some students confuse between refraction and reflection concepts. They try to explain that "the light rays reflect back and forth in the vessel then refract to eyes". Beside, some students and teachers try to explain by drawing light rays but they were wrong direction.

The second question:

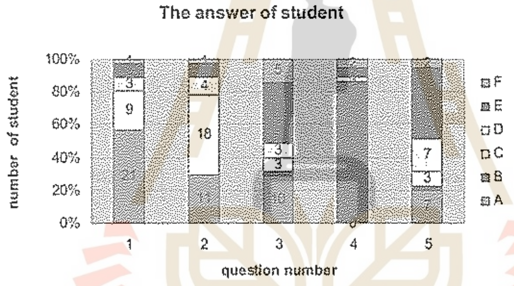

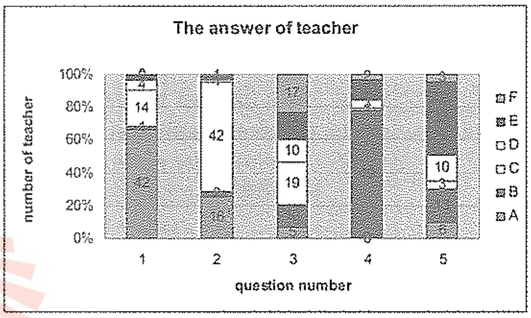

People \ Question number	Correct answer				
	2.1	2.2	2.3	2.4	2.5
student	56%	48%	35%	86%	40%
teacher	67%	67%	30%	78%	44%

The concepts that use to imply in this part are complicate than the first question. The question numbers which make both of them confused (lower 50%) are 2.3 and 2.5. In 2.3 is a total refraction phenomenon, it occurs when a refractive index of the first medium more than the second medium. For 2.5, it is impossible to occur in this phenomenon because when light rays pass the first medium, an identical angle and a refracted angle will correspond to Snell's law. Noticed that the question number 2.2 still make students confuse more than teacher.

The third question:

3.1)

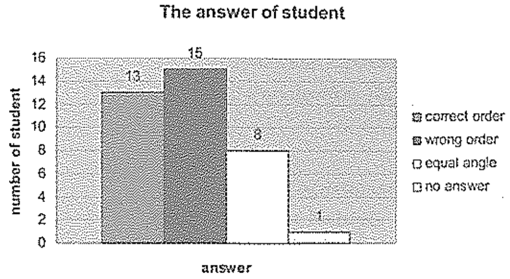

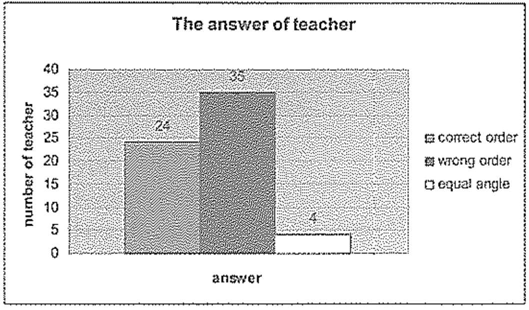

This question uses the concepts that different light wavelengths have different velocity when they pass through a medium so, if they pass through the same medium and the same identical angle, each wave length has different refracted angle. The numbers of student and teacher who had a correct answer are 35% and 38% respectively. Most of them can not order a refraction angle. It is very surprise for me for some both of them who answered that each light has an equal refractive angle.

3.2)

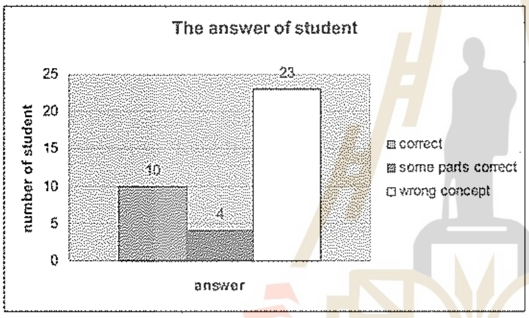

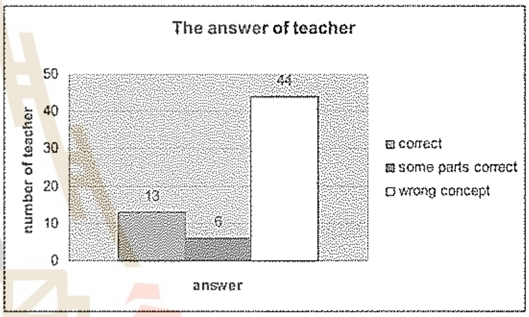

This question uses the concepts that different light wavelengths have different velocity in a medium when they pass through the same medium. So, each wave length has different refraction index. Most of them imply that "Water has only one refractive index".

All of results show that Thai students and Thai physics teacher have misunderstanding concepts in refraction, especially in refractive index topics. It is a big problem in physics teaching of Thailand. This results are data for my next research which help Thai student and physics teachers to understand better in refraction concepts.

ชื่อไทย: กรีฑา แก้วคง
Email: `kwkhng@hotmail.com`

[1] S. H. S. Abdullah and K. M. Salleh, *"Malaysian School Children Misconceptions of Light"*, School of Applied Physics, Universiti Kebangsaan Malaysia, 43600 Bangi, Selangor, Malaysia.
[2] David R. Sokoloff, *"Action Research and the Light and Optics Conceptual Evaluation"*. [Online]. Available: `http://www.uoregon.edu/~sokoloff/ActionResearch.doc`.

Proceedings of the First National Symposium on Physics Graduate Research (1^{st} NSPG)
29 June – 1 July 2006, Chulabhorn Dam, Khon San, Chaiyaphum, Thailand

Device for Measuring Total Harmonic Distortion of AC Voltage

เครื่องวัดผลรวมความเพี้ยนฮาร์มอนิกส์ของแรงดันไฟฟ้ากระแสสลับ

RUNGROJ MAOLANON*
National Nanotechnology Center, 111 Thailand Science Park,
130 Paholyothin Rd., Klong Luang, Pathumthani, 12120, Thailand

WICHIT SIRICHOTE
Department of Applied Physics, Faculty of Science,
King Mongkut's Institute of Technology Ladkrabang, Bangkok, 10520, Thailand

A device used for measuring total harmonic distortion (THD) of AC voltage has been designed and built. The device consists of two microcontroller boards: 1) the 8-bit MCU for signal capturing and 2) the 16-bit MCU for Fast Fourier Transform computing. The AC voltage signal was captured by a 12-bit analog-to-digital converter. The embedded firmware running on 16-bit board computes 128-point FFT. The THD was calculated up to 64-order of harmonic components. We have recorded the sample measurements of THD for residential and academic building.

ได้ออกแบบและสร้างเครื่องวัดผลรวมความเพี้ยนฮาร์มอนิกส์ของแรงดันไฟฟ้ากระแสสลับ เครื่องวัดประกอบด้วย บอร์ดไมโครคอนโทรลเลอร์สองส่วน ส่วนแรกเป็นบอร์ดไมโครคอนโทรลเลอร์ขนาด 8 บิต ทำหน้าที่เก็บสัญญาณ และบอร์ดไมโครคอนโทรลเลอร์ ขนาด 16 บิต ทำหน้าที่คำนวณฟาส์ทฟูเรียร์ทรานฟอร์ม สัญญาณแรงดันไฟฟ้ากระแสสลับจะถูกแปลงด้วยตัวแปลงอนาลอกเป็นดิจิตอลความละเอียด 12 บิต โปรแกรมที่บรรจุบนบอร์ด 16 บิต จะคำนวณฟาส์ทฟเรียร์ทรานฟอร์ม 128 จุด ค่าผลรวมความเพี้ยนฮาร์มอนิกส์คำนวณได้ถึง 64 ลำดับ ได้ทดลองเก็บข้อมูลตัวอย่างการวัด THD ที่บ้านพักอาศัยและอาคารเรียนในมหาวิทยาลัย

PACS numbers: 82.80.Nj, 84.30.Jc, 91.25.ga
Keywords: Total Harmonic Distortion, THD, Power Quality

INTRODUCTION

Quality of the AC electrical supply plays an important role of economic development. One of the quality parameters is the waveshape of AC voltage waveform. Since the power grid provides nearly perfect sinusoidal voltage source output. The waveshape of low voltage distribution lines however when connected to customer's loads will be distorted by nonlinear loads. Such load, e.g. the rectifying circuit built by diode-capacitor, which is commonly used by input circuit of switching power supply, has the AC current drawn only near the peak voltage. When a number of them are connected to a given voltage feeder, it will flatten the peak of voltage waveform, resulting 3^{rd} harmonic appeared. The other loads that tie in parallel to the nonlinear load will then be supplying with such distorted voltage. To measure the waveshape distortion of fundamental frequency, Fourier analysis is used to determine the amplitude of harmonic components. The total harmonic distortion of AC voltage was defined [1] as the ratio of the sum of the RMS voltages of all harmonic components to the RMS voltage of the fundamental frequency by the equation

$$\mathrm{THD} = \sqrt{\frac{1}{(V_1)^2}\sum_{n=2}^{\infty}(V_n)^2} \times 100\% \qquad (1)$$

Where THD is total harmonic distortion in percent, V is the amplitude of RMS voltage, $n = 2, 3, 4, \ldots$ is harmonic component.

The standard limit of THD [2] for low voltage distribution lines (< 69 kV) that recommended by IEEE 512-1992 is 5%. This research developed a low-cost microcontroller based device that uses Fast Fourier Transformation for computing the amplitude of harmonic components of voltage waveform and computes THD. The device can record THD with time, printing the result and up-loading data to PC.

HARDWARE DESCRIPTION

The hardware block diagram is shown in Fig. 1. The instrument consists of two microcontroller boards. The first board was built with MCS51 as the front-end circuit and the second board is FFT machine built with Intel 16-bit microprocessor, 80C186EB. The AC voltage input is sampled and converted to digital data by the LTC1298 SPI interface 12-bit ADC. The number of sample is 128 points. The time domain data stream is sent to the 16-bit MCU board through RS485 port. The 16-bit board receives the data and transforms to frequency domain by FFT algorithm and computes THD. The THD is then sent back to the MCS51 for data logging. The spectrum data can be sent to the terminal for data graphing. The RTC circuit on MCS51 board provides real-time clock for time stamping when recording THD to RAM. The LCD display is used to show THD.

SOFTWARE DESCRIPTION

The firmware running on MCS51 was developed with c language. The program was compiled by Keil compiler. The real-time clock interrupts CPU every 5 min. The CPU reads date and time, then triggers the ADC to convert analog input. The converted data is saved to RAM first, and sent to the 16-bit board. The MCS51 wait for THD calculation by 16-bit board. When calculation is completed, the value THD will be received and saved with time stamp. The firmware on 16-bit board is mainly FFT program developed with c language and compiled by Pacific compiler. The FFT algorithm [3] is well known and available as the open source. We modify by adding function that communicates with MCS51 through RS485 port.

Table I: %THD between 256 and 128 points FFT.

Harmonic number	256 points	128 points
1	128.000	64.000
2	0.000	0.000
3	64.000	32.000
4	0.000	0.000
5	31.999	16.000
6	0.000	0.000
7	0.000 037	0.000 051
8	0.000	0.000
9	0.000 001	0.000 002
10	0.000	0.000
11	0.000 006	0.000 005
%THD	55.901 714 590	55.901 734 220

EXPERIMENTAL RESULTS AND DISCUSSION

Number of Sample Point Testing

The FFT algorithm running on 16-bit MCU board was tested by HP-VEE V5.01 software. The test is to find appropriate number of sample for FFT calculation between 256 and 128 points. The superimposed waveform by three-frequency sine waves, i.e. 50 Hz, 150 Hz and 250 Hz was produced by HP-VEE with 256 and 128 points. Fig. 2 and Fig. 5 show the pure sine wave of three frequencies. The superposition waveforms are shown in Fig. 3 and Fig. 6. Fig. 4 and Fig. 7 show harmonic spectrum. We found that the spectrum of three frequencies is shown clearly separated. Table I shows the result of THD calculation. We found THD computed by 128 and 256 points has shown no significant difference. Thus to reduce calculation time, we chose 128 sample points for FFT calculation. With the clock frequency of 16 MHz on 16-bit board, calculation time for 128 points takes approx. 28 seconds.

Test with Square Wave Signal

The square wave signal is used to input to the harmonic meter, HP-VEE and manual calculation. Fig. 8 shows the square wave signal produced by

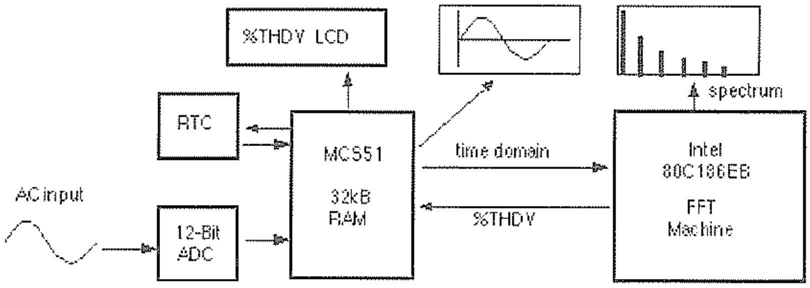

Figure 1: Hardware block diagram.

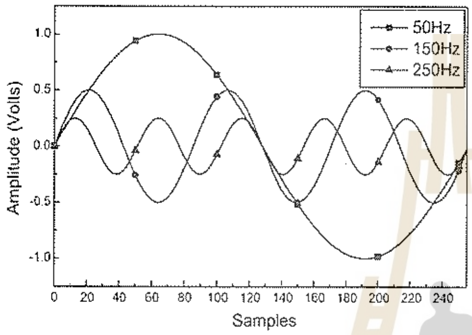

Figure 2: Three-frequency sine waves [256 points].

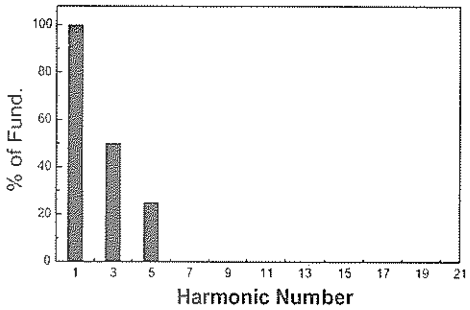

Figure 4: Harmonic spectrum of three-frequency sine waves [256 points].

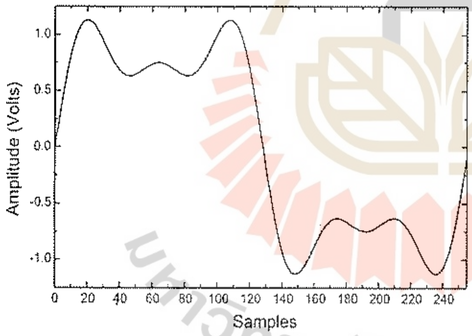

Figure 3: Superposition waveform [256 points].

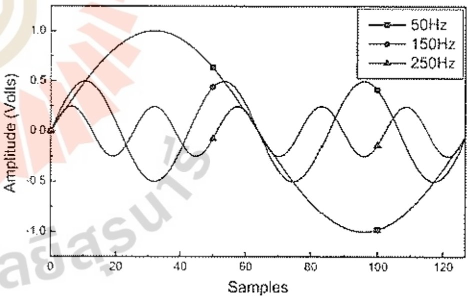

Figure 5: Three-frequency sine waves [128 points].

HP-VEE software. The harmonic spectrum plotted by harmonic meter, HP-VEE and manual-calculation are shown in Fig. 9, 10 and 11. Table II shows result of THD calculation by three methods. The value by harmonic meter and HP-VEE are shown nearly the same, 48.3%. By manual calculation is shown less than 0.8%. This test confirmed the accuracy of algorithm for FFT calculation.

Table II: %THD by three methods.

Harmonic number	Harmonic Meter	HP-VEE FFT	Manual Calculation
1	81.500	81.502	81.496
2	0.008	0.011	0.000
3	27.190	27.182	27.165
4	0.002	0.008	0.000
5	16.338	16.326	16.299
6	0.006	0.011	0.000
7	11.692	11.693	11.643
8	0.006	0.003	0.000
9	9.129	9.126	9.055
10	0.008	0.006	0.000
11	7.501	7.498	7.409
%THD	48.318 258 260	48.300 150 070	47.527 748 280

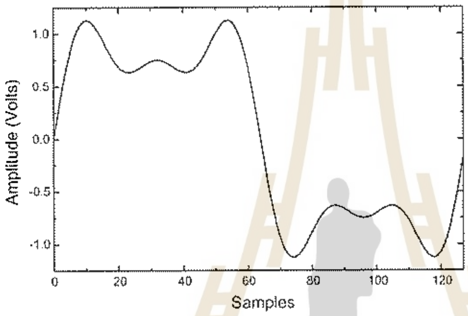

Figure 6: Superposition waveform [128 points].

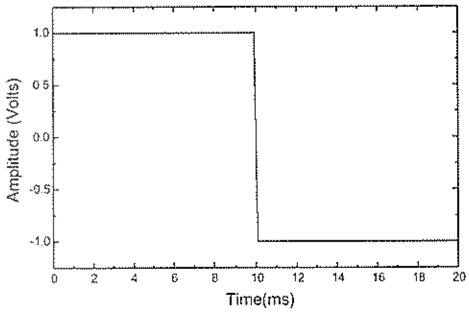

Figure 8: Square wave test signal.

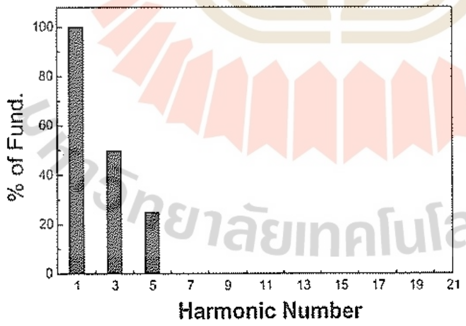

Figure 7: Harmonic spectrum of three-frequency sine wave [128 points].

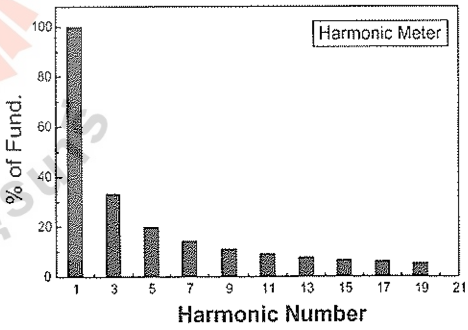

Figure 9: Harmonic spectrum by harmonic Meter, THD = 48.3%.

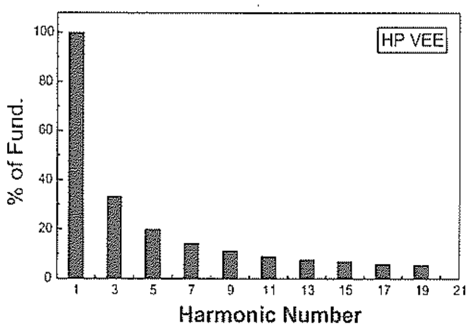

Figure 10: Harmonic spectrum by HP-VEE, THD = 48.3%.

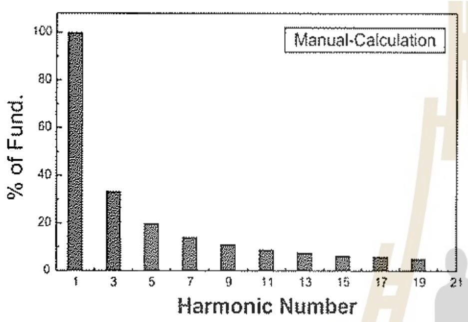

Figure 11: Harmonic spectrum by manual calculation. THD = 47.5%.

Test with Nonlinear Load

The nonlinear load shown in Fig. 12 was built with diode-capacitor rectifying circuit. The circuit is commonly used in most desktop PC switching power supply. Our harmonic meter was configured to 128 samples FFT. When the load is connected to the AC supply, the consequent flatten-top voltage waveform is shown in Fig. 13. Fig. 14 shows harmonic spectrum, we found the amplitude of 3^{rd} harmonic is 16% of the fundamental frequency. The THD is 16.4%.

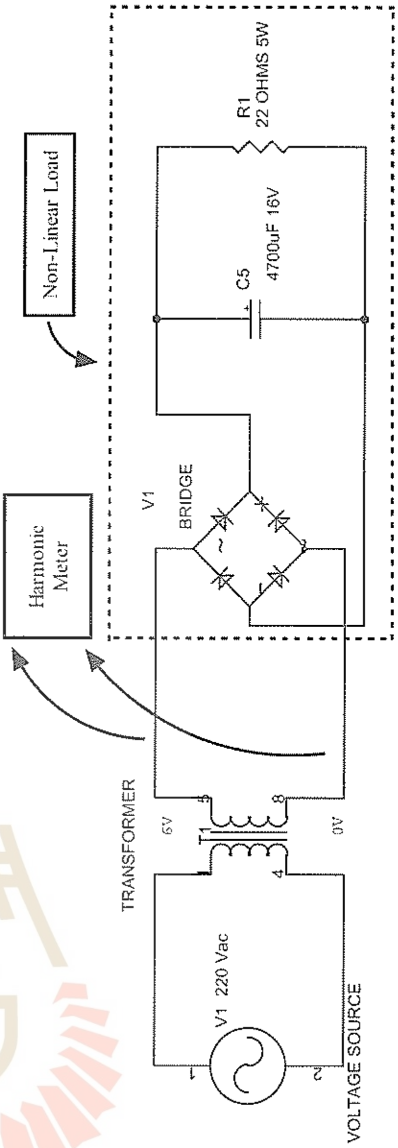

Figure 12: Nonlinear load: rectifying circuit built by diode-capacitor.

Sample of THD Measurement

We have recorded THD with time for two locations, i.e. residential and academic building. The AC supply at the point of common coupling (PCC) is used to measure. Fig. 15 shows result of data logging for 24 hours at residential. Each record was sampled every 5 minutes. We found that THD has changed with time and the value was not larger than 3%. Fig. 16 shows the result for academic building. We found THD is changed with time from approx. 1.5% to 3% then fall down to 1.5%. The peak is quite broad during daytime.

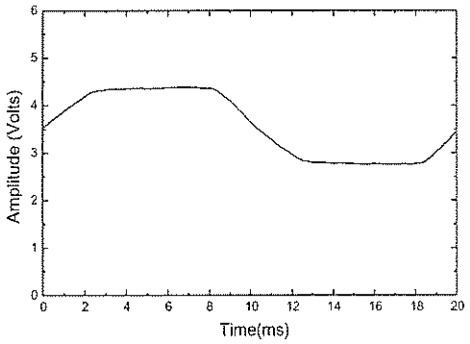

Figure 13: Flatten-top voltage waveform developed across diode-capacitor circuit.

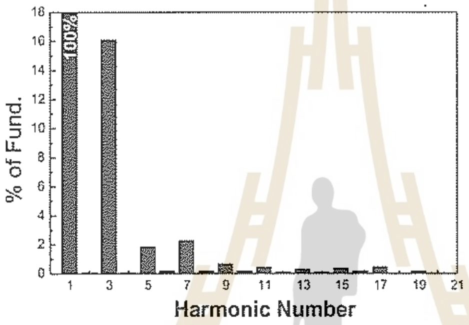

Figure 14: Harmonic spectrum of diode-capacitor load, 3rd harmonic appeared THD = 16.4%.

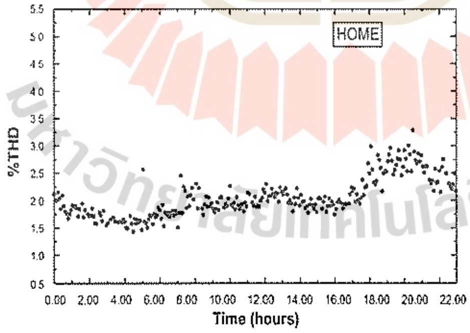

Figure 15: Sample plot of %THD with time for residential.

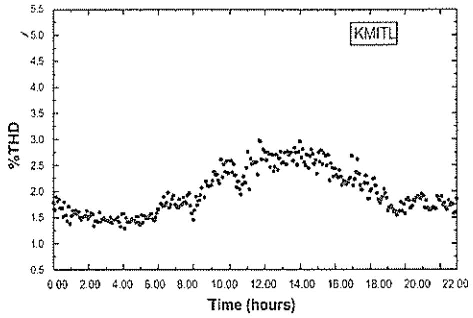

Figure 16: Sample plot of %THD with time for academic building.

CONCLUSION

We have developed a low-cost device for measuring total harmonic distortion of AC voltage. The device is tested with HP-VEE and real signal. The device can be used for measuring the 3rd harmonic appeared in electrical power system.

---

* ชื่อไทย: รุ่งโรจน์ เมาลานนท์
Email: `rungroj@nanotec.or.th`

[1] R. C. Dugan, M. F. McGranaghan, H. Wayne Beaty, *"Electrical Power Systems Quality"*, McGraw-Hill, New York (1996).

[2] IEEE 519-1992, *"IEEE Recommended Practices and Requirements for Harmonic Control in Electrical Power Systems"*, Institute of Electrical and Electronics Engineers, New York (1992).

[3] E. Oran Brigham, *"The Fast Fourier Transform and Its Applications"*, Prentice-Hall, Singapore (1988).

1st NSPG
Proceedings of the First National Symposium on Physics Graduate Research (1st NSPG)
29 June – 1 July 2006, Chulabhorn Dam, Khon San, Chaiyaphum, Thailand

Homemade Quartz Crystal Microbalance Systems for Alcohol Sensor

ระบบตาชั่งผลึกที่สร้างขึ้นสำหรับทดสอบแอลกอฮอล์

WIRIYA SUWANNET,[1,*] RAWAT JAISUTTI,[1] ONANONG CHAMLEK,[1]
TEERAKIAT KERDCHAROEN,[1] TANAKORN OSOTCHAN,[1] ORAWAN JARUBUNDIT,[2]
PANUS KUEN-ASA,[3] KHET DONPRAJAM,[4] and SIRIPAT PRATONTEP[5]

[1] *Capability Building Unit for Nanoscience and Nanotechnology, Department of Physics, Faculty of Science, Mahidol University, Bangkok, 10400, Thailand*
[2] *Department of Physics, Faculty of Science, Prince of Songkla University, Songkhla, 90112, Thailand*
[3] *Faculty of Science, Ubon Ratchathani Rajabhat University, Ubon Ratchathani, 34000, Thailand*
[4] *Faculty of Science and Technology, Rajabhat Maha Sarakham University, Maha Sarakham, 44000, Thailand*
[5] *National Nanotechnology Center, 111 Thailand Science Park, 130 Paholyothin Rd., Klong Luang, Pathumthani, 12120, Thailand*

Quartz crystal microbalance systems were developed in-house for detecting the various alcohol odors. Quartz crystal at frequency of 2.000 MHz for oscillator circuit was extracted from the metal case and copper and zinc phthalocyanine as sensing layer were coated on quartz surface by thermal vacuum evaporation. This quartz was placed into two chambers with the volume of 11.200 and 2.665 liters which have the connection to the solenoid valve and electric fan in order to remove the odor vapor after the measurement cycle. The constructed oscillator circuit was also place in the chamber and the CMOS logic signal is connected to frequency counter circuit outside. The Visual Basic and LabVIEW were employed to control the homemade and commercial 32-bit counters and both counter circuits exhibit about the same levels of noise. Several alcohol types including acetone, propane, ethanol, tetra-hydrofuran, methanol, nail washing, 100 pipers whisky and masterblend whisky were used and the odor concentration dependence was studied by varying the alcohol amount of 0.5, 1.0 and 5.0 ml.

ระบบตาชั่งเล็กด้วยผลึกที่ได้พัฒนาขึ้น สามารถใช้ทดสอบกลิ่นของแอลกอฮอล์ชนิดต่าง ๆ ได้นำผลึกควอทซ์ที่ความถี่ 2.000 MHz ออกจากกระป๋องโลหะ และเคลือบด้วยพทาโล-ซยาไนน์ที่มีโลหะประกอบเป็นทองแดงและสังกะสี มาใช้เป็นชั้นตรวจวัดบนผิวหน้าของควอทซ์ ด้วยการระเหยสารสารในสุญญากาศ นำควอทซ์ที่เคลือบสารแล้วไปบรรจุไว้ในโถแก้ว ที่มีปริมาตร 11.200 และ 2.665 ลิตร โดยเชื่อมต่อกับโซลินอยด์วาล์วและพัดลมเพื่อใช้ในการระบายกลิ่นหลังจากทำการวัด วงจรออสซิลเลเตอร์ที่สร้างขึ้นจะบรรจุอยู่ในโถแก้วนี้ และสัญญาณความถี่ CMOS จะเชื่อมต่ออยู่กับวงจรนับภายนอก 32 บิทที่สร้างขึ้นและแบบสำเร็จ ซึ่งถูกควบคุมโดยคอมพิวเตอร์โดยเขียนด้วย Visual Basic และ LabVIEW ตามลำดับ แอลกอฮอล์ที่นำมาทดสอบได้แก่ อะซิโตน, โพรเพน, เอทานอล, เตตระไฮโดรฟูแลน, เมทานอล, น้ำยาล้างเล็บ, สุรายี่ห้อ 100 pipers และ masterblend โดยได้ศึกษาเปรียบเทียบผลที่ปริมาณแอลกอฮอล์เป็น 0.5, 1.0 และ 5.0 มิลลิลิตร

Keywords: Quartz crystal microbalance, phthalocyanine, alcohol sensor.

INTRODUCTION

Quartz Crystal Microbalance (QCM) is well-known tool for the determination of film thickness during the thermal evaporation. A piezoelectric quartz crystal resonator is a precisely cut slab from a natural or synthetic crystal of quartz. The QCM consists of a piezoelectric AT-cut quartz sandwiched by a pair of electrodes. When the electrodes are connected to an oscillator, the quartz crystal starts to oscillate at its resonance frequency due to the piezoelectric effect.

When thin film was deposited on the crystal surface, the resonant frequency decreases in proportion to the mass of the film. A resonant oscillation is achieved by including the crystal into an oscillation circuit where the electric and the mechanical oscillation are near to the fundamental frequency of the crystal. The fundamental frequency depends on the thickness of the film. Some parameters are influenced the resonant frequency including the thickness, the density and the shear modulus. The resonant frequency decreases proportionally to the mass of the adsorbed layer according to the Sauerbrey's equation [5]

$$\Delta f = \frac{[2f_0^2 + \Delta m]}{[A \times (\rho_q \mu_q)]} \qquad (1)$$

where Δf is measured frequency shift, f_0 is resonant frequency of the fundamental mode, Δm is mass change per unit area, A is piezoelectrically active area, ρ_q is density of quartz, μ_q is shear modulus of quartz.

Basic application of QCM is a mass sensing device with the ability to measure very small mass changes on a quartz crystal resonator in real time. The sensitivity of the QCM is approximately 100 times higher than an electronic fine balance with a sensitivity of 0.1 µg. It means that the QCM is capable of measuring mass changes as small as a fraction of a single-layer of atoms. The high sensitivity and the real time monitoring of mass changes on the surface of QCM make it very attractive technique for a large range of applications. In this paper the construction of QCM is described to make a sensor to detect various alcohol in vapor phase.

METHODOLOGY

Two QCM systems was constructed consisting of a large chamber with the volume of 11.20 l and a small chamber with the volume of 2.665 l, the quartz crystal at frequency 2.00 MHz for using oscillator circuit was extracted. Then deposited thin film of copper or zinc phthalocyanine as a sensing layer by thermal vacuum evaporation. This quartz was connected to the oscillator circuit and placed into the chambers as shown in Fig. 1.

The first system is a large chamber with two port, the top port is connected to solenoid valve 1 and syringe to inject an alcohol and the side port is connected to the solenoid valve 2 and fan. The oscillator circuit was placed inside the chamber and connected to homemade 32-bit counter which controlled by `ET-RS8255` interface card. The `ET-RS8255` interface card is also used to three relays connected to fan and two valves. This interface card is connected to computer via `RS-232` control and collect the data by developed program written by Visual Basic. The second system is a small chamber with only one port of the top so valve, fan and syringe are connected to this port. The 32-bit counter circuit is commercial National Instrument (NI) model `PCI-6023E` which can be used to control relay for solenoid valve and fan, the LabVIEW was used to develop the software program to control and collect the data.

The based line for measure frequency was set for a half hours, the alcohol with the various concentration of 0.5, 1 and 5 ml was drop onto the filter paper for 3 hours to measure frequency change. After the setting time relay coil is switched on to open valve and turn on the fan an in order to remove alcohol vapor. Alcohol used in this experiment were acetone, propane, ethanol, tetrahydrofuran, methanol, nail remover, 100 pipers whisky and masterblend whisky.

RESULTS, DISCUSSION AND CONCLUSION

Both home- made QCM systems were able to excite phthalocyanine coated quartz to oscillate and measure the frequency shift in alcohol vapor with a desire range. Measuring cycle consists of evaluating the stable fundamental frequency for half hour and three hours after dropping alcohol then recovery period by opening the solenoid valve and fan for a half hour.

There are counter signal errors occurring in both systems as indicated in Fig. 2. This may be due to the digital signal error at some bits and at some short time. However this error can be removed eas-

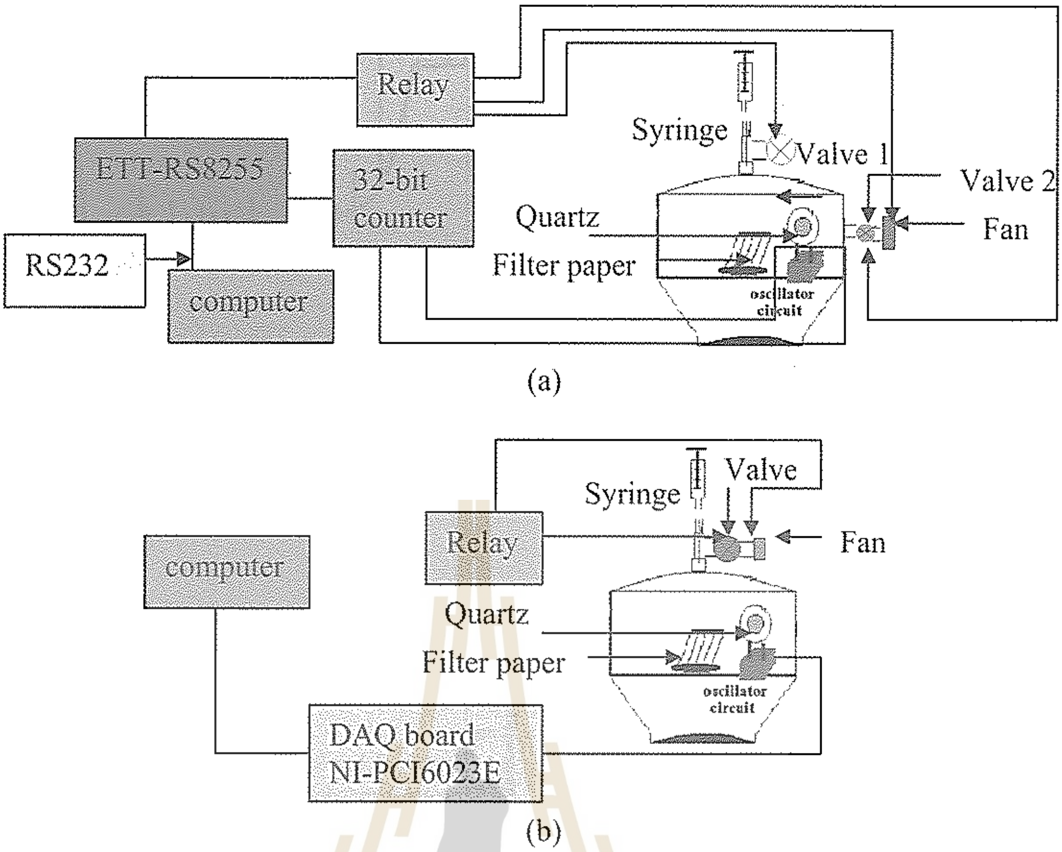

Figure 1: (color online). Schematic for constructed QCM systems. (a) the first and, (b) the second system.

ily since it is a jump process. Actually the homemade frequency counter can perform as good as the commercial NI counter card even the data bus for the NI card is directly connected to the PCI computer board.

Normally the base frequency is stable after the QCM system is on for a while and this frequency is set to be zero therefore the frequency at this region remain constant about zero in this region. The several types of alcohol were dropped and normally the frequency is dramatically decreased and slightly decreased after dropping one hour. Until reach three hours once the solenoid valve and fan turn on the frequency is suddenly increased back to the base frequency. This illustrates that the alcohol vapor is physically attach to the phthalocyanine film and detach the film when the fan remove the vapor out of the chamber.

The significant different features of response frequency shifts can be observed for various types of alcohol including masterblend whisky, hundred pipers whisky, nail remover, methanol, acetone, ethanol, propane, and tetrahydrofuran. From Fig. 3, four groups of vapor characteristic can be categorized. The frequencies of two whisky vapors are slowly decrease for the whole period while the other alcohol vapors exhibit the frequency increases at the beginning and then decrease. Vapors of methanol and nail remover have short increasing time and saturate at about two hours while the vapors of acetone and tetrahydrofuran display the saturate early at only half hour after dropping. Vapors of ethanol and propane exhibit the long deceasing time.

In order to investigate the selectivity of each metal complex in the phthalocyanine film, the

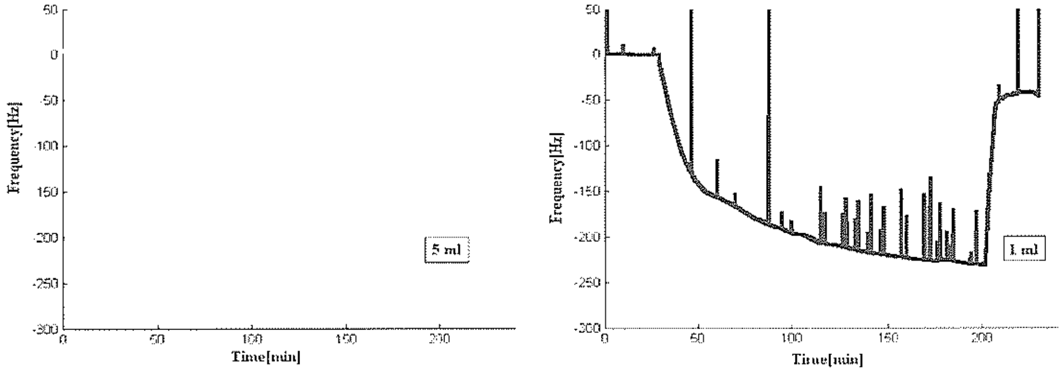

Figure 2: (color online). Frequency shift as a function of measuring time for CuPc coated quartz with masterblend whisky vapor of (left) home-made frequency counter system I at 450 ppm vapor and (right) commercial NI counter card system II at 375 ppm. The spike shape is probably originated from digital noise which occurring in both counter systems.

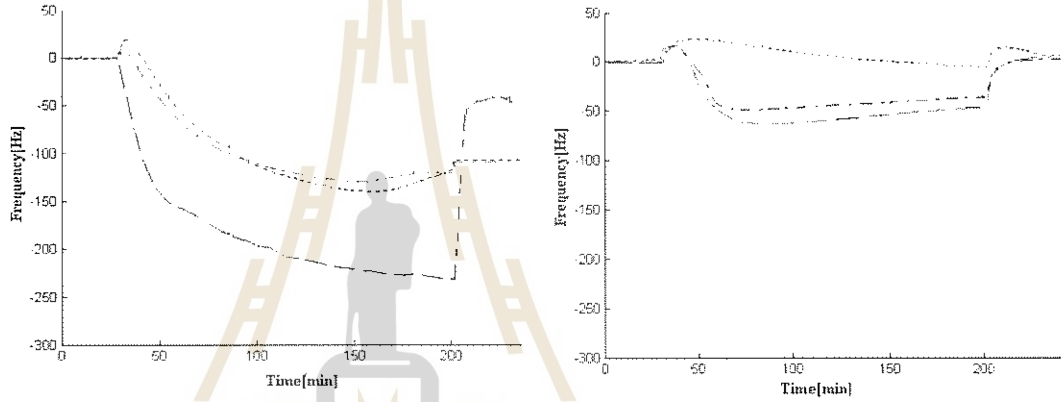

Figure 3: (color online). Frequency shift as a function of measuring time of various alcohol vapors at concentration of 375 ppm including (left) masterblend whisky, hundred pipers whisky, nail remover, methanol and (right) acetone, ethanol, propane, and tetrahydrofuran represented by dashed line, solid line, dotted line, dashed and dotted line respectively.

quartz coated with Cu phthalocyanine and Zn phthalocyanine were examined the QCM performance at the same type of alcohol. The typical example for hundred pipers whisky was demonstrated in Fig. 4. This indicates the same feature with slightly higher sensitivity for Cu phthalocyanine film.

Two home-made QCM systems were constructed for detecting the various type of alcohol with phthalocyanine coated quartz. The home-built 32 bit counter demonstrates the error level as much as that in commercial counter PC card. The frequency changes occurs in Cu phthalocyanine and Zn phthalocyanine films have the same feature for the various types of alcohol. From the feature of frequency change the four groups of alcohol vapor can be classified including I) masterblend whisky and hundred pipers whisky, II) nail remover and methanol III) acetone and tetrahydrofuran IV) ethanol and propane. This feature can be used to further to identify alcohol vapor type.

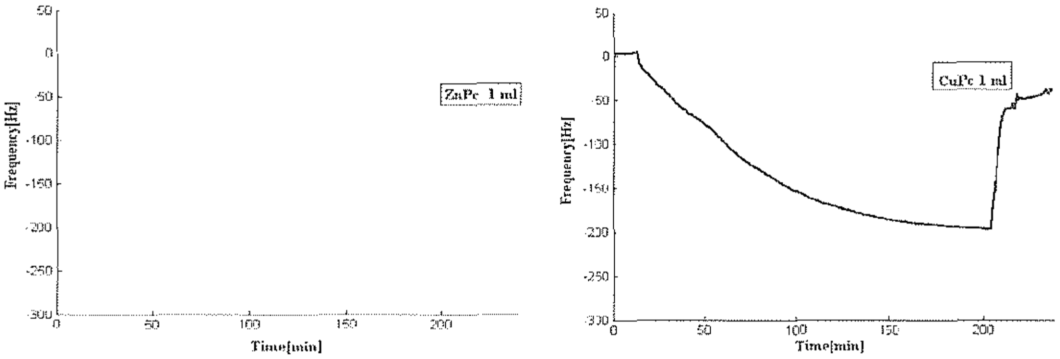

Figure 4: (color online). Frequency shift as a function of measuring time for CuPc coated quartz with hundred piper whisky vapor for quartz coated by (left) Zn phthalocyanine and (right) Cu phthalocyanine films.

---

* ชื่อไทย: วิริยา สุวรรณเนตร
Email: `suwannet_wiriya@hotmail.com`

[1] V. M. Mecea, *"Is Quartz Crystal Microbalance Really a Mass Sensor?"*, Sensors and Actuators A **128** (2), 270–277 (2006).

[2] C. A. Mills *et al.*, *"A Multiplexed Impedance Analyzer for Characterizing Polymer-Coated QCM Sensor Arrays"*, IEEE Sensors J. **6** (4), 996–1002 (2006).

[3] I. Goubaidoulline, G. Vidrich and D. Johannsmann, *"Organic Vapor Sensing with Ionic Liquids Entrapped in Alumina Nanopores on Quartz Crystal Resonators"*, Anal. Chem. **77** (2), 615–619 (2005).

[4] C. K. O'Sullivan and G. G. Guilbault, *"Commercial Quartz Crystal Microbalances—Theory and Applications"*, Biosensors and Bioelectronics **14** (8–9), 663–670 (1999).

[5] R. P. Buck *et al.*, *"Piezoelectric Chemical Sensors (IUPAC Technical Report)"*, Pure Appl. Chem. **76** (6), 1139–1160 (2004).

Fabric and Fiber Modification Using Radio Frequency Plasma Process

การดัดแปรสิ่งทอและเส้นใยโดยกระบวนการพลาสมาความถี่วิทยุ

THIDARAT SUPASAI,* SATREERAT KAMPANGKEAW HODAK, and BOONCHOAT PAOSAWATYANYONG
Department of Physics, Faculty of Science, Chulalongkorn University,
Bangkok, 10330, Thailand

We have studied the hydrophobicity improvement of fabrics using radio-frequency (RF) inductively coupled SF_6 plasma. The plasma was generated in the pressure of 0.005–1 torr and with the RF power of 25–75 watts. A set of fabrics including polyethylene terephthalate (PET), mixed Thai silk, Thai silk and cotton are treated under different operating conditions. Treated fabrics were characterized by scanning electron microscopy, water contact angle and absorption time measurement as a function of storage time after treatment. The atomic species in SF_6 plasma were measured by optical emission spectroscopy (OES). The results show spectrum line of F I in SF_6 plasma which is believed to increase the hydrophobicity of fabrics. Compared with untreated fabrics, treated fabrics improve the absorption time from 0–30 mins to about 200 mins depending on the types of fabrics, and the contact angles significantly increase about two times. The suitable operating conditions were at pressure of 0.5 torr and RF power of 50 watts.

ผู้วิจัยได้ศึกษาเกี่ยวกับการปรับปรุงสมบัติการไม่ซึมน้ำของผ้าโดยใช้ พลาสมาของแก๊สซัลเฟอร์เฮกซะฟลูออไรด์ พลาสมาถูกสร้างขึ้นโดยใช้หลักการเหนี่ยวนำกำลังไฟฟ้าด้วยคลื่นความถี่วิทยุ ที่ช่วงความดัน 0.005–1 ทอรร์ และ ช่วงกำลังคลื่นความถี่วิทยุ 25–75 วัตต์ ผ้าที่ใช้ศึกษาซึ่งประกอบด้วย โพลีเอทธีลีนเทเรฟธอลเลต ผ้าไหมผสม ผ้าไหมแท้ และผ้าฝ้าย จะถูกปรับปรุงสมบัติการไม่ซึมน้ำภายใต้เงื่อนไขการเกิดพลาสมาที่แตกต่างกัน ผ้าที่ผ่านการปรับปรุงสมบัติแล้วจะถูกวิเคราะห์เชิงกายภาพ โดยใช้การถ่ายภาพด้วยกล้องจุลทรรศน์อิเล็กตรอนแบบส่องกวาด การวัดค่ามุมสัมผัสของน้ำ การจับเวลาที่ผ้าใช้ในการดูดซับน้ำ ตลอดจนความสามารถในการดูดซับน้ำเมื่อเวลาผ่านไป นอกจากนี้แล้ว ได้ใช้เทคนิคออพติคอลอิมิสชันสเปกโทรสโกปี เพื่อวิเคราะห์ชนิดของอะตอมในพลาสมา ผลการทดลองพบว่า พลาสมาของแก๊สซัลเฟอร์เฮกซะฟลูออไรด์มีประสิทธิภาพในการปรับปรุงสมบัติการไม่ซึมน้ำของผ้าทุกชนิด ผ้าที่ผ่านการปรับปรุงแล้วจะใช้เวลาใน การดูดซับน้ำเพิ่มขึ้นจาก 0–30 นาที เป็น 200 นาทีขึ้นอยู่กับชนิดของผ้า และค่ามุมสัมผัสของน้ำมีค่าเพิ่มขึ้นประมาณสองเท่าด้วยเช่นกัน ส่วนผลการวัดออพติคอลอิมิสชันสเปกโทรสโกปี พบว่ามีส่วนประกอบของฟลูออรีนในพลาสมา ซึ่งเชื่อว่าเป็นตัวการสำคัญ ในการช่วยเพิ่มสมบัติการไม่ซึมน้ำของผ้า เงื่อนไขพลาสมาที่เหมาะสมในงานวิจัยนี้อยู่ที่ความดัน 0.5 ทอรร์ และกำลังคลื่นวิทยุ 50 วัตต์

Keywords: Hydrophobicity, SF_6 plasma, RF plasma

INTRODUCTION

At present, the finishing of textiles by plasma processes have advantageously replaced many wet chemical applications. This is due to the minimal contamination and the high acquiring speed of the plasma processes. Moreover, most plasma process only produces minimal gases exhaust, hence, more environmentally friendly. There are several possible activations during the plasma treatment i.e. surface deposition, polymerization, grafting, and etching. These activations can modify surface properties of the material while leave the bulk characteristic unaffected. The improvement in hydrophobic property can be imparted to the fabrics through low temperature plasma treatment employing fluorine-base gas. In this work, SF_6 is used as plasma gas media and source of fluorine atoms producing fluorination on the sample surface. The main aim of this study is to optimize plasma conditions for textile treatments and to improve the hydrophobicity of the fabrics.

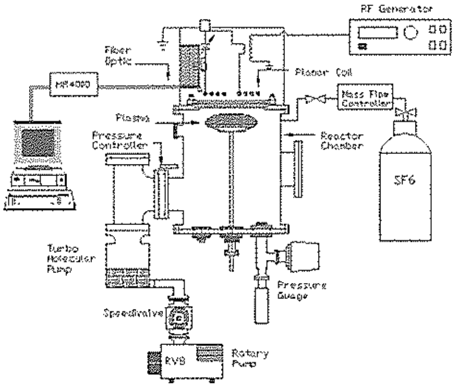

Figure 1: Schematic diagram of the RF-ICP system.

EXPERIMENTAL SETUP

Plasma reactor

The schematic diagram of radio-frequency inductively coupled plasma (RF-ICP) is shown in Fig. 1. The system consists of three main parts; a) vacuum chamber made from stainless steel in a cylindrical form, b) power coupling module consists of an RF generator, an impedance matching network and a planar coil, and c) plasma diagnostic system (OES). Base pressure of the chamber, 2×10^{-5} torr, can be achieved utilizing a turbo molecular pump backed by a rotary pump. After the base pressure is reached, the SF_6 enters the chamber via mass flow controller, and the pressure during the process is monitored by a Pinari gauge. The operating conditions are set at the pressure of 0.005, 0.05, 0.5 and 1 torr with RF power of 25, 50 and 75 watts. The treatment times is fixed at 1 minutes. It is observed that at RF power higher than 75 watts, the plasma is unstable while at pressure higher than 1 torr, the fabrics are usually damaged. The sample fabric is fixed at center of discharge, 4 cm. below the quartz plate.

Characterization of the treated samples

The simple method to measure the wettability of which opposed to the ability to repel water, is the measurement of water contact angle, a tangent angle (pointing into the body of liquid) measured between surface of sample and the liquid droplet at the contact point. In this work, the water droplets contact angles are measured by Tantac CAM-PLUS contact angle meter. Furthermore, the contact angle also relate to the wok of adhesion W_a, defined as work required to separate unit area of interface between liquid and solid. Higher contact angle represents lower work of adhesion, in other words, more ability to repel water. Due to large deviation in contact angle measurement, resulting from the roughness and irregularity of surfaces, another method to measure the hydrophobicity known as the absorption time measurement is implemented to correlate with the plasma parameters. The water droplets (40 μl in volume) are dripped on the sample surface using a micropipet at three random positions of each sample fabrics. The data of the absorption time are obtained by averaging the time used of these three droplets. The absorption time is restricted to a maximum of 210 minutes. After this, the water volume lost is considered mostly due to evaporation.

RESULT AND DISCUSSION

The contact angle results in Table I show a dramatic increase of hydrophobicity in all PET, cotton and mixed Thai silk samples. Prior to the treatment by plasma process, the water droplet on these fabrics is rapidly absorbed into the fabric surface, while after treatment, the water droplet can be observed on the surface with contact an-

Table I: Contact angle of water on PET, mixed Thai silk, Thai silk and cotton fabrics before and after SF_6 plasma treatment.

Type of fabrics	Contact angle (degree)	
	Before treatment	After treatment
PET	–	139 ± 1
Mixed Thai silk	–	142 ± 3
Thai silk	101 ± 5	144 ± 3
Cotton	–	140 ± 1

Fabric absorbed water rapidly.

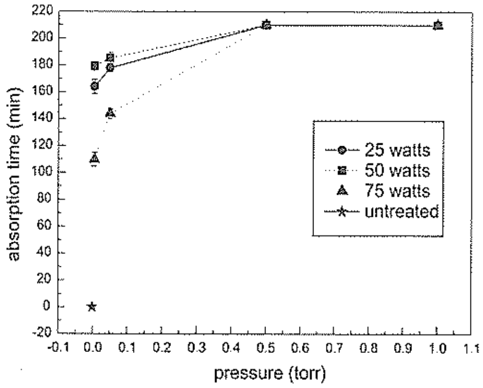

Figure 2: Water droplet absorption time on cotton which were treated for 1 min at different pressures and RF powers. Untreated cotton absorbed water rapidly.

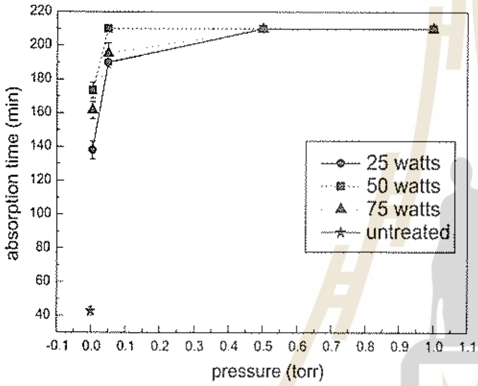

Figure 3: Water droplet absorption time on Thai silk which were treated for 1 min at different pressures and RF powers.

gles between 135°–145°. In case of Thai silk, a contact angle after treatment increase from 101° to 144°. Our study show that these improvement in hydrophobicity does not depend on operating condition or the types of fabrics. As a result, any clear trend of the hydrophobicity as a function of the plasma conditions is not obtained.

All treated fabrics demonstrate increasing of hydrophobicity. Fig. 2 and 3 show the results of absorption time measurement as a function of pressure at different RF power of cotton and Thai silk respectively. The measurement was performed instantly after 1 minute treatment of SF_6 plasma.

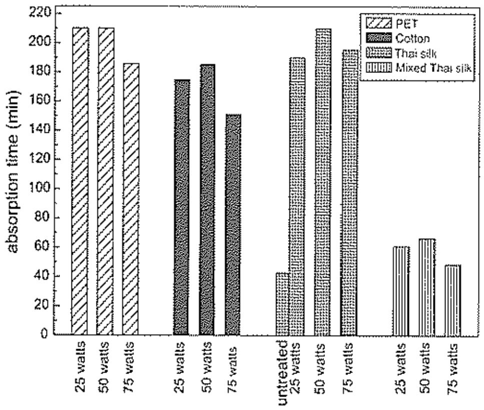

Figure 4: (color online). Absorption time of PET, cotton, Thai silk and mixed Thai silk as function of RF power. Plasma pressure and treatment time are 0.05 torr and 1 min, respectively.

In both fabrics, best improvement in absorption time was obtained at the RF power of 50 watts. At a fixed RF power and treatment time, the data shows that treatment at pressure higher 0.5 torr will maximize the absorption time for cotton. Similar result was also found for Thai silk, but rapid improvement would be obtained at the operating pressure higher than 0.05 torr. As can be seen from Fig. 2 and 3, the suitable condition is at the pressure of 0.5 torr and RF power of 50 watts.

Fig. 4 shows a comparison of absorption time on PET, cotton, Thai silk, mixed Thai silk as a function of RF power at pressure of 0.05 torr and treatment time of 1 min. Again, due to the rapid absorption of water droplet on untreated PET, cotton and mixed Thai silk, the absorption time on these samples could not be measured. The result of untreated Thai silk absorption time is about 40 min. The best hydrophobic property improvement is obtained in PET samples.

We have measured the storage time effect on hydrophobic property of all fabrics, as shown in Fig. 5. The results indicate that hydrophobicity stability after the exposure of SF_6 plasma depend on the type of fabrics. The best hydrophobicity stability was obtained in PET samples in which the maximum limit of absorption time (210 min) still obtained after 14 days. On the contrary, in

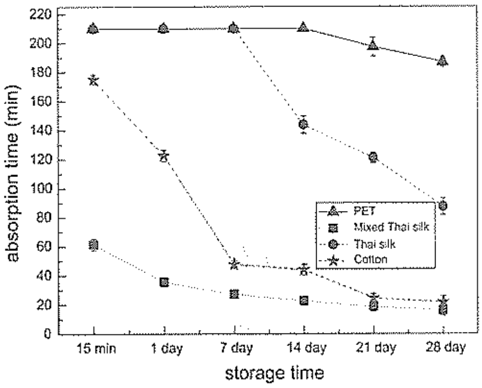

Figure 5: (color online). Absorption time of PET, cotton, Thai silk and mixed Thai silk, treated for 1 min at pressure of 0.05 torr and RF power of 25 watts, measured at different times after treatment.

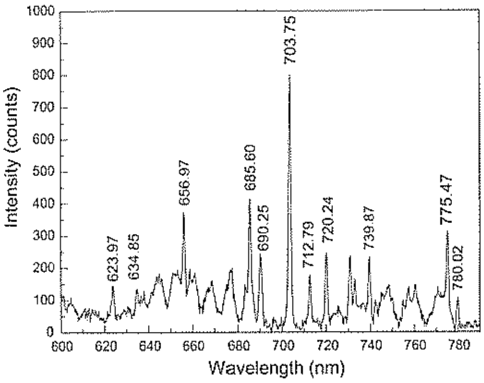

Figure 6: OES spectrum of SF_6 plasma at pressure of 0.05 torr and RF power of 25 watts was identified by using NIST atomic wavelength table. The F I (excited fluorine) peaks are presented range 600–800 nm.

case of cotton, the hydrophobicity gradually decrease to a minimum at 21 days.

The OES spectrum of SF_6 plasma as illustrated in Fig. 6 presents spectra lines of F I (excited fluorine) which is believed to be the source of hydrogen abstracting and attached with carbon composite in the fiber lead to C–F bonds which increase the hydrophobicity of the fabrics. The work of C. W. Kan *et al.* [9] shows that the hydrophobic properties are not observed when the fabric is treated by nitrogen or oxygen plasma. Fig. 7 shows SEM image of Thai silk sample. It can be seen that the surface of treated samples (b) is roughen by SF_6 plasma compared with untreated sample (a). Primarily, we expect that the change of sample surface is resulted from both etching and deposition of C–F residue.

CONCLUSION

The improvement in hydrophobicity of PET, mixed Thai silk, Thai silk and cotton were observed with the utilization of SF_6 plasma treatments. The suitable operating condition in our RF-ICP system is obtained at pressure of 0.5 torr and RF power of 50 watts.

---

* ชื่อไทย: ธิดารัตน์ สุภาสัย
Email: `pumthidarat@hotmail.com`

[1] E. Selli *et al.*, *"Characterisation of Poly(ethylene Terephthalate) and Cotton Fibres After Cold* SF_6 *Plasma Treatment"*, J. Mater. Chem. **11** (8), 1985–1991 (2001).

[2] B. Paosawatyanyong, J. Sci. Res. Chula. Univ. **29**, 198–211 (2004).

[3] E. Selli *et al.*, *"Surface Modifications of Silk by Cold* SF_6 *Plasma Treatment"*, Macromol. Chem. Phys. **202** (9), 1672–1678 (2001).

[4] P. Chaivan *et al.*, *"Low-Temperature Plasma Treatment for Hydrophobicity Improvement of Silk"*, Surf. Coat. Technol. **193** (1–3), 356–360 (2005).

[5] E. C. Rangel *et al.*, *"Enhancement of Polymer Hydrophobicity by* SF_6 *Plasma Treatment and Argon Plasma Immersion Ion Implantation"*, Surf. Interface Anal. **35** (2), 179–183 (2003).

[6] C. Riccardi *et al.*, *"A* SF_6 *RF Plasma Reactor for Research on Textile Treatment"*, Plasma Sources Sci. Technol. **10** (1), 92–98 (2001).

[7] J. R. Roth, *Industrial Plasma Engineering: Volume 2—Applications to Nonthermal Plasma Processing*, Institute of Physics Publishing, Bristol and Philadelphia (2001).

[8] National Institute of Standard and Technology, *"NIST Atomic Spectra Database"*. [Online]. Available: `http://physics.nist.gov/PhysRefData/ASD/`.

[9] C. W. Kan *et al.*, *"Surface Properties of Low-*

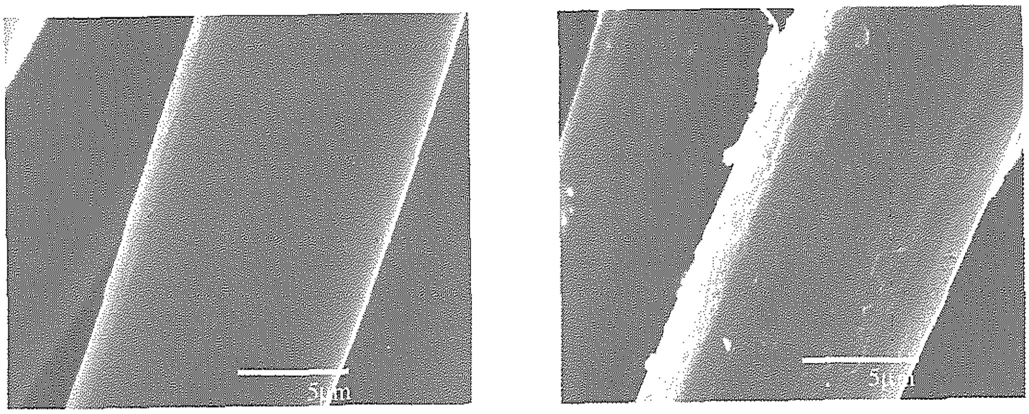

(a) (b)

Figure 7: SEM photograph of Thai silk at 5000×; (a) untreated, and (b) treated sample after exposure to SF_6 plasma for 1 min at pressure of 0.05 torr and RF power of 25 watts.

Temperature Plasma Treated Wool Fabrics", J. Mater. Proc. Tech. **83** (1–3), 180–184 (1998).

Growth and Characterization of NiFeN Thin Film by Reactive Gas Timing RF Magnetron Sputtering

การปลูกฟิล์มบางนิเกิลเหล็กไนไตรด์ โดยอาร์เอฟแมกนีตรอนสปัตเตอริง แบบควบคุมเวลาก๊าซไวปฏิกิริยาและคุณลักษณะของฟิล์ม

CHEWA THASSANA,[1,*] WICHARN TECHITDHEERA,[1] PITIPORN THANOMNGAM,[1] and JITI NUKEAW[2]

[1] *Computational Physics Research Laboratory,*
Department of Applied Physics, Faculty of Science,
King Mongkut's Institute of Technology Ladkrabang, Bangkok, 10520, Thailand
[2] *Quantum and Optical Semiconductor Research Laboratory,*
Department of Applied Physics, Faculty of Science,
King Mongkut's Institute of Technology Ladkrabang, Bangkok, 10520, Thailand

Growth of NiFeN thin films on glass substrate at room temperature by reactive gas timing rf magnetron sputtering, with condition on rf power, time period and flow rate of argon and nitrogen gas, respectively. The crystal structure of thin films was investigated by XRD show fcc structure of Ni_3FeN (200) plane. The lattice constants of thin films increased with increasing of flow rate and time period of nitrogen gas. The surface morphologies of thin films was investigated by AFM show grain size range of 30–150 nm.

การปลูกฟิล์มบางนิเกิลเหล็กไนไตรด์บนฐานรองรับกระจกที่อุณหภูมิห้องด้วยระบบอาร์เอฟแมกนีตรอนสปัตเตอริง แบบควบคุมเวลาก๊าซไวปฏิกิริยา ด้วยเงื่อนไขเปลี่ยนแปลงคาบเวลาก๊าซอาร์กอนและก๊าซไนโตรเจน, เปลี่ยนแปลงอัตราการไหลของก๊าซไนโตรเจน และเปลี่ยนแปลงค่ากำลังคลื่นอาร์เอฟ ตามลำดับ จากการศึกษาโครงสร้างด้วยการเลี้ยวของรังสีเอ็กซ์ แสดงให้เห็นว่า ผลึกเรียงตัวแบบ fcc ในระนาบ (200) และค่าคงที่แลตทิซเพิ่มขึ้นตามการเพิ่มของอัตราการไหล และคาบเวลาของก๊าซไนโตรเจน และจากกล้องจุลทรรศน์แรงอะตอมพบว่า ขนาดของเม็ดผลึกมีค่าประมาณ 30 ถึง 150 นาโนเมตร

PACS numbers: 81.15.-a, 68.55-a, 68.55.-a
Keywords: NiFeN thin film, RF magnetron sputtering, XRD and AFM

INTRODUCTION

There are many methods in growth of NiFeN thin films such as rf magnetron sputtering [1, 2, 5], rf diode sputtering [6], d.c. magnetron sputtering [3], dual ion beam sputtering [5] and dc and rf toroidal discharge [8], etc. The most researches emphasize on a growth of NiFeN thin films on glass substrate and silicon base using $Ar + N_2$ gas mixture rf magnetron sputtering [2, 4, 5, 8]. When nitrogen partial pressure increased, the diffraction peak is slightly shifted a lower side. The lattice constant is also decreased [2] and increased proportional to the rf power [1].

This work is a growth of NiFeN thin film using reactive gas timing rf magnetron sputtering on glass substrate at room temperature. The thin film structures and surfaces were analyzed using XRD and AFM, respectively.

EXPERIMENTAL METHOD

NiFeN thin films were prepared by reactive gas timing rf magnetron sputtering on glass substrate at room temperature. Base pressure of the order of 2×10^{-6} mbar was obtained. The pressure when releasing Ar and N_2 gas into chamber is about $(3.2\text{–}4.0) \times 10^{-6}$ mbar and $(1.5\text{–}2.5) \times 10^{-2}$ mbar, respectively depends upon the growth conditions. The distance between target to substrate is 5 cm and rf power is 300 watt. The thin film structures and surfaces were then analyzed using XRD and AFM respectively. The first condition is no gas timing control. The second condition is chang-

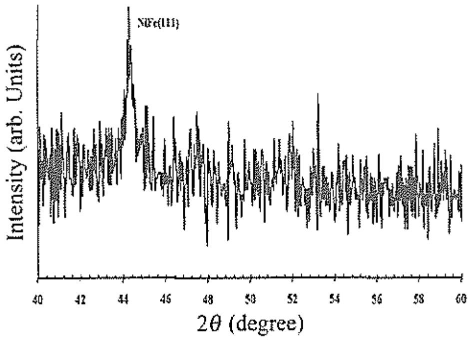

Figure 1: (color online). XRD peak of NiFe films prepared with no gas timing.

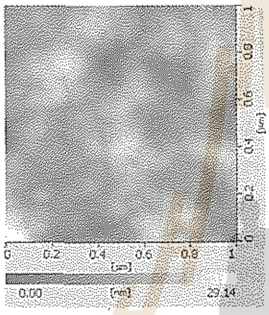

Figure 2: (color online). AFM image of NiFe film prepared with no gas timing.

ing a time period of Ar and N_2 gas to 25:2, 30:2 and 40:2 seconds. The third condition is changing the flow rate of Ar and N_2 to 11:4.5, 11:5.0 and 11:5.5 sccm. The last condition is changing the rf power to 200, 300 and 400 watt.

RESULTS AND DISCUSSION

Structure and surface of thin film with no gas timing control.

Fig. 1 show XRD pattern of NiFe in (111) plane [1, 6, 7]. The lattice constant calculated from the (111) peak, is about 3.5602 *angstrom*. Fig. 2 show AFM image of NiFe film, the grain size is about 70–120 nm

Table I: Effect of the condition varied a time period of Ar and N_2 gas (rf power is 300 W, flow rate of Ar:N_2 gas is 12:5.5 sccm).

Time period of Ar and N_2 gas (second)	2θ (°)	Lattice const (Å)	Grain size (nm)
20:2	48.32	3.7626	40–60
30:1	49	3.7136	30–40
30:2	48.80	3.7279	50–60
40:2	49.20	3.6994	30–40

Table II: Effect of the condition varied flow rate of N_2 gas (rf power is 300 W, time period of Ar and N_2 gas is 30:2 second).

Flow rate of Ar and N_2 gas (sccm)	2θ (°)	Lattice const (Å)	Grain size (nm)
11:4.5	49.24	3.6966	50–60
11:5.0	49.12	3.7051	80–150
11:5.5	49	3.7136	40–50

Structure and surface of thin film with Ar and N_2 gas timing control.

The effect of changing a time period of Ar and N_2 gas are shown in Table I. When a time period of Ar and N_2 gas changed, the lattice constant and gain size of thin films changed since the N_2 content of film changed [2, 4, 5, 8]. The XRD pattern of the films are given in Fig. 3. All the films had fcc (200) plane. The lattice constant calculated from the (200) peak, are also shown in Table I. In Fig. 3, it can be seen that the intensity of fcc (200) peak decreased and the diffraction peak position is slightly shifted a lower side, the lattice constant is increased with the time period of N_2 gas is increased [2]. When a time period of Ar increased, the diffraction peak position is slightly shifted a higher side so the lattice constant is decreased. That peak was broader, which means the grain size was smaller, which correspond with Fig. 4. It shows the AFM image of NiFeN films, the grain size is about 30–60 nm.

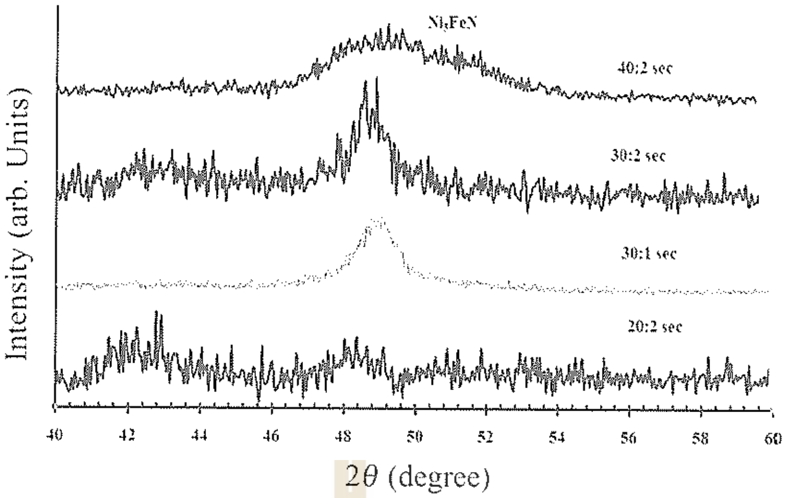

Figure 3: (color online). XRD pattern of NiFeN films prepared with different time period of Ar and N_2 gas.

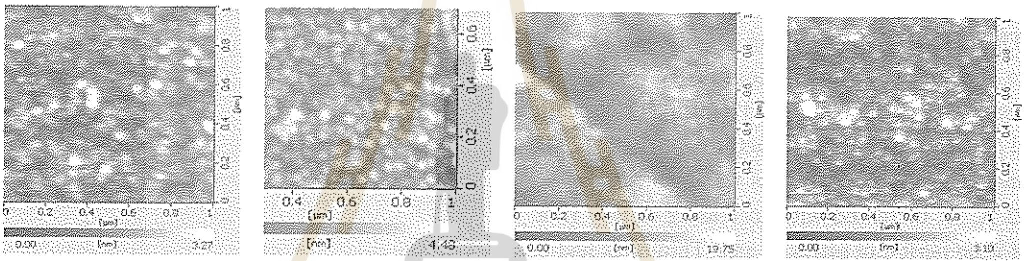

(a) (b) (c) (d)

Figure 4: (color online). AFM image of NiFeN films prepared with different time period of Ar and N_2 gas. (a) 20:2, (b) 30:1, (c) 30:2 and (d) 40:2 second.

Table III: Effect of the condition varied rf power (flow rate of Ar and N_2 is 12:5.5 sccm, time period of Ar and N_2 gas is 30:2 second).

RF Power (watt)	2θ (°)	Lattice const (Å)	Grain size (nm)
200	48.92	3.7193	70–100
300	49.08	3.7079	50–60
400	48.6	3.7423	40–50

Structure and surface of thin film with Ar:N_2 gas flow rate control.

The effect of changing the flow rate of Ar and N_2 gas are shown in Table II. When flow rate of N_2 gas is increased, the lattice is also increased since the probability of occupation of nitrogen atom at the interstitial site between Ni and Fe atom increased cause a distortion and expansion of the unit cell [2]. The XRD pattern of the films are given in Fig. 5. The lattice constant of films calculated from the (200) peak, are also in Table II. The diffraction peak position is slightly shifted a lower side, the lattice constant is increased. Fig. 6 shows the AFM image of of NiFeN films, the grain size is about 40–150 nm.

Structure and surface of thin film with rf power control.

The effects of the changing the rf power are shown in Table III. Fig. 7 XRD pattern, when rf power increased from 200 to 300 watt, the lattice constant decreased since Ni increased [4]. But power increased from 300 to 400 W, the lattice constant increased since Ni decreased [1], and N_2 occupy interstitial sites increased [4]. Fig. 8 shows the AFM image of of NiFeN films, the grain size is about 40–100 nm.

CONCLUSIONS

The influence of sputtering conditions on structure and surface morphologies of NiFeN films was investigated. NiFe film had fcc in (111) plane and NiFeN films had fcc structure of Ni_2FeN (200) plane. The lattice constants was about 3.7136 ± 0.02 Å. It increased with increasing of flow rate and time period of nitrogen gas. Thin films had a grain size was about 30 to 150 nm.

---

* ชื่อไทย: ชีวะ ทัศนา
Email: `sci_cen@yahoo.com`

[1] X. H. Li and Z. Yang, *"Effects of Sputtering Conditions on the Structure and Magnetic Properties of* Ni–Fe *Films"*, Mater. Sci. Eng. B **106** (1), 41–45 (2004).

[2] R. Gupta and M. Gupta, *"Nanocrystallization and Amorphization Induced by Reactive Nitrogen Sputtering in Iron and Permalloy"*, Phys. Rev. B **72** (2), 024202 (2005).

[3] J. G. Kim *et al.*, *"Magnetic Properties of Sputtered Soft Magnetic* Fe–Ni *Films with an Uniaxial Anisotropy"*, Thin Solid Films **440** (1–2), 54–59 (2003).

[4] H. Y. Wang *et al.*, *"The Structure and Magnetic Properties of* FeNiN *Films"*, J. Appl. Phys. **91** (3), 1453–1457 (2002).

[5] M. Chiba, K. Morio and Y. Koizumi, *"Magnetic Properties and Microstructure of* Ni–Fe *Nitride Films by Reactive Sputtering"*, J. Magn. Magn. Mater. **242–245** (2), 949–951 (2002).

[6] H. Gong *et al.*, *"Highly Oriented* NiFe *Soft Magnetic Films on* Si *Substrates"*, J. Appl. Phys. **85** (8), 5750–5752 (1999).

[7] X. Bi *et al.*, *"Change of Coercivity of Magnetic Thin Films with Non-Magnetic Layers and Applications to Spin Valve"*, J. Magn. Magn. Mater. **268** (3), 321–325 (2004).

[8] R. Valencia *et al.*, *"Nitriding of AISI 304 Stainless Steel by PIII in DC and RF Toroidal Discharges"*, Braz. J. Phys. **34** (4B), 1594–1597 (2004).

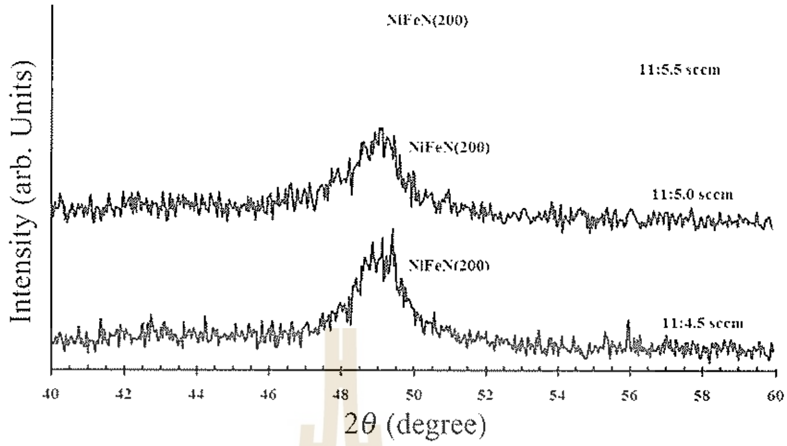

Figure 5: (color online). XRD pattern of NiFeN films prepared with different Ar:N_2 gas flow rate.

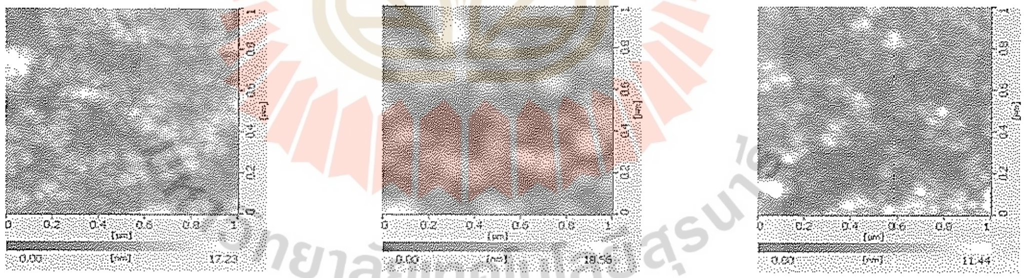

(a) (b) (c)

Figure 6: (color online). AFM image of NiFeN films prepared with different Ar:N_2 gas flow rate (a) 11:4.5, (b) 11:5.0 and (c) 11:5.5 sccm.

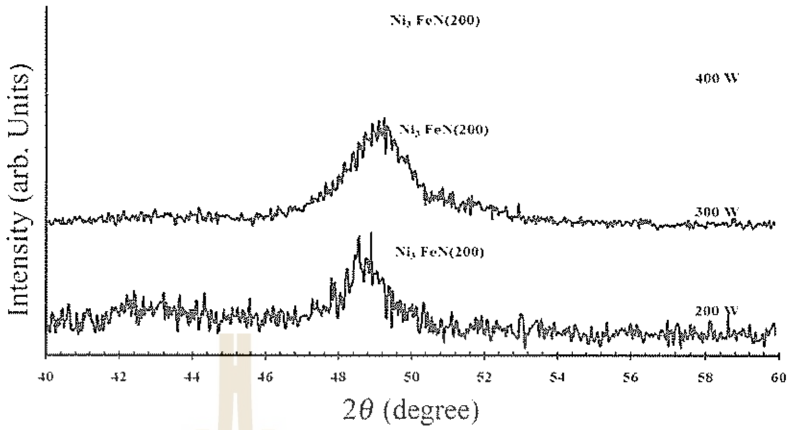

Figure 7: (color online). XRD pattern of NiFeN films prepared with different rf power.

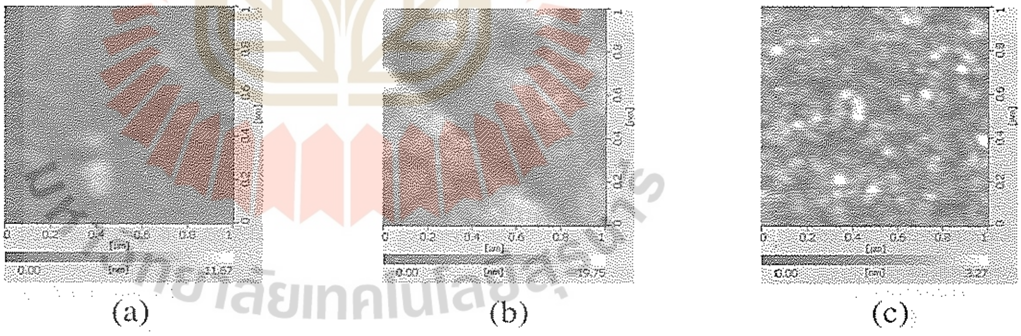

(a) (b) (c)

Figure 8: (color online). AFM image of NiFeN films prepared with different rf power. (a) 200, (b) 300 and (c) 400 W.

The Expansion of the Nd:YAG Slab and The Thermal Lens Effect in 3 W Single Side Pump Nd:YAG Laser

การขยายตัวของผลึกนีโอดีเมียมแย็กชนิดสแลบและการเกิดเทอร์มัลเลนส์ ในระบบเลเซอร์แบบซิงเกิลไซด์ปั๊มที่มีกำลัง 3 วัตต์

JINTAWAT TANAMATAYARAT,* KWAN ARAYATHANITKUL, and RATCHAPAK CHITAREE
Department of Physics, Faculty of Science, Mahidol University,
Bangkok, 10400, Thailand

In the diode side pumped Nd:YAG laser, the laser diode array is used as a pump source. The diode array does not produce only energy for lasing process but it also produces heat to the laser medium. This heat is the main factor that causes the expansion of laser medium, which results in the phenomenon called thermal lens effects. In this research the thermal lens effects are studied in the continuous pumping condition. During the pumping process the Nd:YAG slab behaves like a convex lens. The experiments is divided into two parts: 1) The measurement of the focal length of the thermal lens and 2) The study of the expansion of the Nd:YAG crystal.

ในระบบนีโอดิเมียมแย็กเลเซอร์ที่ใช้เลเซอร์ไดโอดเป็นแหล่งกระตุ้นนั้น เลเซอร์ไดโอดไม่ได้ปล่อยพลังงานให้กับตัวกลางเลเซอร์ เฉพาะความยาวคลื่นที่ใช้ในการเปลี่ยนระดับพลังงานที่ทำให้เกิดเลเซอร์เท่านั้น แต่ยังปล่อยพลังงานให้กับตัวกลางเลเซอร์ในรูปของความร้อนอีกด้วย ความร้อนนี้ทำให้เกิดการขยายตัวของผลึกเลเซอร์ และยังทำให้เกิดปรากฏการณ์ที่เรียกว่าเทอร์มัลเลนส์ ในการศึกษาทดลองครั้งนี้เราสนใจเฉพาะเทอร์มัลเลนส์ในกรณีที่ตัวกลางเลเซอร์ถูกกระตุ้นแบบต่อเนื่อง สำหรับ เทอร์มัลเลนส์ในตัวกลางเลเซอร์นีโอดิเมียมแย็กชนิดสแลบ จะมีลักษณะคล้ายเลนส์นูน โดยในที่นี้จะแบ่งการทดลองเป็นสองขั้นตอนใหญ่ ๆ คือ การทดลองเพื่อวัดความยาวโฟกัสของเทอร์มัลเลนส์และการทดลองเพื่อดูการขยายตัวของผลึกเลเซอร์

PACS numbers: 42.60.Pk, 42.55.Rz, 42.55.Xi
Keywords: Thermal Lens, Nd:YAG Laser

INTRODUCTION

The study of the thermal lens effects began in 1964 when Gordon *et al.* observed the changing of the transient power and beam divergence of the output of a helium-neon laser after placing transparent samples in the laser cavity [1]. In 1984, Eggleston *et al.* [2] presented the mathematical model of the thermal effects in both rod and slab laser medium. For the slab model the cooler plates are placed at the top and the bottom of the slab. Energy is pumped at the top face of the slab. The temperature gradient is only in the vertical axis of the slab. The stress can be calculated from the temperature gradient. The index of refraction is in the same form as lens-like medium. Finally the focal length of thermal lens can be calculated by ray optics. In 2003, Ermolaev *et al.* [3] published the paper that discussed how the focal power of the thermal lens, that appears in the active element of a Nd:YAG laser with transverse pumping by thirty linear laser-diode arrays having a total optical power of up to 600 W, depends on the pump power and the temperature of the laser diodes. The optimum working temperature as a function of the diode current is determined. The power balance during diode pumping is considered, and the contributions of various mechanisms to the thermal processes in the crystal of the active element are determined. A practical technique is described for calculating thermal lenses in solid-state lasers with transverse diode pumping.

According to our works, we set the single diode side pump Nd:YAG laser whose laser medium is in slab geometry. We tried to compare the measured focal length of the thermal lens in our experiment with the calculated one [2]. Finally, we studied the expansion of the laser medium. We wanted to know it had a uniform expansion or not. After that the result would be compared with the mathematical model.

METHODOLOGY

The Nd:YAG laser in the experiment is set in sided-pump configuration. The slab is placed between the coolant plates as shown in Figure 1. The laser diode (model `ARR31C040W080803A11B80`, Northrop Grumman Space Technology) is used as a pump source and is placed at the side of the slab. The curve mirror which has the radius of curvature of 1.50 m is used as the back mirror. The flat mirror which has the reflection 95% is used as the front mirror. The cavity length is 12.5 cm. The relation between the diode current (I) of the laser diode and the output power of Nd:YAG (1064 nm) when the coolant temperature (T_c) is set at 22 °C is measured. Then the laser resonators are removed. The experiment for the measurement of the thermal lens is set as shown in Figure 2. HeNe laser is used as a probe beam and is passed through the laser medium while laser diode is on. The focal point is found and the focal length of the thermal lens is calculated. Finally, we tried to see the expansion of the slab then the experiment is set as shown in Figure 3. The HeNe laser was passed into Mach–Zehnder interferometer that Nd:YAG slab is placed at one arm [4]. The parallel beam of HeNe laser is passed through the slab while it is heated by laser diode. When the diode current was changed the interference pattern would be changed

RESULTS, DISCUSSION AND CONCLUSION

According to the Nd:YAG laser configuration set up, the relation between the input current of the laser diode and the output power of Nd:YAG (1064 nm) when the coolant temperature is set at 22 °C is shown in Figure 4. The threshold current is about 25 A. The maximum output power of laser is about 3.2 W.

Using the concept of heat transfer, the stress

Figure 1: (color online). Diode-sided pump Nd:YAG laser in the experiment.

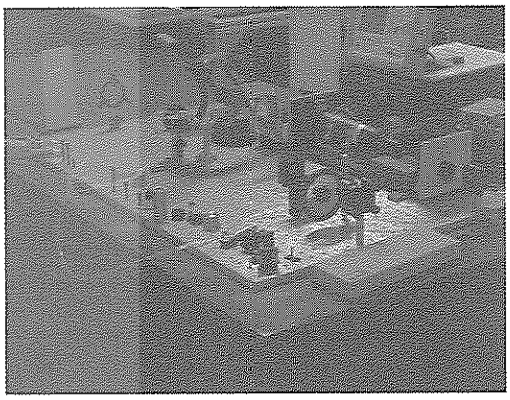

Figure 2: (color online). The experiment for measure the focal length of the thermal lens.

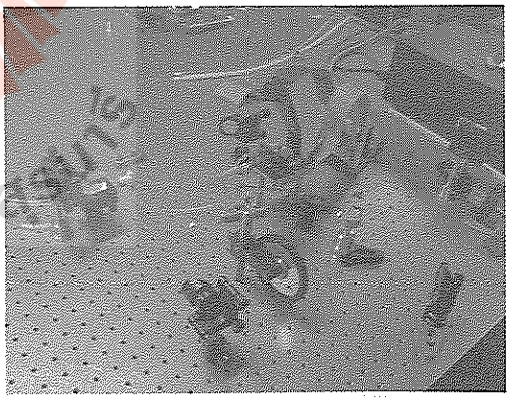

Figure 3: (color online). The experiment for studying the expansion of the slab.

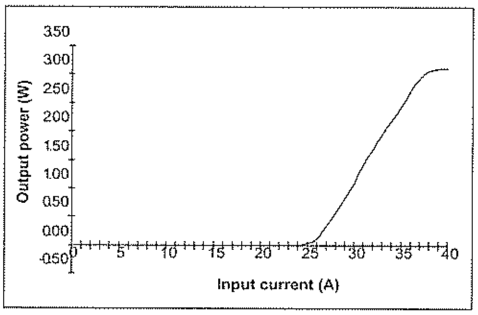

Figure 4: Graph between diode current and the output power of Nd:YAG laser when the coolant temperature is set at 22 °C.

and strain, the indexes of refraction and the ray matrix, the focal length of the thermal lens can be calculated by [5];

$$f_x = \frac{1}{n_x^0 l \alpha_x} \quad \text{and} \quad f_y = \frac{1}{n_y^0 l \alpha_y}. \tag{1}$$

Where

$$n_x^0 = n_0 + \frac{\mathrm{d}n}{\mathrm{d}T}\left(\frac{Qd^2}{24k}\right) - \frac{Qd^2}{24M_s}(B_\perp + B_\parallel), \tag{2a}$$

$$\alpha_x = \frac{2}{n_x^0}\left[\frac{\mathrm{d}n}{\mathrm{d}T}\left(\frac{Q}{2k}\right) - \frac{Q}{2M_s}(B_\perp + B_\parallel)\right], \tag{2b}$$

$$n_y^0 = n_0 + \frac{\mathrm{d}n}{\mathrm{d}T}\left(\frac{Qd^2}{24k}\right) - \frac{Qd^2}{12M_s}B_\perp, \tag{2c}$$

$$\alpha_y = \frac{2}{n_y^0}\left[\frac{\mathrm{d}n}{\mathrm{d}T}\left(\frac{Q}{2k}\right) - \frac{Q}{M_s}B_\perp\right] \tag{2d}$$

where f_x and f_y are the focal length of the slab for x and y, respectively, d is the height of the slab, l is the length of the slab, k is the thermal conductivity ($\mathrm{W\,cm^{-1}\,K^{-1}}$), Q is heat generated per unit volume ($\mathrm{W\,cm^{-3}}$), $B_\parallel$ and $B_\perp$ are stress optic coefficient which give the change in the optical index for stress applied parallel and perpendicular to the polarization axis, respectively, $M_s = \dfrac{(1-\nu)k}{\alpha E}$, E is Young's modulus, ν is the Poisson's ratio and α is the thermal expansion coefficient.

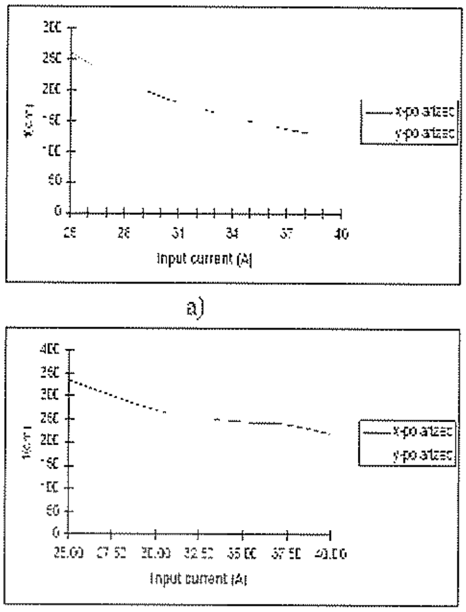

a)

b)

Figure 5: (color online). a) Theoretical relationship between the focal length of the thermal lens in the Nd:YAG slab and the input current, b) Graph between the measured focal length of the thermal lens and the input current.

At $T_c = 22$ °C, the relationship between the input current of laser diode and the calculated value of the focal length of the thermal lens as shown in equation (1) are shown in Figure 5 a) and the relationship between the input current of laser diode and the measured value of the focal length of the thermal lens is shown in Figure 5 b). When comparing the focal length of the thermal lens from the theory to one from the experiments we find that the theoretical focal lengths are shorter than that from the experiment. This implies that the heat generated in the slab is removed faster so that the temperature of the slab is not high as in the theory. The stress is reduced as temperature. The index of refraction of slab is not changed much as that expected from the theory. Thus the focal lengths of the thermal lens in the slab are longer than in the calculations.

When the input current is greater than 35 A, the tendency of the slope of the graph is changed. This implies that when the input current is a high value, the heat generated in the slab increases. The cooler can not remove heat as the same rate as when operated with lower input current. There-

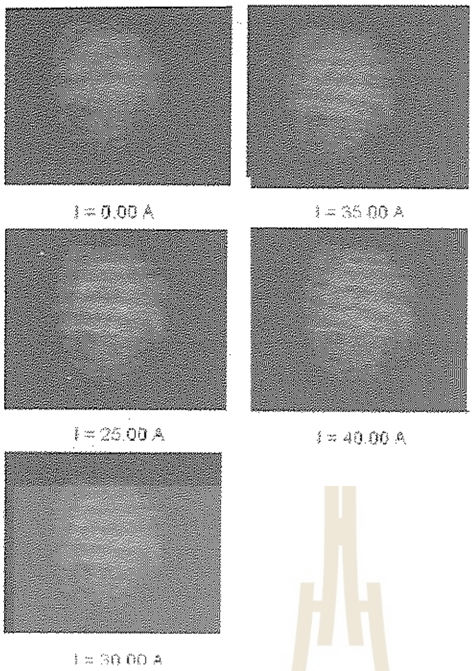

I = 0.00 A

I = 35.00 A

I = 25.00 A

I = 40.00 A

I = 30.00 A

Figure 6: (color online). Interference pattern from the Mach–Zehnder interferometer corresponding to diode current = 0, 25, 30, 35 and 40 A.

fore the slab contains more heat leading to the shorten of the focal length of the thermal lens.

According to the experiment for studying the expansion of the Nd:YAG crystal. The interference patterns of HeNe laser from the experiments when input current is set at 0, 25, 30, 35, and 40 A are shown in Figure 6. When $I = 0.00$ A the fringes in interference pattern are quite straight. This means that the refractive index of the slab is uniform. After increasing the input current of the laser diode, fringes in the interference pattern are not uniform which implies that the refractive index of the slab is not uniform leading to the distortion of the wave front of the HeNe beam which pass through the slab. The right side of the interference pattern fringes is wider than the left side. Analyzing from the laser system the HeNe laser beam which produces the wider fringes at the right zone passes through the slab at the region near the laser diode. This means that the expansion of the slab and the thermal lens effects give a strong effect at the region which is in contact to the laser diode. It can be concluded that the temperature in plane xz of the slab is actually not uniform and the heat is transferred in two dimensions. When heat is not transferred only in y direction of slab, the thermal lens effects in y direction will be less than the effects when the heat is transferred in only y direction. Thus the focal length of the thermal lens will be longer.

---

[*] ชื่อไทย: จินตวัฒน์ ตันอมาตยรัตน์
Email: `jintawatmail@yahoo.com`

[1] International School of Photonics, Cochin University of Science and Technology, *"Thermal Lens Spectroscopy"*. [Online]. Available: `http://www.photonics.cusat.edu/Research_Thermal%20lens.html`.

[2] J. M. Eggleston *et al.*, *"The Slab Geometry Laser—Part I: Theory"*, IEEE J. Quantum Electron. **QE-20** (3), 289–301 (1984).

[3] V. S. Ermolaev *et al.*, *"Study of the Thermal Lens in a* 150-W *Solid-State Processing Laser with Semiconductor Pumping"*, J. Opt. Technol. **70** (11), 789–793 (2003).

[4] S. D. Sims, A. Stein and C. Roth, *"Dynamic Optical Path Distortions in Laser Rods"*, Appl. Opt. **5** (4), 621–626 (1966).

[5] H. Kogelnik, *"Imaging of Optical Modes—Resonators with Internal Lenses"*, Bell Syst. Tech. J. **44** (3), 455–494 (1965).

Particle Sizing by Using Absolute Values of the Wavelet Transform of the Particle Holograms

การหาขนาดอนุภาคโดยวิธีการหาค่าสัมบูรณ์การแปลงเวฟเลทจากฮอโลแกรมของอนุภาค

SIRIWAT SOONTARANON* and JOEWONO WIDJAJA
School of Laser Technology and Photonics, Institute of Science,
Suranaree University of Technology, Nakhon Ratchasima 30000, Thailand

A new method for sizing particles from in-line Fraunhofer holograms by using wavelet transform is proposed. The amplitude transmittance of the holograms is a modulation of a chirp signal with an envelope function whose minima is proportionally equal to the product of the particle size and the spatial frequency of the chirp function. By wavelet transforming the hologram and taking an absolute value of its resultant transformation, the spatial frequency at the minima positions can be obtained. The particle size which is merely a function of this frequency can then be calculated. Feasibility study of the proposed method is done by conducting simulation and experimental verifications for line object.

ผู้วิจัยได้นำเสนอวิธีการใหม่ ในการหาขนาดของอนุภาคจากฮอโลแกรม แบบอินไลน์ฟรานโฮเฟอร์ ด้วยวิธีการแปลงเวฟเลท แอมปลิจูดทรานสมิทแทนท์ของฮอโลแกรมเป็นการกล้ำกันระหว่าง สัญญาณแบบเชิร์พและเอ็นเวโลปฟังก์ชัน ซึ่งมีตำแหน่งของมินนิมาแปรผันกับผลคูณระหว่าง ขนาดของอนุภาค และความถี่เชิงตำแหน่งของสัญญาณเชิร์พ เมื่อทำการแปลงเวฟเลทและหาค่าสัมบูรณ์ของผลที่ได้ เราจะได้ความถี่เชิงตำแหน่ง ณ จุดมินนิมา จากนั้นจึงสามารถคำนวณหาขนาดของอนุภาคซึ่งเป็นฟังก์ชันของความถี่นี้ได้ ได้มีการศึกษาเพื่อยืนยันความสามารถนำไปใช้งานจริงได้ของวิธีการนี้ โดยการจำลองสถานการณ์ ด้วยคอมพิวเตอร์และการทดลองจริงกับวัตถุที่มีลักษณะเป็นเส้น

PACS numbers: 42.40.-i
Keywords: Particle sizing, in-line particle holography, wavelet transform.

INTRODUCTION

Particle size measurement from in-line particle holograms by using absolute value of the wavelet transform (WT) is proposed in order to improve accuracy of our previously proposed method [1]. By illuminating opaque or semi-transparent particles with a collimated coherent light, a hologram which is an interference pattern between light waves diffracted from particles and a directly transmitted light wave is generated. In a conventional reconstruction process, the hologram is illuminated with the same coherent light. The information about the particle size can be obtained by analyzing a reconstructed image of the particle. However, in real applications, we may deal with a huge number of particles. As a consequence, the conventional reconstruction process is very tedious and time consuming.

An amplitude transmittance of the in-line Fraunhofer hologram of a small line object with a radius of a can be mathematically expressed as [2]

$$I(x) = 1 - \frac{4a}{\sqrt{\lambda z}}\cos\left(\frac{\pi x^2}{\lambda z} - \frac{\pi}{4}\right)\left[\frac{\sin(2\pi a x/\lambda z)}{2\pi a x/\lambda z}\right] + \frac{4a^2}{\lambda z}\left[\frac{\sin(2\pi a x/\lambda z)}{2\pi a x/\lambda z}\right]^2 \quad (1)$$

where λ and z are the wavelength of the illuminating light and the distance between the particle

---

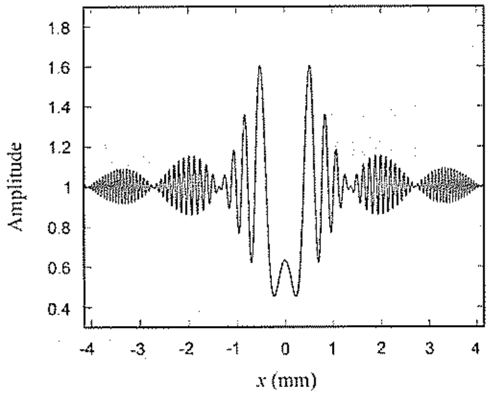

Figure 1: Simulated in-line hologram of a line object.

and the recording plane, respectively. The first term of Eq. (1) corresponds to the directly transmitted light. The second term corresponds to a modulation between a chirp signal and a sinc function. The particle size information is encoded into the zero-crossing positions of the sinc function. These positions are referred as the minima positions of the interference pattern. The third term is a square of the sinc function whose amplitude is much smaller than the other terms. Figure 1 shows a computer plot of Eq. (1), from which the above properties of three terms can be obviously observed.

METHODOLOGY

According to Eq. (1) the frequency of the chirp signal is $x/\lambda z$, while the minima positions of the interference pattern appear at $2ax/\lambda z = n$ where n is $1, 2, 3, \ldots$. Thus, the frequencies of the chirp signal at the minima positions are found to be $n/2a$. By taking this into consideration, the size of particles can be calculated, provided that the spatial frequencies of the chirp signal at the minimum positions are known. In the proposed method, the digitized holograms captured by a charge-coupled device sensor are analyzed by computing the absolute value of its wavelet transformation. The WT of a signal pattern $s(x)$ is defined as [3]

$$W(t,d) = \frac{1}{\sqrt{d}} \int_{-\infty}^{\infty} g^{*}\left(\frac{x-t}{d}\right) s(x)\, \mathrm{d}x, \qquad (2)$$

where d and t are the dilation and the translation parameters, respectively. Equation (2) can be considered as a cross correlation between the signal $s(x)$ and the dilated wavelet $g(x/d)$. When the frequency content f of the signal $s(x)$ in the region subtended by $g^{*}\left((x-t)/d\right)$ matches the center frequency of the dilated wavelet $g(x/d)$, a correlation peak is generated along the dilation d at the position t where the frequency f occurs. This peak is found to be proportional to the amplitude of the signal $s(x)$.

In the general case of signals that $s(x)$ is an amplitude modulated signal, the amplitudes of the resultant correlation peaks are determined by the amplitude of the modulating function. Therefore, besides its excellent ability of providing the time-frequency simultaneously, the WT extracts the modulating information of the signals being analyzed. A further insight into this property may be gained by analyzing mathematically the modulated signal on the use of the WT.

For the sake of simplicity, we consider that a modulated signal is given by

$$s(x) = \cos(2\pi f_1 x)\, \cos(2\pi f_0 x) \qquad (3)$$

where the first cosine term corresponds to the carrier signal while the second one is the modulating signal. Here, the carrier frequency f_1 is greater than the modulating frequency f_0. By using a Morlet wavelet of the form

$$g(x) = \exp\left(\mathrm{i}2\pi f_g x\right)\, \exp\left(-\frac{x^2}{2}\right) \qquad (4)$$

as an analyzing wavelet, the absolute value of the WT of the signal $s(x)$ is found to be

$$
\begin{aligned}
\left|W(t,d)\right| = \sqrt{\frac{\pi d}{8}} \Bigg\{ & \exp\left[-4\pi^2(f_0-f_1)^2\left(d-\frac{f_g}{f_1-f_0}\right)^2\right] \\
& + \exp\left[-4\pi^2(f_0+f_1)^2\left(d-\frac{f_g}{f_1+f_0}\right)^2\right] \\
& + 2\cos(4\pi f_0 t)\exp\Bigg[-2\pi^2(f_0-f_1)^2\left(d-\frac{f_g}{f_1-f_0}\right)^2 \\
& \qquad -2\pi^2(f_0+f_1)^2\left(d-\frac{f_g}{f_1+f_0}\right)^2\Bigg]\Bigg\}^{1/2} \qquad (5)
\end{aligned}
$$

Equation (5) consists of the summation and multiplication of two Gaussian functions which produced a Gaussian-like function whose maximum peak appears at $d = f_g/f_1$. This position is regarded as the one where the frequency of the dilated wavelet f_g/d matches the frequency of the modulating signal f_1. Therefore, the cosine function in the third term of Eq. (5) is confined by the Gaussian-like function centered at the dilation $d = f_g/f_1$. When the dilation $d = f_g/f_1$ is achieved, Eq. (5) reduces to

$$
\left|W(t,d)\right|\Big|_{d=f_g/f_1} = \sqrt{\frac{\pi f_g}{2f_1}}\exp\left(-\frac{2\pi^2 f_g^2 f_0^2}{f_1^2}\right)\left|\cos(2\pi f_0 t)\right| \qquad (6)
$$

Equation (6) confirms that the absolute value of the WT gives the information about the modulating signal with its absolute value $|\cos(2\pi f_0 t)|$. As a function of dilation $2a/d$, Fig. 2 illustrate a 3-D plot for the absolute value of the WT of the Fig. 1 which is cut along the dilation $d = f_g/f_1$. Evidently, the minima of the absolute value of the WT output appear at the correct zero-crossing points of the sinc function. By determining the frequencies of the chirp function at these minima, the object size can then be calculated.

RESULTS AND DISCUSSIONS

In a preliminary verification, the in-line hologram of an optical fiber with the diameter of 125μm was experimentally generated under illumination of the coherent light operating at the wavelength of 543.5 nm. The hologram was recorded by using a CCD camera HAMAMATSU C5948 with the resolution of 640 × 480 pixels in the area of 8.3 × 6.3 mm. Figure 3 shows a comparison of the errors in measurements of the diameter of the optical fiber, where the circle and cross signs correspond to the previously proposed envelope reconstruction method and the absolute value of the WT, respectively. It is obvious from the figure that the errors in measurements using the proposed method are significantly reduced. The reason of this reduction is that the proposed method employs only the frequency of the chirp signal at the minimum position of the envelope function for evaluating the object size. Since the information of the recording distance is not required as in the envelope reconstruction method, its measurement errors do not affect the measurements in the size of the object.

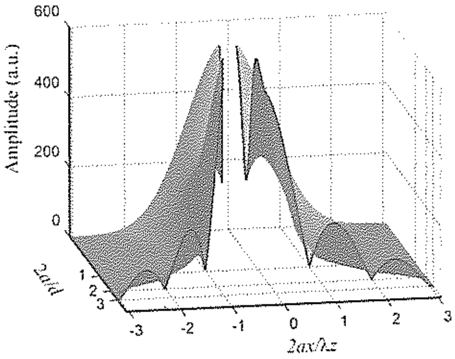

Figure 2: The 3-D plot of the absolute value of the WT of Fig. 1 which is cut along the dilation $d = f_g/f_1$.

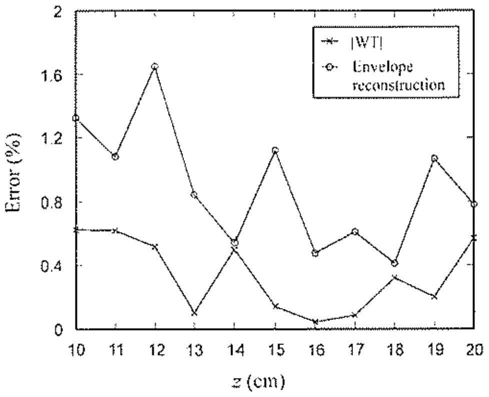

Figure 3: Errors in measurements of the fiber size from the experimentally generated holograms by using the envelope reconstruction method and the absolute value of the WT.

CONCLUSION

We have proposed and verified experimentally a novel method for sizing the particles from the in-line holograms by using the absolute value of the WT. The proposed method takes an advantage of the property of the WT whose absolute value could extract the positions of the minima of the envelope function. Since the resultant extracted minima are functions of the dilation of the wavelet, the frequencies of the fringes at the minima of the envelope function are measured. The size of the particles can be finally calculated from the relationship between the frequencies with the positions of the minima. Unlike the previous method, the information of the recording distance is not used for determining the object size and, therefore, the errors in measurements do not affect the accuracy of the proposed method.

Acknowledgements

The financial support from the Thailand Research Fund through the Royal Golden Jubilee Ph.D. Program (Grant No. PHD/0188/2542) is acknowledged.

---

* ชื่อไทย: ศิริวัช สุนทรานนท์
Email: `bom_chon@hotmail.com`

[1] S. Soontaranon, J. Widjaja and T. Asakura, *"Direct Analysis of In-line Particle Holograms by Using Wavelet Transform and Envelope Reconstruction Method"*, Optik **113** (11), 489–494 (2002).
[2] G. A. Tyler and B. J. Thompson, *"Fraunhofer Holography Applied to Particle Size Analysis. A Reassessment"*, Opt. Acta **23** (9), 685–700 (1976).
[3] R. Kronland-Martinet, J. Morlet and A. Grossmann, *"Analysis of Sound Patterns Through Wavelet Transforms"*, Int. J. Patt. Recog. Artificial Intell. **1** (2), 273–302 (1987).

NSPG
Proceedings of the First National Symposium on Physics Graduate Research (1st NSPG)
29 June – 1 July 2006, Chulabhorn Dam, Khon San, Chaiyaphum, Thailand

Decoherence in Josephson Junction Phase Qubit

ดีโคฮีเรนส์ในรอยต่อโจเซฟสันเฟสคิวบิต

RACHSAK SAKDANUPHAB* and SOJIPHONG CHATRAPHORN
Department of Physics, Faculty of Science, Chulalongkorn University,
Bangkok, 10330, Thailand

Josephson junction is a one of promising devices to be used as a quantum bit or known as qubit in a quantum computer. The dynamics of a current-bias Josephson junction can be described by using the Resistively and Capacitively Shunted Junction (RCSJ) model, which is analogous to the classical motion of a particle in a tilted washboard potential. In this work, quantum theory and approximation methods are used to calculate and explain quantum properties of the Josepson junction. We can see that the energy levels in the washboard potential can be quantum mechanically quantized, and thus used as a qubit in quantum computation. The wave functions of the states in the potential well are relatively similar to that of the harmonic oscillator due to the shape of the washboard potential. The tunneling rate from the n^{th} energy level exponentially increases with bias current and the first excited state is three orders of magnitude more than the ground state. The decoherence time in a Josephson junction can be found by considering the Rabi's oscillation in the presence of current noise in the junction. The decoherence time depends on the magnitude of the current noise. This result can be used to determine the feasibility of using Josephson junction as a qubit.

รอยต่อโจเซฟสันเป็นอุปกรณ์ที่คาดหวังว่าจะนำมาใช้เป็นควอนตัมบิตหรือเรียกอีกอย่างหนึ่งว่าคิวบิตในควอนตัมคอมพิวเตอร์พฤติกรรมทางไฟฟ้าของรอยต่อโจเซฟสันสามารถอธิบายได้ด้วยแบบจำลอง RCSJ ซึ่งจะคล้ายกับการเคลื่อนที่ของอนุภาคในบ่อพลังงานศักย์แบบกระดานซักผ้าเอียง ในงานนี้เราศึกษาถึงคุณสมบัติทางควอนตัมของรอยต่อโจเซฟสันโดยใช้ทฤษฎีควอนตัมและการประมาณทางควอนตัมในการคำนวณและอธิบายผลที่เกิดขึ้น ซึ่งเราพบว่าระดับพลังงานในบ่อศักย์ สามารถที่จะถูกควอนไทซ์และนำไปใช้เป็นคิวบิตสำหรับควอนตัมคอมพิวเตอร์ได้โดยฟังก์ชั่นคลื่นของสถานะต่าง ๆ ในบ่อศักย์มีลักษณะคล้ายกับฟังก์ชั่นคลื่นของการสั่นแบบฮาร์โมนิก ทั้งนี้เนื่องจากรูปร่างของบ่อศักย์มีความคล้ายคลึงกัน โดยที่อัตราการทะลุผ่านกำแพงศักย์ของระดับพลังงานหนึ่ง ๆ มีค่าเพิ่มขึ้นแบบเอกซ์โพเนนเชียล เมื่อค่ากระแสที่ไบแอสมีค่าสูงขึ้น โดยสถานะกระตุ้นที่หนึ่งมีอัตราการทะลุผ่านมากกว่าสถานะพื้นอยู่ประมาณ 10^3 เท่า และช่วงเวลาดีโคฮีเรนส์ในรอยต่อโจเซฟสันสามารถคำนวณได้จากการพิจารณา Rabi's oscillation เมื่อมีสัญญาณรบกวนในกระแสที่ไบแอส เราพบว่าช่วงเวลาดีโคฮีเรนส์ขึ้นอยู่กับขนาดของค่ากระแสรบกวน ซึ่งผลในส่วนนี้สามารถบอกถึงความเป็นไปได้ในการนำรอยต่อโจเซฟสันมาใช้เป็นคิวบิต

PACS numbers: 13.85.Hd, 24.10.Jv, 24.85.+p
Keywords: Josephson junction, Quantum Computation. Phase Qubit

INTRODUCTION

Quantum computers are promising to solve certain difficult problems in computer science, such as factoring prime number, searching algorithms and running simulations of quantum mechanical system faster than classical ones. Quantum computers use a quantum system instead of a classical system, storing information as well as operating computation under the principle of quantum mechanics. Today, there are many proposed quantum systems such as Nuclear Magnetic Resonance (NMR), Optical, Solid State, and Superconducting that are used to build quantum computers [1]. Josephson junction is one of the promising devices to be used as a quantum bit (qubit) in a quantum computer. Josephson junction is a superconducting device, which consists of two superconductors separated by a thin insulating barrier such as Nb/AlO$_x$/Nb and Al/AlO$_x$/Al. The behavior of Josephson junction is described by the Josephson relations, $I_s = I_c \sin\gamma$ and $V = (\hbar/2e)\mathrm{d}\gamma/\mathrm{d}t$ where

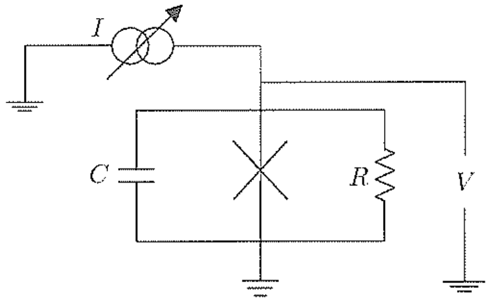

Figure 1: The equivalent circuit diagram of Josephson junction.

I_s is the tunneling current, I_c is the critical current of the junction. γ is the phase different of the superconducting order parameter, and V is the voltage across the junction. The Josephson junction can be considered by using the equivalent circuit diagram known as the RCSJ (Resistively and Capacitively Shunted Junction) model as shown in Fig. 1; [2]. The system is analogous to the classical motion of a fictitious particle moving in a tilted washboard potential

$$U(\gamma) = \left(\frac{\hbar}{2e}\right) I_c \left(\cos\gamma + \frac{I_{dc}}{I_c}\gamma\right), \qquad (1)$$

where $U(\gamma)$ is the potential energy and I_{dc} is the total applied current through the junction. This potential is the key to study the quantum properties of the Josephson junction such as energy levels in the potential well (the information states 0 and 1 can be stored in the ground state $|0\rangle$ and the first excited state $|1\rangle$ of the junction, respectively), state wave functions of the qubit, the tunneling rates of the states, and the decoherence times of the states. These are basic knowledge necessary for the experimental work in quantum computation.

METHODOLOGY

In the calculation, the washboard potential can be approximated by a cubic parabola potential when the applied bias current is close to the critical current. The potential can be rewritten as

$$U(q) = 3U_0\left(\frac{q}{q_0}\right)^2\left[1-\left(\frac{2q}{3q_0}\right)\right], \qquad (2)$$

where $q = \gamma - \sin^{-1}(I_{dc}/I_c)$, U_0 is the barrier height and q_0 is the position of the maximum as shown in Fig. 2. The energy levels and the wave functions of the cubic parabola potential can be found by solving the time independent Schrödinger equation numerically. According to the one dimensional Schrödinger equation

$$-\frac{\hbar^2}{2m}\frac{\partial^2\psi_n}{\partial x^n} + U(x)\psi_n = E_n\psi_n, \qquad (3)$$

the approximation wave function $w_j^{(n)}$ is considered in an interval (a, b) under the three conditions

1. $x_j = hj$; $j = 1, 2, 3, \ldots, N-1$
2. $w_j^{(n)} = \psi_n(x_j)$
3. $w_0^{(n)} = w_N^{(n)} = 0$ (boundary condition), where $x_0 = a$, $x_N = b$ and h is the step size defined by $h = (b-a)/N$.

The interval of the wave function is divided to N points and the wave function $\psi_n(x_j)$ at any point x_j is approximated by wave function $w_j^{(n)}$, as well as using the boundary condition at the ends of the interval. Following the derivative approximations

$$\psi_n''(x_j) \approx \frac{1}{h^2}\left[w_{j-1}^{(n)} - 2w_j^{(n)} + w_{j+1}^{(n)}\right], \qquad (4)$$

$$\psi_n'(x_j) \approx \frac{1}{2h}\left[w_{j+1}^{(n)} - w_{j-1}^{(n)}\right], \qquad (5)$$

the approximated wave function can be inserted into the Schrödinger equation, and a system of equations for solving the eigenvalue problem can be obtained. A large number of energy eigenvalues and eigenfunctions can be found but only the eigenvalues and the eigenfunctions inside the well ($E < U_0$) are used to study the quantum mechanical behavior of the junction.

The tunneling rates at each energy level of the Josephson junction can be calculated using the semiclassical method. According to the WKB formula, the tunneling rate from the n^{th} energy level is

$$\Gamma_n = \frac{1}{T(E_n)}\exp\left[-\frac{2}{\hbar}\int_{x_2}^{x_1}|p(x)|\,\mathrm{d}x\right] \qquad (6)$$

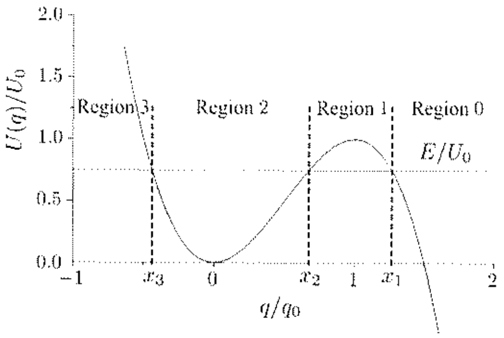

Figure 2: The cubic parabola potential.

$$p(x) = \sqrt{2m\left[E - U(x)\right]} \tag{7}$$

where $T(E_n)$ is the period of the classical motion at energy E_n. This quantum effect is a problem in quantum computation because a particle prepared in a state inside the well can leave the system.

Finally, the decoherence times of the Josephson junction in the presence of current noise can be observed by considering the Rabi's oscillations. We first current bias the Josephson junction and keep only the two-state system of the qubit and add two external current sources, a microwave current $I_{\mathrm{\mu w}}(t)$ and noise current $I_{\mathrm{n}}(t)$ as perturbations. The microwave current is the ac current with angular frequency ω_{10} equivalent to the energy spacing between the ground state and the first excited state. The noise current is chosen in a form of Gaussian random noise. According to the Hamiltonian in the interaction picture, $H = H^0 + H'(t)$, the unperturbed Hamiltonian can be written in a matrix notation as

$$H^0 = \begin{pmatrix} E_0 & 0 \\ 0 & E_1 \end{pmatrix}, \tag{8}$$

and the perturbed Hamiltonian in a matrix notation is

$$H' = \begin{pmatrix} \dfrac{I_{\mathrm{n}}(t)}{2}\left(\dfrac{\partial E_{10}}{\partial I_{\mathrm{dc}}}\right) & I_{\mathrm{\mu w}}\sqrt{\dfrac{\hbar}{2C\omega_{10}}}\,\mathrm{e}^{\mathrm{i}\omega_{10}t} \\ I_{\mathrm{\mu w}}\sqrt{\dfrac{\hbar}{2C\omega_{10}}}\,\mathrm{e}^{\mathrm{i}\omega_{10}t} & -\dfrac{I_{\mathrm{n}}(t)}{2}\left(\dfrac{\partial E_{10}}{\partial I_{\mathrm{dc}}}\right) \end{pmatrix} \tag{9}$$

where E_{10} is energy spacing between ground state and first excited state. The state of two-level system can be written in a superposition of the basis states $|0\rangle$ and $|1\rangle$, given by

$$|\psi(t)\rangle = \mathrm{e}^{-\mathrm{i}E_0t/\hbar}c_0(t)\,|0\rangle + \mathrm{e}^{-\mathrm{i}E_1t/\hbar}c_1(t)\,|1\rangle = \begin{pmatrix} \mathrm{e}^{-\mathrm{i}E_0t/\hbar}c_0(t) \\ \mathrm{e}^{-\mathrm{i}E_1t/\hbar}c_1(t) \end{pmatrix}, \tag{10}$$

where $c_0(t)$ and $c_1(t)$ are the probability amplitudes of finding the system in the state $|0\rangle$ and state $|1\rangle$ at time t, respectively. We insert the Hamiltonian and the state of qubit into the Schrödinger equation $\mathrm{i}\hbar\,\mathrm{d}|\psi(t)\rangle/\mathrm{d}t = H|\psi(t)\rangle$, and solve the ordinary differential equations numerically by using the 2nd order Runge–Kutta method, i.e. midpoint method.

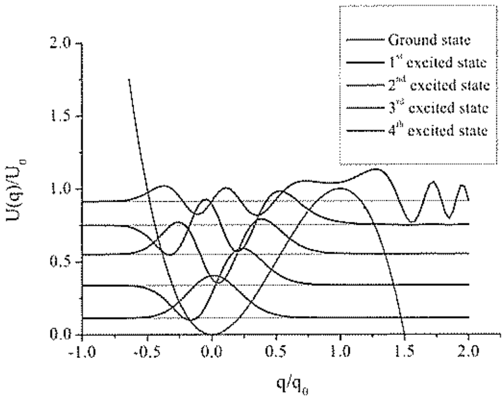

Figure 3: (color online). The five state wave function in the cubic parabola potential.

RESULTS, DISCUSSION AND CONCLUSION

The energy eigenvalues and the numerical wave functions of the first five states are shown in Fig. 3. It can be seen that they are somewhat similar to the wave functions of the harmonic oscillator because the shape of cubic parabola potential is almost similar to the parabola potential. The energy levels inside the well depend on the junction parameters such as the critical current (I_c) and the capacitance (C) as well as the applied bias current (I_{dc}). When the bias current is raised, the potential well becomes shallow, thus decreasing the number of energy levels. The energy level spacing between the ground state and the first excited state is in the range of microwave frequency (GHz). A microwave current can be applied as a perturbation to observe the transition between the two lowest lying states.

The tunneling rate describing the transmission of the particle through the potential barrier is exponentially decayed with the action per period of time. The period of classical motion is

$$T(E_n) = \oint \frac{\partial p}{\partial E}\,\mathrm{d}x = 2q_0\sqrt{\frac{m}{U_0}}\,\frac{1}{\sqrt{x_1 - x_3}}\ \mathrm{EllipticK}\left(\sqrt{\frac{x_{12}}{x_{13}}}\right), \tag{11}$$

where EllipticK is the complete elliptic integral of the first kind. The Euclidean action across the classically forbidden region (region 1) is

$$\int_{x_2}^{x_1} \left|p(x)\right|\,\mathrm{d}x = S_{\mathrm{f}} = 2q_0\sqrt{mU_0}\,\frac{\pi}{8}\,x_{12}^2\sqrt{x_{23}}\;{}_2\mathrm{F}_1\left(-\frac{1}{2},\frac{3}{2},3,-\frac{x_{12}}{x_{23}}\right), \tag{12}$$

where ${}_2\mathrm{F}_1(\nu,\lambda,\lambda+\mu,\beta)$ is the Gaussian hypergeometric function. The tunneling rates of the ground state and the first excited state are shown in Fig. 4. It can be seen that the tunneling rates of the first excited state are about 3 orders of magnitude more than these of the ground state.

For the Josephson junction, noise current is one of the cause of decoherence in the qubit. The Rabi's oscillations of the two-state system under the influence of the noise current are used to observe a decay of the probability of the states. We found that the probability of $\left|c_0(t)\right|^2$ and $\left|c_1(t)\right|^2$ oscillate and exponentially decay with time in range of nanoseconds as shown in Fig. 5. The microwave current causes the oscillation of probability $\left|c_0(t)\right|^2$ and $\left|c_1(t)\right|^2$ and a period of the oscillation depends on the amplitude of microwave current. The noise current causes the decay of the

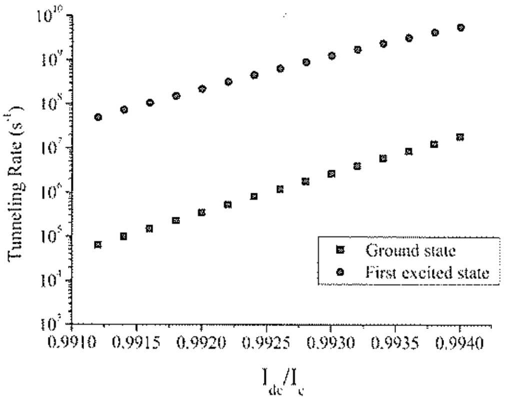

Figure 4: (color online). The tunneling rates of the ground state and the first excited state.

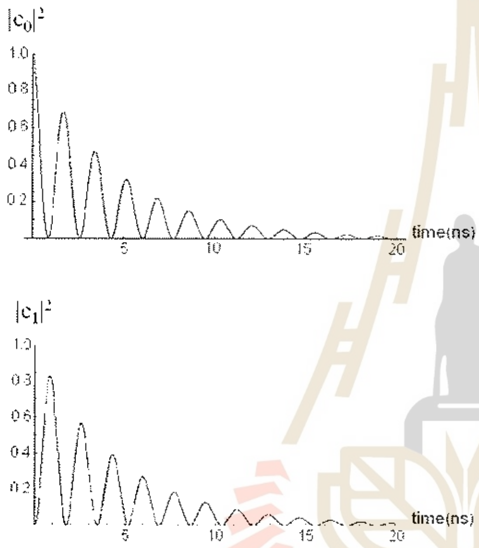

Figure 5: The Rabi's oscillation with current noise amplitude 10 nA.

oscillations. We are interested in the amplitudes of the noise current that cause the decay of the Rabi's oscillation. If we increase the noise current amplitude, the probability of finding the state will decay faster and the decoherence time becomes shorter as shown in Table. 1. This result is in a good agreement with the experimental results [3].

The quantum properties of Josephson junction that have been studied are necessary for using the Josephson junction as a quantum bit. The methods used here yield the results that are agree with the previous result by P. Kopietz *et al.* [4] and show that the Josephson junction phase qubit can be a good candidate for a quantum computer.

Table 1: Decoherence time in Josephson junction with noise current for a junction parameter I_c = 14.12 μA and C = 4 pF.

Noise current (nA)	Decoherence time (ns)
1	21
5	4.2
10	2.0
15	1.4
20	1.0

---

[*] ชื่อไทย: ราชศักดิ์ ศักดานุภาพ
Email: `chin_phy@hotmail.com`

[1] R. Hughes *et al.*, *"Quantum Information Science and Technology Roadmapping Project"*, (2002). [Online]. Available: `http://qist.lanl.gov`

[2] W. Buckel and R. Kleiner, *Superconductivity: Fundamentals and Applications*, 2nd ed., Weinheim, Wiley-VCH (2004).

[3] A. J. Berkley *et al.*, *"Decoherence in a Josephson-Junction Qubit"*, Phys. Rev. B **68** (6), 060502 (2003). [arXiv: `quant-ph/0303001`].

[4] P. Kopietz and S. Chakravarty, *"Lifetime of Metastable Voltage States of Superconducting Tunnel Junctions"*, Phys. Rev. B **38** (1), 97–110 (1988).

Part II

Abstracts

APSRS01

X-Ray Absorption Study of TiO_2 and TiS_2 at the Siam Photon Laboratory

การศึกษาการดูดกลืนรังสีเอกซ์ของ TiO_2 และ TiS_2 ณ ห้องปฏิบัติการแสงสยาม

Darin Onkaw*[1] Sutassana Na Phattalung[1] Michael Francis Smith[2]
Wantana Klysubun[2] Sukit Limpijumnong[1,2] and Saroj Rujirawat[1,2]

1. *School of Physics, Institute of Science, Suranaree University of Technology, Nakhon Ratchasima 30000, Thailand*
2. *National Synchrotron Research Center, P.O. Box 93, Nakhon Ratchasima 30000, Thailand*

X-ray absorption spectroscopy using synchrotron radiation light source is a powerful technique to identify local structure around the interested atomic specie. At present, the titanium-based compounds have got a lot of attention from many research groups for using in several applications. In this study, we used the Siam Photon Source's x-ray absorption facility (BL-8), to study the local structure around Ti atoms in titanium dioxide (TiO_2) and titanium disulfide (TiS_2). The two systems have a similar chemical formula but different crystal structures. The x-ray absorption near edge structure (XANES) spectra and the extended x-ray absorption fine structure (EXAFS) spectra around Ti-K edge for TiO_2 and TiS_2 powders were collected and compared, using Ti-foil as a standard. The experimental data was analyzed using FEFF code. The results from theoretical analysis agreed well with the known crystal data. Moreover, it this found that the calculated electron partial density of states related nicely to the XANES spectra.

การวัดสเปกตรัมการดูดกลืนรังสีเอกซ์โดยใช้แหล่งกำเนิดแสงซินโครตรอนนั้นเป็นเทคนิคที่สามารถบ่งชี้ถึงโครงสร้างรอบ ๆ อะตอมที่เราสนใจได้อย่างมีประสิทธิภาพ ในปัจจุบัน สารประกอบไทเทเนียมได้รับความสนใจจากกลุ่มการวิจัยหลายแห่งในการนำไปประยุกต์ใช้ได้ในหลาย ๆ ด้าน สำหรับงานวิจัยครั้งนี้ เราได้ทำทดลองที่สถานีลำเลียงแสง ณ ห้องปฏิบัติการแสงสยาม (BL-8) เพื่อศึกษาการเรียงตัวของอะตอมในผลึกรอบ ๆ อะตอมไทเทเนียมของสารไทเทเนียมไดออกไซด์ (TiO_2) และไทเทเนียมไดซัลไฟด์ (TiS_2) ซึ่งสารตัวอย่างทั้งสองชนิดนี้มีสูตรทางเคมีที่คล้ายคลึงกัน แต่มีโครงสร้างผลึกแตกต่างกัน เราได้ทำการทดลองเพื่อวัดและเปรียบเทียบสเปกตรัมในย่าน x-ray absorption near edge structure (XANES) และ extended x-ray absorption fine structure (EXAFS) โดยใช้สเปกตรัมจากแผ่นไทเทเนียมบริสุทธิ์เป็นมาตรฐานในการวัด จากนั้นทำการวิเคราะห์ผลการทดลองโดยใช้โปรแกรม FEFF ซึ่งพบว่า ผลคำนวณตามทฤษฎีสอดคล้องกับข้อมูลโครงสร้างผลึกที่เคยมีการศึกษาไว้ นอกจากนี้ ยังพบว่า ผลการคำนวณความหนาแน่นสถานะย่อยของอิเล็กตรอนสอดคล้องเป็นอย่างดีกับสเปกตรัม XANES ที่ได้จากการวัด

PACS numbers: 61.10.Ht
Keywords: XANES, EXAFS, TiO_2, TiS_2, Ti-K edge

---

* ชื่อไทย: ดาริน อ่อนขาว Email: `darin@nsrc.or.th`

APSRS02

Suppression of Higher-Order Light from VLSPG Monochromator of BL4 beamline at SPL

Moragote Buddhakala*,[1] Ratchadaporn Supruangnet,[1] Somchai Chumpolkulwong,[1]
Hideki Nakajima[2] and Prayoon Songsiriritthigul[1,2]

1. *School of Physics, Institute of Science, Suranaree University of Technology, Nakhon Ratchasima 30000, Thailand*
2. *National Synchrotron Research Center, P.O. Box 93, Nakhon Ratchasima 30000, Thailand*

This report provides the results obtained from the evaluations of the varied line-spacing plane grating monochromator of the BL4 beamline at the Siam Photon Laboratory. The avaluations were performed by using photoionization measurement technique. The monochromator was design and constructed to meet the demand for the resolving power, $E/\Delta E$, of 5000 with sufficient photon flux for angle resolved photoemission experiments ($\sim 10^9$–10^{10} photons/s). Photoionization spectra taken from the $2,0_4$ resonance of doubly excited helium reveal a resolving power ~ 5000. However, photon flux at this high resolving power is very low and is lower than calculation. The effects of the width of the aperture located between the entrance slit and the focusing mirror, the alignment and position of the exit slit on the performance of the monochromator are discussed.

งานนี้ ได้นำเสนอผลของการหาค่าพารามิเตอร์ที่เหมาะสมเพื่อหาประสิทธิภาพของ โมโนโครเมเตอร์ ณ สถานีทดลอง BL4 ห้องปฏิบัติการแสงสยาม ซึ่งเป็นแบบ varied line-spacing plane grating monochromator โดยใช้เทคนิคการวัดสเปกตรัมที่ได้จากโฟโตไอออไนเซชัน โมโนโครเมเตอร์ที่ออกแบบมาในเบื้องต้นเพื่อให้ได้ค่ากำลังการแยกแยะเท่ากับ 5000 โดยมีค่าฟลักซ์ของโฟตอนสำหรับการทดลองที่เกี่ยวกับ Angle resolved photoemission ประมาณ $\sim 10^9$–10^{10} โฟตอน/วินาที และสเปกตรัมจากโฟโตไอออไนเซชัน ที่ได้จากการวัด ณ ตำแหน่งพีค $2,0_4$ ซึ่งเกิดจากรีโซแนนซ์ของ doubly excited ของอะตอมของก๊าซฮีเลียมโดยผลจากการแปรค่าพารามิเตอร์ต่าง ๆ เช่น ความกว้างของสลิต ณ ตำแหน่งขาเข้า หรือขาออกได้นำมาหาค่าประสิทธิภาพของโมโนโครเมเตอร์

---

* ชื่อไทย: มรกต พุทธกาล Email: `morak555@yahoo.com`

APSRS03

Progress on Electron Beam Profile Measurement at the Siam Photon Source

สถานะของระบบวัดลักษณะของลำอิเล็กตรอน ณ เครื่องกำเนิดแสงสยาม

Noppadon Deethae*[1], Supan Boonsuya[2], Samreang Duangnil[2], Pikul Prawatsri[2],
Pattanapong Janphuang[2] and Saroj Rujirawat[1,2]

1. *School of Physics, Institute of Science, Suranaree University of Technology, Nakhon Ratchasima 30000, Thailand*
2. *National Synchrotron Research Center, P.O. Box 93, Nakhon Ratchasima 30000, Thailand*

Beam profile is one of the important parameters used in the evaluation of the light source's performance. An electron beam profile measurement system is under construction at the Siam Photon Laboratory. The system is designed to work either in visible or x-ray regions. In the visible range, the electron beam profile would be obtained using projection lens and a CCD camera. The electron beam size will be obtained from light interferometers. In the x-ray range, a pin hole will be used to project x-ray image on a YAG crystal and the beam size will be deduced from the profile. The system will be installed at the beam port of bending magnet no. 2 and named "beam-line 2" for the moment. At present, we have constructed the beam-line chambers and mask using ultra high vacuum technology developed in the laboratory. The vacuum test is finished and the vacuum level as good as 1×10^{-10} Torr is achieved for the NSRC-made beam-line 2's chambers. The recent test results and near-future plan will be discussed in this report.

ขนาดของลำอิเล็กตรอนเป็นหนึ่งในข้อมูลเริ่มต้นที่สำคัญ ในการประเมินประสิทธิภาพของเครื่องกำเนิดแสงซินโครตรอน ระบบวัดลักษณะของลำอิเล็กตรอนที่อยู่ในระหว่างการสร้างโดยห้องปฏิบัติการแสงสยาม ได้ถูกออกแบบให้ใช้งานกับแสงซินโครตรอนทั้งในย่านแสงปกติและย่านรังสีเอ็กซ์ ในย่านแสงปกติ ภาพของลำอิเล็กตรอนจะถูกสร้างจากเลนส์ไปเกิดภาพบนกล้อง CCD ซึ่งขนาดของลำอิเล็กตรอนจะวัดได้โดยใช้มาตรแทรกสอดในย่านรังสีเอ็กซ์ กล้องรูเข็มจะสร้างภาพรังสีเอ็กซ์บนผลึก YAG และขนาดของลำอิเล็กตรอนจะถูกวัดจากภาพถ่ายรังสีเอ็กซ์ที่ได้ ระบบดังกล่าวนี้จะติดตั้งที่ช่องเปิดลำแสง ณ แม่เหล็กเลี้ยวเบนที่ 2 เรียกชื่อเป็น "แนวลำเลียงแสงที่ 2" ปัจจุบันเราได้สร้างห้องสุญญากาศสำหรับแนวลำเลียงแสงที่ 2 และฉากบังแสงโดยใช้เทคโนโลยีสุญญากาศระดับสูงมากที่ได้พัฒนาขึ้นในห้องปฏิบัติการแสงสยาม และหลังจากทำการทดสอบ ได้ระดับสุญญากาศอยู่ในระดับที่ดีกว่า 1×10^{-10} Torr ซึ่งในการนี้จะได้เสนอข้อมูล ผลทดสอบล่าสุด รวมทั้งแผนดำเนินการพัฒนาระบบในอนาคตอันใกล้

PACS numbers: 07.85.Qe
Keywords: SR Beam measurement, X-ray pinhole image monitor, SR-Interferometer

---

* ชื่อไทย: นพดล ดีแท้ Email: `zigma922@yahoo.com`

APSRS04

Study of Si(100) 2×1 Surface by Electron Diffraction and Photoemission Using Synchrotron Radiation

Ratchadaporn Supruangnet*

School of Physics, Institute of Science, Suranaree University of Technology,
Nakhon Ratchasima 30000, Thailand

A $c(4 \times 4)$ reconstruction can be formed on the clean Si(100) surface by special surface treatment techniques. We have studied the surface reconstruction of this metastable phase, which is prepared by thermal annealing, using low energy electron diffraction (LEED) and Auger electron spectroscopy (AES). The surface structure transition between (2×1) and $c(4 \times 4)$ reconstruction has been observed at annealing temperature range of 450–575 °C.

ในการเกิดการจัดเรียงตัวใหม่บนพื้นผิวของซิลิกอนระนาบ (100) รูปแบบ $c(4 \times 4)$ นั้น สามารถจะทำการเตรียมได้โดยอาศัยเทคนิคทางพื้นผิว เราได้ทำการศึกษาการเกิดการจัดเรียงตัวใหม่ของรูปแบบนี้ซึ่งทำการเตรียมโดยวิธี แอนนีล และวิเคราะห์ผลการทดลองโดย ลีด และออเจร์ อิเล็กตรอน ดิฟแฟรกชั่นได้ทำการสังเกตการเปลี่ยนโครงสร้างพื้นผิวระหว่างรูปแบบ (2×1) และ $c(4 \times 4)$ ที่อุณหภูมิอยู่ในช่วง 450–575 องศาเซลเซียส

Keywords: Reconstruction, LEED

---

* ชื่อไทย: รัชฎาภรณ์ ทรัพย์เรืองเนตร   Email: aufeekku@hotmail.com

CMMP01

First Principles Study of Mn Impurity Location of $PbTiO_3$

การศึกษาตำแหน่งของสารเจือ Mn ในสาร $PbTiO_3$

Adisak Boonchun,*[1,2] Michael Francis Smith,[2] Benya Cherdhirunkorn,[3] and
Sukit Limpijumnong[1,2]

1. *School of Physics, Institute of Science, Suranaree University of Technology, Nakhon Ratchasima 30000, Thailand*
2. *National Synchrotron Research Center, P.O. Box 93, Nakhon Ratchasima 30000, Thailand*
3. *Faculty of Science and Technology, Thammasat University, Bangkok, Thailand*

A first principles simulation of Mn dopants in $PbTiO_3$ has been done to determine the location, charge state, and electronic structure of the Mn impurity. We find that it is energetically favorable for the Mn ion to substitute for Ti (as opposed to substituting for Pb, O or interstitial positions) under all thermal equilibrium crystal growth conditions. The charge of the Mn impurity is determined to be neutral when the Fermi level is near the middle of the bandgap.

งานวิจัยนี้เน้นศึกษาตำแหน่ง, ประจุ และโครงสร้างทางอิเล็กทรอนิกของสารเจือแมงกานิสในสารประกอบ $PbTiO_3$ โดยใช้วิธีคำนวนแบบเฟิร์สพรินซิเพิล ผลของการคำนวนอธิบายได้ว่า สารเจือ Mn มีโอกาสแทนที่ในตำแหน่งอะตอม Ti (มากกว่าตำแหน่งอะตอม Pb, ตำแหน่งอะตอม O หรือแทรกในที่ตำแหน่งที่ว่าง) ทุกสถานะการปลูกผลึกที่เป็นไปได้ ที่ระดับเฟอร์มี บริเวณกึ่งกลางช่องว่างระดับพลังงานประจุของสารเจือ Mn เป็นศูนย์

PACS numbers: 31.15.Ar, 61.72.Bb, 61.72.Ww
Keywords: First Principles calculation, crystal defects, electronic structure

CMMP05

Wurtzite to Graphite-like Phase Transformation in ZnO: First Principle Calculations

การเปลี่ยนโครงสร้างของซิงค์ออกไซค์จากโครงสร้างแบบเวิร์ทไซท์ไปเป็นโครงสร้างที่คล้ายแกรไฟท์: การศึกษาแบบเฟิร์สปรินซิเปิล

Kanoknan Sarasamak*[1] and Sukit Limpijumnong[1,2]

1. *School of Physics, Institute of Science, Suranaree University of Technology,*
   Nakhon Ratchasima 30000, Thailand
2. *National Synchrotron Research Center, P.O. Box 93,*
   Nakhon Ratchasima 30000, Thailand

The transformatiom of ZnO from the wurtzite structure to the ZnO structure with a graphite-like structure is studied using a first principle calculations. The calculations show that this structure is the results of a phase transformation this structure is the results of a phase transformation from from the wurtzite structure under uniaxial tensile loading of $[01\bar{1}0]$. The calculated transformation barrier between 2 structures is shown by the enthalpy surface and the transformation has a low enthalpy barrier of ~ 0.06 eV.

การคำนวณแบบเฟิร์สปรินซิเปิลถูกใช้เพื่อศึกษาการเปลี่ยนโครงสร้างของซิงค์ออกไซค์จากโครงสร้างแบบเวิร์ทไซท์ไปเป็นโครงสร้างที่คล้ายแกรไฟท์ ในการศึกษาพบว่า การเปลี่ยนโครงสร้างลักษณะนี้เป็นผลจากแรงดึงในทิศทางเดียวคือ ในทิศทาง $[01\bar{1}0]$ แบริเออร์ของการเปลี่ยนโครงสร้างระหว่าง 2 โครงสร้าง ถูกแสดงโดยการพล็อตพื้นผิวเอนทัลปี และเอนทัลปีแบริเออร์ของการเปลี่ยนโครงสร้างมีค่าต่ำประมาณ 0.06 อิเล็กตรอนโวลต์

PACS numbers: 61.50.Ks

Keywords: First-principles, phase transformation, ZnO, wurtzite

---

* ชื่อไทย: กนกนันทน์ สารสมัคร Email: `kanoknans@hotmail.com`

CMMP06

Effect of Sintering Behavior on Piezoelectric Properties of PZT and PZT doped with Pr_6O_{11}

ผลของการซินเทอร์ต่อสมบัติเพียโซอิเล็กทริกของ PZT และ PZT ที่โดพด้วย Pr_6O_{11}

Krit Koyvanich*and Supreya Trivijitkasem

Department of Physics, Faculty of Science, Kasetsart University,
Bangkok 10900, Thailand

Effect of sintering behavior on physical and piezoelectric properties of two different types of lead zirconate titanate (PZT) ceramics was investigated. Pure PZT and doped PZT with praseodymium oxide 3 mol% (PPZT) were sintered at 1200, 1250 and 1300 °C for 1 h. It was observed that the electrical properties of each system were largely controlled by sintering temperature; the relative permittivity (ε_r) and dissipation factor ($\tan\delta$) of PPZT were improved significantly by increasing sintering temperature. A resonance and anti-resonance indentation technique was employed to determine the coupling factor (k) of the ceramics. It was found that plannar coupling factor (k_p) and piezoelectric coefficient (d_{33}) of PZT were improved with Pr_6O_{11} additive. The k_p and d_{33} of PPZT were between 57.8 61.5% and 470 504 pF, respectively.

การศึกษาผลของอุณหภูมิซินเทอร์ที่อุณหภูมิ 1200, 1250 และ 1300 °C เป็นเวลา 1 ชั่วโมง ต่อสมบัติทางกายภาพและสมบัติเพียโซอิเล็กทริกของเซรามิกเลดเซอร์โคเนตไตตาเนต (PZT) และ PZT ที่โดพด้วยพลาซิโอดิเมียมออกไซด์ (Pr_6O_{11}) 3 mol% (PPZT) พบว่าสมบัติทางไฟฟ้าของเซรามิกแต่ละระบบขึ้นอยู่กับอุณหภูมิซินเทอร์ สภาพยอมสัมพัทธ์ (ε_r) และค่าสูญเสียไดอิเล็กทริกของ PPZT ดีขึ้นตามอุณหภูมิซินเทอร์ที่เพิ่มขึ้น เมื่อใช้เทคนิคเรโซแนนซ์และแอนติเรโซแนนซ์หาค่าคัพปลิงแฟกเตอร์ของเซรามิก พบว่าค่าคัพปลิงแฟกเตอร์ตามแนวระนาบ (k_p) และ ค่าสัมประสิทธิ์เพียโซอิเล็กทริก (d_{33}) ของ PPZT มีค่ามากกว่าของ PZT โดยค่า k_p และ d_{33} ของ PPZT อยู่ในช่วง 57.8–61.5% และ 470–504 pF ตามลำดับ

PACS numbers: 76.30.Kg, 77.65.-j, 77.65.Bn, 77.80.Dj, 77.22-d, 77.22Ch

Keywords: Piezoelectric, PZT, Pr_6O_{11}, Sintering Temperature

---

* ชื่อไทย: กฤช โกยวาณิชย์ Email: `krit_com@hotmail.com`

CMMP07

Thermal Properties of Degradable High Density Polyethylene Plastic Film

สมบัติทางความร้อนของแผ่นฟิล์มพลาสติกพอลิเอทิลีนความหนาแน่นสูงที่เจือสารย่อยสลาย

Nattha Thaweegan*and Supreya Trivijitkasem

Department of Physics, Faculty of Science, Kasetsart University,
Bangkok 10900, Thailand

Thermal properties and degradability of high density polyethylene (HDPE) blended with $CaCO_3$ were studied by Differential Scanning Calorimetry (DSC). Four different heating and cooling rates 5, 10, 15 and 20 °C/min under nitrogen environment were performed. In endothermic process, the phase transition peak shifted to lower temperature with the heating rate ascending. In exothermic process, the results showed similar evolution of crystallinity temperature and the corresponding enthalpy as the endothermic process. The nonisothermal crystallization kinetics were investigated by Ozawa method derived from Avrami analysis. The addition of $CaCO_3$ increased Ozawa exponents m, but decreased logarithm of crystallization rate constant $\ln Z(T)$ of pure HDPE-film. Crystallization activation energy of pure HDPE film calculated from Kissinger equation was increased as the higher content of $CaCO_3$.

การศึกษาสมบัติทางความร้อน ของพอลิเอทิลีนความหนาแน่นสูงที่เจือ $CaCO_3$ ในปริมาณที่แตกต่างกัน ด้วยเครื่องแคลอรีเมตรีแบบส่องกราดอนุพันธ์ โดยอัตราการเพิ่ม และลดอุณหภูมิคงตัว 4 อัตราคือ 5, 10, 15, และ 20 °C/min ภายใต้ก๊าซไนโตรเจนพบว่า ในกระบวนการดูดกลืนความร้อน เมื่ออัตราการเพิ่มอุณหภูมิมากขึ้น อุณหภูมิหลอมเหลวจะเลื่อนไปทางอุณหภูมิที่ต่ำกว่า และในกระบวนการคายความร้อน เมื่ออัตราการลดอุณหภูมิมากขึ้นอุณหภูมิการเกิดผลึก จะเลื่อนไปทางอุณหภูมิที่ต่ำกว่าและมีค่าเอนทัลปีมากขึ้น ซึ่งมีลักษณะคล้ายคลึงกับกระบวนการดูดกลืนความร้อน ค่าพารามิเตอร์จลน์ของกระบวนการตกผลึกที่คำนวณโดยวิธี Ozawa ซึ่งประยุกต์มาจากทฤษฎี Avrami พบว่าเมื่อปริมาณ $CaCO_3$ เพิ่มขึ้น ค่าเอกซ์โพเนนต์ Ozawa มีค่าเพิ่มขึ้น แต่ลอการิทึมของค่าคงตัวอัตราการตกผลึก $\ln Z(T)$ มีค่าลดลง พลังงานก่อกัมมันต์ของแผ่นฟิล์ม HDPE ที่คำนวณจากทฤษฎี Kissinger มีค่าเพิ่มขึ้นตามปริมาณ $CaCO_3$ ที่เพิ่มขึ้น

PACS numbers: 65.40.De, 42.70.Jv, 65.60.+a
Keywords: Thermal properties, HDPE

---

* ชื่อไทย: ณัฐฐา ทวีกันต์ Email: `kong6262@hotmail.com`

CMMP08

A Nitrogen-Carbon Molecule in GaAs: A First Principles Study

โมเลกุล ไนโตรเจน-คาร์บอนในแกเลี่ยมอาร์เซไนด์: การศึกษาแบบเฟิสต์พรินซิเพิล

Sukit Limpijumnong[1,2] and Pakpoom Reuanchan*[1]

1. *School of Physics, Institute of Science, Suranaree University of Technology, Nakhon Ratchasima 30000, Thailand*
2. *National Synchrotron Research Center, P.O. Box 93, Nakhon Ratchasima 30000, Thailand*

First-principles calculation shows that NC molecule prefers to occupy the anion (As or P) site over the interstitial site in GaAs. Both CN molecules occupying the anion site and the interstitial site maintain their molecular characteristics rather well. The C–N bond distances and vibration frequencies are comparable to those of a free molecule. The calculated vibration frequencies of the CN molecules occupying the anion sites in GaAs are in a good agreement (within a computational error bar) with the recent infrared spectroscopy measurement [W. Ulrici and B. Clerjaud, Phys. Rev. B **72**, 045203 (2005).].

การศึกษาแบบเฟิสต์-พรินซิเพิล แสดงให้เห็นว่าโมเลกุลไนโตรเจน-คาร์บอนมักจะไปอยู่แทนที่ตำแหน่งของแอนไอออน มากกว่าตำแหน่งของช่องว่างในผลึกแกลเลียมอาร์เซไนด์ ในทั้งสองตำแหน่งโมเลกุลไนโตรเจน-คาร์บอนยังคงรักษาคุณสมบัติของโมเลกุลไว้ ความยาวพันธะและความถี่ของการสั่นยังอยู่ในช่วงที่เปรียบเทียบกับโมเลกุลอิสระได้ ความถี่ในการสั่นที่คำนวณได้ของโมเลกกุลไนโตรเจน-คาร์บอนที่ไปแทนที่ตำแหน่งแอนไอออนในผลึกแกเลี่ยมอาร์เซไนด์สอดคล้องกับผลการทดลองการวัดอินฟาเรด-สเปคโตรสโคปีเมื่อเร็วๆนี้ [W. Ulrici and B. Clerjaud, Phys. Rev. B **72**, 045203 (2005).]

PACS numbers: 61.72.Ji, 78.30.Fs, 63.20.Pw
Keywords: first-principles, complexes, local vibration modes

---

* ชื่อไทย: ภาคภูมิ เรือนจันทร์ Email: sendtoyo2004@yahoo.com

CMMP10

Effect of the Geometry of Metal–Insulator–Superconductor Junction on Its Tunneling Spectroscopy

รูปทรงของรอยต่อของ โลหะ–ฉนวน–ตัวนำยวดยิ่ง ที่มีผลกระทบต่อการทะลุผ่านในรอยต่อ

Rarm Phinjaroenphan*

School of Physics, Institute of Science, Suranaree University of Technology,
Nakhon Ratchasima 30000, Thailand

The width of each layer of a metal–insulator–superconductor junction gives rise to features in the conductance spectrum of the junction. Tomasch oscillations in the conductance spectrum are due to the finite superconducting layer in the junction. The period of oscillations depends on the superconducting gap, the Fermi velocity and the thickness of the superconductor. The finite layer of metal causes another type of oscillations called McMillan–Rowell oscillations. Similarly, the period of the oscillations depends on the Fermi velocity and the thickness of the metal.

ความกว้างในแต่ละชั้นของรอยต่อ โลหะ–ฉนวน–ตัวนำยวดยิ่ง ให้ลักษณะเฉพาะของเส้นสเปคตรัมของสภาพการนำไฟฟ้าของรอยต่อ และการที่ชั้นของตัวนำยวดยิ่งมีค่าไม่เป็นอนันต์ มีผลทำให้เส้นสเปคตรัมมีการเปลี่ยนแปลงขึ้นลง ซึ่งเรียกการว่า การสั่นของ Tomasch oscillations โดยระยะระหว่างจุดต่ำสุด 2 จุดที่อยู่ถัดกันมีค่าขึ้นกับ ค่าช่องว่างพลังงานของตัวนำยวดยิ่ง ความเร็วเฟอร์มี และค่าความหนาของชั้นตัวนำยวดยิ่ง การที่ชั้นของโลหะมีค่าไม่เป็นอนันต์ จะทำให้เส้นสเปคตรัมของสภาพการนำไฟฟ้ามีการเปลี่ยนแปลงขึ้นลงเรียกว่า McMillan–Rowell oscillations โดยระยะระหว่างจุดต่ำสุด 2 จุดที่อยู่ถัดกัน มีค่าขึ้นกับ ความเร็วเฟอร์มี และ ความหนาของชั้นโลหะ

PACS numbers: 74.20.-z, 74.25.Fy
Keywords: metal-insulator-superconductor junction, the conductance spectrum, Tomasch oscillations, McMillan–Rowell oscillations

---

[*] ชื่อไทย: รามย์ พิณเจริญพันธุ์ Email: `rarm_m@hotmail.com`

CMMP11

First Principles Study of Native Defects in Anatase TiO_2

การศึกษาความบกพร่องของอนาเทส-ไทเทเนียมไดออกไซด์ โดยการศึกษาเฟิร์สพรินซิเพิล

Sutassana Na Phattalung*[1] Michael Francis Smith[2] Kwiseon Kim[3] Mao-Hua Du[3]
Su-Huai Wei[3] Shengbai Zhang[3] and Sukit Limpijumnong[1,2]

1. *School of Physics, Institute of Science, Suranaree University of Technology,*
   Nakhon Ratchasima 30000, Thailand
2. *National Synchrotron Research Center, P.O. Box 93,*
   Nakhon Ratchasima 30000, Thailand
3. *National Renewable Energy Laboratory, Golden, Colorado, USA*

Native point defects in anatase TiO_2 are investigated using first-principles pseudopotential calculations based on density-functional theory. We found that antisite defects, namely Ti-antisite (Ti_O) and O-antisite (O_{Ti}), have high formation energy and are not stable. Titanium interstitial (Ti_i) is a quadruple donor defect with the lowest formation energy under p-type conditions. On the other hand, Ti vacancy (V_{Ti}) is a quadruple acceptor defect with the lowest formation energy under n-type conditions. Oxygen interstitial (O_i) spontaneously moves to bond strongly with a lattice O, leading to a neutral O_2 dimer substituting on an O site. Interestingly, our calculations show that all four fundamental native defects (Ti_i, O_i, V_{Ti}, and V_O) do not introduce any defect level inside the band gap.

การศึกษาความบกพร่องของผลึกอนาเทส-ไทเทเนียมไดออกไซด์ โดยการคำนวณเฟิร์สซิเพิลซึ่งอาศัยทฤษฎีเดนซิตีฟังก์ชันนัล พบว่าแอนไทไซท์ซึ่งประกอบด้วย ไทเทเนียม-แอนไทไซด์ (Ti_O) และ ออกซิเจน-แอนไทไซด์ (O_{Ti}) มีค่าพลังงานการเกิดสูง และไม่เสถียร ส่วนความบกพร่องที่เกิดจากการมีอะตอมไทเทเนียมเกินมาในช่องว่างผลึก(Ti_i) จะแสดงคุณสมบัติเป็นควอดดรูเพิลดอเนอร์ ด้วยค่าพลังงานการเกิดต่ำที่สุดภายใต้เงื่อนไขพี-ไทป์ ส่วนความบกพร่องที่เกิดจากการขาดอะตอมไทเทเนียม (V_{Ti}) จะแสดงคุณสมบัติเป็นควอดดรูเพิลแอคเซบเตอร์ ด้วยค่าพลังงานการเกิดต่ำที่สุดภายใต้เงื่อนไขเอ็น-ไทป์ ความบกพร่องที่เกิดจากการมีอะตอมออกซิเจนเกินมาในช่องว่างผลึก (O_i) จะเคลื่อนที่ไปสร้างพันธะกับออกซิเจนหนึ่งอะตอมในผลึกเกิดเป็นออกซิเจนไดเมอร์แทนที่อะตอมออกซิเจนในแลตทิซนั้นด้วยประจุศูนย์ได้เองโดยธรรมชาติ น่าสนใจเป็นอย่างยิ่งว่าไม่มีความบกพร่องของผลึกชนิดใดเลยที่สร้างชั้นพลังงานที่เกิดจากความบกพร่องของผลึกหรือดิเฟกท์เลเวล ในแถบช่องว่างของพลังงาน

PACS numbers: 71.15.Mb, 73.20.Hb, 71.20.-b
Keywords: native defects, anatase, TiO_2

---

* ชื่อไทย: สุทัศนา ณ พัทลุง Email: `sutphysics@hotmail.com`

CHEP03

$\bar{\mathrm{p}}$D Atom in Paris Potential

อะตอมของปฏิโปรตอน–ดิวเทอรอนในศักย์ปารีส

Chakrit Nualchimplee*, Yupeng Yan, Prasart Suebka and Chinorat Kobdaj

School of Physics, Institute of Science, Suranaree University of Technology,
Nakhon Ratchasima 30000, Thailand

The $\bar{\mathrm{p}}$D atomic state problem is studied in the latest version of the Paris $\overline{\mathrm{N}}$N potential. The small energy shifts and decay widths resulting from the short range strong interaction of the $\bar{\mathrm{p}}$D atomic state are accurately derived by solving the dynamical equation of the system in a suitable numerical approach based on the Sturmian function, which is able to account for both short range nuclear potential (for both the local and nonlocal) and the long range Coulomb force and to provide directry the wave function of the $\bar{\mathrm{p}}$D atoms with complex eigenvalue $E = E_{\mathrm{R}} + \mathrm{i}(\Gamma/2)$.

เราศึกษาปัญหาของอะตอมของปฏิโปรตอน–ดิวเทอรอนในศักย์ปารีส ซึ่งเป็นศักย์แบบปฏินิวคลีออน–นิวคลีออนล่าสุด พร้อมทั้งคำนวณเส้นสเปกตรัมของพลังงานที่เลื่อนออกจากเส้นสเปกตรัมของอะตอมดิวเทอรอนปกติ และคำนวณความกว้างของเส้นสเปกตรัมดังกล่าวนั้นซึ่งเป็นผลมาจากแรงนิวเคลียร์แบบเข้มซึ่งเกิดจากอันตรกิริยาระหว่างอะตอมของปฏิโปรตอน–ดิวเทอรอนโดยใช้วิธีการเชิงตัวเลขซึ่งมีพื้นฐานมาจากฟังก์ชันของสเตอเมียน ซึ่งเป็นวิธีการที่สามารถใช้แก้ปัญหาได้ทั้งในกรณีศักย์ที่เกิดจากแรงนิวเคลียร์ซึ่งเป็นแรงพิสัยใกล้ (สำหรับทั้งในกรณีที่ศักย์ขึ้นกับตำแหน่งและในกรณีที่ศักย์ไม่ขึ้นกับตำแหน่ง) และในกรณีศักย์ที่เกิดจากแรงคูลอมบ์ซึ่งเป็นแรงพิสัยไกล และได้คำนวณฟังก์ชันคลื่นของอะตอมของปฏิโปรตอน–ดิวเทอรอน ซึ่งพบว่าค่าไอเกนของพลังงานของระบบที่ได้เป็นค่าเชิงซ้อนโดยมีค่าเป็น $E = E_{\mathrm{R}} + \mathrm{i}(\Gamma/2)$

PACS numbers: 13.75.Cs, 02.60.-x
Keywords: Antiproton–deuteron atom, Sturmian function

---

[*] ชื่อไทย: ชาคริต นวลฉิมพลี Email: `nchakrit@hotmail.com`

CHEP05

Calculation of ρ^0 Decay in Two-Step Process of $e^+e^- \rightarrow \pi^+\pi^-$

การคำนวณการสลายตัวของ ρ^0 ในกระบวนการสองขั้นของ $e^+e^- \rightarrow \pi^+\pi^-$

Kritsada Kittimanapun*and Yupeng Yan

School of Physics, Institute of Science, Suranaree University of Technology,
Nakhon Ratchasima 30000, Thailand

It is found that the reactions of electron–position to hadron–antihadron pair is dominated by the multi-step process, in which the electron–position pair annihilates into a virtual photon, then the virtual photon decays into a quark–antiquark pair, then the primary quark–antiquark pair forms a vector meson, and finally the vector meson decays into a hadron pair. We would show, in this work, the evaluation of the reaction of ρ^0 to $\pi^+\pi^-$ in the 3P0 quark model which has been proved the most successful non-relativistic quark model. The work forms one part of the further study of the reactions electron–position to hadron–antihadron.

ในปฏิกิริยาการชนกันของโพสิตรอนและอิเล็กตรอนและให้กำเนิดคู่ฮาดรอนและปฏิฮาดรอนนั้น พบว่ามีกระบวนการที่มีหลายขั้นตอนเกิดขึ้น โดยเริ่มจากการชนกันของอิเล็กตรอนและโพสิตรอนให้กำเนิดโฟตอนเสมือน ต่อจากนั้นโฟตอนเสมือนสลายไปเป็นคู่ของควาร์กและปฏิควาร์ก หลังจากนั้นคู่ของควาร์กและปฏิควาร์กสร้างอนุภาคที่เรียกว่า เวกเตอร์เมซอน และในขั้นตอนสุดท้าย เวกเตอร์เมซอนสลายตัวไปเป็นคู่ฮาดรอน ในงานชิ้นนี้ได้แสดงให้เห็นกระบวนการการเปลี่ยนแปลงของ ρ^0 ไปเป็น $\pi^+\pi^-$ ในแบบจำลองควาร์ก 3P0 ที่ซึ่งประสบผลสำเร็จมากที่สุดในบรรดาแบบจำลองควาร์ก และผลงานชิ้นนี้เป็นส่วนหนึ่งในการศึกษาปฏิกิริยาของโพสิตรอนและอิเล็กตรอนที่ซึ่งเปลี่ยนแปลงเป็นคู่ฮาดรอนและปฏิฮาดรอน

PACS numbers: 13.66.Bc
Keywords: e^+e^- annihilation

---

* ชื่อไทย: กฤษดา กิตติมานะพันธ์ Email: `oou_kritsada@hotmail.com`

CHEP06

Particles Correlations in Quantum Field Theory

สหสัมพันธ์ของอนุภาคในทฤษฎีสนามควอนตัม

Nattapong Yongram*

School of Physics, Institute of Science, Suranaree University of Technology,
Nakhon Ratchasima 30000, Thailand

Explicit computations are carried out of polarization correlations of simultaneous measurements of spin of two particles produced in fundamental processes directly from quantum field theory. The expression of these polarization correlations, following from these dynamical computations are non-speculation involving no arbitrary input assumptions, are seen to depend on speed. It is remarkable that these expressions for the polarization correlations show clear violation of Bell's test.

ได้แสดงการหาสมการสำหรับคำนวณค่าสหสัมพันธ์โพลาไรเซชันของสปินของอนุภาค 2 ตัว ที่วัดได้พร้อมกันและเกิดขึ้นในกระบวนการต่าง ๆ ที่อธิบายได้ในทฤษฎีสนามควอนตัม สมการของสหสัมพันธ์โพลาไรเซชันเหล่านี้ได้มาจากการคำนวณเชิงพลวัตโดยไม่มีการคาดการณ์และไม่มีการใช้สมมุติฐาน พบว่าสมการที่ได้ขึ้นอยู่กับอัตราเร็ว สมการสหสัมพันธ์โพลาไรเซชันที่ได้ แสดงให้เห็นความขัดแย้งอย่างชัดเจนเมื่อทดสอบตามวิธีการทดสอบของเบลล์

PACS numbers: 12.20.Ds, 12.20.Fv, 03.65.Ud
Keywords: Specific calculations, Experimental tests, Entanglement and quantum nonlocality (e.g. EPR paradox, Bell's inequalities, GHZ states, etc.)

---

* ชื่อไทย: นัฏพงษ์ ยงรัมย์ Email: `nyongram@gmail.com`

CHEP08

Closed-Time Path in Quantum Field Theory

วิถีปิดของเวลาในทฤษฎีสนามควอนตัม

Seckson Sukkhasena*

School of Physics, Institute of Science, Suranaree University of Technology,
Nakhon Ratchasima 30000, Thailand

The quantum dynamical principle pioneered by Schwinger has proved to be a most valuable tool in describing the dynamics of elementary particles and in carrying out endless computations in high-energy physics. The quantum dynamical principle allows one to obtain directly the vacuum-to-vacuum transition amplitude, e.g., in positive sense of time, in field theory or the transformation function in quantum physics. I will show some calculation of the closed-time path in the quantum field theory by using the Schwinger dynamical principle in describing the dynamics of spin-0 charged and uncharged particles.

หลักพลวัตควอนตัมซึ่งเสนอโดยชวิงเงอร์ได้พิสูจน์ว่าเป็นเครื่องมือหนึ่งที่มีประโยชน์มาก สำหรับใช้ในการบรรยายพลศาสตร์ของอนุภาคมูลฐาน รวมถึงการคำนวณทางฟิสิกส์ที่พลังงานสูงด้วย นอกจากนั้นหลักพลวัตควอนตัมยังอนุญาตให้สามารถคำนวณค่าของแอมพลิจูดการเปลี่ยนสถานะสุญญากาศไปสุญญากาศได้โดยตรง ซึ่งวิถีของเวลาเป็นไปในทางบวก ในทฤษฎีสนามหรือการแปลงสถานะของฟังก์ชั่นในฟิสิกส์ควอนตัม โดยในการบรรยายนี้จะมีการนำเสนอตัวอย่างการคำนวณของวิถีปิดของเวลาในทฤษฎีสนามควอนตัม โดยการใช้หลักพลวัตของชวิงเงอร์ในการบรรยายพลศาสตร์ของอนุภาคที่มีสปินศูนย์ ที่มีประจุและไม่มีประจุ

PACS numbers: 11.10.-z, 02.30.Sa, 03.50.-z, 03.65.-w
Keywords: Quantum Dynamical Principle, closed-time path, spin-0 charged and uncharged particles

---

[*] ชื่อไทย: เสกสรร สุขะเสนา Email: `seckson@hotmail.com`

EFP01

Conceptual Surveying on Mechanical Wave

การสำรวจความเข้าใจของนักเรียนในวิชาฟิสิกส์เรื่อง คลื่นกล

Apisit Tongchai*, Kwan Arayathanitkul, Chernchok Soankwan, Narumon Emarat
and Ratchapak Chitaree

*Department of Physics, Faculty of Science, Mahidol University,
Bangkok 10400, Thailand*

This study is about surveying students' concepts on mechanical wave by using Wave Diagnostic Test (WDT). The test was developed by Micheal C. Wittmann at University of Maryland. It is composed of ten items separated into two parts. The first part is eight free response questions (FR). The second consists of two-multiple choice multiple response questions. These two questions are the same as the first test to ask students for the second time in multiple-choice, multiple-response (MCMR) format. There are two main concepts within the test, propagation and superposition of waves. The sample is Thai physics education students and high school students. From the results of the study, we found that most students have misconceptions in wave concepts for example wave propagation, speed of waves and superposition of waves. When we compared our results with the results from Wittmann, we found that both results are almost identical.

งานวิจัยนี้เป็นการสำรวจความเข้าใจของนักเรียนในเรื่องคลื่นกล โดยใช้แบบทดสอบความเข้าใจเรื่องคลื่น (Wave diagnostic test: WDT) ที่พัฒนาโดย Micheal C. Wittmann ที่ University of Maryland แบบทดสอบประกอบด้วยคำถามจำนวนสิบข้อ โดยแบ่งออกเป็นสองตอน ตอนแรกเป็นคำถามปลายเปิด (Free response version: FR) จำนวนแปดข้อ ตอนที่สองเป็นคำถามแบบตัวเลือก (Multiple choice, Multiple response format: MCMR) จำนวนสองข้อที่เหมือนกันกับตอนแรกซึ่งนักเรียนต้องทำในตอนที่สอง แบบทดสอบนี้วัดความเข้าใจในเรื่องคลื่นอยู่สองหัวข้อหลักคือ การแพร่กระจายของคลื่นและการซ้อนทับของคลื่น กลุ่มวิจัยเป็นนักศึกษาระดับบัณฑิตศึกษาสาขาฟิสิกส์ศึกษา และนักเรียนระดับมัธยมศึกษาตอนปลาย ผลการสำรวจพบว่า นักเรียนมีความเข้าใจที่คลาดเคลื่อนในหลักการของคลื่นอยู่มาก เช่น การแพร่กระจายของคลื่น อัตราเร็วคลื่น และการซ้อนทับของคลื่น ผู้วิจัยได้เปรียบผลการสำรวจกับผลการวิจัยของ Wittmann พบว่าผลการสำรวจแทบไม่แตกต่างกัน

Keywords: Mechanical Wave, Wave propagation, Wave Superposition

---

* ชื่อไทย: อภิสิทธิ์ ธงไชย Email: `G4737167@student.mahidol.ac.th`

EFP03

Investigation of Students' Misconception in Direct Current

การศึกษาความเข้าใจที่คลาดเคลื่อนของนักเรียนในเรื่อง ไฟฟ้ากระแสตรง

Supasilp Fuengfung*[1] Kwan Arayathanitkul[2] and Chernchok Soankwan[2]

1. *Institute for Innovation and Development of Learning Process, Mahidol University, Bangkok 10400, Thailand*
2. *Department of Physics, Faculty of Science, Mahidol University, Bangkok 10400, Thailand*

In this research, we will present the results of the study of misconception of direct current by using the Electric Circuits Concept Evaluation (ECCE) with the first year student of Rajamankala Universty of Technology Bangkok. The ECCE standardized test, developed by Ron Thornton and David Sokoloff at Oregon University was used to test students' understanding in the concept of direct current. The translated version of the ECCE was used with Thai first year civil engineering and industrial education students at Rajamankala University of Technology Bangkok.

The standardized test was used before and after the traditional teaching on the topic of direct current. The results show that many students have misconception in fundamental topics such as brightness of bulbs in parallel circuit, potential difference across the bulb in series circuit, and current through bulbs in complex circuit.

The analyzed results from the test show poor student performance. This indicates the need for new teaching method in the topic of currents to make student gain better understanding in the topics of the direct current.

งานวิจัยนี้เป็นการศึกษาเกี่ยวกับความเข้าใจที่คลาดเคลื่อนของนักศึกษาในเรื่องไฟฟ้ากระแสตรง โดยการใช้แบบทดสอบการวัดความเข้าใจเรื่องวงจรไฟฟ้า The Electric Circuits Concept Evaluation (ECCE) ซึ่งเป็นแบบทดสอบที่พัฒนาโดย Ron Thornton และ David Sokoloff ที่มหาวิทยาลัยโอเรกอน กับนักศึกษาวิศวกรรมโยธา และ คุรุศาสตร์อุตสาหกรรม ชั้นปีที่ 1 ที่มหาวิทยาลัยเทคโนโลยีราชมงคลกรุงเทพ

โดยแบบทดสอบจะใช้ก่อนและหลังการเรียนในเรื่องไฟฟ้ากระแสตรง ซึ่งผลปรากฏว่านักศึกษามีความไม่เข้าใจที่คลาดเคลื่อนเกี่ยวกับพื้นฐานของไฟฟ้ากระแสตรง เช่น ความสว่างของหลอดไฟเมื่อต่อหลอดไฟแบบขนาน ความต่างศักย์ที่คร่อมหลอดไฟฟ้าเมื่อต่อหลอดไฟแบบอนุกรม และ ขนาดของกระแสไฟฟ้าที่ไหลผ่านหลอดไฟในวงจรไฟฟ้าแบบผสม

จากผลการวิเคราะห์แสดงให้เห็นว่านักศึกษามีความเข้าใจที่คลาดเคลื่อนในหลายเรื่องของไฟฟ้ากระแสตรง ดังนั้นจากการวิจัยแสดงให้เห็นว่า ควรจะมีวิธีทางด้านการเรียนการสอนแบบใหม่ที่ช่วยให้นักศึกษามีความเข้าใจที่ถูกต้องในเรื่องไฟฟ้ากระแสตรงให้มากขึ้น

---

* ชื่อไทย: ศุภศิลป์ เฟื่องฟุ้ง Email: `supasilpp@hotmail.com`

EFP04

The Use of Interactive Lecture Demonstrations in Force and Motion to Teach High School-Level Physics

การใช้รูปแบบการสอนสาธิตเชิงปฏิสัมพันธ์ในเรื่องแรงและการเคลื่อนที่สำหรับชั้นมัธยมศึกษาตอนปลาย

Kwan Arayathanitkul[1], Chernchok Soankwan[1], Narumon Emarat[1] and
Umpol Jairuk*[2]

1. *Department of Physics, Faculty of Science, Mahidol University, Bangkok 10400, Thailand*
2. *Institute for Innovation and Development of Learning Process, Mahidol University, Bangkok 10400, Thailand*

This paper presents the results of an experiment using interactive lecture demonstrations (ILDs) in force and motion to teach high-school students. The microcomputer-base ILDs were employed with 152 students at Wutsutti High School, Bangkok, in the second semester of academic year 2005. The ILDs, developed by Thornton and Sokoloff consist of a sequence of simple physics experiments on various types of motion. To evaluate this teaching-learning method, the Force and Motion Conceptual Evaluation (FMCE) test, translated into Thai language, was given to the students once before the beginning of the course and once after finishing the ILDs.

After using the ILDs it was found that, in overall, there was a 0.3 normalized gain in student's performance. There were very high gains in acceleration and Newton's third law of motion. These results suggest that ILDs can indeed help develop high-school students' conceptual understanding in force and motion.

งานวิจัยนี้เป็นการแสดงผลการใช้วิธีการสอนแบบบรรยายประกอบการสาธิตเชิงปฏิสัมพันธ์ (ILDs) ในเรื่องแรงและการเคลื่อนที่ของนักเรียนระดับมัธยมศึกษาตอนปลาย โดยการนำเอาคอมพิวเตอร์มาช่วยในการแสดงผลประกอบการสาธิต กลุ่มตัวอย่างในการศึกษาเป็นนักเรียนโรงเรียนวัดสุทธิวราราม กรุงเทพฯ จำนวน 152 คนในภาคเรียนการ ศึกษาที่ 2 ประจำปีการศึกษา 2547 ILDs ได้รับการพัฒนาขึ้นโดย Thornton และ Sokoloff (1998) ซึ่งเป็นรูปแบบการสอนที่ประกอบด้วยการทดลองทางฟิสิกส์ที่เกี่ยวข้องกับการเคลื่อนที่ที่หลากหลาย การประเมินประสิทธิภาพการสอนในรูปแบบนี้ ใช้แบบทดสอบแนวคิดเชิงวิทยาศาสตร์มาตรฐานในเรื่องแรงและการเคลื่อนที่ (FMCE) ฉบับภาษาไทยซึ่งได้มีการแปลขึ้นใช้ในคณะวิทยาศาสตร์มหาวิทยาลัยมหิดล โดยมีการทดสอบก่อนและหลังการเรียนการสอน

ภายหลังการสอนแบบ ILDs พบว่า normalized gain เท่ากับ 0.3 ซึ่งมีค่าสูงกว่าการสอนแบบเดิม (การบรรยาย) ในปี 2546 พบว่า normalized gain เท่ากับ 0.1 นอกจากนี้ยังพบว่า normalized gain จะสูงมากในกลุ่มเรื่องความเร่งและกฎข้อที่ 3 นิวตัน ผลการศึกษาชี้ให้เห็นว่า ILDs เป็นวิธีหนึ่งที่ช่วยให้นักเรียนมีความเข้าใจในเรื่องแรงและการเคลื่อนที่ ได้ดีขึ้นกว่าเดิม

Keywords: ILDs, FMCE, normalized gain

---

* ชื่อไทย: อำพล ใจรักษ์ Email: `ajairuk@yahoo.com`

NP02

Co-Synthesis of Gold Nanoparticles and Singlewalled Carbon Nanotubes on Quartz Substrates

การสังเคราะห์ร่วมของอนุภาคนาโนทองและท่อนาโนคาร์บอนชนิดผนังชั้นเดียวบนแผ่นรองรับควอตซ์

Naratip Songmee*and Pisith Singjai

Department of Physics, Faculty of Sciencs, Chiang Mai University,
Chiang Mai 50200, Thailand

Gold nanoparticles and single-walled carbon nanotubes (SWNTs) were co-synthesized on quartz substates by alcohol catalytic chemical vapor deposition. The substates were first deposited with gold thin films and were then coated with Co catalyst by coventional DC sputtering and dip-coat methods, respectively. The synthesis were carried out at 750 °C for 30 min under a pressure of 10 Torr. Characterizations of the as-grown product were performed by scanning electron microscopy and Raman spectroscopy. The results show that gold nanoparticles are distributed over SWNT bundles and have a diameter in the range of 20 to 100 nm, whereas the diameter of SWNTs are in the range of 0.9 to 1.5 nm. It is clearly seen that the SWNT yield decreases with the presence of the gold thin films and the mean size of the gold nanoparticles increases with increasing the gold film thickness.

งานวิจัยนี้ได้สังเคราะห์ร่วมอนุภาคของนาโนทองและท่อนาโนคาร์บอนชนิดผนังชั้นเดียว โดยวิธีตกสะสมไอเคมีจากไอของเอธานอลซึ่งใช้เป็นแหล่งกำเนิดคาร์บอน แผ่นรองรับควอตซ์ถูกนำไปเคลือบด้วยทองก่อนนำไปเคลือบโคบอลต์คะตะลิสต์โดยใช้เทคนิคแบบสปัตเตอริ่งด้วยไฟฟ้ากระแสตรงและวิธีจุ่มเคลือบตามลำดับ ทดลองสังเคราะห์ที่อุณหภูมิ 750 °C นาน 30 นาที ภายใต้ความดัน 10 Torr ผลการวิเคราะห์โดยจุลทรรศนศาสตร์อิเล็กตรอนแบบส่องกราดและรามานสเปคโตรสโคปี พบว่าผลิตภัณฑ์ที่ได้เป็นอนุภาคของนาโนทองกระจายตัวอยู่บนมัดของท่อนาโนคาร์บอนชนิดผนังชั้นเดียวและมีขนาดเส้นผ่านศูนย์กลางอยู่ในช่วง 20 ถึง 100 นาโนเมตร ในขณะที่พบว่าท่อนาโนคาร์บอนมีขนาดเส้นผ่านศูนย์กลางอยู่ ในช่วง 0.9 ถึง 1.5 นาโนเมตร เป็นที่แน่ชัดว่าปริมาณของท่อนาโนคาร์บอนชนิดผนังชั้นเดียวลดลงเมื่อมีฟิลม์บางของทองและขนาดโดยเฉลี่ยของอนุภาคนาโนทองเพิ่มขึ้นเมื่อความหนาของฟิลม์ของทองมากขึ้น

Keywords: co-synthesized, Gold nanoparticles, Single-Walled Carbon Nanotubes

---

* ชื่อไทย: นราธิป สงมี Email: `naratip_songmee@hotmail.com`

NRP01

Optimization of the ^{252}Cf-Based Explosive Detection System by Monte Carlo Simulation

การหาระบบตรวจวัตถุระเบิดที่ใช้แหล่งกำเนิดนิวตรอนชนิด ^{252}Cf ที่เหมาะสมจากการจำลองด้วยวิธีมอนติคาร์โล

Worasit Uchai[1], Sommai Changkian*[1] Han-Cheng Sun[2] and Zhong-Qi Wang[2]

1. *School of Physics, Institute of Science, Suranaree University of Technology, Nakhon Ratchasima 30000, Thailand*
2. *China Institute of Atomic Energy, P.O. Box 275(18), Beijing 102413, People's Republic of China*

The optimization of the ^{252}Cf-based Explosive Detection System (EDS) is performed by using Monte Carlo computer code. The EDS geometry has the rectangular shape with the inspection cavity surrounded by multi-layer of moderator, neutron and gamma-ray shielding materials. The dimensions of three moderators, namely, heavy water, light water and polyethylene were used in the optimization. The maximum thermal neutron flux in the inspection cavity for each moderator was simulated. Li_2CO_3 and Pb were used as neutron and gamma-ray shielding materials, respectively. Their thicknesses were optimized to obtain the minimum total dose at the outer surfaces of the EDS walls. The sensitivity and the minimum total dose of the EDS were estimated.

การหาระบบตรวจวัดวัตถุระเบิดที่ใช้แหล่งกำเนิดนิวตรอนชนิด ^{252}Cf ที่เหมาะสมจากการจำลองด้วยวิธีมอนติคาร์โลในการจำลองนี้ใช้รูปทรงที่เป็นทรงเหลี่ยมโดยมีตัวหยุดยั้งรังสีที่เป็นพื้นผิวหลายชั้นโดยมีชั้นป้องกันนิวตรอน ชั้นป้องกันรังสีแกมมาโดยชั้นหยุดยั้งรังสีที่ทำการจำลองมีวัตถุตัวอย่างคือ น้ำมวลหนัก น้ำมวลเบา และโพลีเอธิลีน ค่าเทอร์มอลนิวตรอนฟลักซ์สูงสุดที่ได้ในอุโมงค์ตรวจวัดเป็นตัวกำหมดค่าที่เหมาะสมอย่างหนึ่ง ลิเธียมคาร์บอเนต และตระกั่วใช้เพื่อกำบังนิวตรอนและรังสีแกมมา ความหนาของผนังแต่ละชนิดที่ทำให้ระบบมีความปลอดภัยต่อผู้ปฏิบัติงานและปริมาณเทอร์มอลนิวตรอนสูงสุดที่ได้จากการจำลองจะใช้ในการสร้างเครื่องตรวจวัดในห้องปฏิบัติการณ์ต่อไป

Keywords: Explosive Detection, Neutrons

---

[*] ชื่อไทย: สมหมาย ช่างเขียน Email: `Schangkian@hotmail.com`

O02

Development of a Waveguide-Based Near-Field Microwave Microscope

การพัฒนากล้องจุลทรรศน์สนามไมโครเวฟระยะใกล้ระบบท่อนำคลื่น

Salisa Wangtong*and Anupong Srongprapa

Applied Microwave Research Laboratory, Department of Applied Physics,
King Mongkut's Institute of Technology Ladkrabang, Bangkok 10520, Thailand

A near-field x-band microwave microscope using a probe in the form of open-end rectangular waveguide capped by metallic diaphragm with 2×2 mm^2 rectangular slot was developed. Images of various flat metallic samples are obtained by measuring the reflected wave signal corresponded to each 1 mm position as the probe is 2 dimensions automatically scanned over them. For 1 mm separation between the probe end and the sample surface, the image resolution in the direction perpendicular to the slot was 5 mm.

บทความนี้ นำเสนอการวิจัยพัฒนาสร้างระบบกล้องจุลทรรศน์สนามไมโครเวฟระยะใกล้ ที่ใช้หัวโพรบย่านความถี่แถบเอกซ์ มีลักษณะเป็นช่องเปิดสี่เหลี่ยมที่มีขนาดกว้าง 2 มิลลิเมตร ยาว 20 มิลลิเมตร ตรงด้านปลายท่อนำคลื่นสี่เหลี่ยม การสร้างภาพของวัตถุโลหะแบน กระทำโดยการตรวจวัดสัญญาณการสะท้อนของคลื่น ที่ค่าตำแหน่งต่าง ๆ ในแนวราบ 2 มิติของการเลื่อนวัตถุอย่างอัตโนมัติเทียบกับหัวโพรบ ทุก ๆ ระยะ 1 มิลลิเมตร ผลการทดสอบระบบที่มีระยะห่างจากหัวโพรบกับผิวชิ้นงาน 1 มิลลิเมตร ได้ความละเอียดการแยกแยะภาพในระดับ 0.5 มิลลิเมตร ในทิศตั้งฉากกับแนวยาวของช่องเปิด

Keywords: Near-field microwave microscope, Probe

---

* ชื่อไทย: ศลิษา วังทอง Email: `s7064109@kmitl.ac.th`

คณะกรรมการ

1. **คณะกรรมการดำเนินงาน:**

อธิการบดีมหาวิทยาลัยเทคโนโลยีสุรนารี	ที่ปรึกษา
นายกสมาคมฟิสิกส์ไทย	ที่ปรึกษา
ผู้อำนวยการศูนย์ปฏิบัติการวิจัยเครื่องกำเนิดแสงซินโครตรอนแห่งชาติ	ที่ปรึกษา
คณบดีสำนักวิชาวิทยาศาสตร์	ที่ปรึกษา
ศ. ดร. วิรุฬห์ สายคณิต	ที่ปรึกษา
ศ. ดร. สุทัศน์ ยกส้าน	ที่ปรึกษา
ผศ. ดร. ขจรยศ อยู่ดี	ที่ปรึกษา
หัวหน้าสาขาวิชาฟิสิกส์	ประธานกรรมการ
คณาจารย์สาขาวิชาฟิสิกส์	กรรมการ
คณาจารย์สาขาวิชาเทคโนโลยีเลเซอร์และโฟตอนนิกส์	กรรมการ
อ. ดร. ขรรค์ชัย โกศลทองกี่	กรรมการและเลขานุการ
นางสาวธัญลักษณ์ ธีรภัทรางกูร	ผู้ช่วยเลขานุการ

2. **คณะอนุกรรมการพิจารณาบทความ:**

หัวหน้าสาขาวิชาฟิสิกส์	ประธานอนุกรรมการ
คณาจารย์สาขาวิชาฟิสิกส์	อนุกรรมการ
คณาจารย์สาขาวิชาเทคโนโลยีเลเซอร์และโฟตอนนิกส์	อนุกรรมการ
อ. ดร. ขรรค์ชัย โกศลทองกี่	อนุกรรมการและเลขานุการ

3. **คณะอนุกรรมการฝ่ายวิชาการ:**

นายศุภปิยะ สิระนันท์	ประธานอนุกรรมการ
นายเสกสรร สุขะเสนา	อนุกรรมการ
นายอายุทธ ลิ้มพิรัตน์	อนุกรรมการ
นายนครินทร์ พัฒนบุญมี	อนุกรรมการ

นางสาวพรรัตน์ ศรีสวัสดิ์	อนุกรรมการและเลขานุการ

4. คณะอนุกรรมการฝ่ายวิชาการ:

อ. ดร. ขรรค์ชัย โกศลทองกี่	ประธานอนุกรรมการ
นายมรกต พุทธกาล	อนุกรรมการ
นายธนัญชัย ดาศรี	อนุกรรมการ
นายยุทธพงษ์ อินทร์กง	อนุกรรมการ
นายเสกสรร สุขะเสนา	อนุกรรมการ
นางสาวพรรัตน์ ศรีสวัสดิ์	อนุกรรมการ
นายไทยปัญญา จันปุ่ม	อนุกรรมการ
นางสาวกาญจนา ลิมป์บุญส่ง	อนุกรรมการ
นางสาวสุทัศนา ณ พัทลุง	อนุกรรมการ
นายอุฤทธิ์ เจริญอินทร์	อนุกรรมการ
นายกฤษกร ปาสาใน	อนุกรรมการ
นายอายุทธ ลิ้มพิรัตน์	อนุกรรมการและเลขานุการ

5. คณะอนุกรรมการฝ่ายเทคโนโลยีสารสนเทศ:

นายชลัมภ์ อุ่นอารีย์	ประธานอนุกรรมการ
นายศุภปิยะ สิระนันท์	อนุกรรมการ
นายนครินทร์ พัฒนบุญมี	อนุกรรมการ
นายภาคภูมิ เรือนจันทร์	อนุกรรมการ
นายอดิศักดิ์ บุญชื่น	อนุกรรมการ
นายกฤษดา กิตติมานะพันธ์	อนุกรรมการ
นายอนันท์ สัจจา	อนุกรรมการ
นายวันเฉลิม พูลสวัสดิ์	อนุกรรมการและเลขานุการ

6. คณะอนุกรรมการฝ่ายจัดหารายได้ ต้อนรับและลงทะเบียน:

นางสาวธัญลักษณ์ ธีรภัทรางกูร	ประธานอนุกรรมการ
นางชุติมา วัฒนชุมพล	อนุกรรมการ
นางสาวภัทราวรรณ์ สุนทราศรี	อนุกรรมการ
นางสาวธิดารัตน์ รายพิมาย	อนุกรรมการ
นางสาวสุกัญญา จารุศิริวัฒนา	อนุกรรมการ
นายอนุสรณ์ ตองอ่อน	อนุกรรมการ
นายสมชาย ชุมพลกุลวงศ์	อนุกรรมการ

นายมาโนชญ์ เฮงวัฒนะ	อนุกรรมการ
นายธนัญชัย ดาศรี	อนุกรรมการ
นายนพดล ดีแท้	อนุกรรมการ
นายอุฤทธิ์ เจริญอินทร์	อนุกรรมการ
นายกฤษกร ปาสาใน	อนุกรรมการ
นางสาวกนกนันท์ สารสมัคร	อนุกรรมการ
นายจิรโรจน์ ต. เทียนประเสริฐ	อนุกรรมการ
นางสาวอารีรัตน์ ดาวงศา	อนุกรรมการ
นางสาวรัชฎาภรณ์ ทรัพย์เรืองเนตร	อนุกรรมการ
นางดาริน อ่อนขาว	อนุกรรมการและเลขานุการ

7. คณะอนุกรรมการฝ่ายสวัสดิการ:

นางสาวธัญลักษณ์ ธีรภัทรางกูร	ประธานอนุกรรมการ
นางรัตติยา งอนชัยภูมิ	อนุกรรมการ
นายสมพงศ์ ปุงคานนท์	อนุกรรมการ
นายฐิติ สุทธิวงศ์	อนุกรรมการ
นายสุระ สุคนนท์	อนุกรรมการ
นายนำโชค จิตรแจ้ง	อนุกรรมการ
นางปัญญา เพียรปรุ	อนุกรรมการ
นางชุติมา วัฒนชุมพล	อนุกรรมการ
นางสาวปรางค์ขาว ปรุเขตต์	อนุกรรมการ
นางดวงพร ชื่นเกษม	อนุกรรมการ
นายชาคริต นวลฉิมพลี	อนุกรรมการ
นายสมหมาย ช่างเขียน	อนุกรรมการ
นายรามย์ พิณเจริญพันธุ์	อนุกรรมการ
นายวันเฉลิม พูลสวัสดิ์	อนุกรรมการ
นายอนันท์ สัจจา	อนุกรรมการและเลขานุการ

Scientific Program

29 มิถุนายน 2549

11.00 – 12.00 น. ลงทะเบียน

12.00 – 13.00 น. รับประทานอาหารกลางวัน

13.00 – 14.00 น. พิธีเปิด

Plenary Session A

Chair: Assoc. Prof. Dr. Prapan Manyum (SUT)

14.00 – 14.30 น. ปาฐกถาเรื่อง บทบาทฟิสิกส์ไทยในเวทีโลก

โดย ศ.ดร.ถิรพัฒน์ วิลัยทอง นายกสมาคมฟิสิกส์ไทย

Plenary Session B

Chair: Assoc. Prof. Dr. Prapan Manyum (SUT)

14.30 – 15.15 น. บรรยายหัวข้อ การประยุกต์ใช้แสงซินโครตรอน

โดย รศ.ดร.วีระพงษ์ แพสุวรรณ ผู้อำนวยการศูนย์ปฏิบัติการวิจัยเครื่องกำเนิดแสงซินโครตรอนแห่งชาติ

15.15 – 16.00 น. ถ่ายภาพหมู่และอาหารว่าง

Parallel Session C1 Condensed Matter and Material Physics

Chair: Dr.Paradorn Pakdeevanich (PSU)

16.00 – 16.20 น. CMMP01 Adisak Boonchun (SUT)

First Principles Study of Mn Impurity Location of Pb TiO_3

16.20 – 16.40 น. CMMP05 Kanoknan Sarasamak (SUT)

First Principles Study of the Wurtzite–to–Graphite-Like Phase Tranformation in ZnO

16.40 – 17.00 น. CMMP08 Pakpoom Ruanchan (SUT)

A Nitrogen-Carbon Molecule in GaAs: A First Principles Study

17.00 – 17.20 น. CMMP11 Sutassana Na Phattalung (SUT)

First Principles Study of Native Defects in Anatase TiO_2

17.20 – 17.40 น. CMMP10 Rarm Phinjaroenphan (SUT)

Effect of the Geometry of Metal–Insulator–Superconductor Junction on Its Tunneling Spectroscopy

Parallel Session C2 Accelerator Physics and Synchrotron Radiation Sciences

Chair: Dr. Burin Gumjudpai (NU)

16.00 – 16.20 น. APSRS01 Darin Onkaw (SUT)
X-Ray Absorption Study of TiO_2 and TiS_2 at the Siam Photon Laboratory

16.20 – 16.40 น. APSRS02 Moragote Buddhakala (SUT)
Evaluation of the Monochromator of the BL4 Beamline at the Siam Photon Laboratory

16.40 – 17.00 น. APSRS03 Noppadon Deethae (SUT)
Progress on Electron Beam Profile Measurement at the Siam Photon Source

17.00 – 17.20 น. APSRS04 Ratchadaporn Supruangnet (SUT)
LEED Study of the c(4×4) Reconstruction of Si(100)

17.20 – 17.40 น. APSRS05 Tananchai Dasri (SUT)
Initial Magnetic Measurements of Soft X-Ray Undulator for the Siam Photon Source

17.40 – 18.30 น. พักผ่อน

18.30 – 20.00 น. รับประทานอาหารเย็น

Plenary Session D

Chair: Assoc. Prof. Dr. Prasart Suebka (SUT)

20.00 – 21.30 น. เสวนาหัวข้อ ฟิสิกส์ไทย จากอดีตสู่อนาคต
โดย ศ.ดร.ถิรพัฒน์ วิลัยทอง (นายกสมาคมฟิสิกส์ไทย)
รศ.ดร.ประสาท สืบค้า (อธิการบดี มทส.)
รศ.ดร.วีระพงษ์ แพสุวรรณ (ผู้อำนวยการ ศซ.)
ผศ.ดร.สดชื่น วิบูลยเสข
และรศ.ดร.บัญชา พนเจริญสวัสดิ์

%%

30 มิถุนายน 2549

07.00 – 08.00 น. รับประทานอาหารเช้า

Plenary Session E

Chair: Dr. Khanchai Khosonthongkee (SUT)

08.00 – 08.40 น. บรรยายเรื่อง การวิจัยเอกภพวิทยายุคใหม่ในประเทศไทย
โดย ดร.บุรินทร์ กำจัดภัย นักวิจัยรุ่นใหม่ดีเด่น สกว.-สกอ. ประจำปี พ.ศ. 2548

<u>Parallel Session F1</u> Condensed Matter and Material Physics

Chair: Dr. Sukanya Tatchatraiphop (SUT)

08.50 – 09.10 น. CMMP04 Kamon Aiempanakit (KMUTT)
Effect of Annealing Ambienton Structural, Electrical and Optical Properties of ITO Films

09.10 – 09.30 น. CMMP06 Krit Koyvanitch (KU)
Effect of Sintering Behavior on Piezoelectric Properties of PZT and PZT doped with Pr_6O_{11}

09.30 – 09.50 น. CMMP07 Nattha Thaweegan (KU)
Thermal Properties of Degradable High Density Polyethylene Plastic Film

09.50 – 10.10 น. CMMP09 Pitak Eiamchai (KMUTT)
A Spectroscopic Ellipsometry Study of TiO_2 Thin Films Prepared by Ion-Assisted Electron-Beam Evaporation

<u>Parallel Session F2</u> Astronomy and Astrophysics, Nuclear and Radiation Physics, Cosmology and High Energy Physics

Chair: Dr. Burin Gumjudpai (NU)

08.50 – 09.10 น. AA01 Kitiyanee Asanok (KKU)
OH Masers Associated with Bipolar Molecular Outflows in Onsala1 Star-Forming Region

09.10 – 09.30 น. NRP01 Sommai Changkian (SUT)
Optimization of the ^{252}Cf-Based Explosive Detection System by Monte Carlo Simulation

09.30 – 09.50 น. CHEP06 Nattapong Yongram (SUT)
Particles Correlations in Quantum Field Theory

09.50 – 10.10 น. CHEP08 Seckson Sukkhasena (SUT)
Closed-Time Path in Quantum Field Theory

10.10 – 10.30 น. อาหารว่าง

Parallel Session G1 Cosmology and High Energy Physics

Chair: Asst. Prof. Dr. Sodcheun Wiboonsake (CMU/NU)

10.30 – 10.50 น. CHEP01 Ayut Limphirat (SUT)

Pentaquark Production in Neutron–Proton Collisions

10.50 – 11.10 น. CHEP03 Chakrit Nualchimplee (SUT)

$\bar{p}D$ Atom in Paris Potential

11.10 – 11.30 น. CHEP05 Kritsada Kittimanapun (SUT)

Calculation of ρ^0 Decay in Two-Step Process of $e^+e^- \to \pi^+\pi^-$

11.30 – 11.50 น. CHEP07 Pornrad Srisawad (SUT)

Meson Production in Heavy Ion Collisions at Intermediate Energies

Parallel Session G2 Educational and Fundamental Physics

Chair: Assoc. Prof. Dr. Samnao Phatisena (SUT)

10.30 – 10.50 น. EFP01 Apisit Tongchai (MU)

Conceptual Surveying on Mechanical Wave

10.50 – 11.10 น. EFP02 Kreetha Keawkhong (MU)

Science Students' Concepts of Reflection and Refraction of Light at Mahidol University

11.10 – 11.30 น. EFP03 Supasilp Fuengfung (MU)

Investigation of Students' Misconception in Direct Current

11.30 – 11.50 น. EFP04 Umpol Jairuk (MU)

The Use of Interactive Lecture Demonstrations in Force and Motion to Teach High School-level Physics

11.50 – 13.00 น. รับประทานอาหารกลางวัน

Plenary Session H

Chair: Asst. Prof. Dr. Worasit Uchai (SUT)

13.00 – 14.00 น. บรรยายเรื่อง วิทยาศาสตร์และวิทยาศาสตร์เทียมในข่าวและเรื่องราวรอบตัว

โดย ดร.บัญชา ธนบุญสมบัติ นักเขียนและนักวิจัย

ศูนย์เทคโนโลยีโลหะและวัสดุแห่งชาติ

Parallel Session I1 Condensed Matter and Material Physics, Others

Chair: Asst. Prof. Dr. Vittaya Amornkitbamrung (KKU)

14.20 – 14.40 น. CMMP02 Araya Mungchamnankit (KMUTT)

Electron Spin Resonance Study of Gd^{3+} in Zircon

14.40 – 15.00 น. CMMP03 Chittra Kedkeaw (KMUTT)

Impurities in Natural Diamond Observed by ESR Spectroscopy

15.00 – 15.20 น. O01 Rachsak Sakdanuphab (CU)

Decoherence in Josephson Junction Phase Qubit

15.20 – 15.40 น. O02 Salisa Wangtong (KMITL)

Development of a Waveguide-Based Near-Field Microwave Microscope

<u>Parallel Session I2</u> Industrial and Applied Physics, Optics and Photonics

Chair: Assoc. Prof. Wicharn Techitdheera (KMITL)

14.20 – 14.40 น. IAP01 Rungroj Maolanon (Nanotec)

Device for Measuring Total Harmonic Distortion of AC Voltage

14.40 – 15.00 น. IAP02 Wiriya Suwannet (MU)

Homemade Quartz Crystal Microbalance Systems for Alcohol Sensor

15.00 – 15.20 น. OP01 Jintawat Tanamatayarat (MU)

The Expansion of the Nd:YAG Slab and The Thermal Lens Effect in 3 W Single Side Pump Nd:YAG Laser

15.20 – 15.40 น. OP02 Siriwat Soontaranon (SUT)

Particle Sizing by Using Absolute Values of the Wavelet Transform of the Particle Holograms

15.40 – 16.00 น. อาหารว่าง

<u>Parallel Session J1</u> Cosmology and High Energy Physics

Chair: Dr.Buncha Thanaboonsombut (MTEC)

16.00 – 16.20 น. CHEP02 Chakkrit Kaeonikhom (NU)

Israel Junction Conditions on Hypersurface from Variational Principle Approach

16.20 – 16.40 น. CHEP04 Daris Samart (NU)

Cosmological Dynamics from Modified f(R) Gravity in Einstein Frame

16.40 – 17.00 น. CHEP09 Suppiya Siranan (SUT)

Schwinger's Quantum Dynamical Principle and Quantization Problem of Gauge Theories

<u>Parallel Session J2</u> Nanoscale Physics, Ion Beam and Plasma Physics

Chair: Assoc. Prof. Dr. Bancha Panacharoensawad (KU)

16.00 – 16.20 น.	NP01 Chewa Thassana (KMITL) Growth and Characterization of NiFeN Thin Film by Reactive Gas Timing RF Magnetron Sputtering
16.20 – 16.40 น.	NP02 Naratip Songmee (CMU) Co-Synthesis of Gold Nanoparticles and Singlewalled Carbon Nanotubes on Quartz Substrates
16.40 – 17.00 น.	IBPP01 Thidarat Supasai (CU) Fabric and Fiber Modification Using Radio Frequency Plasma Process
17.00 – 18.30 น.	พักผ่อน
18.30 น.	งานเลี้ยงรับรอง

%%%%%%%%%%%%%%%%%%%%%%%%%%%%%%%%%%%%

1 กรกฎาคม 2549

07.00 – 09.00 น.	รับประทานอาหารเช้า

<u>Plenary Session K</u>

09.00 – 10.00 น.	แนะนำงานวิจัยของแต่ละสถาบัน 1. มหาวิทยาลัยขอนแก่น โดย ผศ.ดร.วิทยา อมรกิจบำรุง 2. มหาวิทยาลัยนเรศวร โดย ดร.บุรินทร์ กำจัดภัย 3. สถาบันเทคโนโลยีพระจอมเกล้าเจ้าคุณทหารลาดกระบัง โดย รศ.วิชาญ เตชิตธีระ 4. มหาวิทยาลัยสงขลานครินทร์ โดย ดร.ภราดร ภักดีวานิช 5. มหาวิทยาลัยเกษตรศาสตร์ โดย รศ.ดร.บัญชา พนเจริญสวัสดิ์
10.00 – 10.20 น.	อาหารว่าง
10.20 – 11.00 น.	แนะนำโครงการจัดตั้ง Thai Physics Data Base และ อภิปรายสรุปงาน 1. แนะนำโครงการจัดตั้ง Thai Physics DataBase โดย คุณเสกสรร สุขะเสนา และคุณศุภปิยะ สิระนันท์ 2. ความรู้สึกจากครูสังเกตการณ์ โดยครูศักดิ์ สุวรรณฉาย จากโรงเรียนแก่นนครวิทยาลัย จังหวัดขอนแก่น 3. วิดีทัศน์ ประมวลภาพงาน

11.00 – 12.00 น. มอบเกียรติบัตรและพิธีปิด

รางวัลผู้เสนอผลงานดีเด่นจำนวน 5 รางวัล ได้แก่

- (1) นายอภิสิทธิ์ ธงไชย มหาวิทยาลัยมหิดล
- (2) นายศิริวัช สุนทรานนท์ มหาวิทยาลัยเทคโนโลยีสุรนารี
- (3) นายพิทักษ์ เอี่ยมชัย มหาวิทยาลัยเทคโนโลยีพระจอมเกล้าธนบุรี
- (4) นายจินตวัฒน์ ตันอมาตยรัตน์ มหาวิทยาลัยมหิดล
- (5) นายภาคภูมิ เรือนจันทร์ มหาวิทยาลัยเทคโนโลยีสุรนารี

เกียรติบัตรแก่ผู้เข้าร่วมประชุมและเสนอผลงานทั้ง 12 สถาบัน

- (1) จุฬาลงกรณ์มหาวิทยาลัย
- (2) มหาวิทยาลัยเกษตรศาสตร์
- (3) มหาวิทยาลัยขอนแก่น
- (4) มหาวิทยาลัยเชียงใหม่
- (5) มหาวิทยาลัยมหิดล
- (6) มหาวิทยาลัยเทคโนโลยีพระจอมเกล้าธนบุรี
- (7) สถาบันเทคโนโลยีพระจอมเกล้าเจ้าคุณทหารลาดกระบัง
- (8) มหาวิทยาลัยราชภัฏสมเด็จเจ้าพระยา
- (9) มหาวิทยาลัยสงขลานครินทร์
- (10) มหาวิทยาลัยศรีนครินทรวิโรฒ
- (11) มหาวิทยาลัยนเรศวร
- (12) มหาวิทยาลัยเทคโนโลยีสุรนารี

12.00 – 13.00 น. รับประทานอาหารกลางวัน

13.30 น. เดินทางกลับโดยสวัสดิภาพ

Author Index

พิมพ์ที่ หจก.มิตรภาพการพิมพ์ 1995
267 ถ.มิตรภาพ (ติด ธ.กรุงไทย ใกล้ทางเข้า บขส. เก่า) ต.ในเมือง อ.เมือง จ.นครราชสีมา 30000
โทร. (044) 241476, 244551, 263128 FAX. 244551